TECHNISCHE
UNIVERSITÄT
DRESDEN

Leibniz Institute
for Solid State and
Materials Research
Dresden

Development of Novel Low-Modulus β-Type Ga-/Cu-Bearing Ti–Nb Alloys for Antibacterial Bone Implant Applications

von der

Fakultät Maschinenwesen

der

Technischen Universität Dresden

zur Erlangung des akademischen Grades

Doktoringenieur (Dr.-Ing.)

angenommene

DISSERTATION

von

M. Sc. **Alberta Ludovico Andrea**

Tag der Einreichung: 30.05.2023
Tag der Verteidigung: 23.11.2023

Vorsitzender: Prof. Dr. Gianaurelio Cuniberti (TU Dresden)
Gutachter: Prof. Dr. Kornelius Nielsch (TU Dresden)
Gutachter: Prof. Dr. Jürgen Eckert (Montanuniversität Leoben)

The present Ph.D. work was financially supported by the European Commission within the European Union's Horizon 2020 research and innovation programme under the Marie Skłodowska-Curie grant agreement No. 861046 (BIOREMIA ITN).

BIOREMIA
European Training Network

Contents

Abstract

Commercially available titanium (Ti) alloys, such as Ti–6Al–4V and c.p. Ti, even though established in clinical use as load-bearing bone implant materials in orthopedics and dentistry, possess significant drawbacks that may lead to implant failure: i) presence of alloying elements with harmful health effects, ii) high Young's modulus ($E > 100$ GPa) compared to human cortical bone ($E_{\text{bone}} = 10 - 30$ GPa), and iii) lack of antibacterial activity against multidrug-resistant bacteria, which may lead to implant-associated infections. To overcome the first two drawbacks, a new generation of biocompatible metastable β-type Ti alloys has been developed, in particular β-type Ti–Nb alloys, which are versatile candidates due to their low Young's modulus, high strength-to-weight ratio and improved corrosion resistance.

The present work aims to tackle all three aforementioned issues by developing novel β-type Ti–45Nb-based alloys with potential intrinsic antibacterial activity by adding antibacterial gallium (Ga) and copper (Cu) in minor amounts (up to 8 wt.%) via metallurgical route. Nine alloys with the following chemical compositions: (100-x)(Ti–45Nb)–xGa, (100-x)(Ti–45Nb)–xCu (where x = 2, 4, 6, 8 wt.%), and 96(Ti–45Nb)–2Ga–2Cu, based on alloy design approaches, were produced by controlled casting and homogenization treatment. The effect of antibacterial alloying additions on phase constitution, mechanical characteristics, corrosion, and tribocorrosion response in a simulated physiological environment has been investigated. All nine alloys in the homogenized state display a single-phase β (BCC) phase microstructure, whose lattice parameter is proved to be sensitive to Ga and Cu content, with an almost linear contraction. The mechanical characteristics are strongly influenced by Ga and Cu addition, with a general strengthening effect mainly attributed to substitutional solid solution strengthening, and to grain boundary strengthening in case of Ga. Deformation behavior indicates high mechanical stability of the β phase, suggesting dislocation slip as dominant deformation mechanism. The results demonstrate that strategic alloy design is an effective method to significantly increase strength without adversely affecting the Young's modulus, which remains in the range of good biomechanical compatibility ($E = 64 - 104$ GPa). Evaluation of the corrosion response and metal ion release in simulated physiological environment demonstrates the high corrosion resistance of the nine alloys, whereas tribocorrosion wear resistance increases upon Ga addition. Further thermal (aging) treatments, carried out on a specific Cu-containing alloy, proved the feasibility of tailoring enhanced mechanical, chemical and potentially antibacterial properties by thermally-induced precipitation of Ti_2Cu intermetallic compound.

These novel developed alloys are considered to be promising candidates for biomedical bone implant applications.

Kurzfassung

Kommerziell erhältliche Titanlegierungen wie Ti–6Al–4V und c.p. Ti haben sich zwar in der klinischen Anwendung als lasttragende Knochenimplantate in der Orthopädie und Zahnmedizin etabliert, weisen jedoch erhebliche Nachteile auf, die zu Implantatversagen führen können: i) Vorhandensein gesundheitsschädlicher Legierungselemente, ii) hoher Elastizitätsmodul ($E > 100$ GPa) im Vergleich zu menschlichem Knochen ($E_{\text{bone}} = 10 - 30$ GPa), und iii) fehlende antibakterielle Aktivität gegen multiresistente Bakterien, die implantatbefogene Infektionen verursachen können. Um die beiden erstgenannten Nachteile zu beseitigen, wurde eine neue Generation von biokompatiblen metastabilen Ti-Legierungen des β-Typs entwickelt, insbesondere Ti–Nb-Legierungen des β-Typs, die aufgrund ihres niedrigen Elastizitätsmoduls, ihres hohen Festigkeit-Gewicht-Verhältnisses und ihrer verbesserten Korrosionsbeständigkeit vielseitig einsetzbar sind.

Die vorliegende Arbeit zielt darauf ab, alle drei genannten Probleme durch die Entwicklung neuartiger Legierungen auf Ti–45Nb-Basis mit potenzieller intrinsischer antibakterieller Aktivität zu lösen, indem auf metallurgischem Weg antibakterielles Gallium (Ga) und Kupfer (Cu) in geringen Mengen (bis zu 8 Gew.%) hinzugefügt werden. Neun Legierungen mit den folgenden chemischen Zusammensetzungen: (100-x)(Ti–45Nb)–xGa, (100-x)(Ti–45Nb)–xCu (mit x = 2, 4, 6, 8 Gew.%), und 96(Ti–45Nb)–2Ga–2Cu, basierend auf den Ansätzen des Legierungsdesigns, wurden durch kontrolliertes Gussverfahren und Homogenisierungsbehandlung hergestellt. Der Einfluss antibakterieller Legierungszusätze auf die Phasenzusammensetzung, die mechanischen Eigenschaften, die Korrosion und das Tribokorrosionsverhalten in einer simulierten physiologischen Umgebung wurde untersucht. Alle neun Legierungen weisen im homogenisierten Zustand ein einphasiges β (BCC)-mikrostrukturelles Gefüge auf, dessen Gitterparameter nachweislich empfindlich auf den Ga- und Cu-Gehalt mit einer fast linearen Kontraktion antworten. Die mechanischen Eigenschaften werden durch die Zugabe von Ga und Cu stark beeinflusst, wobei ein allgemeiner Verfestigungseffekt hauptsächlich auf die Substitutionsmischkristallverfestigung und im Falle von Ga auf die Korngrenzenverfestigung zurückzuführen ist. Das Verformungsverhalten zeigt eine hohe mechanische Stabilität der β Phase, was auf Versetzungsgleiten als den dominanten Verformungsmechanismus hindeutet. Die Ergebnisse zeigen, dass strategisches Legierungsdesign eine wirksame Methode ist, um die Festigkeit deutlich zu erhöhen, ohne den Elastizitätsmodul negativ zu beeinflussen, der sich im Bereich guter biomechanischer Kompatibilität befindet ($E = 64 - 104$ GPa). Die Bewertung des Korrosionsverhaltens und der Metallionenfreisetzung in einer simulierten physiologischen Umgebung zeigt die hohe Korrosionsbeständigkeit der neun Legierungen, während die Tribokorrosions-Verschleißfestigkeit durch die

Zugabe von Ga zunimmt. Weitere thermische (Auslagerungs-)Behandlungen, die an einer spezifischen Cu-haltigen Legierungsprobe durchgeführt wurden, haben gezeigt, dass es möglich ist, verbesserte mechanische, chemische und potenziell antibakterielle Eigenschaften durch die thermisch induzierte Ausscheidung der intermetallischen Ti_2Cu Phase zu erzielen.

Diese neu entwickelten Legierungen gelten als vielversprechende Kandidaten für biomedizinische Knochenimplantatanwendungen.

List of Symbols & Abbreviations

List of Symbols (1/2)

Symbol	Explanation	Unit
a_β	Lattice constant of the BCC β phase	m
A	Atomic mass	amu
d_{grain}	Average grain diameter	m
δ_e	Elastic energy	MJ m^{-3}
Δr_a	Average atomic radius difference	m
$\varnothing$	Diameter	m
e/a	Electron-to-atom ratio (equal to n_{ox})	-
ε_T	True strain	-
ε	Engineering strain	-
ε_max	Strain at fracture/maximum strain (engineering)	-
ε_y	Yield strain (engineering)	-
E (E^{US})	Young's modulus (determined by ultrasonic method)	Pa
$HV_{0.1}$	Vickers microhardness	-
K^{US}	Bulk modulus (determined by ultrasonic method)	Pa
k	Proportionality factor	-
K	Strength coefficient	Pa
λ	X-ray wavelength	m
L_0	Gauge length of tensile specimens	m
M_s	Martensitic transformation temperature	°C or K
ν	Poisson's ratio	-
n	Hardening exponent	-
ρ	Density	Kg m^{-3}
r_a	Atomic radius	m
S_0	Cross section of tensile specimens	m
σ_T	True stress	Pa
σ	Engineering stress	Pa
${\sigma_\mathrm{y}}^\mathrm{compr}$	Compressive yield strength (engineering)	Pa
${\sigma_\mathrm{y}}^\mathrm{tens}$	Tensile yield strength (engineering)	Pa
σ_f	Tensile fracture strength (engineering)	Pa
σ_UTS	Ultimate tensile strength (engineering)	Pa
T, T_m	Temperature, melting temperature	°C or K
V_L	Longitudinal acoustic speed of sound waves	m s^{-1}
V_T	Transverse acoustic speed of sound waves	m s^{-1}
Z	Atomic number	-

List of Symbols (2/2)

Symbol	Explanation	Unit
A_a	Anode area	m^2
A_c	Cathode area	m^2
B_a	Tafel anodic constant	V dec^{-1}
B_c	Tafel cathodic constant	V dec^{-1}
D	Wear depth	m
E_{OCP}	Open circuit potential	V
E_{corr}	Corrosion potential	V
E_{wear}	Open circuit potential during sliding wear	V
F	Faraday's constant	C mol^{-1}
i_{exc}	Excess current	A
i_{final}	Current after sliding	A
i_{wear}	Current during sliding	A
j_{corr}	Corrosion current density	A cm^{-2}
j_{pass}	Passive current density	A cm^{-2}
M_{mol}	Molecular mass	g mol^{-1}
n_{ox}	Charge number (equal to e/a)	-
t_{rub}	Sliding (or rubbing) time	s
t_{repass}	Repassivation time constant	s
V_{chem}	Volume loss due to corrosion	m^3
V_{mech}	Volume loss due to mechanical wear	m^3
V_{tot}	Total volume loss	m^3
V_{wac}	Volume loss due to wear accelerated corrosion	m^3

List of Abbreviations

Abbreviation	Explanation
α, α', α"	HCP α phase, HCP (α') and orthorhombic (α") martensites
AC	As-cast
Ag|AgCl	Saturated silver chloride electrode
at.%	Atomic percentage*
β	BCC β phase
BCC	Body centered cubic crystal structure
CE	Counter electrode
CGHE	Carrier gas hot extraction
COF	Coefficient of friction
c.p. Ti	Commercially pure (unalloyed) titanium
CT	Computed tomography
DSC	Differential scanning calorimetry
EAS	Elastic admissible strain
EBSD	Electron back scattering diffraction
EDX	Energy dispersive X-ray spectroscopy
HCP	Hexagonal close packed crystal structure
IAI (BAI)	Implant- (biomaterial-)associated infections
ICP-MS	Inductively coupled plasma - mass spectrometry
ICP-OES	Inductively coupled plasma - optical emission spectroscopy
LOD	Limit of detection
LOQ	Limit of quantification
OCP	Open circuit potential
ω (ω_{ath}, ω_{iso})	ω phase (athermal, isothermal)
PEG	Polyethylene glycol
PBS	Phosphate-buffered saline
PMMA	Polymethyl methacrylate
RE	Reference electrode
RT	Room temperature
SCE	Saturated calomel electrode
SEM	Scanning electron microscopy
SHE	Standard hydrogen electrode
SIM	Stress-induced martensitic transformation
STQ	Solution-treatment and water quenching
THR	Total hip replacement
TJR	Total joint replacement
TNTZ	Ti–29Nb–13Ta–4.6Zr alloy (wt.%)
TNZ	Ti–13Nb–13Zr alloy (wt.%)
WE	Working electrode
XRD	X-ray diffraction
wt.%	Weight percentage*

(* Explanation of the alloy nomenclature used in this work is reported in Appendix A)

Chapter 1

Scope of the Thesis

1.1 Motivation: Failure of Bone Implants

The demand for bone-related implants is on the rise mainly due to the increasingly aging population worldwide and growing needs for a better life quality. Implanted biomaterials play a key role in the current success of orthopedic and dental procedures. Metals are the material of choice for structural (load-bearing) medical devices because of their excellent mechanical properties.

Among metallic biomaterials (stainless steel, Co–Cr alloys, precious metals), titanium (Ti) and its alloys are generally preferred due to their superior biocompatibility and corrosion resistance combined with low density and high specific strength [1]. However, clinically used Ti-based materials, such as commercially pure (c.p.) Ti and Ti–6Al–4V alloy, still have some drawbacks that could lead to implant failure [2]. They exhibit a higher Young's modulus ($E \geq 100$) compared to human cortical bone ($E_{\mathrm{bone}} = 10 - 30$ GPa). Large modulus mismatches cause insufficient loading of bone adjacent to the implant, resulting in stress-shielding effects that cause tissue loss and implant failure [3]. In addition, long-term studies have shown the development of health disorders elicited by the release of metallic ions including aluminum (e.g., neurodegenerative diseases) and vanadium (e.g., genetic damage) into the surrounding tissues and bloodstream [4, 5]. Therefore, great research effort is currently dedicated to the development of new titanium alloys with reduced elastic modulus and improved biological properties. The current focus of metallic biomaterial research is on β-type Ti alloys with no harmful alloying additions, which possess a low elastic modulus and sufficient strength, making them ideal for implant applications. Of particular interest are β-type Ti–Nb-based alloys, which exhibit Young's modulus values of 60 – 69 GPa, significantly lower than those of Ti-based implant materials commonly used in clinical settings (i.e., c.p. Ti, Ti–6Al–4V) [6]. Another leading cause of implant failure is biomaterial-associated infections (BAI) caused by bacterial biofilms. These biofilms may form on the implant surface during surgery, and are often resistant to the body's immune response, making them difficult to eradicate. This is particularly concerning because the bacteria growing in a biofilm are extremely resistant to antibiotic treatment. If antibiotics are unsuccessful, the final option to control the infection is revision surgery, which involves implant removal [7, 8]. Chronic implant-related bone infections are a serious burden on the healthcare system, with high economic and social-associated costs. For instance, for trauma-related bone reconstructions, the infection risk ranges from 10% to 50%, depending on the fracture type [9]. Each year in the European Union alone, over 4 million patients acquire healthcare-associated infections, which cause around 37 000 deaths and cost 7 billion €/year [10]. Half of them are related to medical devices and 80% of these are caused by bacterial biofilms.

Currently, attention is increasingly turning to the development of medical devices which are ‘anti-infective’, ‘antibacterial’ or ‘antibiofilm’. , Since there is currently no standard treatment for implant-/biomaterial-associated infections (IAI, BAI) and since antibiotic treatments are controversial and ineffective for biofilms [7, 8], the best infection control approach is to develop novel preventive measures which specifically focus on the inhibition of both bacterial adhesion and biofilm formation, for instance by acting on the implant material itself. Functionalizing metallic prostheses through innovative compositions or application of coatings can significantly improve the success rate of bone replacement surgeries by preventing or limiting infection-related inflammatory reactions, which can impede new bone formation [11]. Therefore, in recent years, there has been increasing research attention towards developing materials that render the surface of implants resistant to bacterial biofilm contamination.

Within this thesis, novel Ti-based materials with potential antibacterial properties are developed. Focus of the present research is set on the effect of antibacterial gallium (Ga) and copper (Cu) metallurgical additions on the structural characteristics, mechanical, and chemical properties of a β-type Ti–Nb alloy. The selection of the Ti–Nb alloy system was based on its significance as a prototype system that serves as the basis for several alloy formulations relevant for bone implants, distinguished by a low Young’s modulus. The starting composition was the low-modulus Ti–45Nb (wt.%) alloy with a single-phase β microstructure. Small amounts of the metallic elements Ga and/or Cu were added to it to produce novel low-modulus (100-x)(Ti–45Nb)–xGa/Cu alloys (where x = 2, 4, 6, 8 wt.%). The present Ph.D. work was conducted and financed in the framework of a European project (Horizon 2020 - Marie Skłodowska-Curie Initial Training Network/ITN) named BIOREMIA (BIOfilm-REsistant Materials for hard tissue Implant Applications). The ITN project aims to tackle the implant-related infections caused by bacterial biofilms by proposing innovative material-based solutions with enhanced antimicrobial functionality, that will result in improved biological acceptance of implants for hard tissue applications (orthopedics and dentistry).

1.2 Objectives & Organization of the Thesis

Objectives

The overall goal of the present work is to develop novel β-type Ti-based alloys for antibacterial implant applications by investigating the effect of minor metallurgical additions of Ga and Cu on the Ti–Nb alloys’ properties.

The specific objectives of this study are:

- to produce chemically homogeneous bulk Ti–Nb–Ga/Cu alloys (with Ga/Cu content up to 8 wt.%) by controlled casting;
- to characterize their microstructure in as-cast and homogenized state;
- to study how antibacterial Ga/Cu alloying additions impact the mechanical behavior of the developed alloys;
- to investigate how antibacterial Ga/Cu additions affect corrosion and tribocorrosion resistance of the alloys in a simulated physiological environment;
- to study the possibility of creating antibacterial microstructures by aging heat treatments and their impact on the alloys' mechanical and chemical properties.

Organization of the Thesis

This dissertation consists of eight chapters as follows:

Chapter 1 opens the work with the objectives of the thesis and driving motivation.

Chapter 2 presents the theoretical background on structural implant materials and their limitations, with focus on Ti-alloys and their mechanical, corrosion, and tribocorrosion properties. It also includes a section about current trends in metallic biomaterials with enhanced antibacterial functionality for reducing the infection risks, required for understanding the research carried out in this thesis.

Chapter 3 presents the alloy synthesis routes, the experimental conditions, and the characterization methods used throughout this work.

Chapters 4 through 7 present and discuss the results of this study.

Chapter 4 presents the microstructural characteristics and investigates the mechanical behavior of the novel Ga-/Cu-containing Ti–Nb alloys.

Chapters 5 & 6 contain the investigations conducted on the influence of the alloying elements Ga and Cu on the corrosion and tribocorrosion properties of the alloys, as well as their Ga/Cu ion release, in simulated physiological environment.

Chapter 7 reports further studies (microstructural, mechanical and corrosion) conducted on a specific alloy composition (Ti–Nb–Cu) subjected to different aging treatments. The main goal was to prove the tunability of alloy microstructures, which therefore contribute in tailoring specific mechanical and corrosion properties.

Chapter 8 points out the main conclusions of the doctoral thesis and briefly outlines suggestions for future work. The latter are supported by preliminary data and pilot studies: biological assessment and a demonstrator of a dental implant.

The last sections include bibliographic references, list of publications and conference contributions, acknowledgements, and appendices.

Chapter 2

Theoretical Background & State of the Art

2.1 Metallic Biomaterials for Load-Bearing Implants

Implanted medical devices are widely used for diagnostic and therapeutic purposes across many medical specialties. The demand for long-term durable orthopedic and dental implants is being driven by the world population's continued aging, an active lifestyle and greater expectations for life quality. Thus, considerable research efforts have been devoted to identifying suitable biomaterials for the production of structural, durable medical implants.

A biomaterial is any nonviable material intended to interact and interface with biological systems with the aim of treating, evaluating or replacing any organ, tissue or function of the body. Many aspects and issues have to be considered before introducing a new biomaterial to the market, such as the designated anatomic location, toxicology, biocompatibility, chemical and mechanical requirements, ethics, standardization, and regulation. One of the main requirements of a biomaterial is biocompatibility, defined as *'the ability of a material to perform with an appropriate host response in a specific application'* [12]. This definition is based on three pillars: i) the material has to actively perform and not simply exist in the body, ii) the host response should be appropriate for the application and iii) the nature of the response and its appropriateness may vary depending on the situation. Therefore, two key aspects are fundamental when developing a biocompatible material: host reactions induced by the material and the degradation of the material itself in the body environment [13]. There exist many types of biomaterials: polymers, metals, ceramics, (nano)composite materials, and natural biomaterials. Their field of application is exceedingly wide and vast: orthopedics, wound healing, tissue engineering scaffolds, ophthalmic, drug-delivery systems, dental, and cardiovascular applications [14–16]. In all cases, the material biocompatibility is of central importance. The chemical interactions of the implant material in the *in vivo* environment can lead to the release of implant particles into the body fluids, which may trigger an inappropriate immune response. The design and selection of the suitable biomaterial depends on its specific medical application, and it is time-, place- and function-dependent. In the specific case of permanent metallic implants for load-bearing applications, and in order to serve safely and appropriately for a certain period of time without rejection, the metallic material should possess the following essential characteristics, but not limited to [17]:

- excellent biocompatibility and osseointegration (in case of bone prostheses);
- outstanding mechanical properties: specific and impact strength, ductility, fatigue resistance, low stiffness;
- long-term dimensional stability;
- superior corrosion resistance in the body environment;
- improved tribological properties: high wear resistance and low friction;
- processability: machinability, castability, deformability, weldability, powder metallurgy;
- active behavior, e.g., antibacterial, against relevant pathogens.

Metallic materials are widely used for load-bearing implants in various bone-related applications (Fig. 2.1), such as dentistry (artificial tooth roots, denture bases, dental restorations, orthodontic wires, clips, valves) and orthopedic surgery (artificial joints, spinal fixation devices, osteosynthesis devices), to support body weight together with bones and joints, and to help in reconstruction of motor functions [18]. Orthopedic implants fall into two categories: i) permanent implants, acting as substitutes for bone and joints (i.e., for hips, knees, ankles, shoulders, elbow, wrists), and ii) temporary implants, used for the fixation of fracture bones (e.g., ostheosynthesis products, like bone nails, plates, wires, screws). These two different fields of application yield different demands on implant design and properties [19]. In case of permanent implants, the bone conductivity of the implant material should be high, with bioactive surfaces that enable proper tissue ingrowth and vascularization; moreover, they are expected to serve in the human body throughout the life span of the patients. On the other side, in the case of temporary (removable) implant applications, a reduced bioactivity is desirable as they are meant to serve for a relatively short time, only long enough to allow bones to heal. This is particularly true for trauma implants such as bone nails and plates, which lose their function after the fracture healing period, and are subsequently removed.

The metallic biomaterials can be categorized in the following four groups based on the major alloying element (Table 2.1): stainless steels, cobalt-based alloys, titanium-based alloys, and miscellaneous others (e.g., NiTi, alloys of Mg and Ta, precious metals and their alloys, etc.) [17]. Presently, a large number of nontoxic and allergy-free metallic materials with good mechanical and biological compatibility is in clinical use or under development. Despite this large number, only a few are capable of long-term success in the clinical practice. Moreover, current metallic biomaterials do not possess bio-functionalities (e.g., bio-activeness, osseointegration, antibacterial properties), therefore modifications such as structuring and chemical and/or physical functionalization are required.

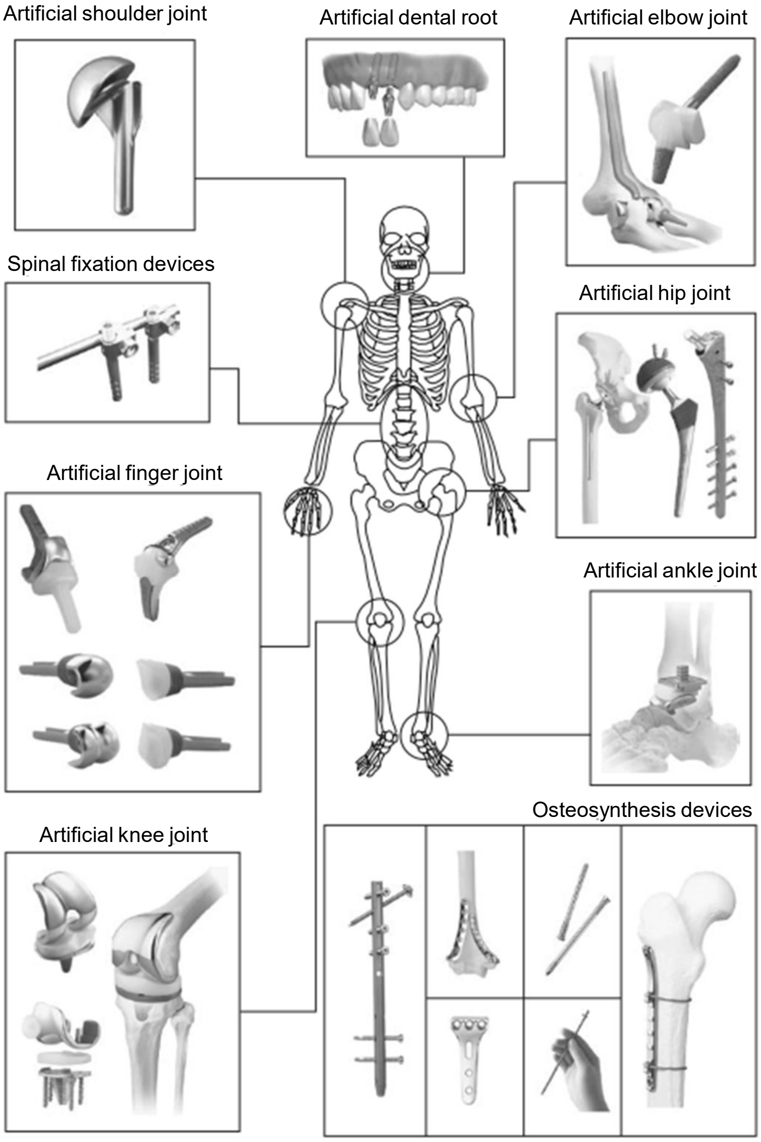

Figure 2.1: Various bone-related metallic implants that are used *in vivo* for orthopedic surgery and dentistry (reproduced from Ref. [20]).

In the present work, the attention is focused on Ti-based metallic biomaterials for bone-related implant applications (orthopedics and dentistry). Pure titanium and its medical-grade alloys have been extensively used as medical implants owing to their high biocompatibility, corrosion resistance, and lower Young's modulus, compared to other metallic biomaterials [1].

Table 2.1: Main categories of metallic biomaterials and their applications as implants [21, 22].

Type	Application	Representative commercial products
Ti alloys (c.p. Ti and Ti–6Al–4V)	Stem and cup of THRs Dental implants Intervertebral discs replacement Bone screw and plates	*The Tether*™ - Vertebral Body Tethering System, *Tigran*™ PTG, *INTER FIX*™ RP Threaded Fusion Device
Stainless steels (316 and 316L)	Temporary devices (screws, hip fracture nails and plates) THRs	*Express*™ SD (Boston Scientific)
Co–Cr alloys	TJRs (wrought alloys) Dentistry castings Surgical wire Heart valve	*Sigma*® Total Knee System, *ANTHEM* Total Knee System (Smith+Nephew)
Ni–Ti alloys	Vascular stents Orthodontic dental archwires Catheter guide wires Orthopedic staples	*Niti-S*™ Gastrointestinal Metallic Stent, *Homer Mammalok*™
Mg alloys	Cardiovascular stents	*Magmaris*® Coronary Resorbable Magnesium Scaffold (Biotronik)
Ta alloys	Wire suture Radiographic marker	*Trabecular Metal*™ Technology (Zimmer Biomet)
Noble alloys	Dental prosthesis	*Trias*® Implant System (Servo-dental)

(THR/TJR: total hip/joint replacement)

2.1.1 Mechanical Behavior & Stress-Shielding Effect

Metallic materials are used in a broad range of applications as bone implant materials due to their fine mechanical reliability *in vivo*. The human bone is a living complex hierarchically structured and anisotropic system which plays many roles in the body environment: body weight support and movement assistance, protection of organs, and more. Human bones are satisfactorily tough and strong with high fatigue resistance, however, due to trauma or disease, bone is often damaged or lost, therefore substitution with artificial medical devices is needed.

The success of a metallic biomaterial for load-bearing applications depends on its ability to meet several criteria, including strength, toughness, ductility, fatigue and wear resistance, and bone bonding capacity. In addition to these properties, it is crucial that the device has an elastic modulus similar to that of human bones ($E_{\text{bone}} = 10 - 30$ GPa), which allows for optimal load transfer and distribution. Hence, device stiffness is of outstanding importance. Long-term studies indicate that insufficient load transfer from the artificial implant material to the surrounding hard tissues may result in bone resorption, eventual loosening and fracture of the prosthetic device (Fig. 2.2a). This phenomenon, termed *stress-shielding* (Fig. 2.2b), is a direct result of the stiffness mismatch between the artificial implant, and the adjacent bone [3].

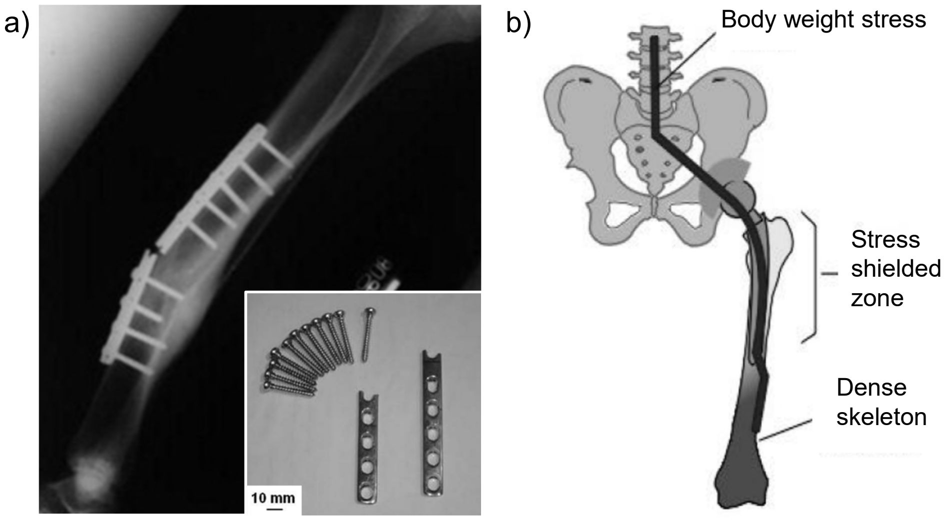

Figure 2.2: (a) Radiography of a failed stainless steel implant inside a patient and (inset) the same implant after removal (adapted from Ref. [23]). (b) Scheme of the stress-shielding effect (reproduced from Ref. [3]).

Matching the biomechanical requirements of a bone is of absolute relevance. Metallic materials can bear significant loads and undergo plastic deformation prior to failure. However, Ti and its alloys are generally preferred because of their lower elastic modulus. The stiffness mismatch was identified as major reason for implant loosening and failure, therefore a reduction of stiffness of the implant material is an important design consideration to be taken into account [21]. A summary of their mechanical properties, together with those of cortical bone, is given in Table 2.2. The mechanical working conditions of the human body are complex: skeletal bone implants (artificial hip joints, knee joints, plates, and spinal fixations) and dental implants suffer from fatigue due to intense cyclic loading. A material undergoing cyclic loading can fracture far below its ultimate tensile strength, and even below its yield strength: fatigue fractures occur under normal service conditions with no prior warning, thus making them very dangerous and difficult to predict [24]. Many current metallic materials in the clinical practice were first developed for other applications (structural materials, aerospace applications, etc.) and later converted to biomedical applications. From this perspective, modern research aims at the improvement of current biomedical devices and at the development of next-generation biomaterials with outstanding properties and biofunctionalities.

Table 2.2: Mechanical properties of implant alloys and cortical bone [25].

Material	Young's modulus (GPa)	Ultimate tensile strength (MPa)	Fracture toughness (MPa m$^{1/2}$)
Co–Cr alloys	240	900 – 1540	$\cong$ 100
Stainless steels	200	540 – 1000	$\cong$ 100
Commercial Ti alloys	105 – 125	900	$\cong$ 80
Cortical bone	10 – 30	130 – 150	2 – 12

2.1.2 Corrosion and Tribology of Metallic Biomaterials

Corrosion is defined as the deterioration of a material due to the interaction with the surrounding environment. Material degradation can be caused by chemical, electrochemical or physical reactions, or by a combination of them. Corrosion of metals in an aqueous environment is inevitable because metallic elements, except noble metals (e.g., Au, Pt), are thermodynamically more stable in the oxidized state, forming metal oxides with different stoichiometries depending on the metal most favorable oxidation state (M_2O with M^{1+}, MO with M^{2+}, M_2O_3 with M^{3+}, MO_4 with M^{4+}). Corrosion phenomena on medical devices cause loss of integrity and surface functionality. Corrosion accelerates wear, fatigue and fretting fatigue and, conversely, such damage facilitates and accelerates corrosion [26].

The physiological environment is generally hostile to all sorts of foreign materials, therefore the effects of such an environment on the chemical properties of an implant material are a primary concern. Metallic materials *per se* do not show any toxicity thanks to their high chemical stability with respect to the chemistry of the body environment. However, degradation products such as metallic ions, wear debris, and micro- and nanoparticles, can still be released into body tissues and fluids, and this depends on multiple factors: environmental conditions (pH, chloride concentration, dissolved oxygen, temperature, etc.), electrochemical effects (galvanic effects, pitting or crevices, etc.), mechanical factors (surface defects, microcracks, etc.), and human cell concentrations around the implant site. The presence in the body fluids of electrolytes (Cl^-, Ca^{2+}, Na^+, Mg^{2+}, ${PO_4}^{3-}$, ${SO_4}^{2-}$, etc.), other organic acid anions and complex compounds such as phospholipids, natural fats, proteins, sugars, amino acids, and other biomolecules, produce a severely corrosive environment that can damage the implant. As a consequence, corrosion processes may alter the physiological bio-environment. Besides, corrosion products may cause allergic reactions and carcinogenesis. Variations in the pH of body fluids are generally minimal because these are buffered solutions (pH 7.35 – 7.45); however, during an inflammation at the implant site, the host immune response can generate reactive oxidizing species (e.g., H_2O_2), which may contribute to localized acidification and further corrosion of the implant material. Corrosion of metallic materials can also be influenced by the presence of host cells at the implant site (macrophages, fibroblasts, osteoblasts, osteoclasts). In conclusion, corrosion of a metallic implant might alter adjacent tissues in three ways: i) electrical current, affecting cell behavior, ii) change in chemical environment due to the corrosion process and iii) metal ions, which may affect cellular metabolism [26].

Electrochemical corrosion consists of the anodic oxidation reaction coupled with a cathodic electron consumption. In case of metals, the anodic reaction consists of the oxidation of the metal to ionic species, in case of passive metals, the metal reacts with water to form an oxide/hydroxide layer. The cathodic reaction consists of the reduction of electrochemically active species of the electrolyte, and can vary depending on its chemical composition and pH. The Pourbaix diagrams are a useful tool for predicting the likelihood of corrosion, passivation or immunity of a given metal under specific environmental conditions, most typically in aqueous solutions. The diagrams plot the thermodynamic stability of different oxidation states of a metal as a function of pH and electrode potential. Fig. 2.3 shows a simplified

Pourbaix diagram for the titanium–water system. The shaded grey area, which mainly falls within the passivation zone of titanium, is particularly relevant for physiological systems, and its boundaries represent extreme conditions which are not usually encountered in the human body environment.

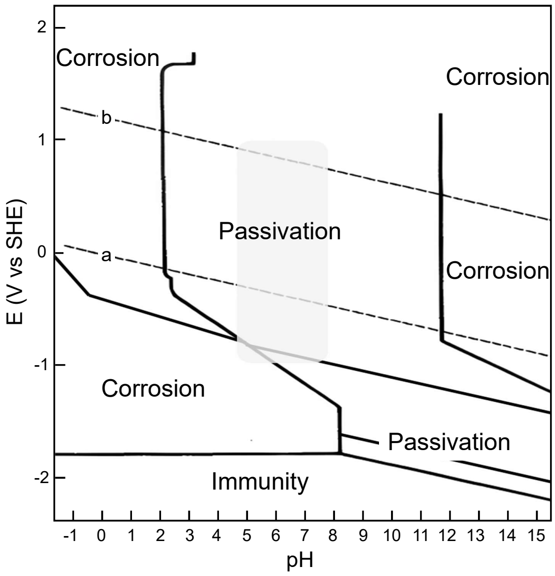

Figure 2.3: Simplified Pourbaix diagram of the titanium–water system at 25°C showing domains of corrosion, immunity and passivation. Dashed lines (a, b) indicate the range of water stability. The shaded area indicates possible conditions for physiological systems (adapted from Ref. [27]).

Metals show a variety of corrosion morphologies (Fig. 2.4), which can be roughly classified into general (uniform) and local (non-uniform) corrosion:

- Uniform corrosion involves the whole surface of the metal. General corrosion of passive alloys in the human body is rarely observed.
- Galvanic corrosion can take place when two metals with different corrosion potential are placed in electrical contact in an electrolyte. Galvanic corrosion then takes place on the less noble metal. However, when the difference in corrosion potential is small, galvanic corrosion may not occur.
- Pitting corrosion is a type of local corrosion that results in the formation of small cavities (pits) limited to a small area, while the greater part of the passivated part is unattacked. Pitting corrosion takes place on passive alloys in presence of halogen species, which attack surface defects and locally break the passive film.
- Crevice corrosion is a type of localized corrosion that occurs when the metal is partially shielded from the surrounding environment (e.g., deep crack, narrow openings, joints). The crevice environment, where mass diffusion is restricted, becomes rich in dissolved oxygen and halogen ions, thus further decreasing the pH and increasing corrosion rate and metal dissolution. In metallic biomaterials, it can take place on interfaces, such as head/stem in artificial hip joints and screw/hole in bone plates.

- Intergranular corrosion is a type of local corrosion that selectively takes place at grain boundaries.

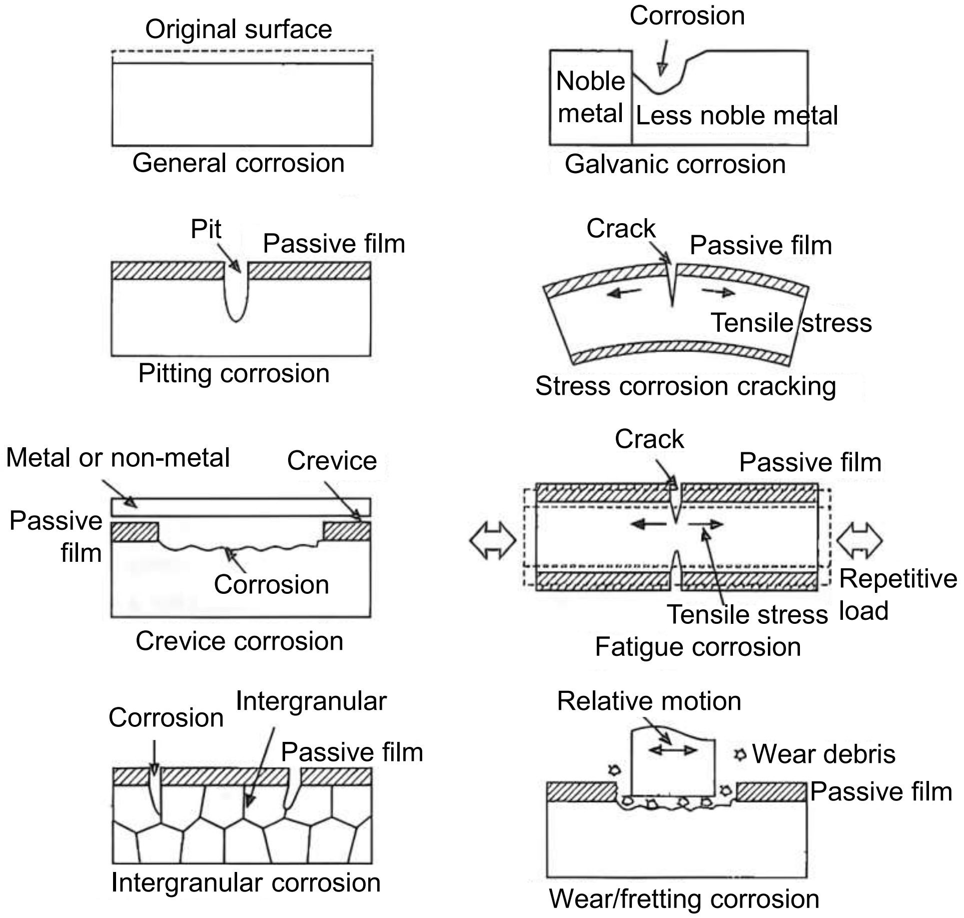

Figure 2.4: Corrosion morphologies (reproduced from Ref. [28]).

In many biomedical applications, implant materials can be exposed to very complex service conditions, including static and dynamic loading, and relative motion with soft or hard surfaces in contact. The human body possesses a great variety of frictional and sliding interfaces. The relative motion between the implant surface and surrounding tissues might accelerate wear of both surfaces, thus stimulating chronic inflammation and creating a more severe chemical environment [26]. Common examples of bio-tribology, i.e., the science of friction, wear and lubrication in biological systems, include: replacement of heart valves, pump lubrication in artificial hearts and in contact lenses, wear of dental implants, artificial joints, and plates and screws in bone fracture repair.

The synergistic action of mechanical loading (wear) and corrosion (chemical and electrochemical) leads to the irreversible degradation of implant surfaces [29], indeed, tribology and tribocorrosion have emerged as primary fields in bio-engineering. Degradation of the implant material due to the simultaneous chemical and mechanical effects may occur under a variety of conditions, as illustrated in Fig. 2.5 for a dental implant.

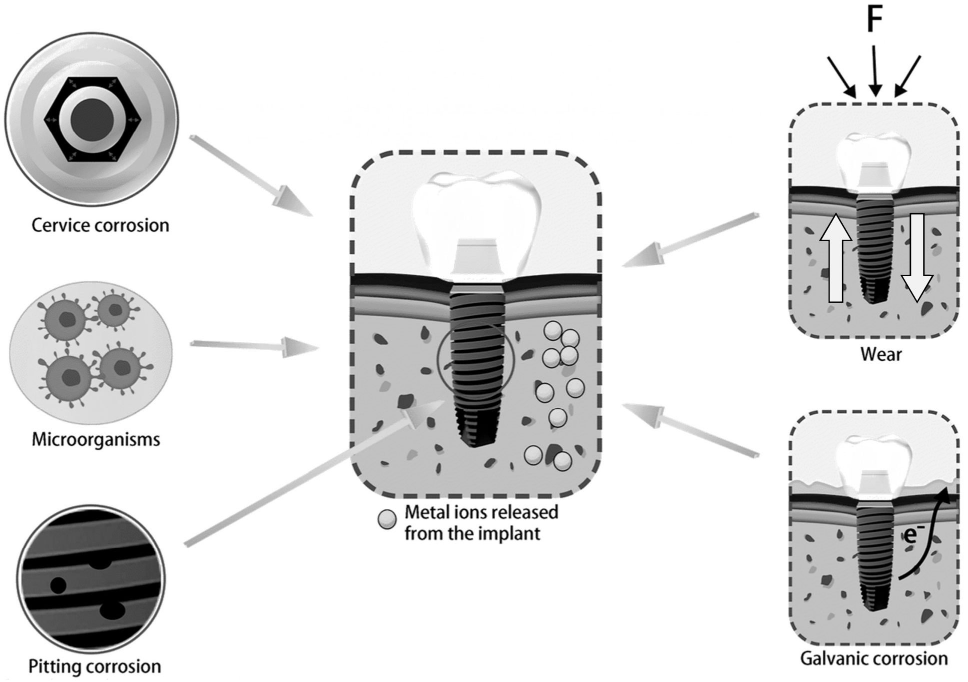

Figure 2.5: Degradation mechanisms involving mechanical and chemical effects on a dental implant (reproduced from Ref. [30]).

Biomedical applications of metallic implant materials often involve contact deformation and corrosion. Wear and abrasion of the metallic implant material against hard tissues affect the integrity of the passive oxide film, thus enhancing corrosion phenomena. Implants inserted in a human body encounter a particularly aggressive environment, being surrounded by blood-rich tissue, serum proteins, high chloride concentrations, and more. All these components also influence the corrosion behavior and release of harmful metallic ions, which might delay the recovery process after surgery [31]. Sliding contacts occur also between parts of the same implant, such as femoral head and acetabular cup in artificial joints, for which tribocorrosion-driven failure is fairly common [32]. Mechanical forces acting at the interface of sliding surfaces cause a repeated damage of the oxide film, leading to accelerated corrosion and causing structural deterioration of the implant. The capacity of the oxide film to regenerate itself plays a key role in further determining the corrosion behavior of the implant: the sooner the film is repaired, the lower the amount of metal ions released in the body. Low wear resistance is also responsible for the appearance of wear debris, which might cause inflammatory reactions and pain [33, 34].

From a relevant clinical standpoint, the main categories of wear and tribocorrosion in load-bearing implants (e.g., hip implant, Fig. 2.6) can be grouped as follows: metal or ceramic on polyethylene, metal-on-metal, ceramic-on-ceramic, ceramic-on-metal, and taper tribocorrosion [32]. Polyethylene wear produces submicron particles, with local inflammatory effects, while metal wear is typically associated with elevated systemic levels of metallic ions. Clinical studies and retrieval examinations [35–37] demonstrated that excessive wear of metal and/or UHMWPE (ultra high molecular weight polyethylene, used in acetabular cups) is the principal mode of failure for long term use of total joint replacements (TJR), which, together with debris accumulation, leads to adverse cellular response and hence inflammation, bone cell lysis, osteolysis, infection, and pain. Excessive wear is mainly due to a lack of good or sufficient lubrication. The high UHMWPE wear rates associated with the alloy counterparts have been attributed to the mechanical instability of the metal oxide layer. High stress can induce breakdown of the surface passive layer. The exposed bare metallic surface may either repassivate or adhesively bond to the polymer surface. The latter leads to cyclic layer disruption and reformation, resulting in gradual consumption of the alloy material. Friction, which is the force resisting the relative motion between two sliding surfaces, dictates the efficiency of sliding surface contact. Friction is also responsible of wear (loss of material or body deformation), which is very often the limiting factor affecting service life of the medical device. Therefore, minimization of friction and wear is necessary to extend the medical device life. Corrosion can be closely related to tribology, as it results in surface degradation able to promote and accelerate wear. The combined action of these phenomena produces wear particles and debris that are prone to diffusing in the surrounding soft tissues and to migrating to more remote organs [38]. In view of all this, tribocorrosion behavior represents one of the most important mediators of the body response to the medical implant. An attentive and accurate evaluation of such processes is essential [39].

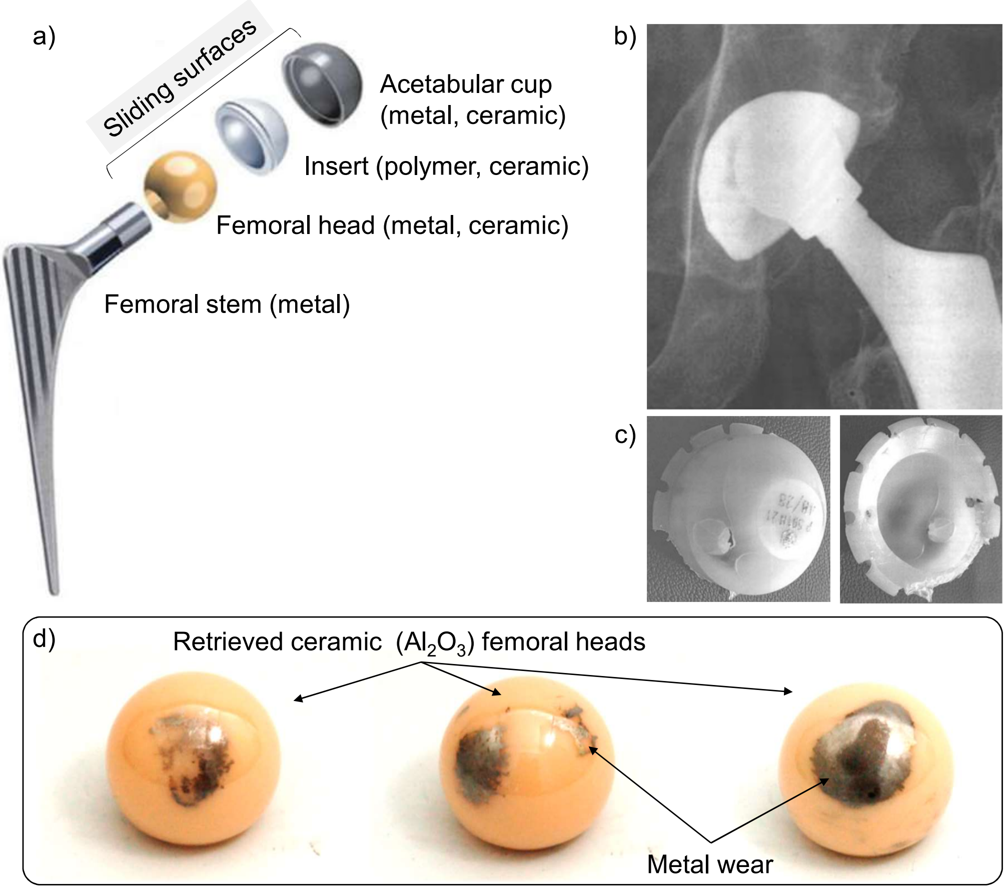

Figure 2.6: (a) Main components of an artificial hip joint [40]. (b) Radiography of a total hip arthroplasty showing significant worn polyethylene and associated osteolysis and (c) worn acetabular cup extracted at revision [41]. (d) Retrieved alumina femoral heads with metallic wear transfer [42].

2.2 Titanium-Based Alloys & Their Properties

This section gives an overview and presents the current state of knowledge of relevant titanium-based medical alloys and their structural characteristics, mechanical, and chemical properties. Every year, over 1000 tons of Ti-based biomedical devices are implanted in patients worldwide [43]. Titanium (Ti) and its alloys offer distinct advantages for load-bearing applications in comparison to other metallic biomaterials. Their Young's modulus is roughly half that of stainless steels and cobalt-molybdenum alloys. Moreover, they have higher specific strength (strength-to-density ratio), superior biocompatibility and great corrosion resistance. As a result of these attractive properties, Ti alloys have become the preferred biomaterial for bone-related applications.

2.2.1 Classification & Structures

The element titanium (Ti) is a low-density transition metal ($Z = 22$) that can be considerably strengthened by selective alloying and thermomechanical processing. Its incomplete valence *d*-shell (electron configuration: [Ar] $3d^2$ $4s^2$) enables it to form substitutional solid solutions with many elements having a size factor within ± 20%. Pure Ti has a high melting temperature ($T_m = 1768$°C) and undergoes an allotropic transformation at 882°C, changing from hexagonal close packed (HCP, α-phase, space group $P6_3/mmc$) to body centered cubic (BCC, β phase, space group $Im\bar{3}m$) crystal structure above this temperature (Fig. 2.7a) [44].

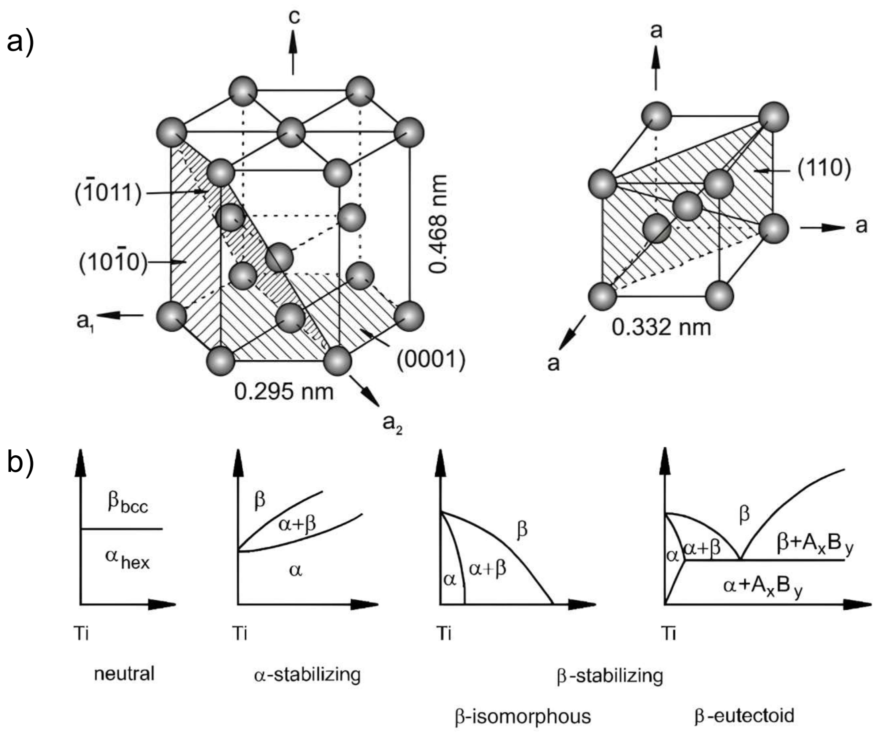

Figure 2.7: (a) Crystal structures of HCP α and BCC β, and (b) effect of alloying elements on Ti phase diagrams (adapted from Ref. [44]).

Solute substitutional or interstitial elements strongly influence the allotropic transformation temperature of titanium. In this regard, alloying elements for titanium can be grouped into: α-stabilizers (C, N, O, Al, Ga), β-isomorphous stabilizers (V, Nb, Mo, Ta), β-eutectoid stabilizers (Si, Cr, Mn, Fe, Cu), and neutral elements (Zr, Sn). The β-isomorphous elements have complete solubility in the β phase, while β-eutectoid elements have limited solubility and can form intermetallic compounds by eutectoid decomposition of the β phase (Fig. 2.7b). The properties of Ti alloys depend upon composition, relative proportions of the α/β phases, thermal and mechanical treatment conditions [44]. Based on the crystal structure, Ti alloys can be categorized into four types: α alloys, near-α alloys, $\alpha+\beta$ alloys, and β alloys [44].

- **α alloys** primarily consist of the α phase and exhibit excellent corrosion resistance and high (specific) strength, and are easily deformable, thus making them ideal for applications such as aerospace components and medical implants.
- **Near-α alloys** have a combination of α and small amounts of β phases. They are a classic high-temperature alloy type with excellent creep behavior and high-temperature strength, and high fatigue strength.
- **$\alpha+\beta$ alloys** contain a mixture of α and β phases, providing a balance of properties such as high strength and stiffness, good ductility, and excellent weldability. Ti–6Al–4V is the most popular one, accounting for over 50% of all alloys in use today. These alloys are widely used in the aerospace industry, as well as in automotive, chemical processing and medical applications.
- **β alloys** mainly consist of the β phase and are the most versatile class. They offer the highest strength-to-weight ratios and exhibit attractive combinations of strength, toughness and fatigue, and corrosion resistance. Moreover, they possess the lowest Young's modulus among the other types, which makes them suitable for load-bearing implant applications, together with their high biocompatibility. Sub-classifications of β alloys are discussed in Sec. 2.3.

The most conventional used alloy as medical implant in the clinical practice (e.g., bone fixation plates, stems of artificial hip joints, etc.) is the $\alpha+\beta$ Ti–6Al–4V. It shows good workability, weldability and heat treatment ability as well as good strength, toughness and corrosion resistance. The main drawback is its high Young's modulus (E = 114 GPa), which leads to the previously mentioned stress-shielding effect. Furthermore, some concerns regarding the long-term safety of the elements V and Al were raised: their release in the human body is reported to be responsible for health issues such as Alzheimer's disease, osteomalacia and neuropathy [2, 45]. Therefore, extensive research efforts were made to develop new Ti-based alloys with no cytotoxicity and with better biomechanical compatibility. In this regard, β-Ti alloys are extremely promising candidates.

2.2.2 Key Mechanical Properties

Titanium alloys specifically developed as substitutional materials for hard tissue should meet certain mechanical requirements for their reliable use in the human body. There are essentially four ways to improve the properties of Ti alloys: alloying, processing, induced porosity and metal-matrix composites.

- *Alloying* provides the basis to increase strength (e.g., age hardening, solid solution strengthening), allows the generation of ordered structures (e.g., intermetallic compounds), governs physical properties (e.g., coefficient of thermal expansion, density, elasticity) and the chemical resistance [33].
- *Processing* allows accurate tuning of the property profile, different microstructures can be generated by means of thermomechanical treatments to enhance strength, toughness, ductility, creep resistance, stress corrosion. Processing techniques of mechanical alloying (solid-state powder processing) and rapid solidification broaden the spectrum of possibilities [46, 47].
- *Induced porosity* extends the possibilities of improving mechanical properties. A controlled amount of porosity in an implant alloy allows to better mimic bone morphology, structure and function, thus improving osseointegration, and provides customized mechanical properties, such as low stiffness. Major drawback of porous bodies is their limited strength [48, 49].
- The fourth option consists of combining different materials (metallic and/or non-metallic) to create a *composite* with superior behavior. Such approach overcomes the limits of the basic attributes of main materials classes. Nature, volume fraction, orientation and boundaries of the matrix and the strengthening component have a major influence on chemical and mechanical behavior of the composite [50].

Young's Modulus

The Young's modulus (E) represents a major demanding condition to avoid the so-called stress-shielding effect. Large modulus mismatches between implant material and surrounding body tissues cause insufficient loading of bone adjacent to the implant, resulting in stress-shielding effects that cause tissue loss and implant failure [3]. According to *Wolff's law*, bone density and its architecture depend on magnitude and direction of the applied load [21]. Indeed, it has been proved that, when tension or compression loads and bending moment are reduced, decreased bone thickness and increased bone mass loss arise [1]. Accordingly, a reduction of implant's Young's modulus (and stiffness, implicitly) to a value similar to that of the bone is desired in order to provide the necessary 'isoelastic behavior' for an efficient load transfer between implant material and bone [2]. Most recent research efforts have been focused on reducing the Young's modulus of implant alloys. Values of E of relevant biomedical titanium alloys are reported in Fig. 2.8. Generally, E of recently developed β-type Ti alloys is in the range 51 – 98 GPa, which is smaller than E of α- and $\alpha+\beta$-type alloys.

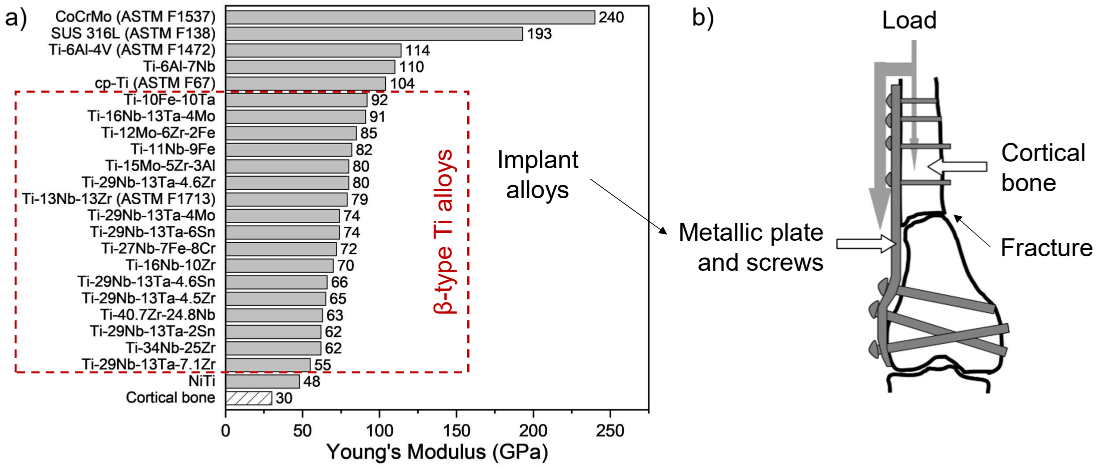

Figure 2.8: (a) Comparison of the Young's modulus of different implant alloys with human cortical bone [51]. (b) Scheme illustrating the load distribution during bone healing when a metallic bone fixator is used. The mismatch in Young's modulus between the fractured bone and the metallic implant results in the majority of the body load being supported by the metallic implant (adapted from Ref. [52]).

Strength

Strength of α- and α+β-type alloys is moderately low at room temperature, for instance the four grades of c.p. Ti exhibit yield strength and ultimate tensile strength in the range 170 – 480 MPa and 240 – 550 MPa, respectively. The low mechanical strength and low fatigue strength prevent α-type Ti alloys from being used in load-bearing applications. The α+β Ti alloys contain a higher content of β-stabilizers than near-α alloys, therefore they possess a higher β phase fraction (about 5 – 30 vol%). Moreover, they are heat treatable, hence their mechanical properties can be tuned and optimized. Volume fractions of α and β phases significantly vary according to alloy chemistry, heat treatment (temperature and holding time) and cooling rates. As a consequence, the α+β Ti alloys possess greater yield strength and ultimate tensile strength than α-type. The β-type Ti alloys, containing high amount of β-stabilizers, are also heat treatable, hence their strength can be enhanced. Such phenomenon is mainly attributed to dispersion strengthening due to the partial $\beta \rightarrow \alpha$ transformation. The β-type Ti alloys have comparable strength with α+β-type, but maintain a lower E value. A suitable balance between strength and stiffness has to be found to best mimic bone behavior [53].

An ideal biomedical material is expected to have the combined properties of low Young's modulus and high strength to sustain a long-term service period and to reduce the risk of revision surgery.

Table 2.3: Mechanical properties of α-, $\alpha+\beta$- and β-type Ti alloys for load-bearing implant applications [17, 53].

Alloy designation (wt.%)	E (GPa)	σ_y (MPa)	σ_{UTS} (MPa)	ε_{max} (%)
α microstructure				
c.p. Ti (ASTM grade 1)	105	170	240	24
c.p. Ti (ASTM grade 2)	105	275	345	20
c.p. Ti (ASTM grade 3)	105	380	450	18
c.p. Ti (ASTM grade 4)	105	480	550	15
$\alpha+\beta$ microstructure				
Ti–6Al–4V (annealed)	110 – 114	825 – 869	895 – 930	6 – 10
Ti–6Al–4V (mill annealed)	101 – 110	795 – 875	960 – 965	10 – 15
Ti–6Al–7Nb (annealed)	114	880 – 950	900 – 1050	8 – 15
Ti–5Al–2.5Fe	110	820	900	6
Ti–3Al–2.5V	100	585	690	15
β microstructure				
Ti–13Nb–13Z (aged)	79 – 84	836 – 908	973 – 1037	10 – 16
Ti–12Mo–6Zr–2Fe	74 – 85	1000 – 1060	1060 – 1100	18 – 22
Ti–29Nb–13Ta–4.6Zr (aged)	80	864	911	13
Ti–15Mo (annealed)	78	544	874	21
Ti–15Mo–5Zr–3Al	75 – 88	870 – 970	880 – 980	17 – 20
Ti–16Nb–10Hf	81	730 – 740	850	10
Ti–35.3Nb–5.1Ta–7.1Zr	55	547	597	19

2.2.3 Degradation Phenomena of Ti in Physiological Environment

Despite the biochemical and mechanical compatibility of Ti alloys, wear and corrosion still occur, especially in extreme environments like the human body [54]. Corrosion resistance depends on environment, alloy composition and microstructure and it can lead to the loss of structural integrity (with consequent implant failure), surface function and release of small amount of metal ions (e.g., Al, V), which might elicit adverse allergic reactions and even carcinogenesis [20]. These wear and/or corrosion processes may trigger a local inflammatory response known as peri-implantitis, which can ultimately compromise the stability of the implant and even require surgical revision. Abrasive, adhesive, fatigue, fretting and corrosion wear mechanisms have been all identified in load-bearing implants and strongly depend on material composition, surface characteristics, hardness, and corrosion resistance. All these degradation phenomena can be either prevented or inhibited by a surface with high passivation and re-passivation ability.

Ti and its alloys are perceived as ‘biocompatible’ owing to the presence of a passive, inert, stable, and thin film consisting mainly of TiO_2; even though it may also include TiO, $TiO(OH)_2$, or Ti_2O_3 species [55]. The oxide thin layer serves as a barrier film, providing a chemical barrier from further oxidation and preventing the release of deeper metal atoms. However, despite the high corrosion resistance, Ti implants may still experience surface degradation due to the presence of inclusions or discontinuity spots, which can lead to the release of metallic ions and particles, depending on the composition of the alloy. Therefore, careful monitoring and maintenance of Ti implants are necessary to minimize the risk of surface deterioration and ensure their long-term success. A significant aspect of Ti and its alloys is their susceptibility to localized corrosion (i.e., pitting and crevice corrosion), which can happen in the presence of aggressive ions or under high-stress conditions. Small pits or crevices may form and propagate, thus eventually leading to material failure. Crevice corrosion occurs in restricted contacting areas, e.g., between implants, abutments and prosthetic structures, where restricted ingress and egress of physiological fluids and depletion of oxygen lead to a decrease in pH, due to the presence of free H^+ ions, which may result in film breakdown. Pitting in particular is considered as the most dangerous corrosion phenomenon because of its difficulty in prediction and detection. On dental implants made of Ti, pitting occurs when the oxide thin film breaks down locally in the oral environment [55] (Fig. 2.9). Also, dynamic loadings (e.g., mastication, movement) generate micro-motion at the implant-abutment connections which promote wear and wear-accelerated corrosion. The synergistic effects of corrosion and wear cause structural changes, resulting in fretting corrosion, which is the main responsible of metal release in the surrounding body tissues.

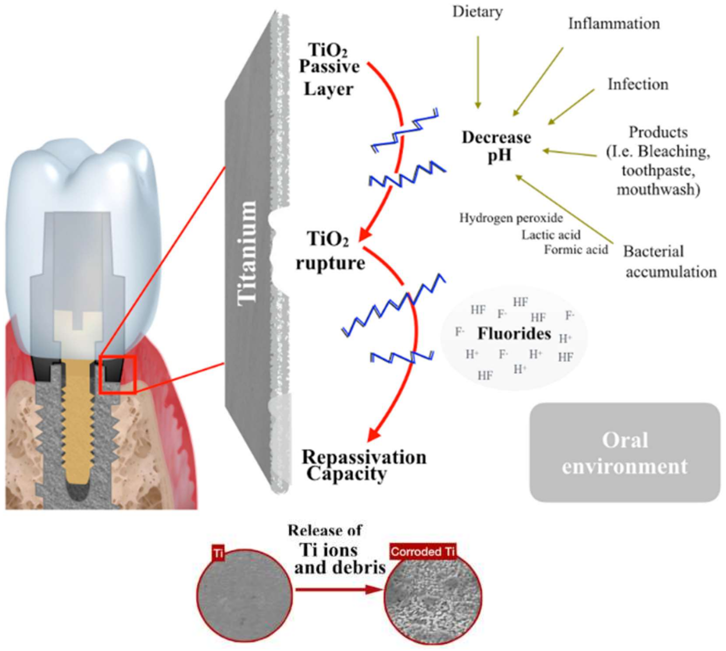

Figure 2.9: Factors affecting corrosion behavior of Ti dental implants in the oral environment (adapted from Ref. [55]).

Currently, there is still no consensus on the best alloy chemical composition suitable for various biomedical applications, however several *in vivo* studies demonstrated the deleterious toxic effects of high concentrations of Co, Cr, Ni, Al, and V, which were detected in the blood of patients [56–58]. For these reasons, many efforts have been made to develop a new class of Ti alloys: β-type Ti alloys are promising materials because of their superior corrosion resistance and presence of non-allergic and non-toxic elements (Nb, Ta, Zr, Mo, Sn). Their overall corrosion behavior is mainly governed by the role of the β-stabilizing agents on the oxide film. On comparing the two $\alpha+\beta$-type Ti–6Al–7Nb and Ti–6Al–4V, it was found that the higher corrosion resistance of the former alloy is due to the formation of niobium oxide (N_2O_5), which is chemically more stable than vanadium oxide (V_2O_5). The beneficial effect observed for Nb on the stability of the titanium oxide film has been attributed to its capacity of reducing anion vacancies in the oxide film [59]. The presence of Nb^{5+} ions increases the number of oxygen ions in the TiO_2 crystal lattice, which annihilates anion vacancies and makes the film less defective and more stoichiometric, and therefore improving passivation properties, and so corrosion resistance, of the resulting film. A recent work systematically investigated the effect of Nb addition (5 – 33 at.%) on the stability and biological corrosion resistance of cast Ti–Zr–Nb alloys in simulated body fluids [60]. It was demonstrated that the addition of Nb can reduce the content of Ti_2O_3 in the passivation film and increase the presence of N_2O_5 species, which relates with the increased corrosion resistance. Moreover, another beneficial effect was the improved stabilization of the passive film, which results in reduced pitting sensitivity. Thus, it was suggested that increasing Nb content above 20 at.% increases the overall biological corrosion resistance of these Ti-based alloys. Similar conclusions were drawn by Hu et al. [61], who studied passive film properties of Ti–45Nb alloy subjected to high-pressure torsion (HPT) processing, which, by grain refinement, facilitates the formation of a thicker and less defective oxide layer, responsible for the improved corrosion resistance (Fig. 2.10).

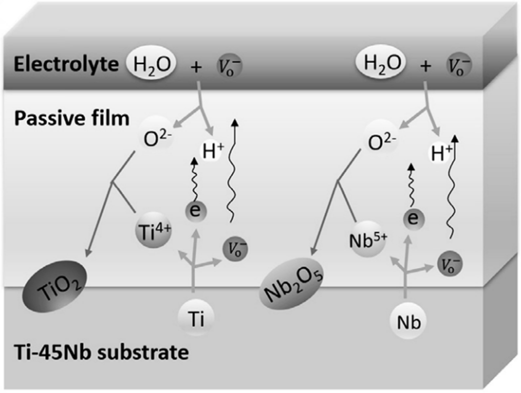

Figure 2.10: Scheme of passive film formation on Ti–45Nb alloy, showing transport of ions, electrons and vacancies (reproduced from Ref. [61]).

The corrosion behavior of β-type Ti–45Nb implant alloy, together with Ti–6Al–4V and Ti–55Ni, was studied in neutral and acidic simulated body fluid solutions resembling different body environments [62]. In neutral solution, the β-Ti–45Nb exhibited excellent corrosion resistance, comparable to that of Ti–6Al–4V, and better than Ti–55Ni alloy. On the other hand, in very acidic environment, the β-Ti–45Nb remained passive, where active dissolution was observed for both the other two alloys, thus suggesting Ti–45Nb a highly advantageous alloy for use in corrosive environments (e.g., body environment). Other studies [63, 64] investigated the effect of alloying indium (In) on the corrosion resistance and biological compatibility in synthetic physiological solutions of a cast and homogenized β Ti–40Nb alloy. It was concluded that small concentrations of In, homogeneously dissolved in the β-phase matrix, do not have a detectable effect on the anodic response of the alloy, thus suggesting high corrosion resistance [63]. The *in vitro* studies [64] on human bone marrow stromal cells (hBMSC) revealed high biocompatibility, due to the high Nb content that alters the passive layer composition.

Despite the improvement in corrosion resistance due to β-stabilizing elements, care should be taken to ensure even chemical distribution of the alloying elements within the matrix by appropriate heat treatment to prevent localized corrosion (e.g., galvanic corrosion between phases with very different Volta potential [65]). Heat treatments that lead to non-uniform chemical distribution are hence detrimental with respect to corrosion. The influence of microstructure on corrosion resistance was investigated by Yu et al. [66] on a Ti–15Mo–3Nb–3Al biomedical implant alloy subjected to homogenization and aging treatments in a strong reducing acid (HCl). It was observed that the solution-treated microstructure (single-phase β) exhibits better corrosion resistance when compared to the aged one (α+β). The decrease in resistance of the aged sample was attributed to the partitioning of α and β stabilizing solute elements occurring during the aging process. In particular, the depletion of beneficial Nb (and Mo) from the α phase, along with partitioning of detrimental Al, could account for the inferior corrosion resistance of the aged alloy. It was therefore concluded that Nb and Mo improved passivity and limited the active corrosion of β-Ti phase. More recently, the effect of unique microstructural features on the electrochemical behavior of conventional (surgically retrieved cast and wrought implants) and additively manufactured (AM) Ti–6Al–4V implants (not previously implanted) was investigated [67]. It was shown that a high composition gradient between α and β phases leads to localized galvanic corrosion.

Ti has poor tribological properties due to its low abrasive wear resistance [68], and c.p. Ti, compared to other Ti alloys, has the highest friction coefficient in steady-state fretting conditions [69]. Extensive literature exists on the wear behavior of Ti–6Al–4V in both dry and wet conditions [70–73], but limited wear data is available for β-type Ti–Nb-based alloys: Ti–40Nb [74], Ti–45Nb [75], Ti–Nb–Sn [76], Ti–Nb–Cu [77], TNZ and TNTZ [78, 79]. Neto et al. [80] investigated the tribocorrosion behavior in simulated body fluids of four β-type Ti–Nb–Ta–Zr alloys and compared it with Ti–6Al–4V. The results indicate that the β-type alloys exhibit lower corrosion contribution to total wear than the α+β alloy, due to the effect of galvanic coupling between phases; however, the two-phase alloy exhibits lower wear rate and material loss. Chapala et al. [81] reported that the α+β microstructure exhibits the best wear resistance compared to β, and that the α:β volume fraction ratio decides the resulting wear properties in Ti alloys. The authors concluded that the microstructure influences the tribocorrosion properties of Ti alloys, where lower wear track volume and material loss were observed in the α+β alloy. In their following study [79], the authors investigated the worn surfaces and the tribofilm to reveal the dominant wear mechanisms and concluded that abrasion wear is always dominant and independent of alloy type, electrochemical condition and contact pressure. Subsurface deformed microstructures were studied by TEM and the β phase experienced a partial transformation to α and ω phases, which resulted in local surface hardening and grain refinement caused by wear and plastic deformation accumulation in the contact area. Guiñón Pina et al. [76] studied the influence of the chemical composition on the triboelectrochemical behavior of β Ti–30Nb–(2,4)Sn alloys in phosphate buffer saline solution and observed that the addition of Sn above 2 wt.% decreases corrosion resistance and hardness, which indicates a dramatic increase in mechanical wear. Another work [77] studied the effect of Nb addition (0 – 15 wt.%) on the corrosion and wear behavior of sintered Ti–5Cu–xNb alloys. Increasing amounts of Nb significantly improved the corrosion resistance, but also increased wear rate. On the other hand, Li et al. [82], who studied the effect of Nb content on wear behavior of Ti–Nb–Ta–Zr and Ti–6Al–4V, concluded that Nb addition improved wear resistance. Copper addition may also enhance wear resistance of Ti alloys [77], but it might significantly affect corrosion resistance, due to pitting corrosion. Enhancement of wear resistance due to Cu addition is often related to the presence of the Ti_2Cu phase [83]. According to numerous studies on Ti–Cu alloys, addition of 5% Cu is sufficient to enhance, and not impair, corrosion resistance, as well as mechanical and antibacterial properties [84]. Because of the complexity of involved phenomena, the tribocorrosion behavior of specific combinations of materials, alloying elements, loadings, and environments can be challenging to predict, therefore experimental studies are necessary.

2.2.4 Biocompatibility and Biological Response of Ti and its Alloys

Once artificial biomaterials are implanted *in vivo*, they induce a cascade of biological reactions through interaction of the implant itself with body fluids, proteins and cells. Body response to the implant and occurring reactions on the surface at different time intervals can be described as follows: adsorption of water molecules on the implant surface (10^{-9} s), adsorption of proteins over water molecules (10^{-6} – 10^{-3} s) and adsorption of host and bacterial cells over proteins (10^{1} – 10^{3} s) [33]. A major factor influencing body reaction is the biomaterial surface, being the first contact. Both chemical composition and topography of the surface are believed to play a significant role in bone contacting implants: they regulate type and degree of interactions at the interface, such as ions and biomolecules adsorption, formation of calcium phosphate layers and interaction with cells (osteoblasts, macrophages, bone marrow cells). Accordingly, the nature of the interface that forms between biomaterial and attached tissue determines the ultimate success or failure of the implanted material. Aiming for bioactive surfaces, able to stimulate tissue response, numerous surface engineering techniques have been studied and adopted: examples include chemical vapor deposition, sol-gel method, plasma electrolytic oxidation, thermal spray coating, laser peening and other [85, 86]. Development of oxide films is considered as a prerequisite for bioactivity.

Titanium is well tolerated and almost inert in the body environment, and it is capable of osseointegration in optimal conditions [54]. Ti alloys, among all metallic biomaterials, are the only ones with the ability to bond with host bones [17]. More specifically, the physiochemical properties (crystallinity, composition, impurity segregation, etc.) of the oxide film are quite relevant. The widely accepted explanation of this positive aspect of Ti alloys is due to the formation on the surface of titanate

(Na_2TiO_3), which ultimately results in the formation of carbonated hydroxyapatite, an important mineral in bone and tooth formation, considered as a critical step for osseointegration [17]. *In vitro* cytotoxicity studies, often conducted with fibroblast L929 cells and osteoblast-like MC3T3 E1 cells, have proved the superior biocompatibility of titanium alloys over stainless steels and Co–Cr alloys. However, their biocompatibility is still an open question and further studies are being made. Reservations have been expressed about Ti–6Al–4V long-term implants, because of the toxicity of V and Al. Such concerns led to the development of β-type Ti-based alloys containing non-toxic elements (Nb, Ta, Zr, Mo). Indeed, addition of Ta remarkably reduces the amount of metal ions released [87]. The β-type Ti alloys are receiving tremendous attention from the researchers working in the biomedical engineering field: in the three last decades, numerous biocompatible alloys containing the aforementioned elements and other have been developed (Table 2.4). Studies have proved higher relative growth of cells for the β-type alloy Ti–15Zr–4Nb–4Ta than for Ti–6Al–4V [88]. Niinomi et al. [89] demonstrated the superior cell viability of the β-type Ti–29Nb–13–4.6Zr alloy compared to Ti–6Al–4V. The *in vitro* studies of Pilz et al. [64] on Ti–40Nb and (Ti–40Nb)–4In alloys proved high biological compatibility on human bone cells due to low metal release and high Nb content. The inflammatory response both *in vitro* and *in vivo* of β-type Ti–45Nb was mitigated due to its reduced corrosion rate and quick passivation properties, which prevent leaching of pro-inflammatory metal ions [61]. Such and other investigations have led to the belief that the newly developed β-type Ti alloys are promising biomaterials from the corrosion, wear and biocompatibility perspectives.

2.3 β-Ti Alloys for Biomedical Applications

This section presents the advances in the development of β-Ti alloys for biomedical implant applications. They are considered as second generation Ti biomaterials and their rapid development took place in the 1990s. One reason for their development is to address the stress-shielding phenomenon caused by the high Young's modulus of current implants. Generally, β-type Ti alloys exhibit a Young's modulus closer to that of human cortical bone [90]. They are among the most versatile class of Ti alloys and offer the highest strength-to-weight ratios and very attractive combinations of strength, stiffness, toughness and fatigue resistance, good corrosion resistance and high biocompatibility. Moreover, these alloys are V- and Al-free, therefore, β-type Ti alloys containing non-toxic elements (Zr, Nb, Ta, Mo, Sn, etc.) have recently attracted considerable attention for orthopedic and dental implant applications.

In general, β-type Ti alloys, based on the range of β phase stability, and therefore amount of β-stabilizers, can be classified as follows: β-rich (α+β), near-β, metastable β and stable β. Near β-Ti alloys are collocated in the region between α+β and metastable β alloys. Within the class of the β alloys, two types can be distinguished: 'high strength' β, located close to the β and α+β alloy boundary in the pseudo-binary phase diagram (Fig. 2.11), and 'heavily stabilized' β, which are located more to the right.

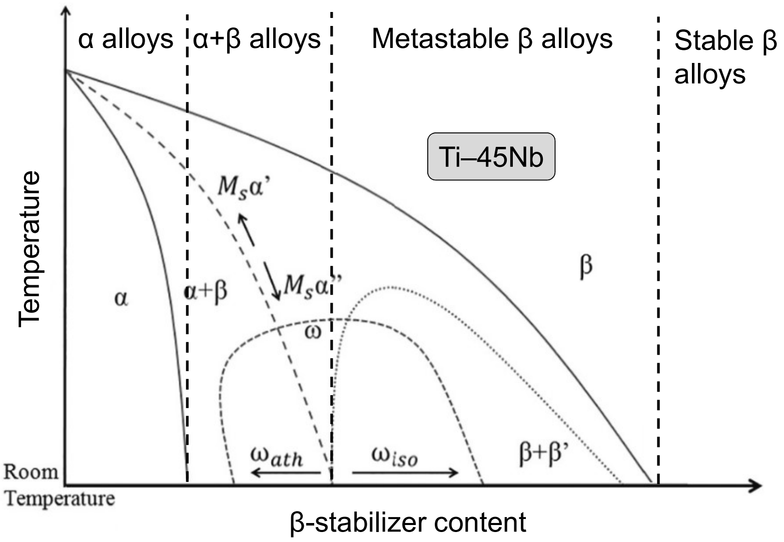

Figure 2.11: Scheme of pseudo-binary isomorphous phase diagram of Ti showing different stability regions depending on the concentration of β-stabilizers (adapted from Ref. [86]).

Theoretical approaches, used alone or in combination, exist to predict the effect of alloy composition and phases constituents, as later presented in Sec. 2.3.1. Heavily stabilized β-Ti alloys contain low volume fraction of α-phase stabilizers, and therefore the maximum achievable strength for these alloys is lower than the strength achievable in the high-strength β alloys. In contrast to $\alpha+\beta$ alloys, β alloys, upon quenching to room temperature, do not transform martensitically, thus resulting in a metastable β phase. However, after aging at 450 – 650°C, the α-phase can still be precipitated as very fine particles (platelets) with a high-volume fraction and distribute throughout the β matrix [17]. As a consequence, aged β alloys can be hardened to higher yield stress levels compared to $\alpha+\beta$ alloys, but they also exhibit higher density and compromised creep strength and tensile ductility. Furthermore, β alloys can be processed at lower temperatures than $\alpha+\beta$ alloys, cold-worked metastable β alloys can contain stress-induced martensites [91]. Another typical aspect of β-Ti alloys is that they exhibit limited to negligible strain hardening, attributed to their specific microstructural characteristics [92]. The Young's modulus of β-type alloys can be significantly reduced by adjusting the concentration of β-stabilizing elements [53, 93]. The most common β-type Ti alloys, together with their mechanical properties (E and σ_{y}) are listed in Table 2.4. Major drawbacks of β Ti alloys include low fatigue strength and poor wear resistance compared to other Ti alloys (c.p. Ti, $\alpha+\beta$ Ti). For load-bearing applications, notch fatigue properties are considered indicative of the performance of hip implants, because they generally have a structured surface with wedges and porous coatings that introduce stress-concentration sites [17]. Generally, β alloys have unsatisfactory fatigue strength, which can be enhanced by microstructure refinement or by aging to precipitate small amounts of ω phase. However, processing parameters must be carefully controlled, as too much ω phase will cause embrittlement and an undesired increase in the Young's modulus [47].

Table 2.4: β-type Ti-based alloys for biomedical implant applications and their mechanical properties (Young's modulus E, yield strength σ_y).

Alloy (wt.%)	E (GPa)	σ_y (MPa)	Ref.
Ti–Mo alloys			
Ti–12Mo–6Zr–2Fe	74 – 85	1000 – 1060	[17]
Ti–15Mo	78	655	[17]
Ti–15Mo–5Zr–3Al	75 – 88	870 – 970	[17]
Ti–15Mo–2.8Nb–0.2Si–0.26O	83	950 – 990	[17]
Ti–Zr alloys			
Ti–30Zr–4Cr	67 – 69	500 – 530	[94]
Ti–30Zr–5Cr	66 – 75	824 – 870	[94]
Ti–30Zr–1Cr–5Mo	69 – 68	524 – 554	[94]
Ti–30Zr–2Cr–4Mo	64 – 74	592 – 636	[94]
Ti–30Zr–3Cr–3Mo	68 – 79	643 – 764	[94]
Ti–Nb alloys			
Ti–11Nb–3.5Fe–7Zr	90 – 93	1011 – 1184	[95]
Ti–13Nb–13Zr (TNZ)	79 – 84	840 – 910	[17]
Ti–16Nb–10Hf	81	730 – 740	[17]
Ti–19Nb–2.5Fe–6Sn	71 – 98	765 – 1261	[95]
Ti–19Nb–2.5Fe–10Zr	69 – 97	1027 – 1132	[95]
Ti–21Nb–10Sn (Ti–Nb_{13}–Sn_5 at.%)	75	772	[96]
Ti–25Nb–2Ta–3Zr	75	864	[97]
Ti–30Nb–2Ta–3Zr	57	663	[97]
Ti–30Nb–(3–10)Cu	67 – 93	650 – 900	[98]
Ti–31Nb–10Sn (Ti–Nb_{20}–Sn_5 at.%)	61	435	[96]
Ti–35Nb–2Ta–3Zr	52	431	[97]
Ti–35Nb–7.9Sn	61	484	[99]
Ti–35Nb–7Zr–5Ta–0.35O	41 – 46	857 – 966	[100]
Ti–37.5Nb–5.2In	49	511	[101]
Ti–38.7Nb–3.6In	51	568	[101]
Ti–38Nb–12Mo	55	663	[102]
Ti–39Nb	69	616	[101]
Ti–39Nb–6Mo	64	621	[102]
Ti–39Nb–9Mo	58	634	[102]
Ti–40Nb	55 – 68	346 – 649	[46]
Ti–40Nb–3Mo	67	535	[102]
Ti–40Nb–2Ta-3Zr	58	589	[97]
Ti–45Nb	64	527	[103]

2.3.1 Design of β-Ti Alloys

Design approaches for the development of novel β-type Ti alloys have become the main strategic tool to predict phase stability, Young's modulus and dominant deformation mechanism. In the following theoretical approaches, the aim is predominantly limited to qualitative variables. Nevertheless, real materials' properties depend on the co-existence of quantitative and qualitative variables (e.g., morphology, microstructure, processing conditions, etc.)

Molybdenum Equivalence

The molybdenum equivalence ($[\mathrm{Mo}]_{\mathrm{eq}}$ or MoE) concept was proposed as general guideline to predict β phase stability [104]. The developed expression, updated, varied and refined over the years, represents the contribution to the β phase stability of each alloying element, in contrast with the most effective β-stabilizer Mo, arbitrarily chosen. It should be noted that this expression is only empirical: neither the interaction among alloying elements, nor their isomorphic or eutectoid character is taken into account. The β phase martensitic transformation temperature (M_s) generally decreases with an increase in $[\mathrm{Mo}]_{\mathrm{eq}}$ value. Hence, the stability of the β phase, or in other words, the amount (wt.%) of alloying elements necessary to suppress M_s, is predicted by this rule as follows: [86]:

$$\begin{aligned}[Mo]_{\mathrm{eq}} = {} & 1.0[Mo] + 1.25[V] + 0.59[W] + 0.33[Nb] + 0.22[Ta] + \\ & + 1.93[Fe] + 1.84[Cr] + 1.51[Cu] + 2.46[Ni] + 2.26[Mn] + \\ & + 3.01[Si] + 0.31[Zr] + 2.67[Co] - 1.47[Al]\end{aligned} \tag{2.1}$$

The constant before each element content (wt.%) in Equation 2.1 is the ratio of the critical Mo concentration to retain the metastable β phase after quenching and to prevent formation of martensitic phases. The effect of α stabilizing agents is included in Equation 2.1 through the aluminum equivalence ($[\mathrm{Al}]_{\mathrm{eq}}$ or AlE) [105]. The coefficient for the α-stabilizer Ga is taken as 0.5, based on the works of Shamblen and Redden [106].

$$[Al]_{\mathrm{eq}} = 1.0[Al] + 0.5[Ga] + 10[O + N] \tag{2.2}$$

In general, a typical $[\mathrm{Mo}]_{\mathrm{eq}}$ value greater than 10 wt.% is considered sufficient to decrease M_s, and therefore to enhance the β phase stability upon quenching [107]. According to the $[\mathrm{Mo}]_{\mathrm{eq}}$ value, β-type Ti alloys can be classified as follows: $\alpha+\beta$ for $[\mathrm{Mo}]_{\mathrm{eq}} < 5$, *near-*$\beta$ for $5 \leq [\mathrm{Mo}]_{\mathrm{eq}} \leq 10$, *metastable* β for $10 < [\mathrm{Mo}]_{\mathrm{eq}} \leq 30$ and *stable* β for $[\mathrm{Mo}]_{\mathrm{eq}} > 30$.

D-Electron Concept

The d-electron alloy design concept was first proposed by Morinaga et al. [108]. The concept is based on the following electronic parameters: i) mean bond order ($\mathrm{B_o}$), a measure of the covalent bond between Ti and the alloying elements and ii) mean d-orbital energy ($\mathrm{M_d}$) [86]. Traditionally, high bond order elements (e.g., V, Nb, Cr, Mo) were the principally alloying constituents in Ti alloys. Recently, the effect of other alloying elements (e.g., Fe, Cu, Ni, Mn) is also being screened. The B_o and M_d values can be used to predict mechanical, chemical properties and deformation mechanism of the alloy [109]. Plots of B_o–M_d, determined from experimental data, haven been developed with the aim of predicting the effect of alloy composition on deformation behavior (Fig. 2.12a). With increasing β phase stability, reflected by either an increase in B_o or decrease in M_d, the deformation mechanism changes from twinning and/or martensitic transformation to dislocation slip [110].

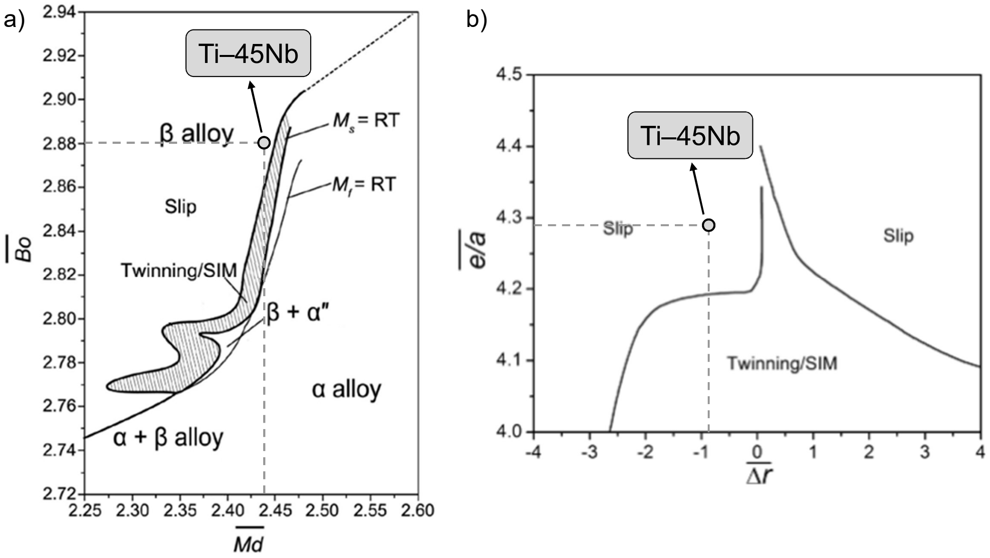

Figure 2.12: (a) B_o–M_d and (b) e/a–Δr_a plots showing regions of dominant deformation mechanisms for solution-treated β-type Ti alloys (adapted from Ref. [111, 112]).

Electron-to-Atom Ratio

Recently, a new semi-empirical approach has been designed [111], and then revised and refined [112], for the prediction of the dominant deformation mechanism in β-Ti alloys and it is based on the average electron-to-atom (e/a) and average atomic radius difference (Δr_a) (Fig. 2.12b). The electron-to-atom is defined as follows:

$$e/a = \Sigma_i^n c_\mathrm{i} e_\mathrm{i} \tag{2.3}$$

where n is the number of alloying elements, c_i is the atomic fraction (at.%) of the ith atom and e_i is the number of valence electrons of the ith atom. The average Δr_a estimates the misfit in atomic size ($\Delta r_\mathrm{a} = \Sigma_i^n c_\mathrm{i}(r_\mathrm{i} - r_\mathrm{Ti})$, where r_i is the atomic radius of the ith atom and r_{Ti} is the atomic radius of Ti). The value of e/a represents the average quantity of electric charge of each positive ion, determined by both attracting and repulsive Coulomb forces caused by surrounding electrons and neighbouring ions. An increase in e/a means an increase in Coulomb forces, and therefore a higher bonding strength among atoms, which consequently induces a higher resistance to atomic movement and lattice shear. It is suggested that the deformation mechanism of β-Ti can only proceed by dislocation slip when e/a > 4.2

and Δr_a < -2.5, beyond this region, deformation occurs by twinning/SIM (stress-induced martensitic transformation). An e/a value of 4.2 represents the boundary above which Coulomb forces and metallic bond strength are too high for lattice shear, and thus deformation can proceed by only slip. Besides, the β phase stability is also observed to increase with e/a; Laheurte et al. [113] suggested that the value of e/a = 4.2 is the lower limit for a stable β phase. For instance, this tool correctly predicted the deformation mechanism of a series of Ti–25Nb–8Zr–(2–8)Cr alloys [92]. The e/a has also been reported to be an additional factor that contributes to low Young's modulus in BCC Ti alloys [100].

The aforementioned alloy design methods are effective tools available for the researchers, however each method has its own advantages and limitations. For instance, the $[\mathrm{Mo}]_{\mathrm{eq}}$ method gives an indication about the range of β stability, but makes it difficult to actually predict phases and properties. On the other hand, the d-electron orbital theory is useful in the prediction of phases and properties, but it necessarily needs experimental confirmation, moreover the effect of α stabilizing agents should also be analyzed.

2.3.2 Ti–Nb Alloys

The great attractiveness of Ti–Nb alloys is due to their outstanding combination of low elastic modulus, high biocompatibility and high corrosion resistance [33], together with superelastic and shape-memory behavior [114–116]. Two stable solid phases exist in the Ti–Nb equilibrium phase diagram (Fig. 2.13) and several metastable phases can coexist depending on Nb content and processing conditions.

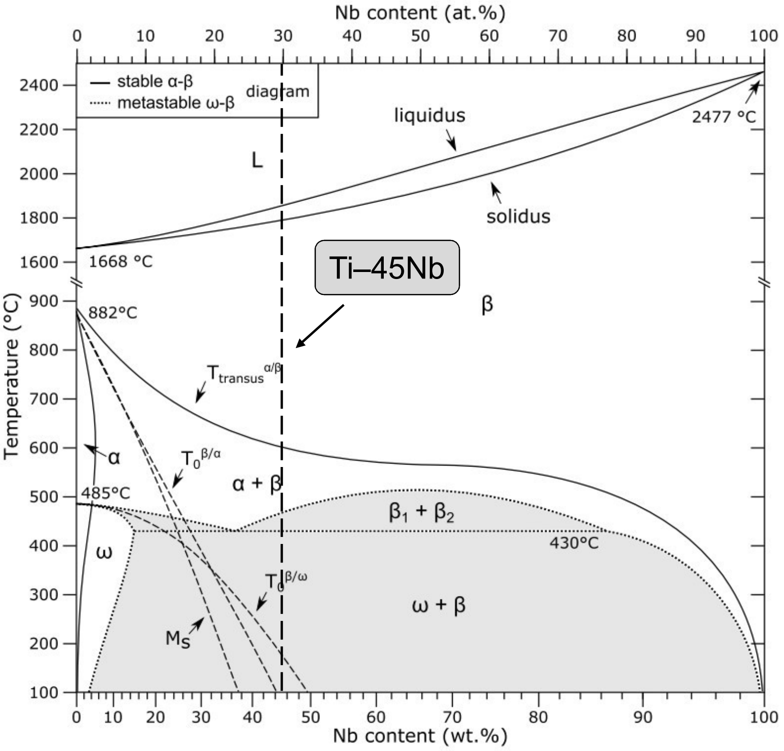

Figure 2.13: Stable and metastable Ti–Nb phase diagrams [117].

Nb is a β-stabilizer and exhibits limited solubility in α-Ti and almost complete solubility in β-Ti [118], when the stable α–β phase diagram is considered. At very low Nb content ($<$ 6 wt.%), the HCP α-phase is stable at room temperature. The β phase can be fully retained at room temperature by rapid quenching for Nb content above $\approx$ 36 wt.% [119]. Depending on the stabilization degree of the high-temperature parent solid solution BCC β phase, the following phase transformations might occur upon cooling: $\beta \rightarrow \alpha$', $\beta \rightarrow \alpha$", $\beta \rightarrow \omega$. The phases α' (hexagonal, *P6₃/mmc*) and α" (orthorhombic, *Cmcm*) form martensitically from the β phase, and their atomic rearrangements strongly depend on the stoichiometry of the parent β phase [120]. These two martensites and the ω-phase compete to form in the metastable BCC matrix. In addition to the $\alpha \rightarrow \beta$ allotropic transformation at 882°C, Ti exhibits a metastable transformation between hexagonal ω-Ti and BCC β-Ti at an estimated temperature of 485°C [121]. The metastable allotropic ω–β transformation can give rise to the possibility for β to athermally transform into ω (ω_{ath}), which is considered to compete with α" upon cooling. The ω may also form from the parent β-phase in a thermally activated manner, accomplished by solute partitioning via diffusion, and is therefore referred to as isothermal ω (ω_{iso}) [122].

Table 2.5: Crystal structures of stable and metastable phases of Ti.

Phase	Bravais lattice	Space group (No.)
β	body centered cubic	$Im\bar{3}m$ (229)
α/α'	hexagonal	$P6_3/mmc$ (194)
α"	c-centered orthorhombic	*Cmcm* (63)
ω	hexagonal	*P6/mmm* (191)

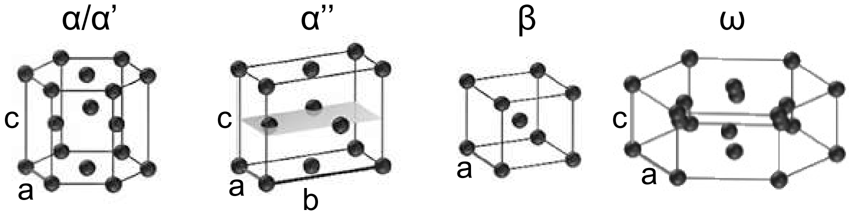

In this sense, the studies conducted by Bönisch et al. [120, 123] have significantly contributed to the field of β Ti–Nb alloys for bone implant applications, by exploring a wide range of compositions (Nb content: 9 – 44.5 wt.%). Their studies aimed at understanding the governing microstructural phenomena during heat treatments, the formation and thermal stability of martensites (α' and α") [123] and their gradual structural changes upon Nb addition [120], phase transformations, precipitation reactions and elastic properties in dependence of the Nb content [119, 124, 125], lattice variations occurring during thermally-induced $\beta \rightarrow \alpha'/\alpha''$ martensitic transformations [126]. In one of their most recent work, they exploited a novel approach for the prediction of temperature-induced structural changes and phase transformations from the Gibbs free energy landscape and studied precipitation pathways involving diffusion-mediated α" phases [127]. Their findings provide important insights into the structural phenomena of β-type Ti–Nb alloys and have profound implications for the development of new low-modulus alloys. Recently, Pilz et al. [47] studied the influence of ω_{iso} precipitation aging on the deformation mechanism of β-Ti–40Nb alloy recrystallized and aged at 573 K for different times. The presence of ω_{iso} (Fig. 2.14a), investigated by TEM, suppresses deformation twinning and stress-induced martensitic transformation (SIM), because ω_{iso} precipitates act as obstacles for long-range martensite formation. Moreover, by acting on the aging holding time, and therefore volume fraction of ω_{iso} precipitation, the authors were able to finely tune the resulting mechanical properties, with values of proof stress in the range 410 – 900 MPa and values of Young's modulus E in the range 70 – 95 GPa (Fig. 2.14b). The high Young's modulus of 95 GPa of the alloy is due to the intrinsic high Young's modulus of ω phase.

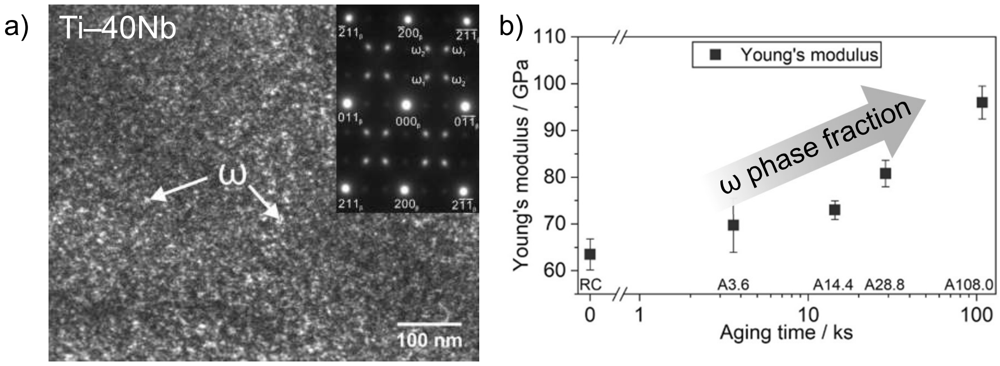

Figure 2.14: (a) Dark field TEM image and corresponding selected area diffraction pattern (inset) showing ω_{iso} phase formed in a recrystallized and aged (573 K, 108 ks) Ti–40Nb alloy, and (b) variation of Young's modulus with aging time (adapted from Ref. [47]).

Stable and metastable phases of β-Ti show different values of elastic Young's modulus (E) and yield strength (σ), which are indeed greatly affected by crystal structure and composition, and they range in the order [86]:

$$E_{\beta} < E_{\alpha"} < E_{\alpha'} < E_{\alpha} < E_{\omega} \tag{2.4}$$

$$\sigma_{\alpha} < \sigma_{\beta} < \sigma_{\alpha"} < \sigma_{\alpha'} < \sigma_{\omega} \tag{2.5}$$

For load-bearing implant applications, it is fundamental to reduce the Young's modulus to match the modulus of human cortical bone ($E_{\mathrm{bone}} = 10 – 30$ GPa), in order to avoid bone resorption in the vicinity of the implant [33]. At the same time, it is necessary to avoid a loss in strength in order to provide a balance between low modulus and sufficient strength. In the work of Hanada et al. [128], the composition dependence between Nb content and Young's modulus E was experimentally demonstrated (Fig. 2.15). At low Nb content (< 5 wt.%), the Young's modulus of the α-type Ti–Nb alloy is close to the value of pure Ti ($E \cong 115$ GPa). The graph shows two minima at Nb content of approximately 15 wt.% and 42 wt.%, where $E \cong 70$ GPa and $E \cong 60$ GPa, respectively. Age-hardening by ω precipitation occurs at Nb content of ≈ 36 wt.%, therefore increasing the value of E. The second minimum corresponds to single-phase β Ti–Nb alloys with the lowest possible Young's modulus, where athermal ω (ω_{ath}) is fully suppressed on quenching.

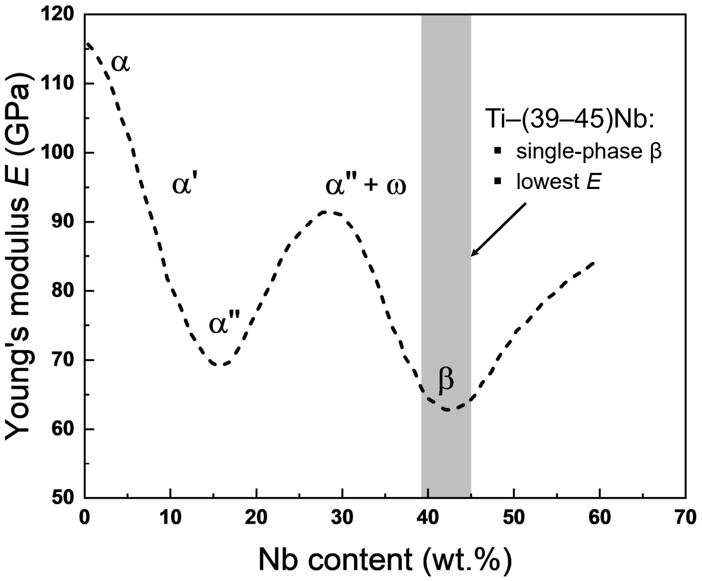

Figure 2.15: Composition dependence of Young's modulus with Nb content in the Ti–Nb binary alloy system (recreated from Ref. [128]).

Several alloy systems were developed with the aim of decreasing the Young's modulus while suppressing ω precipitation: ternary systems such as Ti–Nb–Zr [19, 129, 130], Ti–Nb–Mo [102], Ti–Nb–Sn [96, 99, 131], Ti–Nb–Ag [132], Ti–Nb–In [101, 133], Ti–Nb–Hf [134], Ti–Nb–Ta [135], quaternary systems such as Ti–Nb–Zr–Sn [136], Ti–Nb–Ta–Zr [100, 137], Ti–Nb–Mo–Zr [138, 139], Ti–Nb–Fe–Zr [95], Ti–Nb–Fe–Sn [95]. In the case of indium (In) alloying (up to 5.2 wt.%) to single-phase β Ti–40Nb alloy [101], the parent BCC lattice is observed to expand with In, both experimentally and theoretically. The larger BCC unit cell volume contributed to lowering the Young's modulus ($E = 49$ GPa). The great majority of newly developed implant alloys with low Young's modulus exhibit microstructures mainly consisting of metastable β phase, obtained via homogenization treatment (solution heat treatment and water quenching, STQ). Generally, the STQ condition of β alloys exhibits the lowest Young's modulus, but also the lowest strength (Table 2.4). Strategies to improve strength of metastable β-Ti alloys include solute strengthening by alloying and strengthening by controlled precipitation of α and ω particles [51, 86].

2.4 Current Trends in Metallic Biomaterials with Antibacterial Properties

2.4.1 Material-Based Solutions for Reducing Implant Infections

Biomedical implants have largely increased life quality of millions of people across the globe in the last decades, but infection risk increases alongside. Many implant failures are due to suboptimal mechanics of the device (poor mechanical compatibility), to release of toxic ions (poor wear and corrosion resistance), and to implant-associated bacterial infections. Implant- or biomaterial-associated infections (BAI, IAI) are the most frequent and severe complication occurring in all types of biomaterials (Table 2.6); for example, in the European Union alone, implant-associated infections account for approximately half of all healthcare-associated infections (>4 million/year) [10]. About 20% of all fatalities worldwide are caused by infection diseases [140].

Table 2.6: Incidence of implant-associated infections for different implants and devices, given over implant lifetime [7].

Implant	Infection incidence
Prosthetic hip	2 – 4 %
Prosthetic knee	3 – 4 %
Fixation screw	5 – 10 %
Tibial nail	1 – 7 %
Dental implant	5 – 10 %

Implant infections have an immense clinical incidence, associated morbidity and mortality, and significant economic and social costs, shared across all categories of medical devices. Increasing use of medical devices increases our life expectancy, but exacerbates the mentioned problems. Specifically, permanent implants face two major challenges: lack of native tissue integration and infections [7]. In spite of ongoing advancements in surgical techniques, wound care and device design, and booming growth in scientific publications, BAIs continue to be a significant problem in modern medicine and very few technologies actually found a real clinical application [141]. Conventional antibiotic treatments often fail due to their low concentration at the infection site [142], moreover the presence of bacterial biofilms on the implant surface further impairs antibiotic efficacy. Unfortunately, the lack of a suitable treatment often leaves the extraction of the contaminated device as the only option for eliminating the biofilm [143]. Therefore, great research efforts from both medical and implant manufacturing communities have been focusing on the development of new materials or coatings able to tackle BAIs.

The Bacterial Biofilm

A bacterial biofilm is a colony of bacteria embedded and protected by a self-produced three-dimensional matrix of extracellular polymeric substances (EPS): proteins, polysaccharides, lipids, extracellular DNA, water [144]. This 3D architecture generates a high concentration of available nutrients and reduced oxygen levels, which contribute to the creation of a suitable microenvironment for biofilm growth [145]. Bacterial biofilms are responsible of 80% of human chronic infections [140]. This is because bacteria in a biofilm are 600 times more resistant to disinfectants and 1000 times less vulnerable to antibiotics, compared with the planktonic counterparts. IAIs are mostly caused by Staphylococci (*S. epidermidis*, *S. aureus*) and by Streptococci, Gram-negative bacilli (*P. aeruginosa*, *E. coli*), enterococci and anaerobes (*P. acnes*). Staphylococci are generally the most common cause of orthopedic implant infections [8, 146]. Fig. 2.16 shows the four stages of biofilm development on the implant surface, which is mediated and controlled by several factors: surface properties (surface energy, hydrophilicity/hydrophobicity, functional groups, micro-/nano-roughness, micro-/nano-porosity), environmental conditions (pH, electrolytes, fluid viscosity, host proteins, biomolecules), and bacterial strain [147].

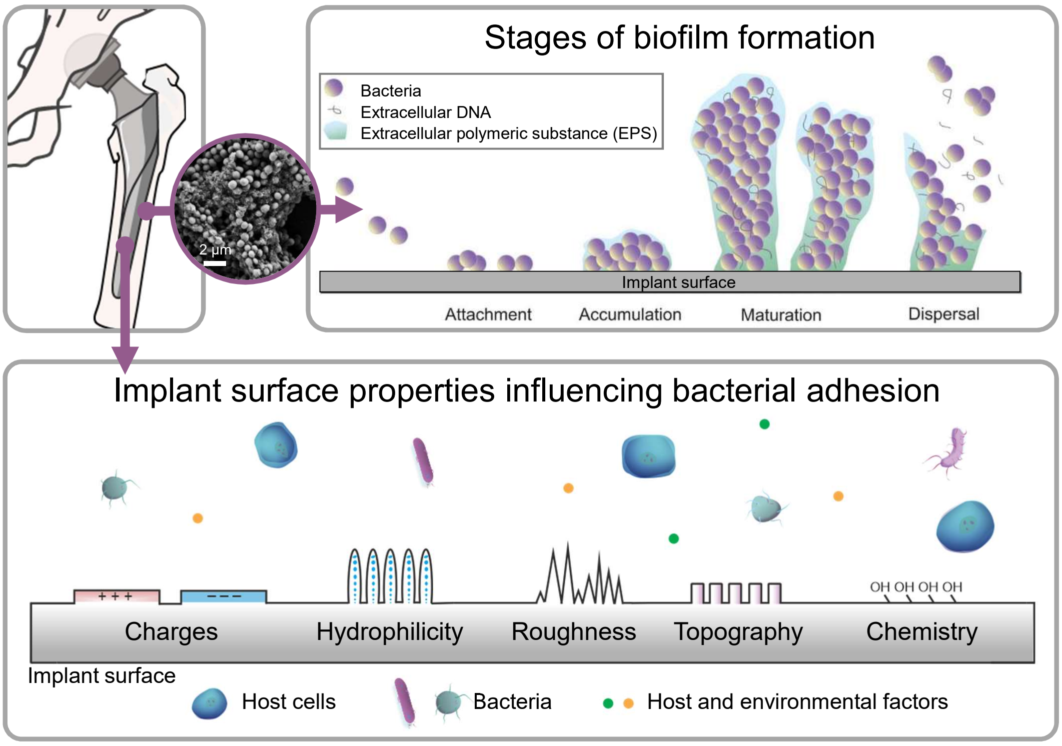

Figure 2.16: Stages of biofilm formation [146] and implant surface properties affecting bacterial adhesion [147].

Race for the Surface

Implant microbial contamination is the prelude to implant-associated infections. Over the years, it has been suggested that the fate of a biomaterial surface may be conceptualized as a *race for the surface* [148]. Such concept describes the competition between host cells and contaminating bacteria for the colonization of the biomaterial surface (Fig. 2.17). If the race is won by the host tissue, then the surface is occupied and defended, and is thus less prone to bacterial colonization. However, if bacterial adhesion takes place before, host defenses cannot prevent the surface colonization, biofilm formation and infection [8]. On a time scale, in the first nanoseconds, the implant surface makes contact with water molecules of the biological fluids first, then ions are adsorbed and, in few seconds, proteins cover the whole surface [149]. In the time span of minutes to hours, different kind of cells approach and adhere onto the surface. At the same time, bacteria compete with host cells for surface colonization. Bacterial predominance typically results in biofilm formation, which causes implant infection with consequent activation of immune host cells and, if chronical, implant rejection. In the absence of skin-penetrating trauma, it is likely that contaminating microorganisms have either entered the wound site, or attached to the implant during surgery (perioperative contamination) or during hospitalization, before wound closure (early postoperative contamination) [7]. Causes are as follows: implant surface, surgical equipment and theatre, coming from the patient or contaminated disinfectants [150]. Therefore, no surgical theatre is truly sterile: during a 1-hour standard surgery, the total estimated number of bacteria-loaded particles falling into the wound amounts to about 270 bacteria/cm^2 [7]. Sterile implant surgery may be considered a myth, therefore there is a strong need for intrinsically antibacterial implant materials.

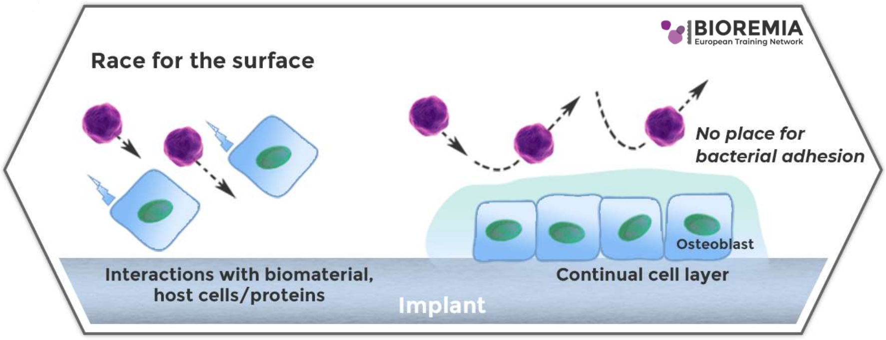

Figure 2.17: Scheme of the competition between bacteria and host cells in the colonization of the abiotic implant surface, known as *race for the surface* (reproduced from bioremia.eu).

Material-Based Bio-Engineering Strategies

An effective way to achieve improved biomaterials is to synergistically combine different design approaches and functionalities. It is essential to monitor and regulate the events that occur on the implant's surface. Possible strategies developed to tackle IAIs include inhibiting the adhesion of planktonic bacteria onto the implant surface, preventing bacteria aggregation, and directly killing the bacterial cells. In general, materials selection and design strategies can be grouped into the following two macro-categories: (i) active and (ii) passive materials/coatings [151]. (i) Active materials/coatings exert a local bactericidal activity, whose mechanism of action can either be by agent-release or by contact-killing. Bactericidal agents include: antibiotics (e.g., gentamicin, amoxicillin, cephalexin, etc.), phytochemicals (e.g., phenolic compounds, alkaloids, organosulfur compounds, etc.), nanoparticles (organic, inorganic, hybrid), quaternary ammonium salts, antimicrobial peptides (AMPs), bactericidal polymers (e.g., chitosan, polypyrrole derivatives, etc.), and metal ions (e.g., Zn, Ag, Cu, Ga, etc.). (ii) Passive materials/coatings prevent bacteria adhesion: antiadhesive polymers (e.g., PEG, PMMA, etc.) and antifouling nanotopographies. On top of that, the active/passive antibacterial functionality can be implemented in both bulk materials or surfaces/coatings, and both approaches have advantages and disadvantages. While not claiming to be exhaustive, potential drawbacks of surfaces/coatings include a limited duration of the antimicrobial activity and coating delamination. In comparison, antibacterial bulk materials (e.g., metals and alloys) offer major advantages: long-term antibacterial activity, easy control and preparation, and no potential drug-resistance. However, some disadvantages should also be considered: mechanical and corrosion properties are largely affected by alloying elements, and potentially harmful metal ions can be released [151].

The ideal strategy to fight biofilms consists in developing multifunctional materials/coatings that mitigate and prevent bacterial colonization while promoting osseointegration, as schematically shown in Fig. 2.18. Both effects are necessary to ensure long-term optimal functionality of the medical implant [152].

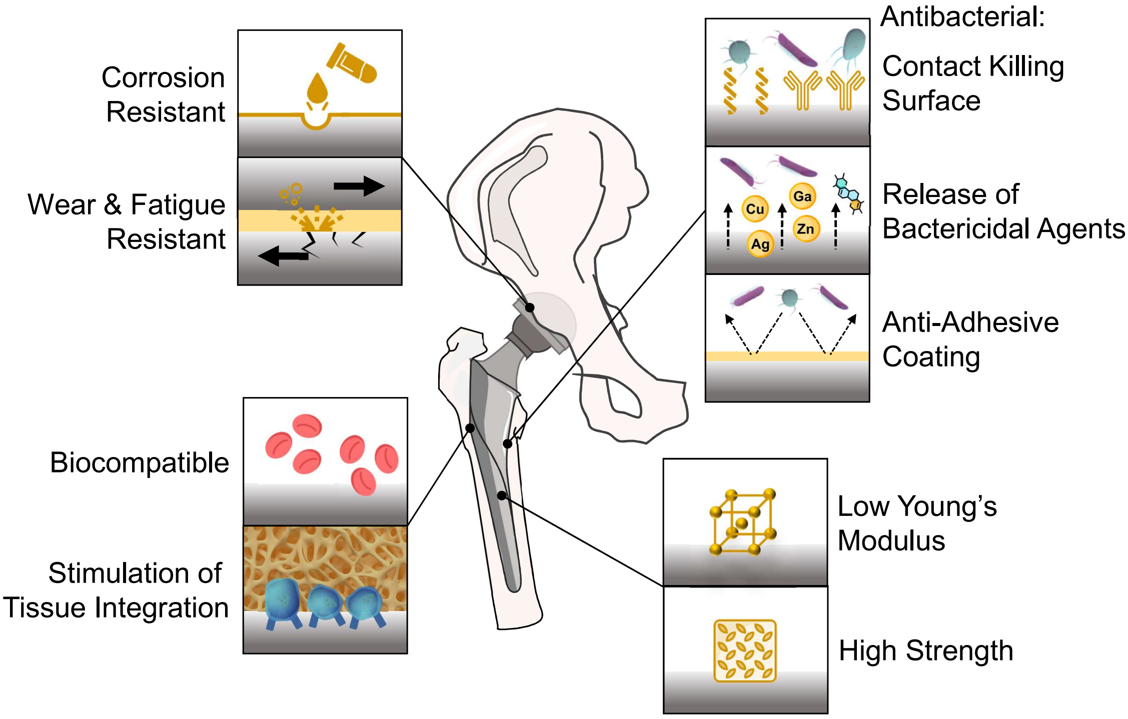

Figure 2.18: Ideal multifunctional implant material designed to simultaneously respond to several biological and mechanical challenges.

2.4.2 Antimicrobial Activity of Metals

Metals have been used as antimicrobial agents since ancient times, until approximately the discovery of antibiotics in the previous century. Now, with the incipient threat of antibiotic-resistance, their use is undergoing a renaissance. Metals and their compounds have a multitude of applications in industry, agriculture and healthcare and can now be found in liquid formulations for hand washing, wound dressings, medical devices such as catheters, antiviral filters, delivery systems, and more [152]. These innovations were made possible following the discovery that some metals effectively disrupt and kill antibiotic-resistant bacterial biofilms [153]. The antimicrobial properties of metals have been documented in many works and continue to be the subject of thorough investigations with the aim of understanding the mechanisms of toxicity and resistance. It is fundamental to mention that, generally, at high doses, metals are toxic to all cell types. However, certain metals can discriminate between bacterial and eukaryotic targets, because both cell types have divergent metal transport systems and metalloproteins [154]. Current knowledge is already leading to the rational design of selective antimicrobial metal agents.

Mechanisms of Metal Toxicity

Metal chemistry is essential in understanding the determinants of antibacterial toxicity. Metals are used not only in the bulk form, but also in the oxidized state, coordinated to inorganic or organic anions. They have multiple sites of action in bacteria, including essential proteins, nutrients, membranes and DNA. The most pertinent determinants of antibacterial toxicity are (i) donor atom selectivity, (ii) reduction potential and (iii) speciation [154]. (i) The *donor atom selectivity* is a specific principle of donor ligand atoms (O, N, S) that show high affinity to specific metals and selectively forms metal-ligand coordination complexes. The preferences of donor ligands provide biomolecules like proteins with selection bias for the correct metal needed for its proper function. However, not all biomolecules are able to properly discriminate, and many can bind metal ions or complexes with similar geometry and electronic structure to the correct cofactors (e.g., Trojan Horse strategy, Sec. 2.4.3). This phenomenon was termed ionic mimicry or molecular mimicry. (ii) In addition, metals can participate in redox reactions because they can accommodate a variable number of valence electrons in their outermost orbitals. Their tendency to acquire electrons is determined by the thermodynamic parameter *reduction potential*, and largely influences reactivity towards biomolecules, and thus toxicity in biological systems. Redox-active metals act as catalytic cofactors in a wide range of enzymes, however not all metals are redox-active, and this is significant for toxicology and antibacterial ability. (iii) Moreover, metals can exist as a multitude of different chemical species (*speciation*), with different solubility and reactivity, and this is determined by various factors: pH, reduction potential, temperature and ionic strength. Essential metals are never free inside a cell, but always bound to specific enzymes, structural and storage proteins.

These determinants can contribute to understanding how specific metal characteristics influence the mechanisms of metal toxicity, presented below, which often act simultaneously to induce bacterial death [154].

- *Reactive oxygen species (ROS).* Some metal ions can lead to the production of intracellular toxic ROS, which include the superoxide ion ($O_2^{\cdot\,-}$), peroxides (H_2O_2), hydroxyl radical ($OH^{\cdot}$). These species are extremely reactive and can further react with practically any biological molecules in the near vicinity via hydrogen abstraction, leaving carbon-centered radicals. There are other possible reduction reactions *in vivo*, including the reduction of disulfide bonds and other protein-like molecules. Studies report that toxic doses of the following metal ions can increase intracellular ROS via Fenton chemistry: Fe(II), Te(IV), Cr(VI), As(III), Cu(II), Co(II).
- *Protein dysfunction and loss of enzyme activity.* Functional groups of protein residues are susceptible to site-specific metal-catalysed oxidation, which might cause loss of catalytic activity and trigger protein denaturation. As an example, the following metal ions are able to damage Fe–S clusters of dehydratases (group of enzymes), independently of ROS: Ag(I), Cd(II), Hg(II), Zn(II), Ni(II), Pb(II), and Co(II).
- *Impaired membrane function.* The polymers constituting bacterial membranes contain highly electronegative chemical groups which might serve as sites of

adsorption of metal ions, leading to severe membrane damage, and consequently bacterial death. Despite the difficulty to confirm whether membrane disruption is a cause or a consequence of cell death, evidences were reported for Ag(I), Al(III), Cd(II), and Cu(II).

- *Interference with nutrient uptake.* Starvation-induced growth arrest has also been linked to metal toxicity. For example, Cr(IV) inhibits sulfate uptake in *S. cerevisiae*, analogously, Ga(III) inhibits Fe(III) uptake in *P. aeruginosa*.
- *Genotoxicity.* Several metal ions (Mn(II), Co(II), As(III), Cd(II), Mo(IV), Cr(VI), and Sb(III)), together with some organomercury complexes, are mutagenic in bacteria.

2.4.3 Gallium & Copper as Antibacterial Agents

Among the many antibacterial metals (Ag, Co, Cr, Cu, Fe, Ga Mn, Ni, Pb, Zn), gallium (Ga) and copper (Cu) have shown a great potential in eradicating bacterial biofilms [151, 155], and are the focus of the present research work.

Gallium

Gallium (Ga) is a silvery white metal of the main group 13 of the periodic table with a melting point (T_m) of 29.8°C. Gallium compounds, many of which already approved for clinical use, have been of great interest to the medical community for several years. They have advanced in preclinical and clinical investigations and have shown therapeutic and diagnostic activity in bacterial infections [156, 157], tumours [158], inflammatory conditions [159] and in bone diseases, such as in the treatment of hypercalcemia and osteoporosis [160] (Table 2.7).

Table 2.7: Gallium compounds in clinical use and in development [161].

Gallium compound	Diseases investigated
1st generation (evaluated in clinical trials)	
Ga nitrate, Ga chloride	hypercalcemia, bladder cancer, lymphoma, lung cancer, other cancers, microbial infections
2nd generation (pre-clinical, Phase I and II clinical trials)	
Ga maltolate	hepatoma, lymphoma, microbial infections
Ga citrate	microbial infections
KP46	lung cancer, melanoma, other cancers
3rd generation (pre-clinical trials)	
Ga-pyridine, -phenolate	prostate cancer
Ga-thiosemicarbazones, Ga-hydrazones, Ga-azoles, Ga-thiolato, Ga-corroles Ga-protoporphyrin	various cancers

Chemically-resistant materials that can release Ga ions in a controlled way over extended periods of time would be desirable for biomedical applications. The biological features of Ga have piqued the curiosity of scientists, who have started to explore them in various systems. Indeed, Ga-containing bioactive materials (Fig. 2.19) can be classified in glasses, ceramics, polymers, coatings, scaffolds, composites, and metallic alloys [162]. For instance, Ga-doped phosphate glasses exhibit, by controlled ion release, significant bactericidal activity against *S. aureus* [163], similarly, single-crystalline β-Ga_2O_3 nanorods generate sufficient ROS, by photocatalytic oxidation reaction, to efficiently kill *E. coli* and *S. aureus*, even better than the antibiotic streptomycin [164].

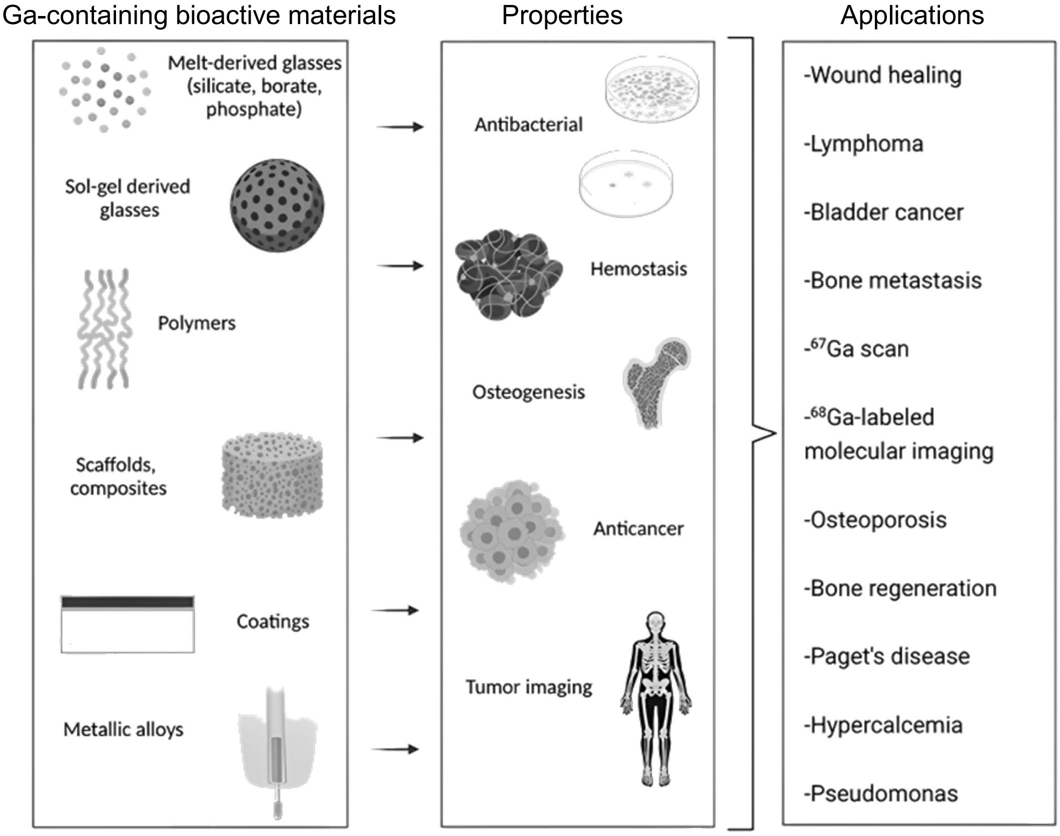

Figure 2.19: Gallium-bearing bioactive materials and their biomedical applications (reproduced from Ref. [162]).

Gallium is one of the few metals that expands by approximately 3% as it cools down and can diffuse into the lattice of many metals to form alloys: solder alloys [165], Pu–Ga [166], Mg–Ga [167] and Ti–Ga [168, 169] alloys. Biodegradable Mg–Ga alloys have recently been the subject of a considerable body of literature regarding their use in biomedical applications for bioresorbable implants that would gradually dissolve as the healing process progresses. The investigations of Kubásek et al. [170] on Ga addition up to 7 wt.% in cast Mg–Ga alloys revealed a significant strengthening and hardening effect, due to different mechanisms: Hall-Petch hardening, solid solution hardening and Mg_5Ga_2 precipitation hardening. Moreover, their studies evaluated the biocompatibility of these alloys, and the presence of Ga did not result in cytotoxicity. Biomedical Ti-based alloys containing Ga as alloying element will be discussed in Sec. 2.5.

Antibacterial Activity of Ga: the Trojan Horse Strategy

Gallium ion has recently emerged as a new generation of antibacterial agent that may treat and prevent bacterial infections. Ga(III) possesses a potent growth-inhibitory activity, both *in vitro* (on planktonic bacteria and biofilms) and *in vivo* against a number of IAI-responsible bacteria [156] (Table 2.8). On the other hand, evaluating the cytotoxicity of Ga(III) is not straightforward, as it highly depends on Ga speciation. For example, gallium maltolate is well tolerated when orally administered to healthy human volunteers, while showing cytotoxicity towards human carcinoma cells [171]. $Ga(NO_3)_3$ is also very well tolerated up to 200 mg/m^2 per day for 5 days, even by elderly patients, when administered intravenously to treat hypercalcemia [158]. *In vitro* studies [172] using $Ga(NO_3)_3$ on rabbit bone cells, murine AW 264.7 (osteoblast-like), MC3T3-1 (osteoblast-like) showed no cytotoxicity up to 100 μM, which is, in certain cases, higher than the amounts needed to exert a powerful antibacterial and antibiofilm activity. Further concerns about alloyed Ga cytotoxicity were clarified in the studies of Kubásek et al. [170] on a series of cast Mg–Ga alloys that showed no pronounced cytotoxicity on osteoblast-like cells at Ga concentration below 310 ng ml^{-1}. The antibacterial activity of Ga against the dangerous multidrug-resistant *A. baumanii* resulted incredibly strong, more than silver (Ag) [173]. The study also showed that gradual release of Ga ions discourages implant colonization and proliferation.

Table 2.8: *In vitro* antibacterial and antibiofilm activity of gallium compounds.

Mode of growth	Microorganism	Compound	Inhibitory concentration (μM)		Ref.
Planktonic	*A. baumanii*	$Ga(NO_3)_3$	IC_{90}	2 – 80	[157]
	P. aeruginosa	$Ga(NO_3)_3$	IC_{90}	1 – 40	[157]
		$GaCl_3$	MIC	32	[157]
		Ga citrate	IC_{90}	20 – 40	[157]
	S. aureus	Ga citrate	IC_{90}	320 – 5120	[157]
		Ga maltolate	MIC	140 – 8988	[157]
	S. epidermidis	Ga maltolate	MIC	225 – 450	[157]
		Ga citrate	IC_{90}	1280 – 2560	[157]
Biofilm	*P. aeruginosa*	$Ga(NO_3)_3$	BIC	0.5	[156]
		$GaCl_3$	BIC	1	[156]
		Ga citrate	MBIC	10	[156]
	S. aureus	Ga maltolate	MBIC	6741 – 13482	[156]
	S. epidermidis	Ga maltolate	MBIC	211 – 6741	[156]

(IC_{90}: concentration that inhibits growth by 90%, MIC: minimum inhibitory concentration causing no visible growth, (M)BIC: (minimum) biofilm inhibitory concentration)

The antibacterial effect of Ga is strongly related to its biochemical similarity to iron (Fe). An unconventional approach to fight bacterial infections is to exploit nutritional vulnerabilities of bacteria, and the iron metabolism is the main candidate [174]. Iron is an essential nutrient for almost all pathogens, because it is necessary in enzymes mediating DNA synthesis, oxidative stress defense, electron transport, and other key processes. The innovative antibacterial strategy consists in 'tricking' the bacteria into assimilating a metal that mimics Fe, but cannot functionally replace it. Ga(III) and Fe(III) are metabolically similar, because of similar properties: charge, electronic configuration, coordination number, octahedral ionic radii of 0.62 Å and 0.64 Å, and tetrahedral ionic radii of 0.47 Å and 0.49 Å for Ga(III) and Fe(III) ions, respectively. One distinct difference is that Ga(III) cannot be reduced under the same physiological conditions as Fe(III), thus sequential redox metabolic reactions, involving Fe(III) $\rightleftharpoons$ Fe(II), are impaired. Hence, supplementation of Ga(III) can disrupt bacterial Fe-dependent metabolic processes and can function as a *Trojan horse*, as bacteria are unable to distinguish Ga(III) from Fe(III) [154]. Another remarkable feature making Ga a valid candidate in antibacterial applications is its ability to accumulate within the inflammatory sites [156]. Despite these positive aspects, therapeutics targeting bacterial iron metabolism have not yet been developed nor approved. The increasing availability of relevant *in vitro* and *in vivo* data suggests that some Ga-bearing formulations could potentially represent a strong complement and/or alternative to the use of conventional antibiotics and antimicrobials for the treatment of bacterial infections on medical devices [156, 174, 175].

Copper

Copper (Cu) is an essential, yet toxic in high amounts, trace element that cannot be synthesized by the human body, thus it has to be introduced by the diet: the World Health Organization (WHO) recommends 2 – 3 mg every day in healthy adults [176]. Cu plays crucial roles in growth and maturation of nervous, bone, hematopoietic and other systems. Furthermore, being equipped with a high redox potential, it functions as a cofactor and is required for structural properties and catalytic activity of a number of important enzymes (e.g., cytochrome *c* oxidase, tyrosinase, etc.), and it is involved in a variety of biochemical reactions (e.g., cellular respiration, connective tissue formation, iron metabolism, free radical eradication, neurological function, etc.) [177, 178].

In view of the global escalation of antibiotic resistance, Cu fits as a powerful ally. Numerous experimental studies have shown that Cu-bearing surfaces eradicated *in situ* a large number of harmful seeded microorganisms (*E. coli*, *S. aureus*, etc.), fungi and viruses [176, 179, 180]. Applications of antibacterial Cu range from water treatment as well as pipelines, fabrics, transportation, healthcare, biomedical devices, work surfaces, touch surfaces (e.g., in hospitals), and more [181–183]. Examples of consumer products containing Cu as active bactericidal ingredient include: Cu triethanolamine (*Pool Solutions® All Purpose Algaecide*) and Cu mixed ethanolamine chelates (*Cutrine® Plus*), Cu(I) oxide (*Cupron® Technology*), Cu powders (*Coppercoat®*) and Cu alloys (*CuVerro®*, *Microguard™*). In recent years, a growing number of researchers have tried to exploit the attractive features of Cu to create new biomedical materials that are advantageous to the human body, based on the significant roles that Cu plays in the body. In these regards, some reviews have been published on Cu-containing glasses and ceramics [184, 185], polymer composites [186] and alloys [176, 187]. Cu-containing materials, including metal alloys, may exhibit both biofunctionality and antibacterial activity, due to the biological activity of Cu ions. For instance, numerous studies have proven the superior abilities of Cu-bearing metallic biomaterials to protect the cardiovascular system [188, 189], to promote osteogenesis [190], and to exert antimicrobial effects [179, 191]. The antibacterial activity and cytocompatibility of Cu ions have been demonstrated *in vitro* on several bacterial strains and cells, and numerous studies report inhibitory concentrations against implant infections-relevant bacteria and tolerance levels for cell viability [176, 192–194]. For instance, the threshold concentration of Cu ions for effective inhibition against growth of *S. aureus* and *E. coli* is 37 μM, at higher concentration, antibacterial activity could increase dramatically [96]. The same authors reported toxicity tolerance levels (IC_{50}) for epithelial HUVECs, osteoblast-like MC3T3-E1 and bone marrow rBBMSCs cells of 327.9 μM, 134.6 μM and 0.7 μM, respectively, thus identifying a threshold concentration at which Cu shows outstanding antibacterial activity without significantly affecting the bone cells viability.

Antibacterial Mechanisms of Cu

Many of the aforementioned antibacterial mechanisms have been proposed for Cu. The most important and widely accepted explanation for Cu-induced cellular toxicity is based on the redox properties of Cu, in fact Cu ions, i.e., cupric Cu(II) and cuprous Cu(I), participate in the production of ROS in a Fenton-type reaction, which can severely damage proteins, lipids and DNA via oxidative stresses [195]. The cupric ion, in presence of biological reductants (e.g., ascorbic acid, glutathione), is reduced to cuprous ion, which is capable of catalysing the formation of reactive hydroxyl radicals ($OH^{\cdot}$) through the decomposition of H_2O_2, a product of mitochondrial oxidative respiration, via Fenton-type chemistry [154]: $Cu(I)+H_2O_2 \rightarrow Cu(II)+OH^{\cdot}+OH^{-}$. Furthermore, experimental studies confirmed that both cupric and cuprous ions induce irreversible DNA damage and oxidation of nucleobases via oxygen free radicals [192, 196]. The Cu-induced bacteria-killing process consists of four steps [195]. The Cu is first released from the Cu-doped surface/material. Second, the bacterial membrane breaks leading to a loss of the cytoplasmic content (Fig. 2.20). The subsequent generation of ROS further damages the bacterial cells by interacting with proteins and lipids, and ultimately, DNA fragmentation results in cell death. In general, the antibacterial properties of Cu are mainly associated with the release of Cu ions, however, Cu interaction with bacterial biofilms is very dissimilar from that with planktonic cells, and this is because of the protective EPS matrix, whose production can be reduced by Cu [183].

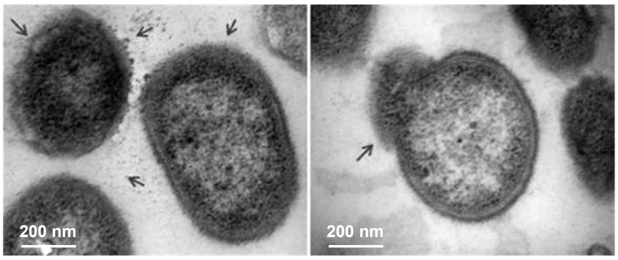

Figure 2.20: TEM micrograph showing *P. gingivalis* bacterial cells treated with a Ti–5Cu (wt.%) alloy. Arrows indicate membrane damage and release of cytoplasmic contents (adapted from Ref. [193]).

The studies of Liu et al. [193] demonstrated effective and sustainable antibiofilm properties of a Ti–5Cu (wt.%) dental implant alloy against oral bacterial species *S. mutans* and *P. gingivalis.* The developed alloy inhibited bacterial adhesion and biofilm formation. Moreover, the same alloy was shown to be biocompatible, with minimal release of Cu ions, well below the recommended daily intake, thus making it a desirable material for future clinical applications.

2.5 Ga-/Cu-Bearing Ti Alloys

Regardless of the advantages of clinically used Ti-based bone implants (c.p. Ti and Ti–6Al–4V), they are prone to bacterial adhesion and colonization, which result in bacterial infections and eventual implantation failure. The design of new antibacterial Ti alloys for implant applications is a research hotspot and antibacterial elements (Ag, Zn, Cu, Ga, etc.) are being added to improve their performances. A brief survey of the literature indicated that vast research has been focused on Ti–Ag alloys. Nonetheless, they possess a significant disadvantage, which is the formation of silver salts that could potentially enter the bloodstream and accumulate in different bodily tissues, resulting in major medical issues; moreover, another significant drawback that restricts its applications is that the antibacterial activity of Ag is highly dependent to pH, humidity and temperature, more than other antibacterial metals [197]. These limitations have encouraged researchers to focus on alternative antibacterial metallic agents. In particular, Ga- and Cu-bearing Ti alloys have recently attracted significant interest due to their ability to, respectively, promote long-lasting antibacterial activity and induce cellular proliferation and differentiation of human osteoblasts, which can enhance the osseointegration of the implant with the surrounding bone tissue [162, 195]. Therefore, the combination of Cu and Ga in Ti alloys may have the potential to improve the clinical performance of implants by reducing the risk of infection and promoting bone healing simultaneously. Table 2.9 contains relevant properties of the pure elements Ti, Nb, Cu and Ga. Table 2.10 summarizes the most recent developments on antibacterial Ti alloys containing Ga and Cu as minor alloying elements for biomedical bone-related applications. A variety of methods, including conventional casting, powder metallurgy and additive manufacturing, have been used to prepare new antibacterial Ti alloys.

Table 2.9: Physical and chemical characteristics of pure elements Ti, Nb, Cu and Ga: atomic number Z, electron configuration, atomic mass A, density ρ, atomic radius r_a [198], crystal structure at 20°C, melting temperature T_m, and Young's modulus E [199].

Element	Z	Electron configuration	A (amu)	ρ (g/cm^3)	r_a (Å)	Crystal structure	T_m (°C)	E (GPa)
Ti	22	[Ar] 3d^2 4s^2	47.87	4.51	1.46	HCP	1668	120.2
Nb	41	[Kr] 4d^4 5s^1	92.91	8.57	1.43	BCC	2468	104.9
Cu	29	[Ar] 3d^{10} 4s^1	63.55	8.94	1.28	FCC	1085	129.8
Ga	31	[Ar] 3d^{10} 4s^2 4p^1	69.72	5.90	1.39	Ortho.	29.8	9.8

Table 2.10: Relevant Ga- and Cu-containing Ti alloys (in wt.%, unless otherwise specified) for biomedical implant applications.

Alloy (wt.%)	Preparation method	Microstructure	Bacterial / cell strains	Effect on bacteria / cells	Application	Ref.
Ga-bearing Ti alloys						
Ti–8Al–3Si–3Zr–(1–20)Ga, Ti–23Ga	casting	intermetallic, eutectic-like	*S. aureus* / hFOB, U2OS	biofilm activity reduced > 80% / not cytotoxic	orthopedic	[200]
Ti–(2–10)Ga	casting	α	L929, MG63	not cytotoxic	dental	[168]
Ti–Nb$_{24}$–Ga$_{3}$ (at.%)	casting and post-treatment	$\beta + \omega_{\mathrm{ath}}$			shape-memory	[114]
Ti–Mo$_{(5–7)}$–Ga$_{(1–8)}$ (at.%)	casting and post-treatment	$\beta + \alpha + \alpha''$			shape-memory	[201]
Cu-bearing Ti alloys						
Ti–(2–4)Cu	casting and post-treatment	α + Ti$_2$Cu	*S. aureus*	AR > 90%	orthopedic, dental	[202]
Ti–5Cu	casting and post-treatment	α + Ti$_2$Cu	*E. coli*	AR: 49.3 – 99.9%	dental	[203]
Ti–(1–10)Cu	casting and post-treatment	α + Ti$_2$Cu + Ti$_3$Cu	*S. epidermidis*	AR: 7 – 46%	dental	[204]
Ti–(5,10)Cu	powder metallurgy	α + Ti$_2$Cu	*S. aureus*	AR: 50 – 99%	orthopedic, dental	[205]
Ti–10Cu	powder metallurgy	α + Ti$_2$Cu	*S. aureus*, *E. coli*	AR > 99%	bone implant	[206]
Ti–57Cu	powder metallurgy	Ti$_2$Cu + TiCu + TiCu$_2$ + TiCu$_4$ + Ti$_2$Cu$_3$	*S. aureus*, *E. coli* / MG-63	AR ≅ 98% / VR: 90 – 100%	orthopedic	[207]
Ti–(5–15)Nb–5Cu	powder metallurgy	$\alpha + \beta$ + Ti$_2$Cu	*S. aureus*, *E. coli*	AR ≅ 100%	bone implant	[208]
Ti–30Nb–(3–10)Cu	powder metallurgy	$\beta + \alpha$ + Ti$_2$Cu			bone implant	[98]
Ti–35Nb–7Zr–(4–13)Cu	powder metallurgy	$\alpha + \beta$ + Ti$_2$Cu + Cu$_x$Zr$_y$	*S. aureus*, *E. coli*	AR: 95.5 – 99.9%	bone implant	[209]
Ti–Nb$_{18}$–Cu$_{3–6}$ (at.%)	casting and post-treatment	$\beta + \alpha''$			shape-memory	[210]
Ti–(6–24)Nb–(1–4)Cu	casting	$\alpha + \beta$ + Ti$_2$Cu (+ α'' + ω)			dental	[211]
Ti–7.5Mo–5Cu	casting and post-treatment	$\alpha + \beta$ + Ti$_2$Cu	*S. aureus*, *E. coli* / MC3T3-E1	AR: 55 – 96% / cytocompatible, induced osteogenic differentiation	orthopedic	[194]
TNTZ–(1–10)Cu	casting and post-treatment	$\alpha + \beta$ + Ti$_2$Cu			dental	[212]
Ti–6Al–4V–5Cu	casting and post-treatment	$\alpha + \beta$ + Ti$_2$Cu	*S. aureus* / MC3T3-E1	AR: 62.5 – 90.2% / RGR: 87.5 – 92.9%	bone implant	[213]
Ti–6Al-4V–(2–6)Cu	additive manufacturing	$\alpha + \beta$ + Ti$_2$Cu	*S. aureus*, *E. coli* / BMSC	AR: 51.5 – 99% / RGR > 90%	bone implant	[214]

(AR: antibacterial rate, RGR: relative growth rate, VR: viability rate)

2.5.1 Ga-Bearing Ti Alloys

The use of gallium in dentistry has a long history, it was recommended as a replacement for toxic mercury in dental alloys as far back as the 1930s [168]. Indeed, mercury-free Ga-containing alloys have been developed for usage in clinical settings (e.g., *Galloy®*, Southern Dental Industries). Considering the aforementioned benefits of Ti as biomaterial, the study of Ti–Ga amalgams for dental applications became promising, also because Ti alloyed with Ga, according to the Ti–Ga phase diagram (Fig. 2.21), has a comparatively lower melting temperature, which then favours the casting procedure. Limited literature is available on Ti alloys containing Ga, mainly binary Ti–Ga alloys for dentistry (Table 2.10). Qiu et al. [168] investigated the effects of Ga addition (up to 10 wt.%) on a series of as-cast binary Ti–Ga alloys for dental applications. The microstructures of these alloys consisted of single-phase α, and Ga addition improved tensile strength (up to 700 MPa) and microhardness (up to 305 HV), as well as castability and corrosion resistance in artificial saliva. Young's modulus also gradually increased with Ga ($E = 103 - 117$ GPa). Besides, these binary Ti–Ga alloys showed no significant cytotoxicity on L929 fibroblast cells and MG63 osteosarcoma cells.

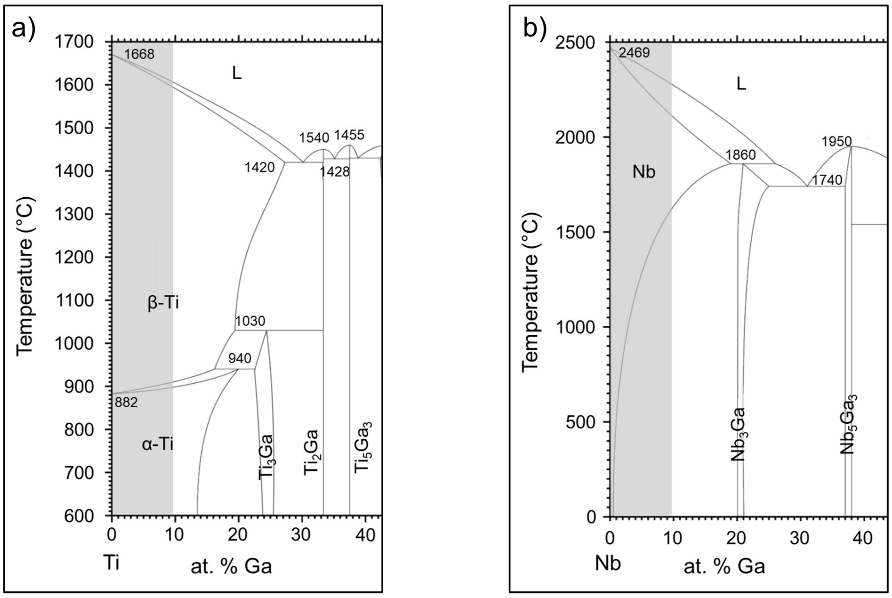

Figure 2.21: (a) Ti–Ga and (b) Nb–Ga binary phase diagrams, shaded areas represent Ti- and Nb-rich sections, relevant for this work [215, 216].

The work of Cochis et al. [200] provides insights into the potential use of Ga-modified (1 – 23 wt.%) cast Ti alloys for biomedical applications. While the article does not provide a detailed microstructural analysis, SEM images reveal the formation of intermetallic phases with hexagonal symmetry and primary crystals following eutectic-like phase. The authors demonstrated that Ga addition results in a time-increasing and concentration-dependent antibacterial activity against various bacterial strains, including *S. aureus* and *P. aeruginosa* (Fig. 2.22a). Interestingly, even small additions of Ga resulted in a significant antibacterial activity, with Ga 1 – 2% alloys reducing *S. aureus* biofilm viability by $< 50\%$, which is considered the minimal effective ratio to define a novel treatment as 'antibacterial'. The addition of Ga

20 – 23% was particularly effective and resulted in a 70 – 80% reduction in bacteria viability. Metal ion release analyses failed to reveal any Ga ions in the medium, thus suggesting that Ga release from these alloys is not effective, therefore, as alternative explanation, the authors concluded that the observed antibacterial effect is due to contact-killing. Furthermore, Ga addition did not result in any cellular toxicity to human fibroblasts and osteoblasts (Fig. 2.22b), suggesting that the Ga-modified titanium alloys may be safe for use in medical implants, and therefore have potential clinical relevance.

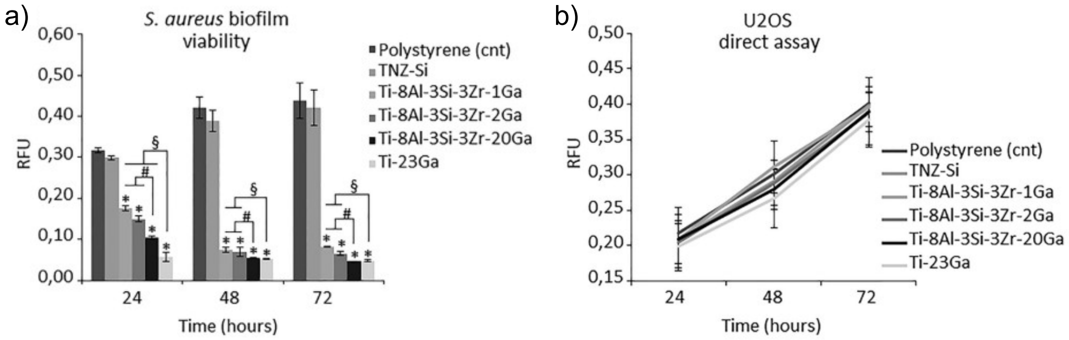

Figure 2.22: (a) Antibacterial effect against *S. aureus* biofilm of Ga-containing Ti alloys and (b) their cytocompatibility on human osteosarcoma U2OS cells (RFU: relative fluorescence units; adapted from Ref. [200]).

According to the author's knowledge, a complete Ti–Nb–Ga ternary phase diagram has not yet been reported, however there have been some experimental investigations, mainly for biomedical shape-memory implant applications: Ti–$Nb_{(18,24)}$–Ga_3 (at.%) alloys produced by casting with solution treatment at 1273 K [114, 217]. The Ti–Nb_{18}–Ga_3 (at.%, or Ti–30Nb–2.5Ga wt.%) alloy was subjected to a solution-treatment for 0.5 h, which resulted in a β+α" microstructure, and which ultimately leads to shape recovery at RT. Similarly, the Ti–Nb_{24}–Ga_3 (at.%, or Ti–38Nb–2.4Ga wt.%) alloy was subjected to a longer solution treatment (2 h) and its microstructure consisted of parent β phase and ω_{ath} phase. The alloy does not exhibit superelasticity at RT, because the reverse martensitic transformation temperature is higher than RT, but shows clear shape recovery. All these findings suggest that Ga-bearing Ti alloys may be a promising approach for developing antibacterial implant materials, even at low concentrations of gallium.

2.5.2 Cu-Bearing Ti Alloys

Cu-containing Ti alloys with inherent antibacterial effect have become an extremely active area of study [192, 193, 218], moreover Cu has also been used for long time as alloying element for dental casting alloys [219]. Cu was first added to Ti implant alloys to improve their mechanical properties and casting ability [219], and then to provide antibacterial properties [220]. A study [220] on Ti–(1,5)Cu alloys for the prevention of pin tract infection demonstrated the enormous potential of Cu element in the creation of anti-infection implant biomaterials, and it marked a significant turning point for their development. Several more studies reported the powerful antibacterial activity of these alloys, with antibacterial rates close to 100% against relevant IAI-responsible pathogens (Table 2.10). Ti alloyed with Cu has been reported to exhibit interesting properties such as good mechanical performance [204], good biocompatibility, and acceptable corrosion [221] and biocorrosion resistance [222], which can be optimized by changing Cu content and processing routes. Many Cu-containing Ti alloys were studied as implant materials: binary Ti–Cu [223], Ti–6Al–4V–Cu [213, 224, 225], c.p. Ti–Cu [202–204], TNTZ–Cu [212], Ti–Nb–Cu [77, 210, 226], and more. Major drawback is that excessive Cu addition (> 10 wt.%) could lead to cytotoxicity [197], reduced corrosion resistance [205], reduced ductility, and brittleness [204]. In view of these aspects, attentive microstructural design is necessary in order to optimize the mechanical, corrosion and antibacterial properties for the desired application.

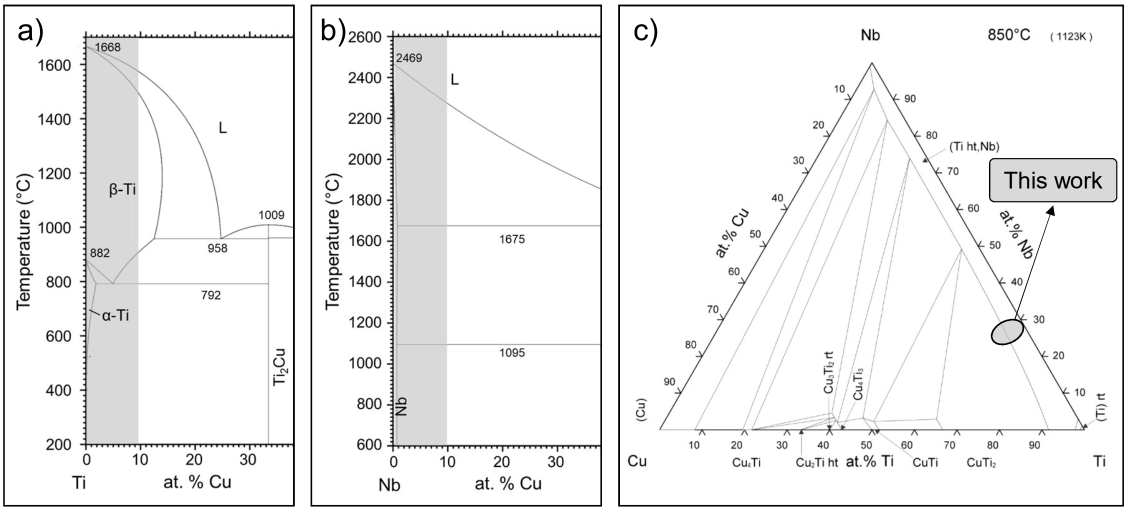

Figure 2.23: (a) Ti–Cu and (b) and Nb–Cu binary phase diagrams, shaded areas represent Ti- and Nb-rich sections, relevant for this work. (c) Isothermal section at 850°C of the Ti–Nb–Cu ternary phase diagram [216, 227].

Interest in this alloy system was also prompted by the very active $\beta \rightarrow \alpha$ transformation kinetics [228], which ultimately leads to fine tuning of resulting microstructural, mechanical and corrosion properties. The binary Ti–Cu equilibrium phase diagram contains several intermediate phases (i.e., $TiCu_4$, $TiCu_2$, Ti_2Cu_3, Ti_3Cu_4, TiCu, Ti_2Cu) [229]. The Ti-rich section is shown in Fig. 2.23a. At approximately Cu 7 wt.%, the eutectoid reaction β-Ti $\rightarrow$ α-Ti + Ti_2Cu occurs, which has also been observed in multicomponent Cu-containing Ti alloys. The binary Nb–Cu equilibrium phase diagram (Fig. 2.23b) is a simple peritectic type [230], and was described with a substitutional solution model for the solution phase [231]. The Ti–Nb–Cu ternary phase diagram (Fig. 2.23c) is complex with several intermetallic compounds and solid solution regions. The phase equilibria of the Ti–Nb–Cu ternary system at 600 and 700°C were recently investigated via thermodynamic modelling coupled with experiments [232]. The solubility of Nb in the binary phases of the Cu–Ti system and the solubility of Cu in the β-(Ti,Nb) phase were measured to be less than 8 at.%. The solid solution and intermediate phases were described by a substitutional model and sublattice model. Moreover, the authors determined a set of thermodynamic parameters that were used to simulate the solidification behavior under non-equilibrium conditions of the as-cast Cu–Ti–Nb alloys. The predicted microstructures were consistent with the experimental ones investigated by electron microscopy and X-ray diffraction. The works of Takahashi et al. [211, 226, 233] on a series of dental cast Ti–Nb–Cu alloys demonstrated the existence of several microstructures (α, α+β, α+β+Ti_2Cu, and in some cases also ω and α”), depending on alloy composition. The resulting mechanical properties were also improved by Cu addition, and the following hardening mechanisms were assessed: solid solution hardening of α, solid solution and precipitation hardening of α- and β-phases, solid solution hardening of β and precipitation hardening of β and ω, solid solution hardening and precipitation hardening of α and Ti_2Cu.

The concentration and distribution of Cu in the alloy regulates the resulting microstructures, which include Cu-rich phases and Ti_2Cu intermetallic compound, and exert a great influence on the overall antibacterial performance. The intermetallic compound Ti_2Cu, which forms under equilibrium solidification conditions in binary Ti–Cu alloys when Cu $<$ 40 wt.%, plays an important role in antibacterial efficacy. Some reports hypothesized that its antibacterial property is attributed to the release of Cu ions from the Ti_2Cu compound (Fig. 2.24a), however this cannot easily happen due to the strong binding force of Cu in the compound (ionic or covalent bonding), compared to Cu atoms in solid solution (metal bonding) [197, 203]. So, recent literature concludes that the Ti_2Cu intermetallic compound exerts antibacterial activity mainly through the contact-killing mechanism, and partially through ion release (Fig. 2.24b). In this case, the Ti_2Cu particles prevent bacterial adhesion, and thus inhibit biofilm formation, and the Cu ions coming from the bulk kill planktonic bacteria near the surface.

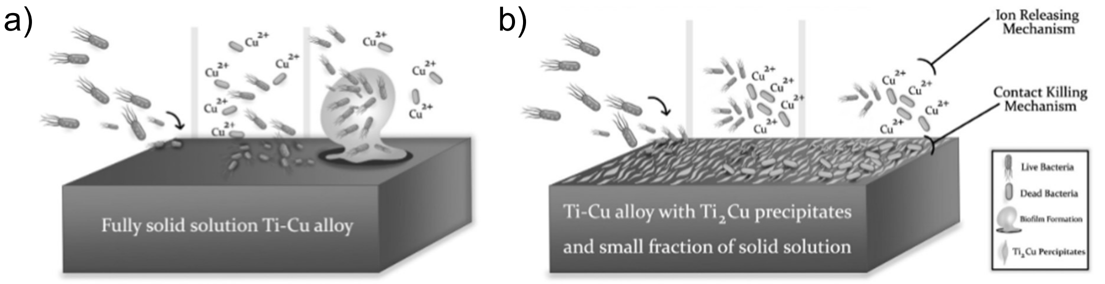

Figure 2.24: Scheme of existing forms of Cu in Ti alloys and their mechanism of action against bacteria: (a) Cu ions released from a solid solution alloy, and (b) contact-killing and ion release from an alloy containing Ti_2Cu precipitates (adapted from Ref. [197]).

This effect has been demonstrated in a work of Zhang et al. [234], where the number of bacteria in suspension with a Ti–3Cu alloy (α+Ti_2Cu) was as high as c.p. Ti, however the bacteria in contact with the Ti–3Cu were totally killed. It was concluded that the precipitation of nanoscale Ti_2Cu significantly improves anti-adhesion and anti-biofilm properties, as well as corrosion resistance. Both effects were explained by proposing the formation of ‘micro-galvanic cells’ between the Ti_2Cu intermetallic compound and the surrounding Ti matrix, which create a charge transfer between the phases that interferes with internal functions of bacteria, culminating in their death [234]. The presence of Ti_2Cu intermetallic compounds in a Ti–12Cu alloy can also significantly increase tribocorrosion and wear properties, due to the increased resistance to plastic deformation [235].

The antibacterial activity of Ti_2Cu also depends on its morphology, size and distribution, whose heterogeneous or homogeneous nucleation can be controlled via different heat treatments processes, as demonstrated in a Ti–7.5Mo–5Cu alloy [194] (Fig. 2.25). These findings show that homogeneously distributed nanoscale Ti_2Cu precipitates exert a more powerful antibacterial activity compared to the coarser ones: 96% and 86% reduction rates, respectively, against *S. aureus*. The authors suggest that metal-based nanomaterials, due to their extremely large surface areas in relation to their size, are strategically advantageous as antibacterial and anti-biofilm agents. Thus, the Ti_2Cu intermetallic compound, formed in Ti–Cu alloys when Cu $<$ 40 wt.%, plays a significant role in the antibacterial efficacy. The combination of nanograined structures with Cu represents a promising approach to control and prevent bacterial infections in medical implants.

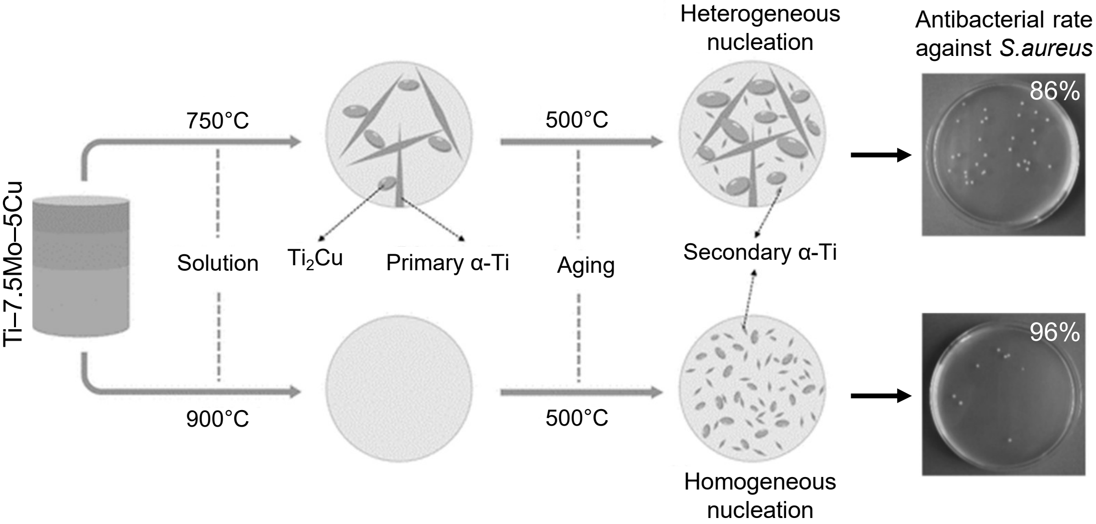

Figure 2.25: Scheme of nucleation mechanisms of Ti_2Cu nanoprecipitates in a Ti–7.5Mo–5Cu alloy subjected to different heat treatments, and resulting antibacterial properties (adapted from Ref. [194]).

Chapter 3

Experimental Procedures

3.1 Materials & Experimental Workflow

3.1.1 Studied Materials

This chapter contains all the relevant information about the studied materials as well as the experimental techniques used for their preparation, processing and characterization. In the present work, a series of Ti–Nb alloys containing the antibacterial alloying elements Ga and Cu has been studied. The selection of the Ti–Nb alloy system was based on its significance as a prototype system that serves as the basis for several alloy formulations relevant for bone implants, distinguished by a low Young's modulus. The starting composition was the low-modulus single-phase β Ti–45Nb (wt.%) alloy. Small amounts of the bactericidal elements Ga and/or Cu (up to 8 wt.%) were added by casting methods to produce novel low-modulus Ti–Nb–Ga/Cu alloys with potential antibacterial properties. The rationale for the selection of the amount of antibacterial additions took into consideration the literature review (Chapter 2) and is hereinafter summarized.

- **Copper**: additions to Ti alloys up to Cu 10 wt.% increase hardness, tensile strength and Young's modulus, but reduce ductility [205, 236]. In order to prevent harmful effects to the human body, Cu less than 10 wt.% is recommended [204]. Bolzoni et al. [237] recently reported that Cu content higher than 7 wt.% can deteriorate corrosion resistance of Ti alloys. Regarding the antibacterial properties, at least Cu 5 wt.% significantly increases antibacterial activity (nearly 100% efficacy) against relevant pathogens (*E. coli*, *S. aureus*) in Ti–Cu alloys [84, 238]. However, the antibacterial activity highly depends on Cu form (if incorporated in solid solution or in intermetallic compounds, e.g., Ti_2Cu) [197]. Xu et al. [194] reported the enhanced antibacterial properties of Ti alloys due to the higher volume fractions of Ti_2Cu compound, which may have a bacteria contact-killing effect. In addition, Ti_2Cu precipitates can significantly improve wear resistance of Ti alloys [235].
- **Gallium**: metallurgical additions up to Ga 23 wt.% to Ti alloys resulted in high cytocompatibility, with high viability and proliferation of human bone

cells [200]. It was shown that minor Ga additions (1 – 2 wt.%) to Ti alloys have highly efficient antibacterial activity without any visible cytotoxic effect [200]. Ga addition up to 10 wt.% to cast Ti–Ga alloys increases strength, microhardness and wear resistance of the alloys due to solid solution strengthening [168].

Taking into consideration all these aspects, the maximum amount of bactericidal additions was limited to 8 wt.%. Increasing amounts up to 8 wt.% of Ga and/or Cu were systematically added to binary Ti–45Nb via metallurgical route (controlled casting). Nine alloy compositions have been studied in the present work:

- (100-x)(Ti–45Nb)–xGa (where x = 2, 4, 6, 8 wt.%);
- (100-x)(Ti–45Nb)–xCu (where x = 2, 4, 6, 8 wt.%);
- 96(Ti–45Nb)–2Ga–2Cu.

The goal of this work is a fundamental study of the structural characteristics, mechanical properties as well as corrosion and tribocorrosion behavior in physiological environment of the novel Ti–Nb–Cu/Ga alloys.

3.1.2 Experimental Workflow

An overview of the experimental workflow and methods used for the alloys' characterization is presented in Fig. 3.1.

After preliminary microstructural investigations on the alloys in as-cast (AC) condition, the focus was directed towards the materials in the homogenized state (solution-treated and water-quenched, STQ), which exhibits better chemical homogeneity compared to the AC state. One representative Cu-containing alloy composition was selected for further thermal treatments (aging) to induce the precipitation of antibacterial Ti_2Cu compound. The starting binary Ti–45Nb alloy is used as reference. Medical grade Ti–6Al–4V ELI (grade 23) is also used as further reference material (Appendix D). The overall chemical composition of the as-cast rods was analyzed with inductively coupled plasma - optical emission spectroscopy (ICP-OES) and carrier gas hot extraction (CGHE). The experimental chemical composition (Table 3.1) of the alloys does not differ from the aforementioned nominal composition, therefore the latter is used throughout the present work. Energy dispersive X-ray spectroscopy (EDX) coupled with scanning electron microscopy (SEM) was used to investigate the local elemental distribution. Microstructure of the alloys was investigated and analyzed by X-ray diffraction (XRD), complemented by SEM and electron backscatter diffraction (EBSD). The elastic properties were studied by means of ultrasonic non-destructive methods and by means of microhardness, uniaxial compression and tensile tests. Deformation behavior and phase stability of strained samples was investigated by means of XRD and SEM-EBSD. Corrosion and tribocorrosion behavior in simulated body fluids were evaluated by means of open circuit potential (OCP) monitoring, potentiodynamic and potentiostatic polarization tests. Tribocorrosion tests were conducted during a 2-month research stay (secondment) at INSA Lyon and Anthogyr S.A.S. (France).

Major Objective

Development of novel **low modulus β-TiNb alloys** with minor additions of **Gallium** and **Copper** for **antibacterial** load-bearing implant applications.

Motivation & Strategies

Drawbacks of current medical implants:

- Poor biocompatibility
- High Young's modulus (results in stress-shielding)
- Inactive against pathogens (results in infections)

Our strategies:

→ **Biocompatible** metals: Ti, Nb
→ **β-type** Ti alloys (low Young's modulus)
→ **Antibacterial** minor additions: **Ga**, **Cu**

Experimental Workflow

Alloy Design

9 alloy compositions:

- (100-x)(Ti–45Nb)–xGa (x = 2, 4, 6, 8 wt.%)
- (100-x)(Ti–45Nb)–xCu (x = 2, 4, 6, 8 wt.%)
- 96(Ti–45Nb)–2Ga–2Cu

Alloys' Synthesis & Thermal Processing

Multi-step production process:

1. Arc melting (3x remelting)
2. Cold-crucible casting (cast rods: ⌀ = 10 mm, length ~ 100 mm)
3. Solution-treatment (1000°C, 24 h) & water quenching
4. Aging treatments (425°C or 640°C, 8h, furnace cooling, for one composition only)

Chemical Analysis

- Global: Inductively Coupled Plasma - Optical Emission Spectrometry (ICP-OES), Carrier Gas Hot Extraction (CGHE)
- Local: Scanning Electron Microscopy (SEM) - Energy Dispersive X-Ray Spectroscopy (EDX)

Crystallography, Alloy Constitution & Thermal Stability

- X-ray Diffraction (XRD) & Rietveld Refinement
- SEM - Electron Backscatter Diffraction (EBSD)
- Differential Scanning Calorimetry (DSC)

Mechanical Characteristics & Deformation Behavior

- Microhardness
- Ultrasonic Pulse-Echo Testing
- Tensile & Compression Testing
- XRD & Rietveld Refinement (for deformed samples)
- SEM & EBSD (for deformed samples)

Corrosion & Tribocorrosion Resistance in Physiological Environment

Tests performed in absence/presence of sliding wear:

- Open Circuit Potential (OCP) monitoring
- Potentiodynamic & Potentiostatic Polarization
- Metal Ion Release:
  - (i) static exposure: ICP-OES
  - (ii) after tribocorrosion tests: ICP-MS (Mass Spectrometry)
- 3D Confocal Microscopy (for worn surfaces)

Figure 3.1: Schematic overview of materials and methodologies adopted in the present work.

3.2 Alloy Preparation & Chemical Analysis

3.2.1 Arc Melting & Induction Cold-Crucible Casting

Cylindrical rods of the nine alloy compositions were prepared using a two-step casting process: arc-melting and cold crucible casting.

The starting binary Ti–45Nb alloy (ASTM B348–13 grade 36) was purchased from ATI - Specialty Alloys & Components, to which highly pure copper (99.9 %, Messinghaus Rehlken Gmbh) and gallium (99.99 %, Haines & Maassen Metallhandelsgesellschaft mbH) metallic elements are added to achieve the desired nominal compositions. Button-shaped pre-alloyed ingots were manufactured in an arc-melter (ALD Vacuum Technologies). Prior to melting, the recipient was evacuated to approximately 10^{-5} mbar and then filled with pure argon (Ar). A piece of titanium was inserted in the chamber and liquefied with the aim of binding traces of oxygen. The ingots were re-melted at least three times to attain chemical homogeneity. These ingots were then cut into multiple pieces and transferred to the next device for the second step of the casting process. The pre-alloyed ingots were then inductively melted in an in-house built cold crucible device (Fig. 3.2a) in a contact-free manner and cast into a water-cooled cylindrical Cu mold in a Ti-gettered Ar (99.998 vol.%) atmosphere. All alloys in the present work were cast into cylindrical Cu crucibles of 10 mm diameter and approximately 100 mm in length. Fig. 3.2b shows an example of rods obtained by this method. Before further processing and subsequent analyses, the cone-shaped top part of the rod visible in the photograph was removed. More than one rod for each composition was prepared. Casting devices were operated by D. Sven and K. Baumgart (IFW Dresden). Fig. 3.2c shows samples prepared for the different investigations described in this work.

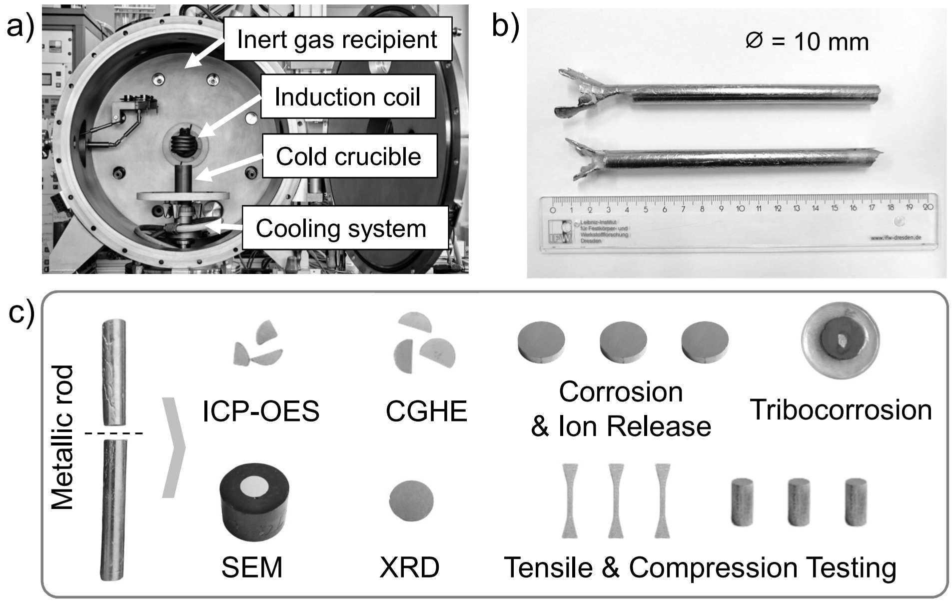

Figure 3.2: (a) Cold-crucible casting device at IFW Dresden, (b) cast Ti-based rods produced by controlled casting, and (c) overview of samples (not in scale) prepared for the analyses described in the present chapter.

3.2.2 Heat Treatments

Homogenization Treatment

All as-cast alloys were homogenized by a two-step heat treatment: solid solution treatment (1000°C, 24 hours) and quenching in water (STQ). This is because cooling rates during cold-crucible casting can result in segregation of the alloying elements during solidification in the as-cast materials. For this procedure, the as-cast rods were inserted in a quartz tube, which was evacuated and then filled with pure Ar and sealed with a glass burner. Then, the tubes were put into a pre-heated furnace at 1000°C for 24 hours, after which they were broken directly into water at RT.

Aging Treatments

Aging heat treatments were carried on a specific alloy composition (Cu 4 wt.%, Chapter 7) to precipitate in a controlled manner a Cu-bearing phase, known for its potential antibacterial properties. For this purpose, the homogenized rods were encapsulated in Ar-filled quartz tubes and inserted into a pre-heated furnace at 425°C or 640°C for 8 hours, and then furnace cooled to RT.

3.2.3 Chemical Analysis

Elemental analysis of the as-cast rods was performed using ICP-OES and CGHE methods. All results are listed in Table 3.1 and are based on three individual measurements according to commercial standards. Since compositional changes were detected to be negligible, the alloys are denoted by their nominal compositions (wt.%): (100-x)(Ti–45Nb)–xGa, (100-x)(Ti–45Nb)–xCu and 96(Ti–45Nb)–2Ga–2Cu. Based on the experimental compositions, the electron-to-atom (e/a) was calculated for each alloy as previously described. The global Ti, Nb, Ga and Cu contents and possible contaminants (Si, Ta, Al, Fe) were analyzed by inductively coupled plasma optical emission spectroscopy (ICP-OES) using iCAP 6500 Duo View. For all the alloys, metal trace impurities are below 0.02 wt.% for Fe and below 0.1% for Ta, Al and Si. The sums of the analyzed fractions deviate from 100%, this could be attributed to a systematic uncertainty of the measurements. These results indicate that the impurity levels are not a significant concern when comparing the alloys. Interstitial impurities of oxygen and nitrogen were determined with a LECO ON836 carrier gas hot extraction (CGHE) analyser. Measured oxygen levels are within the requirements of AMS 4907 (Ti–6Al–4V ELI, < 0.13 wt.%) and of ASTM F67 (c.p. Ti grade 2, < 0.25 wt.%), which are alloys in clinical use. Oxygen and nitrogen contents were analyzed on the as-cast materials only, because according to previous studies [117], they do not significantly change after solution-treatment. For the analyses, carried out by A. Voß and H. Bußkamp (IFW Dresden), samples were extracted from the as-cast rods and ground with SiC paper on all sides to remove the external oxide layer.

Table 3.1: Chemical composition (wt.%) and electron-to-atom ratio (e/a) of the nine Ti alloys investigated in the present work.

		Elemental content (wt.%)					
Alloy	e/a	Ti	Nb	Ga	Cu	O	N
98(Ti–45Nb)–2Ga	4.27	53.61 ± 0.72	43.86 ± 0.73	1.99 ± 0.07		0.099 ± 0.010	0.002 ± 0.001
96(Ti–45Nb)–4Ga	4.25	52.58 ± 0.35	42.77 ± 0.24	3.87 ± 0.05		0.111 ± 0.008	0.004 ± 0.001
94(Ti–45Nb)–6Ga	4.23	51.51 ± 0.36	41.97 ± 0.33	5.83 ± 0.05		0.091 ± 0.015	0.003 ± 0.001
92(Ti–45Nb)–8Ga	4.20	50.23 ± 0.59	41.03 ± 0.31	7.89 ± 0.12		0.088 ± 0.004	0.001 ± 0.001
98(Ti–45Nb)–2Cu	4.24	53.61 ± 0.46	43.70 ± 0.41		1.87 ± 0.11	0.091 ± 0.010	0.002 ± 0.001
96(Ti–45Nb)–4Cu	4.18	52.84 ± 0.55	42.45 ± 0.57		3.95 ± 0.27	0.095 ± 0.006	0.002 ± 0.001
94(Ti–45Nb)–6Cu	4.12	51.22 ± 0.49	42.03 ± 0.93		5.62 ± 0.52	0.109 ± 0.005	0.005 ± 0.001
92(Ti–45Nb)–8Cu	4.04	50.45 ± 0.27	40.88 ± 0.58		8.02 ± 0.49	0.109 ± 0.005	0.001 ± 0.001
96(Ti–45Nb)–2Ga–2Cu	4.21	52.63 ± 0.36	42.91 ± 0.35	2.01 ± 0.03	1.91 ± 0.04	0.100 ± 0.008	0.002 ± 0.001

3.3 Structural Investigations & Thermal Analysis

3.3.1 X-Ray Diffraction & Rietveld Method

X-ray diffraction (XRD) methods were used to identify and quantify crystalline phases of the alloys. XRD analyses were performed with a STOE Stadi P diffractometer in transmission geometry using Mo $K_{\alpha 1}$ ($\lambda = 0.7093$ Å) monochromatic radiation operated at 30 mA and 50 kV. The diffraction data were recorded in the 2θ interval from 10° to 60° with step size of 0.010° and holding time of 90 s per step. Metallic disk-shaped thin films (thickness $\approx 50\ \mu$m) were prepared by wet grinding.

Diffraction patterns were analyzed by Rietveld method [239] using Malvern Panalytical's HighScore Plus software. Peak profiles were modeled using asymmetric pseudo-Voigt shape functions. Background parameters, profile shape parameters (peak positions, maximum intensities, full width at half maximum) and lattice parameters were refined simultaneously. Quality of fitting was evaluated by χ^2 (chi-squared) values and by visual inspection of calculated and experimental profiles. Identification of crystalline phases is based on data from the International Centre of Diffraction Data (ICDD) PDF2 database: ICDD no–04–017–4957 for β-Ti (BCC, space group $Im\bar{3}m$), ICDD no–01–071–4632 for α-Ti (HCP, space group $P6_3/mmc$), ICDD no–04–002–5027 for ω-Ti (HCP, space group $P6/mmm$) and ICDD no–00–015–0717 for tetragonal Ti_2Cu (space group $I4/mmm$).

3.3.2 Electron Microscopy

The metallographic characterization of the alloys was carried out by scanning electron microscopy (SEM). The SEM used in this work was a Zeiss Leo Gemini 1530 equipped with a Bruker Xflash 4010 energy dispersive X-ray spectrometer (EDXS) and a Bruker eFlash HR electron back scattering diffraction (EBSD) detector. The acceleration voltage was set at 20 kV. Different elemental composition areas were detected in composition contrast mode (backscattered electrons) and specifically analyzed using energy dispersive X-ray analysis. EBSD maps for average grain size determination were collected with a step size of 2 μm at magnification 50x. The specimens for microscopy investigations were extracted from the rods, embedded in a cold-hardening resin and polished with a colloidal suspension of SiO_2 (OPS).

3.3.3 Computed Tomography

X-ray absorption CT is a non-destructive imaging method which is used to analyse the inner constitution of solid materials. Because of the production method of the alloys, shrinkage casting defects occurring during the solidification process may be present inside, especially in the innermost section of the rod. For this reason, specimens for tensile and compression tests were all scanned to assess for their structural integrity by recording 2-dimensional scans with a GE Phoenix Nanotom M X-ray absorption CT device. Fig. 3.3 presents examples of test samples suitable and not suitable for testing. For each sample, two radiographies were recorded with GE Datos Acquisition 2.0 software after rotating the sample along the Z-axis, chosen along the sample's maximum length, of a 90°angle. The device, consisting of a tungsten/diamond X-ray tube and a Cu-filter 0.3 mm thick, was operated at 140 kV and 100 μA. Voxel size of 3.33 μm was kept constant for all scans.

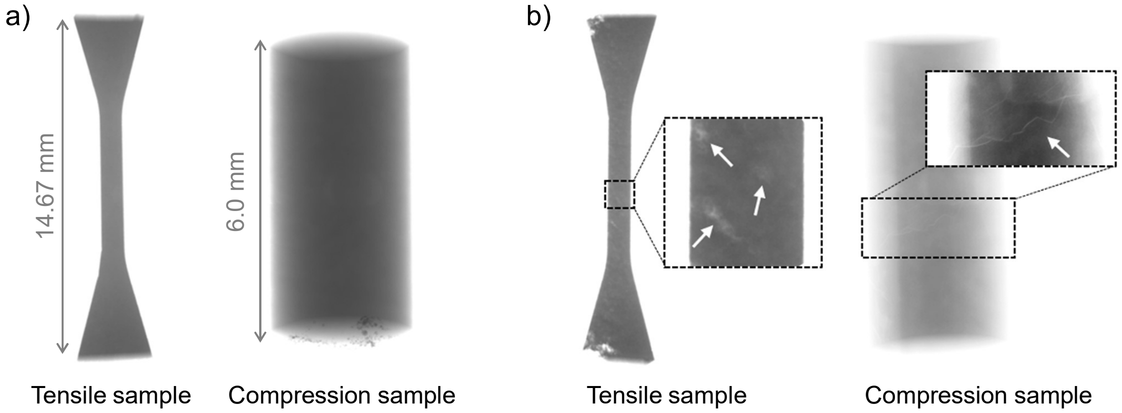

Figure 3.3: 2D radiographies of tensile and compression samples (a) suitable and (b) not suitable for testing because of structural defects, as indicated by the arrows.

3.3.4 3D Confocal Profilometry

These investigations were conducted during a secondment at Anthogyr S.A.S., France. A non-contact S Neox 3D confocal optical profilometer equipped with a 20X Nikon – EPI objective (resolution: 0.65 μm/pixel), driven by Sensomap standard (v. 6.7) software, was used to analyse the wear tracks morphologies of the samples subjected to tribocorrosion tests (Chapter 6). Total wear volume and average depth were evaluated as follows: i) the 3D topography of wear track and surrounding plane surface is measured, ii) a mathematical reference plane is constructed from a least-square fit of the plane surface around the wear track, iii) non-measured empty points are refilled by nearest neighbours smoothing, iv) the total wear volume is computed by subtracting the wear track topography from that of the modelled plane surface.

3.3.5 Differential Scanning Calorimetry

Differential scanning calorimetry (DSC) was used to investigate thermal stability and occurrence of precipitation reactions and phase transformations in Chapter 7. Measurements were conducted with a Netzsch HT-DSC 404 device, with heating and cooling rates of 10°C/min in a continuous argon flow (99.99 vol.%). Test samples (mass $\cong 30 - 70$ mg) were cut by abrasive wheel saw and manually ground with fine grit on all faces to remove surface contamination. Tests were repeated twice.

3.4 Mechanical Characterization

3.4.1 Ultrasonic Pulse-Echo Testing

Ultrasonic testing is a non-destructive method used to gain insight into the elastic properties of a material. Measurements were performed with a computer-controlled ultrasonic pulser-receiver device (Olympus 5900PR) in pulse-echo mode equipped with a normal incident probe of 100 MHz (model V2012) and a shear probe of 20 MHz (model V222), which were used for the measurement of normal and shear velocities of the wave, respectively. Parameters such as damping energy, signal attenuation and gain were adjusted for each measurement in order to obtain the maximum signal intensity. Two disk-shaped metallic samples ($\varnothing = 10$ mm, thickness $= 1.0$ mm) per composition were tested and each sample was measured twice on each side, at least 200 readings per side were collected. Measured acoustic transverse V_T and longitudinal V_L velocities are used for the calculation of Poisson's ratio ν, Young's modulus E^{US} and bulk modulus K^{US}, as follows [240]:

$$\nu = \frac{1 - 2(V_T/V_L)^2}{2 - 2(V_T/V_L)^2} \tag{3.1}$$

$$E^{US} = \frac{{V_L}^2 \rho (1+\nu)(1-2\nu)}{1-\nu} \tag{3.2}$$

$$K^{US} = \frac{E}{3(1-2\nu)} \tag{3.3}$$

3.4.2 Vickers Microhardness

Vickers micro-hardness ($HV_{0.1}$) measurements were performed on embedded and mirror-like polished samples with a Vickers microhardness tester (HMV-2) with a force of 1 N (100 gf) and dwell time of 10 s. At least 12 measurements were collected at 12 chosen sites for each sample.

3.4.3 Uniaxial Tensile and Compression Tests

Deformation behavior was evaluated under uniaxial quasi-static tensile and compressive loading. Tensile tests were performed up to fracture with a PC-controlled minitensile testing module DDS2-System equipped with a 5 kN load cell and a video-extensometer, controlled with VEDDAC software, under a constant tensile speed of 1.375 μm sec^{-1} (strain rate: $3 \cdot 10^{-4}$ s^{-1}). Compression tests were conducted until failure or until 50% height reduction with a strain rate of $1 \cdot 10^{-3}$ s^{-1} using an Instron 8562 testing machine. One sample for all the alloys was tested up to $\approx$ 70% compressive strain. At least three samples of each composition were tested for each method. Samples for both tensile and compression tests were extracted parallel to the long axis of the rods using electrical discharge machining (EDM). Prior to testing, all samples were X-ray scanned to check for structural integrity (Sec. 3.3.3 for further details). Flat bone-shaped tensile specimens, with a total length of 14.67 mm and a gauge length L_0 of 4.9 mm, were mechanically thinned to 0.75 (± 0.03) mm in thickness. Shape and size of tensile samples are shown in Fig. 3.4a. Dimensions were chosen in order to respect the value of 5.65 for the 'short' proportionality factor k, calculated as ratio between L_0 and the square root of the cross section S_0, which is given in DIN EN ISO 6892–1:2019 [241]. The samples *per se* are not proportionality samples according to DIN, since the thickness is less than 3 mm. Cylindrical specimens for compression tests have a height ($h = 6.0$ mm) two times larger than the diameter ($\varnothing = 3.0$ mm), in accordance to DIN 50106:2016–11 [242]. Both loading surfaces were carefully ground to be plane parallel.

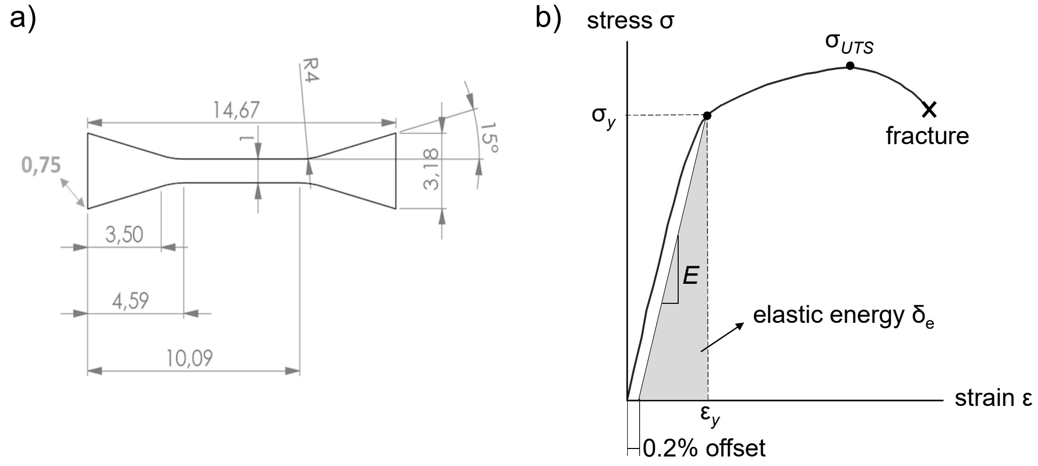

Figure 3.4: (a) Sketch of minitensile sample used for tensile tests (all length values are given in mm). (b) Scheme showing how the mechanical properties are determined from the tensile stress–strain curve.

The force-displacement responses were plotted in terms of engineering stress (σ) and engineering strain (ε) to calculate the desired properties. Young's modulus (E) in tension was measured from the slope at the initial stage before yielding. Yield strength (${\sigma_\mathrm{y}}^\mathrm{tens}$) and yield strain ($\varepsilon_\mathrm{y}$) were determined by the 0.2% offset method, given the fact that the yield point of some β-Ti alloys is not well defined. Ultimate tensile strength (σ_UTS), fracture stress (σ_f) and fracture strain (ε_max) were also determined (Fig. 3.4b). Assuming a linear elastic region, the elastic energy δ_e, which represents the material's maximum capacity to elastically absorb energy, is approximated as the total area under the linear elastic regime in the stress-strain curve, as follows:

$$\delta_\mathrm{e} = \frac{1}{2}\sigma_\mathrm{y}\varepsilon_\mathrm{y} \tag{3.4}$$

The strain hardening exponent n, which represents the balance between work hardening and softening, was calculated from the true stress-strain curves according to the power-law relationship, known as Hollomon equation [243], as suggested in ASTM E646–16 [244], to describe the flow curve in the uniform deformation stage before necking:

$$\sigma_\mathrm{T} = K{\varepsilon_\mathrm{T}}^n \tag{3.5}$$

where K is strength coefficient, σ_T and ε_T are true stress and true strain, respectively. Compressive yield strength (${\sigma_\mathrm{y}}^\mathrm{compr}$) was determined by the 0.2% offset method.

3.5 Corrosion, Tribocorrosion & Ion Release

3.5.1 Electrochemical Methods

For corrosion and tribocorrosion studies, circular electrodes with a thickness of $\approx$ 3 mm and diameter of 10 mm were extracted from the rods and embedded in cold-hardening epoxy resin. Embedded samples were mechanically ground with P2500 silicon carbide emery paper and then rinsed in an ultrasonic bath of high purity ethanol. The exposed circular surface area was estimated for each tested sample from the optical micrographs using ImageJ software [245]. All tests were conducted in air-saturated physiological phosphate-buffered saline solution (PBS, pH $\approx$ 7.4, composition: NaCl 140 mM, KCl 3 mM, phosphate buffer 10 mM, Merck KGaA).

Corrosion Testing

A conventional three-electrode setup, with a jacket for temperature control, was used for corrosion assessment. Test sample (i.e., working electrode WE) was mounted into an in-house built sample holder of appropriate diameter inserted in an Ametek 616 B rotating disk electrode device activated with a very low rotation speed (50 rpm) and immersed in the testing solution. Rotation assists in the prevention of bubbles formation on the working electrode surface, which might cause unwanted fluctuations in the measured current. A platinum (Pt) net was used as counter electrode (CE) and a saturated calomel electrode (SCE, $\mathrm{E_{SCE}}$ = +0.241 V vs. SHE at 25°C) as reference electrode (RE). Measurements were started immediately after sample preparation (several seconds). Electrochemical tests were carried out by means of a Solartron SI 1287 electrochemical interface. Tests were conducted at 37.5°C. The pH was checked before and after every experiment.

The open circuit potential (OCP) was monitored for 4 hours. OCP variations of less than 1 mV/min were considered acceptable to start the subsequent polarization tests. Anodic polarization was started at -200 mV vs. final OCP value and increased with a constant sweep rate of 0.5 mV/s up to a value of +1.0 V vs. SCE. Each test was performed at least three times to verify the repeatability of the results. From the polarization curves, the following parameters were determined: corrosion potential (E_{corr}) and corrosion current density (j_{corr}) by Tafel graphical extrapolation, and passive current density (j_{pass}).

Tribocorrosion Testing

Tribocorrosion studies were conducted during a secondment at INSA Lyon (France).

Electrochemical Setup. A three-electrode setup was used for corrosion assessment under sliding conditions. The setup consisted of the embedded specimen as working electrode (WE), a platinum coil as counter electrode (CE) and a saturated silver chloride (Ag|AgCl) electrode as reference electrode ($E_{Ag|AgCl}$ = + 0.197 V vs SHE). The setup as described was connected to a Gamry ref 600 potentiostat, which was controlled using Gamry Framework software.

Tribometer. The most commonly used methods to investigate tribocorrosion behavior of metallic materials are ball-on-disk, block-on-disk and pin-on-disk [68]. In the present work, sliding tests were performed with a reciprocating pin-on-disk tribometer. The tribometer has a fixed frame that holds the pin support, while the stage holding the electrochemical cell is mobile (Fig. 3.5). The translation movements and load, fixed at 5 N, were applied using a lifting table. Normal load and shear force were measured by a three-axis strain gauge force sensor (Testwell). On top of the sensors, the whole electrochemical cell was mounted and fixed in position. The coefficient of friction (COF) was calculated by the ratio between shear force and normal force. The horizontal displacement was driven by a linear DC motor (H2W Technologies). Sliding displacement was set to 1.6 mm with a reciprocating frequency of 0.5 Hz for 1800 seconds (2 seconds/cycle, which correspond to a distance of 3.2 mm/cycle) and sinusoidal waveform profile, for a total sliding distance of 2.9 m. The tribometer was controlled by LabVIEW software, which allows real time recording of normal force, tangential force and horizontal displacement. The contact was defined by the Ti alloys as first body and a cylindrical (Ø = 6 mm) alumina (Al_2O_3) pin with a curvature radius of 26 mm (measured by profilometry) as second body. This type of pin was selected in order to limit severe adhesive wear typically occurring in metal-metal contact [246]. Moreover, mechanical properties of the pin [247] are higher than the tested Ti alloys, therefore wear was exclusively expected on the metal specimens. The pin was polished with SiC emery paper (grit 4000) before every test with an in-house built pin holder, designed to maintain the same curvature radius. The tribometer operated integrated with the electrochemical setup described above.

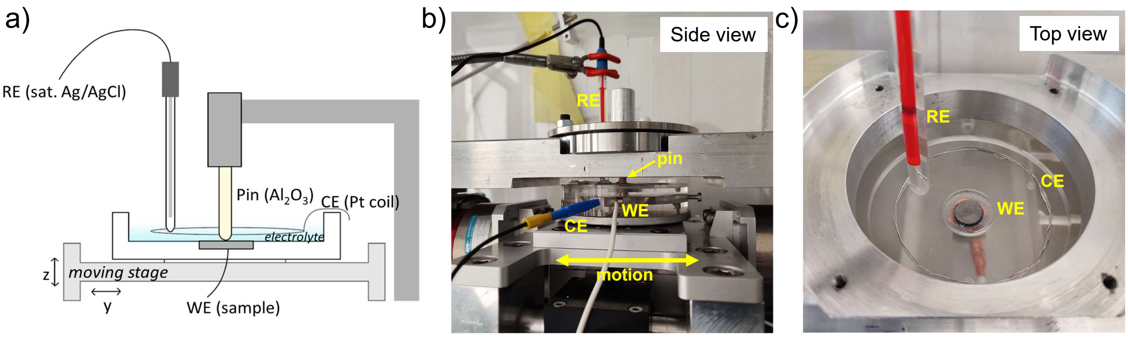

Figure 3.5: (a) Scheme of the tribo-electrochemical setup, (b) side view and (c) top view (without pin holder) of the setup used during the secondment at INSA Lyon (France).

Tribo-Electrochemical (Tribocorrosion) Tests. Two types of tribocorrosion tests were carried out while sliding against the pin: (i) OCP monitoring, and (ii) current monitoring under applied potential (0 V vs last measured OCP potential value). The first method simulates a real system, where the WE potential is controlled only by the physiochemical properties of the surrounding solution and the tribological conditions of the contact. The second method allows real time *in situ* measurement of depassivation and repassivation kinetics. Tests were repeated twice.

(i) *Open Circuit Potential (OCP) Tests*. Initially, OCP was monitored in static conditions for 3600 s, and subsequently with sliding for 1800 s to gain insights on the OCP evolution under the applied 5N load. Sliding was then stopped and OCP was further measured for 3600 s. Data collection frequency was set to 10 Hz to ensure high resolution curves during sliding tests.

(ii) *Potentiostatic Tests*. After OCP stabilization for 3600 s, potentiostatic experiments were performed at an applied anodic potential of 0 V vs OCP to understand the mutual action of corrosion and wear during tribocorrosion. This indicates that the final potential value at 3600 s after OCP monitoring was chosen as applied potential for the subsequent potentiostatic test. Initially, current measurements were carried out without sliding for 300 s, after which sliding took place for 1800 s. Sliding was then stopped and current was monitored for 600 s more.

Quantification of Wear. In a tribocorrosion system, many degradation mechanisms take simultaneously place contributing to material loss. According to Mischler's model [248–250], total volume loss (V_{tot}) is caused by a combination of mechanical wear (V_{mech}), wear-accelerated corrosion (V_{wac}), and corrosion outside the wear track (V_{chem}). Since the latter is negligible in passive alloys [250], V_{tot} can be expressed as follows:

$$V_{tot} = V_{mech} + V_{wac} \tag{3.6}$$

Volume loss due to wear-accelerated corrosion (V_{wac}) can be calculated using Faraday's law (Eq. 3.7) from the average current during wear (i_{wear}). According to Eq. 3.7, excess current (i_{exc}) due to sliding at an applied anodic potential corresponds to an equivalent oxidized metal volume (V_{wac}):

$$V_{wac} = \frac{i_{exc} \cdot t_{rub} \cdot M_{mol}}{n_{ox} \cdot F \cdot \rho} \tag{3.7}$$

where i_{exc} is excess current, t_{rub} is rubbing/sliding time (always 1800 seconds in this work), M_{mol} is alloy molar mass, n_{ox} is charge number for the oxidation reaction, F is Faraday's constant (96485.3 C mol^{-1}), and ρ is density. Excess current i_{exc} is determined by subtracting the initial current (before sliding) from i_{wear}. This calculation is required to discard the eventual contribution of current coming from the sample surface around the wear track, which is anyway negligible as mentioned. Average i_{exc} coming from two independent test under potentiostatic conditions is used for the determination of average V_{wac}. Charge number n_{ox} (or electron-to-atom e/a) was calculated according to Eq. 2.3 (Ch. 2, Sec. 2.3), assuming the valence oxidation states of 4, 5, 3 for Ti, Nb and Ga, and 3 and 5 for Al and V, respectively. Value of i_{exc}, and so volume loss due to wear-accelerated corrosion in OCP conditions, can be also determined according to the galvanic cell model proposed by Vieira et al. [251]. Corrosion potential determined by potentiodynamic tests in absence of wear, cathodic kinetics, potential during rubbing, and anode-to-cathode area ratio are all considered for the calculation of the anodic current flowing through the wear track while rubbing:

$$log(i_{exc}) = \frac{E_{corr} - E_{wear} + B_c}{B_a} - log(\frac{A_a}{A_c}) \tag{3.8}$$

where E_{corr} is corrosion potential, E_{wear} is potential attained during sliding, B_c and B_a are Tafel constants graphically determined by linear regression from the polarization curves, A_a is anode area (wear track), determined *ex situ* by 3D confocal profilometry, and A_c is cathode area, approximated as sample surface area. Total volume loss V_{tot} is determined *ex situ* by 3D confocal profilometry. Thus, it becomes possible to evaluate mechanical wear (V_{mech}), due to rubbing only, from Eq. 3.6, by subtracting V_{wac} from V_{tot}.

3.5.2 Metal Ion Release

Metal ion release studies were conducted in two conditions: (i) static exposure to the electrolyte (at IFW Dresden, Germany) and (ii) after tribocorrosion tests (during secondment at INSA Lyon, France). In case (i), metallic samples are exposed to the corrosive electrolyte for a certain amount of time, after which solutions are retrieved and their ion content is measured by ICP-OES. In case (ii), ions released in solution from the metallic samples during tribocorrosion tests are measured immediately after the tests by ICP-MS (method available at INSA Lyon).

(i) *Static Exposure.* For ion release studies in static conditions, metallic disk-shaped ground samples (⌀ = 9 mm, thickness = 2 mm) were immersed in 2 ml of PBS solution at 37.5°C. Metal ions released in the electrolyte solutions were measured with an iCAP 6500 Duo View Inductively Coupled Plasma - Optical Emission Spectroscopy (ICP-OES) device based on DIN EN ISO 10993–15:2009–10 [252], according to which 1 ml of solution per cm^2 of sample area is used. Each specimen solution, diluted 1:3 with distilled water, was measured twice, and a mean value of the six measurements was determined and reported. Three samples per material and three blanks were tested. The concentration of released ions was calculated in relation to the exposed sample surface in mmol cm^{-2}. Limits of quantification (LOQ) of the device for Ti and Nb are at $7 \cdot 10^{-8}$ mmol cm^{-2}, and for Ga and Cu at $2.5 \cdot 10^{-7}$ mmol cm^{-2}. Two test types were performed:

- 7 days of exposure: samples are immersed in the electrolyte for a total of 7 days, after which the solutions are measured (one time point, studies reported in Chapter 5).
- 14 days of exposure: samples are immersed in the electrolyte solution for 1 hour, 1 day, 3 days, 7 days and 14 days. After each time point, the solution is collected, measured and replaced with fresh solution. This procedure gives immersion times of 1, 24, 48, 96 and 168 hours (five time points, studies reported in Chapter 7).

Testing was conducted by A. Voß (IFW Dresden).

(ii) *After Tribocorrosion Tests.* Metal ions released in the electrolyte solutions after tribocorrosion tests were measured using an iCAP TQe Inductively Coupled Plasma - Mass Spectrometry (ICP-MS) analyzer. For the analyses, 500 μL of the test solutions, coming from the sliding tests under OCP conditions, were mixed with 49.5 mL of a nitric acid HNO_3 solution (2 - 4% v/v), such dilution is chosen to minimize non-spectroscopic interference coming from easily ionizable ions such as Na and K, present in very large concentrations in the electrolyte. Rhodium at 500 ppb is used as internal standard in order to correct non-spectroscopic interference. The metal ions analyzed were Ti-48, Nb-93 and Ga-71, which have detection limits of 21 ppt, 10 ppt and 2.7 ppt, respectively. Fresh PBS solution was also measured as blank. Tests were repeated twice, with solutions coming from two independent sliding tests. Results are reported in Chapter 6. The ICP-MS device was operated by Dr. K. Perrin (INSA Lyon).

3.6 Statistical Analysis

Results in the present work are expressed as mean ± standard deviation. One-factor ANOVA analyses, followed by multiple comparison Tukey-Kramer post-hoc tests at $p = 0.05$, were performed with JASP software [253]. A p-value < 0.05 is considered statistically significant.

Chapter 4

Comparative Study of Structural Characteristics and Mechanical Properties of Ga-/Cu-Containing Ti–Nb Alloys

4.1 Chapter Overview & Aims

Medical implants technology requires highly performant materials for long-term success. Mechanical biocompatibility is, among many, a key factor. This chapter explores the possibility of preparing low-modulus Ga- and/or Cu-bearing Ti-based biomaterials intended for load-bearing implant applications. The influence of antibacterial additions (Ga, Cu) on microstructure and mechanical behavior of the alloys will be investigated.

In the present chapter, fundamental microstructural characteristics and mechanical behavior of newly developed β-type Ti–45Nb-based alloys containing minor additions (up to 8 wt.%) of Ga and/or Cu are studied and discussed. Focus lies on the effects of the alloying elements on the alloys' properties. First, phase formation in as-cast and homogenized (STQ; 1000°C, 24 h) states is investigated by X-ray diffraction and electron microscopy. Thereafter, influence of Ga and/or Cu on elastic and plastic behavior, and their relationship with microstructure, are thoroughly investigated by means of ultrasonic pulse-echo method, microhardness measurements, and uniaxial tensile and compression tests. The chapter closes with a study on the effects of compressive strains on the β phase stability.

4.2 Microstructure of Alloys in As-Cast & Homogenized State

As-Cast State

Preliminary microstructural investigations are conducted on the alloys in as-cast (AC) state. X-ray diffraction (XRD) patterns of the nine AC alloys are shown in Fig. 4.1a, compared to the reference Ti–45Nb. Only β (space group: $Im\bar{3}m$) diffraction peaks are detected for the four Ga-containing Ti alloys, for the mixed alloy 96(Ti–45Nb)–2Ga–2Cu, and for the two Cu-containing Ti alloys with Cu 2 and 4 wt.%. The two alloys containing higher amounts of Cu (6 and 8 wt.%) exhibit additional peaks indexed with the tetragonal Ti_2Cu phase (space group: $I4/mmm$) (Fig. 4.1b), indicating partial decomposition of the β phase at high Cu content. These results are consistent with the studies of Takahashi et al. [226] on a series of as-cast Ti–(5–30)Nb–(2–10)Cu (wt.%) alloys for dental applications: the Cu 6 and 8 wt.% alloys exhibit a dual phase microstructure consisting of β and Ti_2Cu when Nb and Cu contents are greater than 30 and 7.5 wt.%, respectively. In the present alloys, the volume fraction of the Ti_2Cu phase, determined by analyzing the area under the diffraction peaks, increases with Cu content: 3.0% and 7.6%, respectively. Diffraction studies did not reveal presence of additional phases, such as ω or α" martensite, which, if present, are in trace amounts below detection limit. Results of XRD analyses are summarized in Table 4.1, together with calculated lattice parameters for the detected phases.

Table 4.1: Detected phases and lattice parameters (a_β) of the nine as-cast alloys and the reference Ti–45Nb, determined from XRD patterns.

Studied alloys	Phase(s)	Lattice parameter (Å)		
		β	Ti_2Cu	
		a_β	$a=b$	c
Ti–45Nb	β	3.298		
98(Ti–45Nb)–2Ga	β	3.297		
96(Ti–45Nb)–4Ga	β	3.296		
94(Ti–45Nb)–6Ga	β	3.301		
92(Ti–45Nb)–8Ga	β	3.287		
98(Ti–45Nb)–2Cu	β	3.303		
96(Ti–45Nb)–4Cu	β	3.301		
94(Ti–45Nb)–6Cu	$\beta + Ti_2Cu$	3.285	2.943	10.784
92(Ti–45Nb)–8Cu	$\beta + Ti_2Cu$	3.289	2.943	10.770
96(Ti–45Nb)–2Ga–2Cu	β	3.318		

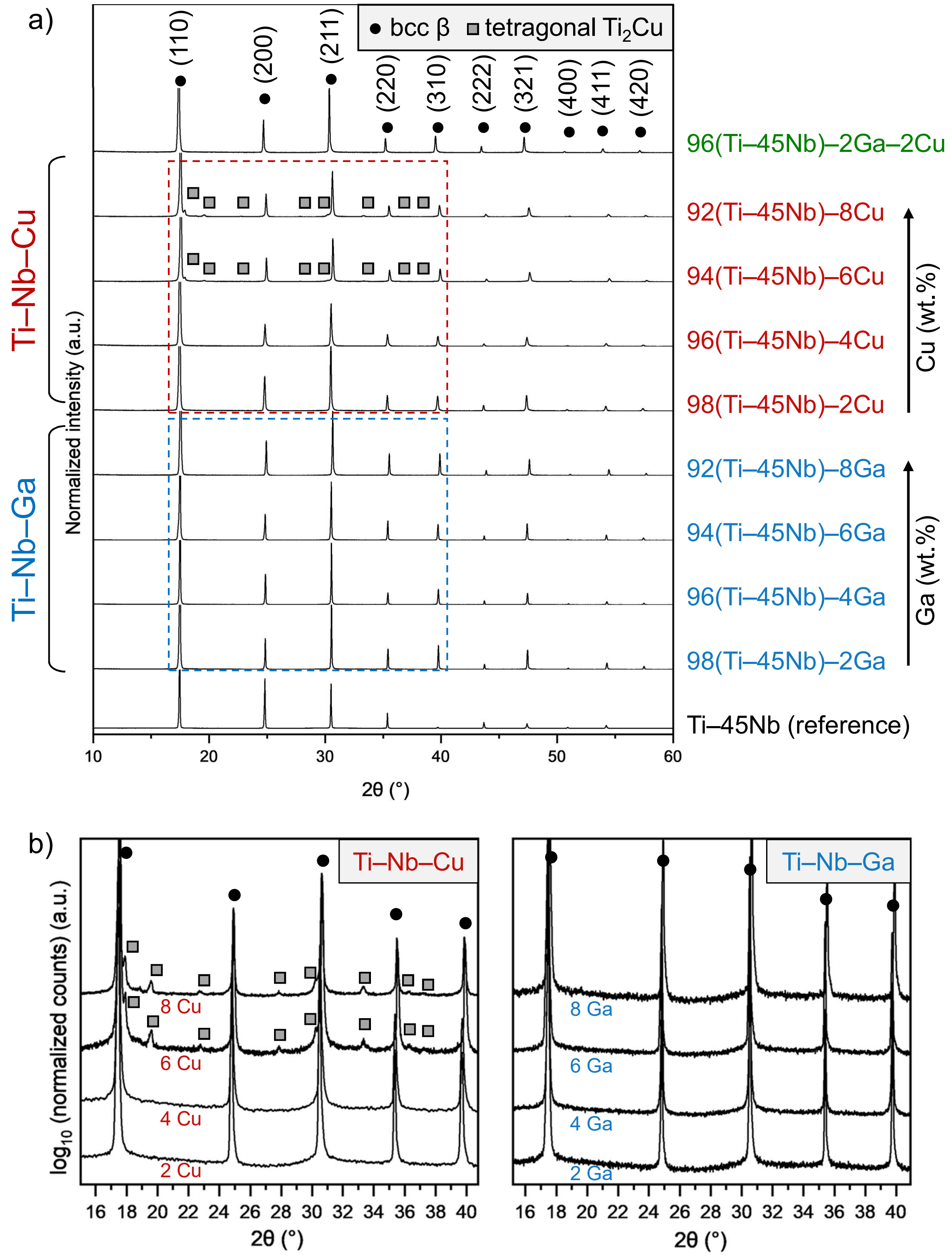

Figure 4.1: (a) X-ray diffractograms of the nine as-cast alloys, and (b) magnification of 2θ region 15 – 41° of the patterns of the four Ti–Nb–Cu and four Ti–Nb–Ga alloys, in logarithmic scale (on vertical axis) to amplify low intensity reflections.

Microstructures of the nine alloys investigated by SEM in backscattered electron (BSE) mode are presented in Fig. 4.2. In BSE imaging, high atomic number (Z) elements tend to produce brighter regions in the image than low Z elements. This is because high Z elements backscatter more electrons than low Z elements, and therefore produce a stronger BSE signal. Therefore, the brighter regions may be associated with high Z elements, whereas darker regions may be associated with low Z elements. Dendritic structures, typical for cast alloys, are clearly visible, and their different morphology and size are attributed to compositional variations and different cooling rates upon casting. During cooling to RT, the melt enters the two-phase ($\alpha+\beta$) region from the single-phase (β) region, leading to the formation of Nb-rich dendrites (bright area, $Z_{\mathrm{Nb}} = 41$), surrounded by a Ti-rich interdendritic matrix (dark area, $Z_{\mathrm{Ti}} = 22$), while Cu ($Z_{\mathrm{Cu}} = 29$) and Ga ($Z_{\mathrm{Ga}} = 31$) are enriched in the Nb-lean interdendritic region, mainly dissolved in Ti. The resulting compositional gradients are micrometer-scaled and can be imaged by spatially resolved X-ray spectroscopy (e.g., EDX).

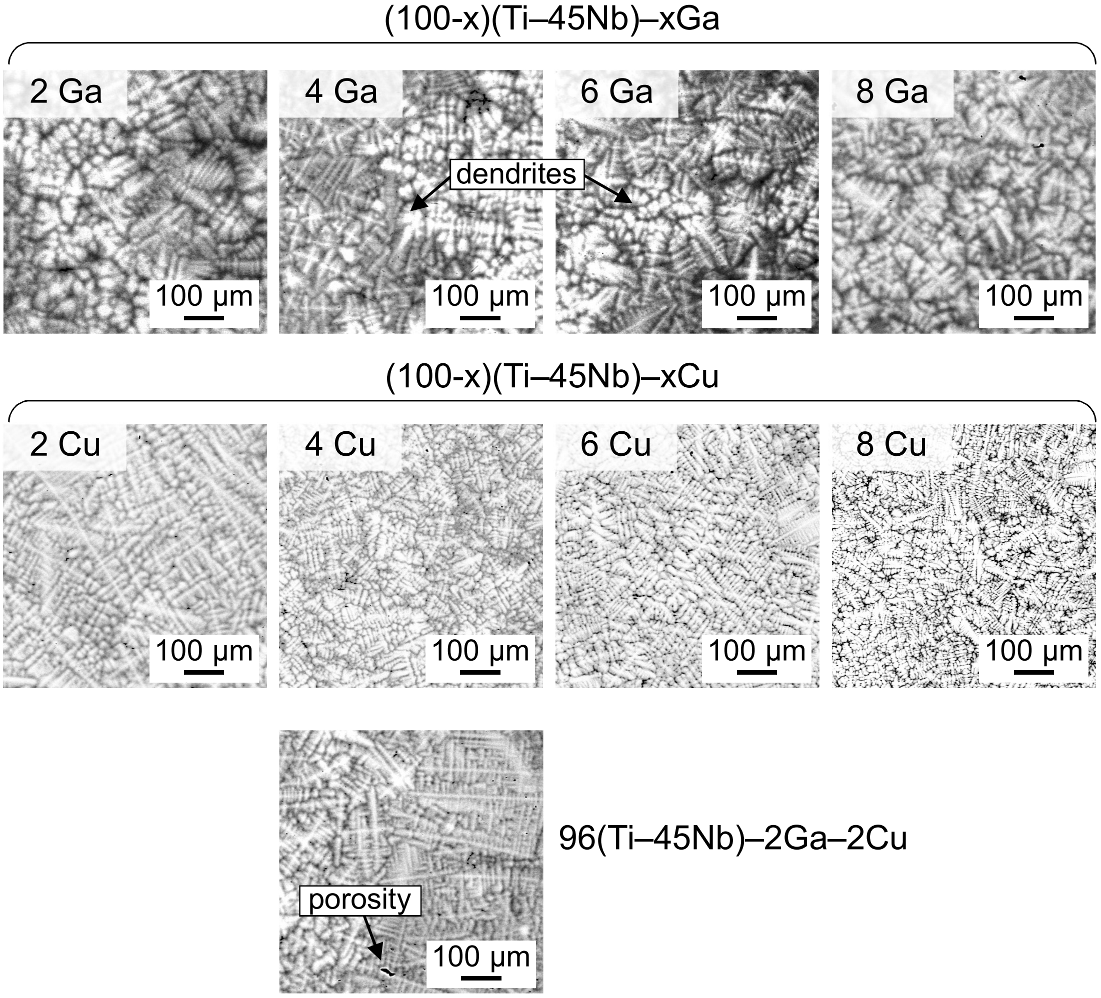

Figure 4.2: Backscattered electron scanning electron microscopy (BSE-SEM) micrographs of the nine alloys in as-cast state.

Elemental mappings confirming the previous statements are reported in Fig. 4.3a for the two alloys with the highest amount (8 wt.%) of Ga and Cu, i.e., 92(Ti–45Nb)–8Ga and 92(Ti–45Nb)–8Cu. EBSD and EDX analyses on Cu 8 wt.% alloy confirm a two-phase microstructure consisting of β-phase matrix and Ti_2Cu intermetallic compound as fine micrometer-sized particles (Fig. 4.3b), whose calculated lattice parameters (Table 4.1) are found to match with literature [254]. Elemental analysis indicates a Ti:Cu ratio of ≈ 2:1, which matches the compound stoichiometry. Similar results were observed in binary Ti–Cu alloys with Cu content up to 10 wt.% subjected to aging treatments [203, 204]. Recent studies [194, 204] have demonstrated the antibacterial ability of this particular compound, as a consequence these findings expand the scope for further studies (Chapter 7).

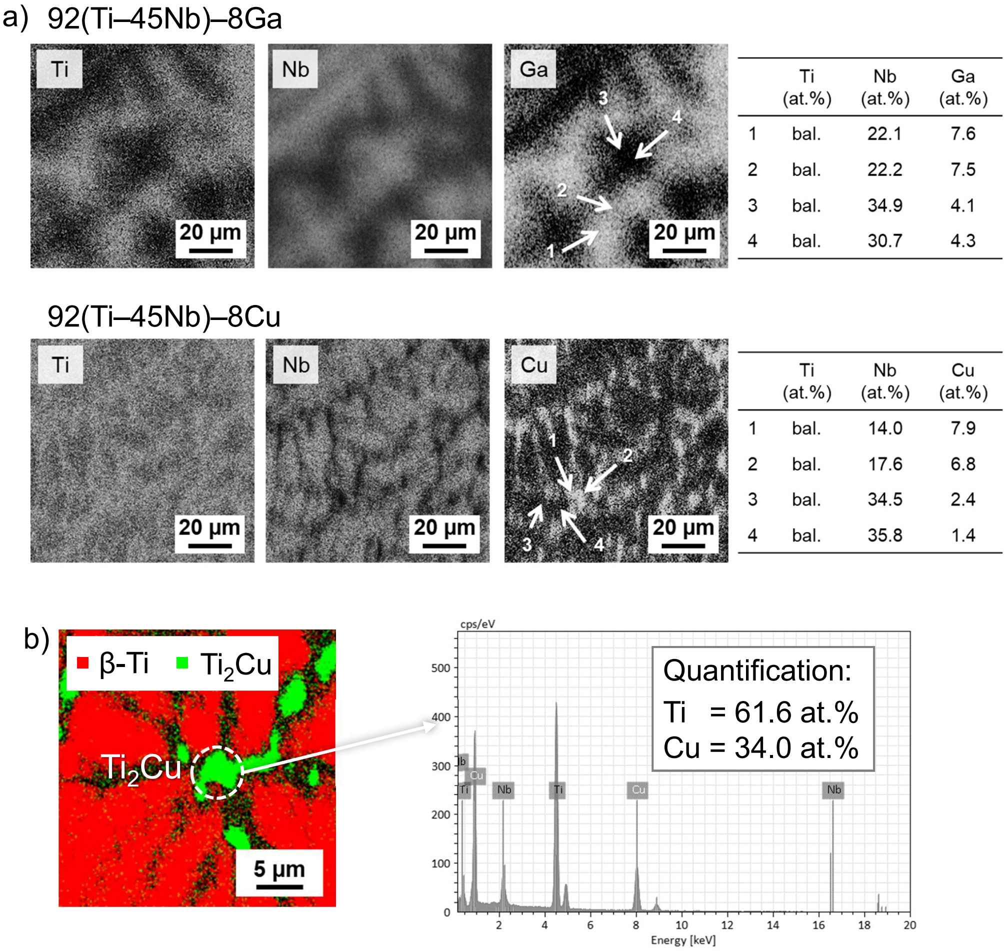

	Ti (at.%)	Nb (at.%)	Ga (at.%)
1	bal.	22.1	7.6
2	bal.	22.2	7.5
3	bal.	34.9	4.1
4	bal.	30.7	4.3

	Ti (at.%)	Nb (at.%)	Cu (at.%)
1	bal.	14.0	7.9
2	bal.	17.6	6.8
3	bal.	34.5	2.4
4	bal.	35.8	1.4

Quantification:
Ti = 61.6 at.%
Cu = 34.0 at.%

Figure 4.3: (a) EDX mappings showing spatial distribution of Ti, Nb and Ga/Cu for 92(Ti–45Nb)–8Ga and 92(Ti–45Nb)–8Cu alloys in as-cast state. Bright areas contain higher concentration of the element indicated. Quantification results of point analysis, as indicated by the arrows, are reported in the two tables. (b) EBSD phase map and EDX spectrum of Ti_2Cu precipitate in 92(Ti–45Nb)–8Cu alloy.

Homogenized State

In order to produce structurally homogeneous microstructures, the as-cast rods were subjected to a solid solution treatment at 1000°C for 24 h and water quenched (STQ). Heating the dendritic microstructures previously shown at temperatures above β-transus eliminates the chemical fluctuations, as shown in Fig. 4.4.

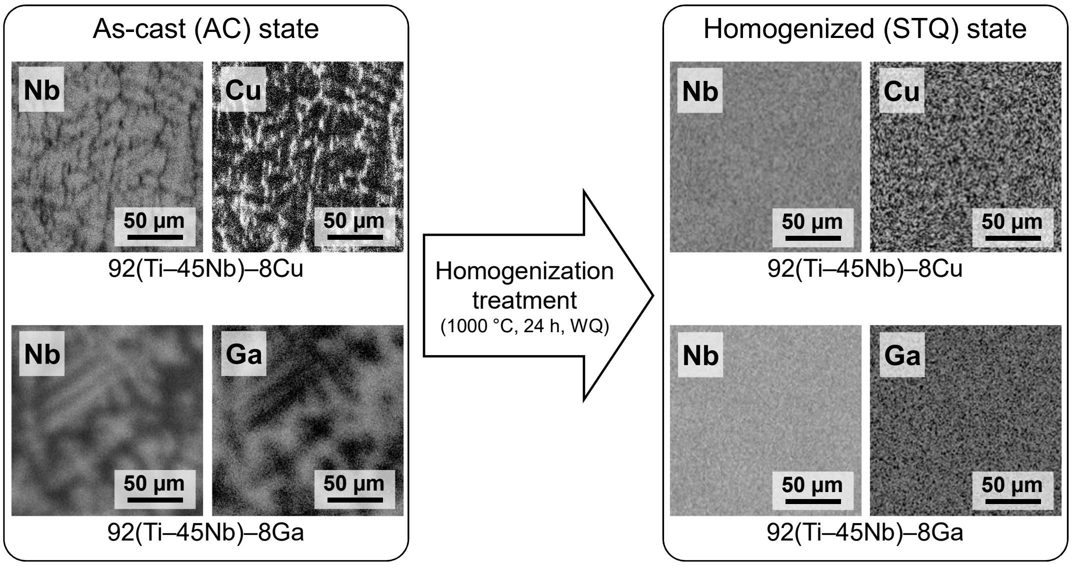

Figure 4.4: EDX mappings on 92(Ti–45Nb)–8Cu and 92(Ti–45Nb)–8Ga alloys showing elemental distribution of Nb and Cu/Ga before and after homogenization treatment. Bright areas contain higher concentration of the element indicated.

The main structural constituent in all alloys in STQ state is single-phase β, as demonstrated by the X-ray diffractograms (Fig. 4.5a). Solution-treatment guarantees also dissolution of the Ti_2Cu phase, where present, thus leading to homogeneous single-phase β microstructures, indicating that all alloying elements are in complete solid solution with Ti and are capable of forming a metastable β phase. This is attributed to the high β-stabilizing effect of Nb, despite Ga being an α-stabilizer and Cu being a β-eutectoid stabilizer. In particular, when Nb content is greater than 40 wt.%, a single-phase β is formed in rapidly quenched Ti–Nb alloys [6]. The magnified inset of the $(110)_\beta$ Bragg peak (Fig. 4.5b) shows only the β reflection, and no other reflections. The relatively high intensity of this peak is due to the existence of a preferred crystal orientation, and the $(110)_\beta$ crystal plane is preferred in BCC crystal system. It is noted that β reflections have shifted to higher angles (2θ), compared to Ti–45Nb. The shift in peak position is consistent with the decrease in the calculated lattice parameters (Fig. 4.5c). Solution-treatment also affects lattice parameters, with an average decrease of $\cong$ 0.3% compared to AC state, due to lattice relaxation and reduction of casting residual stresses. The variations in peak positions and intensities suggest that the lattice parameters are sensitive to Ga and/or Cu content in Ti–45Nb, revealing an almost linear lattice contraction upon their addition. The decrease in unit cell volume of Ti–45Nb upon substitution of Ti and Nb with Ga and/or Cu is due to the smaller atomic radius of these two alloying elements.

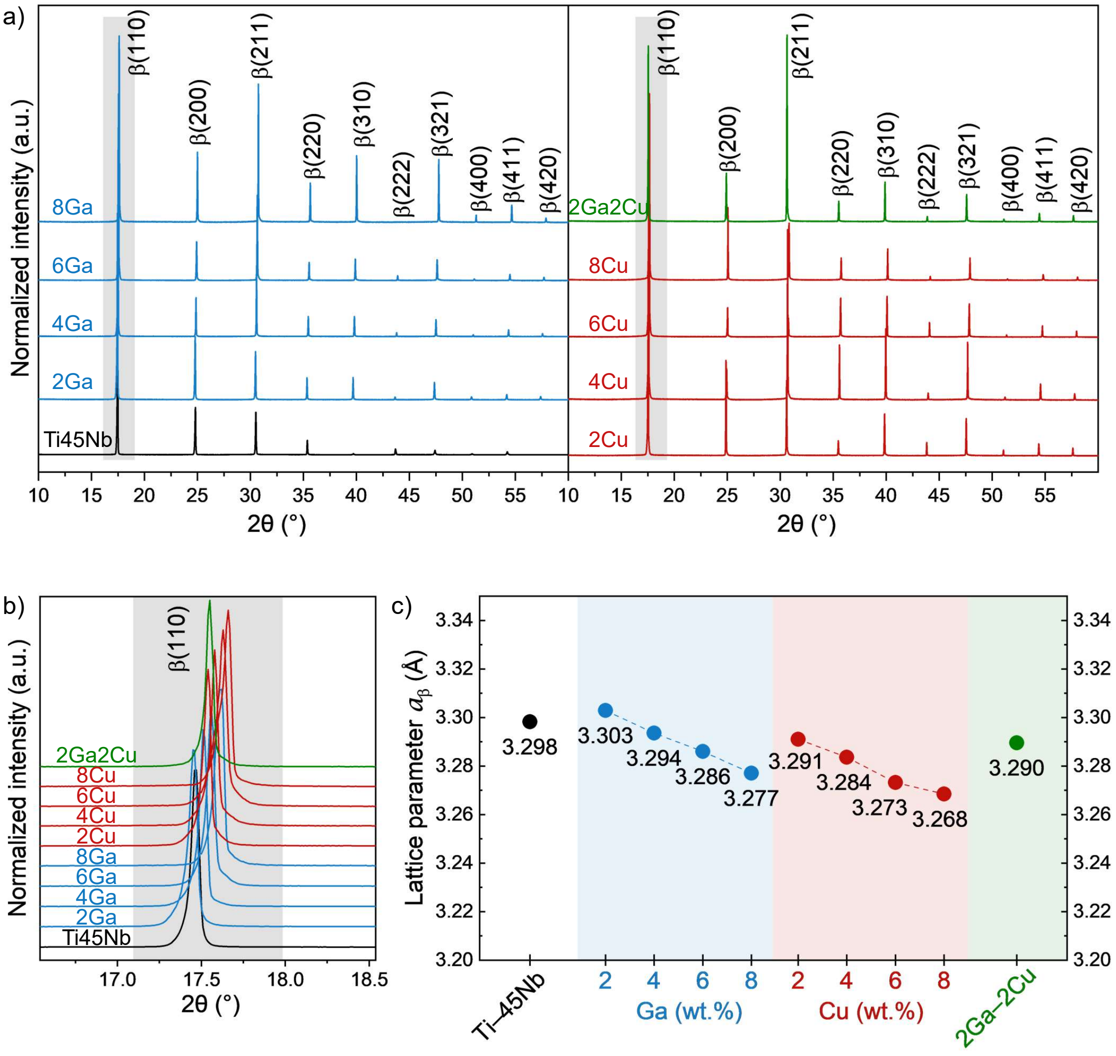

Figure 4.5: (a) X-ray diffractograms of the nine homogenized (STQ) alloys and Ti–45Nb alloy, (b) magnification of $(110)_\beta$ diffraction peak (shaded area), and (c) variation of the calculated cubic lattice parameters a_β (adapted from Ref. [255]).

Fig. 4.6 shows the microstructures obtained after β-solutionizing and quenching, which consist of coarse equiaxed β-grains of consistently different grain sizes (equivalent diameter d_{grain}). Ga-bearing alloys exhibit an average d_{grain} in the range of 55 – 141 μm, Cu-bearing alloys of 215 – 347 μm, the quaternary alloy of 90 μm, and Ti–45Nb of 154 μm. The grain refinement effect observed in the Ga-bearing alloys, where $d_{grain} \cong 9 - 65\%$ smaller than Ti–45Nb, can be attributed to Ga solute atoms, which act as pinning points of grain boundary motion, thus slowing down grain growth during casting and solution-treatment.

In conclusion, XRD and SEM analyses demonstrate that all the alloys in STQ state exhibit a single-phase BCC β microstructure, in which all alloying elements (Ti, Nb, Ga and/or Cu) are in solid solution.

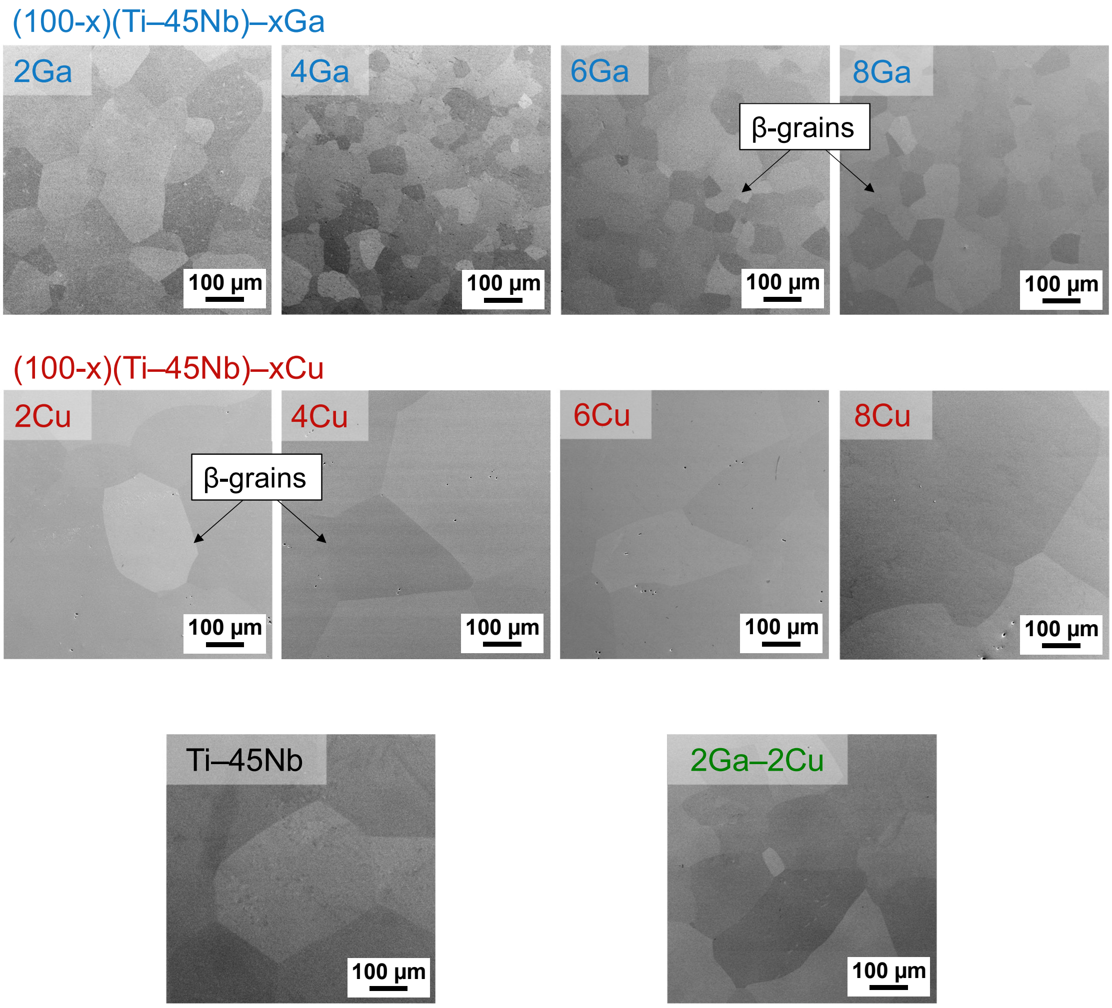

Figure 4.6: SEM micrographs showing the microstructures of the alloys in STQ state.

4.3 Effect of Antibacterial Alloying Additions on Microhardness & Strength

Fundamental understanding of mechanical behavior is a key aspect of material design. In order to evaluate the effect of alloying elements Ga and/or Cu addition to Ti–45Nb in terms of mechanical response, the mechanical behavior is investigated by means of microhardness, tensile and compressive tests, and ultrasonic tests (the latter presented in the next section). A thorough comprehension of the interplay between hardness and strength is important for a variety of reasons: reliable hardness-strength correlations ensure prompt evaluations of the mechanical characteristics of a newly developed material.

Microhardness is a relevant characterization parameter, as it offers an overall measure determined by factors such as solid solution strengthening, strain hardening and microstructural refinement. In contrast to stress-strain tests, only a limited amount of material is needed for such testing methodology, therefore preliminary microhardness evaluation is also conducted on alloys in as-cast state (Appendix B, Fig. B1). Experimental microhardness values on STQ alloys are reported in Fig. 4.7 and listed in Table 4.2. The microhardness of the Ga-bearing alloys increases with Ga addition, from 174 $HV_{0.1}$ (Ga 2 wt.%) to an average value of $\approx$ 228 $HV_{0.1}$ for Ga 4, 6, and 8 wt.%. Cu addition leads to a higher and almost linear increase, with values in the range 184 – 290 $HV_{0.1}$, while the quaternary alloy exhibits an intermediate value of 202 $HV_{0.1}$. Generally, alloying Ga and/or Cu leads to a widespread significant increase of 19 – 97%, compared to Ti–45Nb ($HV_{0.1} = 147$). The absolute highest value of 290 $HV_{0.1}$ was measured for 92(Ti–45Nb)–8Cu alloy.

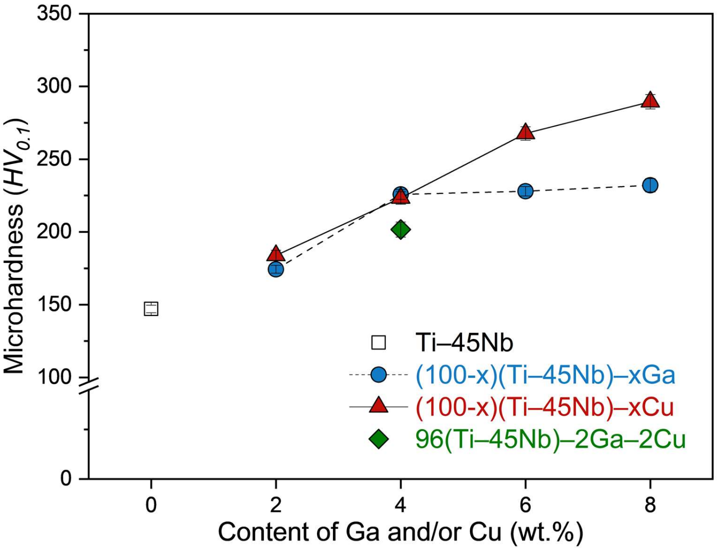

Figure 4.7: Variation of microhardness $HV_{0.1}$ with Ga and/or Cu content.

Before starting the mechanical stress-strain tests, it was essential to evaluate the specimen's structural integrity, because the presence of defects has inevitably an impact on the sample's mechanical behavior. During casting, solidification causes volumetric shrinkage and porosity. For this reason, all tested samples were previously scanned by 2D computed tomography (CT), in order to ensure data validation and reproducibility (Ch. 3, Sec. 3.3.3 for further details).

The engineering stress-strain curves under quasi-static uniaxial tensile and compressive loading are shown in Fig. 4.8 and Fig. 4.9, respectively. The resulting mechanical properties (Young's modulus E, yield strength in tension ${\sigma_y}^{\text{tens}}$, ultimate tensile strength σ_{UTS}, fracture strength σ_{f}, maximum strain at fracture ε_{max}, elastic energy δ_{e}, and yield strength in compression ${\sigma_y}^{\text{compr}}$) are listed in Table 4.2. The two Cu-bearing Ti alloys with Cu 6, 8 wt.% were excluded from the tensile tests, as they could not be machined (Appendix C, Fig. C1), very likely due to the high porosity of the rods. Such drawback is also responsible for the considerably high standard deviation for the same two alloys tested in compression.

Tensile Tests. All tensile stress-strain curves exhibit a distinct yield drop from the upper yield point (UYP) to the lower yield point (LYP), clearly separating the elastic and plastic regimes, which is more pronounced for 94(Ti–45Nb)–6Ga, 92(Ti–45Nb)–8Ga, and 96(Ti–45Nb)–4Cu alloys, as indicated in Fig. 4.8. Distinct yield point is a typical feature of heavily stabilized β-type alloys, which are me-

Table 4.2: Mechanical properties determined from microhardness measurements, tensile and compression tests.

		Tension						Compr.
Alloy	$HV_{0.1}$	E (GPa)	${\sigma_y}^{tens}$ (MPa)	σ_{UTS} (MPa)	σ_f (MPa)	ε_{max} (%)	δ_e (MJm^{-3})	${\sigma_y}^{compr}$ (MPa)
Ti–45Nb	147 ± 3	64 ± 2	423 ± 5	426 ± 5	6 ± 2	22 ± 2	1.90 ± 0.08	386 ± 17
98(Ti–45Nb)–2Ga	174 ± 3	73 ± 3	551 ± 3	556 ± 6	80 ± 3	18 ± 1	2.63 ± 0.11	548 ± 37
96(Ti–45Nb)–4Ga	226 ± 3	77 ± 3	681 ± 8	675 ± 8	485 ± 23	17 ± 2	3.66 ± 0.17	607 ± 17
94(Ti–45Nb)–6Ga	228 ± 3	78 ± 3	602 ± 10	606 ± 9	373 ± 36	30 ± 2	2.92 ± 0.09	604 ± 18
92(Ti–45Nb)–8Ga	232 ± 5	82 ± 2	620 ± 2	618 ± 5	407 ± 47	32 ± 3	2.95 ± 0.06	568 ± 12
98(Ti–45Nb)–2Cu	184 ± 4	75 ± 2	547 ± 9	548 ± 9	96 ± 40	13 ± 2	2.40 ± 0.07	487 ± 11
96(Ti–45Nb)–4Cu	223 ± 4	73 ± 2	539 ± 10	544 ± 10	83 ± 19	28 ± 3	2.51 ± 0.05	525 ± 14
94(Ti–45Nb)–6Cu	268 ± 5	Machining of tensile samples not possible						622 ± 124
92(Ti–45Nb)–8Cu	290 ± 5	Machining of tensile samples not possible						639 ± 44
96(Ti–45Nb)–2Ga–2Cu	202 ± 6	78 ± 2	596 ± 10	612 ± 11	309 ± 37	22 ± 2	2.86 ± 0.07	729 ± 29

chanically stable against stress-induced α" martensite formation at RT [256], on the other hand, the absence of distinct yield points is typical of martensitic alloys, where the elastic-plastic transition is continuous [124]. A similar phenomenon has been observed for other alloys (Al–Mg [257], Cu–Zn [258], mild steels [259], and Ti–Nb-based gum metals [260]), and it was attributed to strain aging, which occurs when solute atoms interact with moving dislocations, slowing down the motion of dislocations and then resulting in an increase in tensile strength and subsequent decrease in ductility. Yield strengths in tension for the Ti–Nb–Ga alloys are in the range 551 – 681 MPa, for Ti–Nb–Cu alloys in the range 539 – 547 MPa and for the quaternary alloy of 596 MPa, thus with an increase of 30 – 60%, 27 – 29% and 41% respectively, compared to the reference Ti–45Nb (${\sigma_y}^{tens}$ = 423 MPa). These values are comparable with those of similar β-type Ti alloys, as reported in Table 2.4 (Ch. 2, Sec. 2.3), and in some cases higher than the β-type Ti–Nb–In alloys [101] previously developed, where compressive yield strengths were in the range 511 – 568 MPa. The developed alloys display significant plasticity in tension, with maximum elongation at fracture (ε_{max}) that, in some cases, is significantly higher than the reference alloy. The alloy 92(Ti–45Nb)–8Ga has the highest ductility of 32%. When the amount of alloying elements Ga and/or Cu is > 2 wt.%, it is possible to observe a long plateau with limited strain hardening after the yield drop. Because of this behavior, σ_{UTS} values are similar to ${\sigma_y}^{tens}$. Fracture strength (σ_f) values also show a considerable increase compared to Ti–45Nb, confirming the strengthening

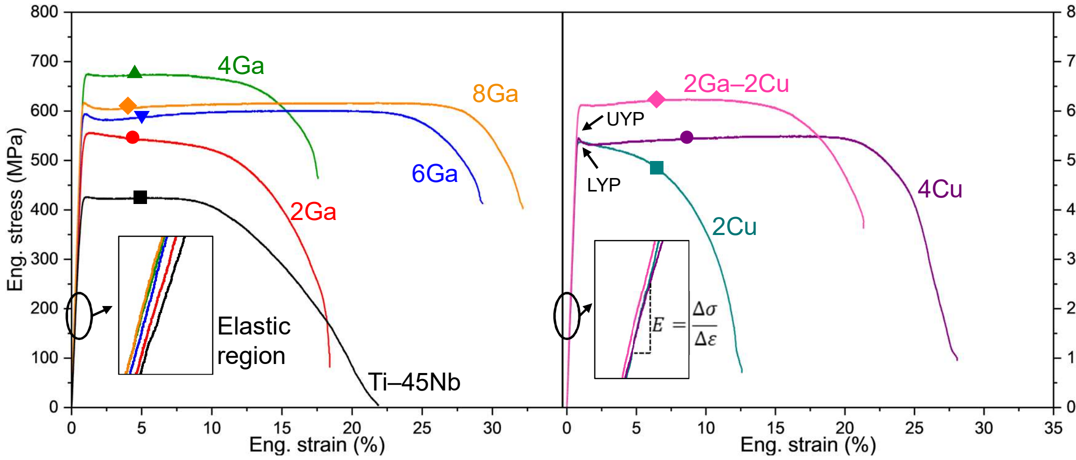

Figure 4.8: Engineering stress-strain curves in tension of the nine developed alloys in STQ state. Insets: magnification of the linear elastic region (adapted from Ref. [255, 261]).

behavior discussed on the basis of the stress-strain curves. The ability of a material to release absorbed energy upon unloading, known as resilience, is measured by the elastic energy (δ_e), calculated by taking the yield strength as elastic limit (Ch. 3, Sec. 3.4, Eq. 3.4). Elastic energy δ_e also significantly increases: 39 – 93%, 26 – 32% and 51% for Ti–Nb–Ga, Ti–Nb–Cu and the quaternary alloy, respectively, compared to Ti–45Nb, suggesting greater capacity of the novel alloys to bear load before permanently deforming. Young's modulus, determined from the linear elastic region of the stress-strain curves in tension, will be discussed in the next section.

Compression Tests. Stopping criterion for compression tests was 50% strain, as all the samples did not fracture during testing (Fig. 4.9). Nonetheless, it is noteworthy to report that when Cu content exceeds 6 wt.%, the tested samples do exhibit signs of cracking, which however occurs too slowly to be visible on the stress-strain curves. This is probably due to the very coarse microstructure, which is typical for the two alloys with the highest amount of Cu. As it is possible to infer from the curves, all alloys display very large compressive deformability, exceeding 50%, suggesting excellent workability. Yield strengths in compression (σ_y^{compr}) also exhibit a considerable increase of 42 – 57%, 26 – 65% and up to 89% for Ti–Nb–Ga alloys, Ti–Nb–Cu alloys and the mixed alloy, respectively, compared to Ti–45Nb (σ_y^{compr} = 386 MPa). Interestingly, some differences in the yielding behavior in tension and compression can be observed: the aforementioned distinct yield point seems to come less in compression, and is therefore replaced by continuous yielding, when Ga content is $\geq$ 4 wt.% and in the Cu-bearing alloys. These aspects are further investigated in Sec. 4.6. Continuous yielding phenomenon, virtual absence of Hookean (linear) ideal elastic behavior and error sources inherent to compression testing make evaluation of Young's modulus susceptible to various inaccuracies, in particular the stress interval selected for its calculation. For these reasons, E is determined by two other methods, as described in the next section.

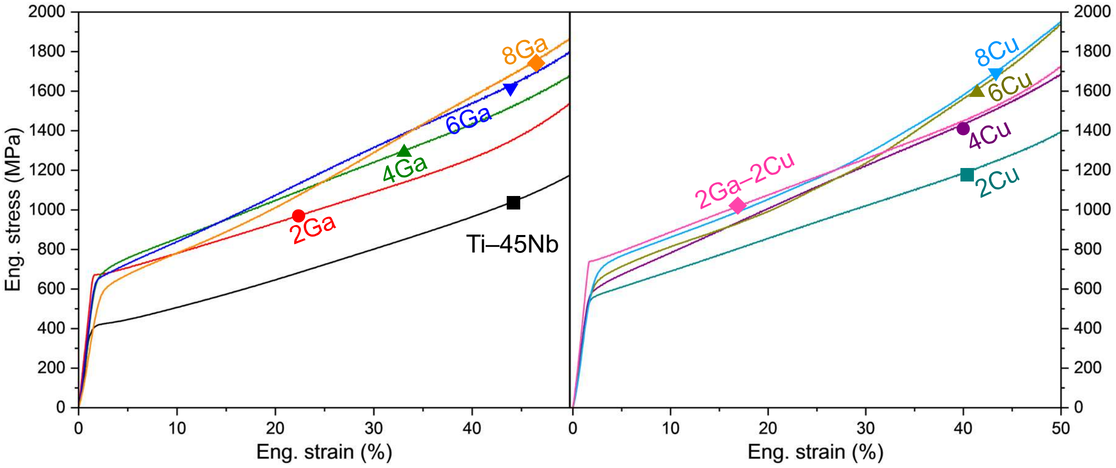

Figure 4.9: Engineering stress-strain curves in compression of the nine developed alloys in STQ state (adapted from Ref. [255, 261]).

Altogether, these results suggest that it is possible to achieve enhanced mechanical properties, such as simultaneous combination of high strength and large plasticity, by properly tuning the alloy composition without further processing, while retaining the desired single-phase β microstructure.

4.4 Variation of Young's Modulus with Ga and Cu Addition

Given the significance of elastic properties (e.g., Young's modulus E) of materials for engineering and medical applications, it is not unexpected that several experimental approaches have been established to evaluate them. Dynamic methods (e.g., pulse-echo) enable substantially higher precision than quasi-static methods such as tensile and compressive testing [262]. Pulse techniques are based on the measurement of transit time of the ultrasonic pulse through the specimen. Both approaches require carefully prepared samples with parallel, flat and smooth surfaces as well as no surface or bulk defects in order to get accurate results.

Fig. 4.10 presents the variation of E with alloying content determined by two methods: pulse-echo ultrasonic (E^{US}) and tensile testing (E). The reference Ti–45Nb alloy shows the lowest value of 63 – 64 GPa, in agreement with the supplier technical data sheet and literature [124]. The four Ga-containing alloys exhibit an almost linear increase of both E and E^{US} with Ga content, with E ranging between 73 – 82 GPa and E^{US} between 64 – 79 GPa, which are up to 28% higher than Ti–45Nb. Cu addition also leads to a significant increase in Young's modulus, however some discrepancies are present between methods. The two methods well agree for the alloy with Cu 2 wt.%, the first discrepancy can be observed in the alloy with Cu 4 wt.%, where E is 73 GPa and E^{US} is 98 GPa. In the other two alloys, where Cu content is 6 and 8 wt.%, E^{US} is greater than 100 GPa. The distribution of the results for these alloys is broader than for the other alloys, as indicated by the error bars. It is noteworthy to mention that discrepancies systematically increase with structural

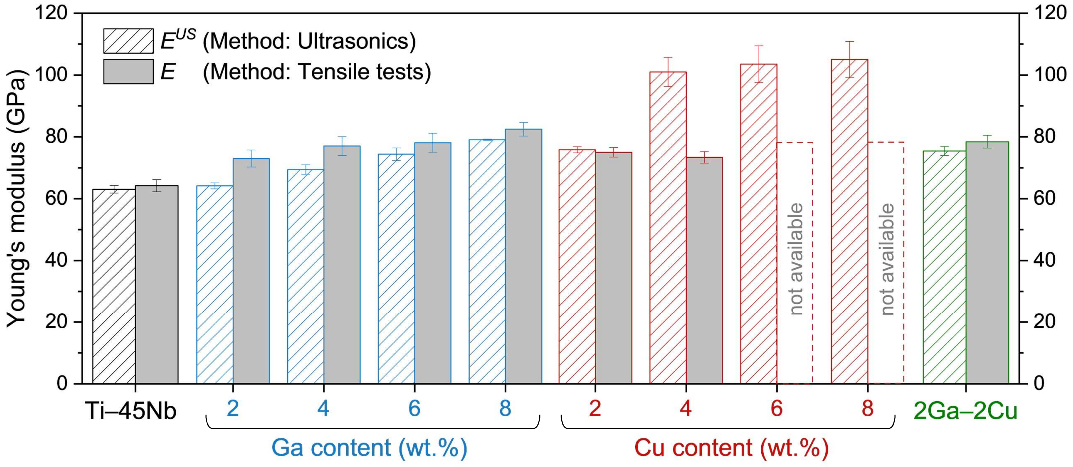

Figure 4.10: Variation of E determined from dynamic pulse-echo method and from tensile stress-strain curves.

heterogeneities such as grain size, microcracks and porosity, major limits of the developed Cu-bearing alloys. Indeed, the scattering of ultrasounds in contact with structural defects, as for the Cu-bearing alloys, causes attenuation, so decrease in velocity, of the transverse wave as well as the longitudinal wave, thus increasing noise level, and therefore inaccuracy in the measurements [263]. The quaternary 96(Ti–45Nb)–2Ga–2Cu alloy has E^{US} and E values of 75 and 78 GPa, respectively, thereby being similar to 4Cu and 4Ga alloys. Despite the increase in Young's modulus due to minor alloying compared to Ti–45Nb, the alloys display a Young's modulus which is compatible for load-bearing implant applications. Moreover, these values are even lower, up to 42% in case of Ga 2 wt.%, if compared to Ti–6Al–4V alloy, where measured E^{US} and E are 111 and 117 GPa, respectively (Appendix D, Table D1).

4.5 Correlation of Structural Characteristics with Mechanical Behavior

Focus of this section is placed on the relationship between microstructural features and mechanical properties previously discussed. Fig. 4.11 correlates strength in tension and compression, microhardness and hardening exponent with grain size, and alloying content for all studied alloys. In general, similar trends between microhardness and yield strengths in tension and compression can be observed, with values increasing with content of alloying elements Ga and/or Cu. Values of n, calculated with the Hollomon equation (Ch. 3, Sec. 3.4, Eq. 3.5) and which represent the degree of strain hardening, are in the range 0.01 – 0.11, and also show an increasing trend with Ga and/or Cu additions. The Ga 2 wt.% alloy exhibits the lowest n value of 0.02, suggesting low strain hardening capacity. Maximum values are observed for Ga 6 and 8 wt.%, suggesting a modest increase in plasticity. More specifically, the curves of strength and microhardness for the four Ti–Nb–Ga alloys display a saturation when Ga 4 wt.%, with no significant increase in the case of Ga 6 and 8 wt.%. This behavior can be correlated with the opposite variation of grain

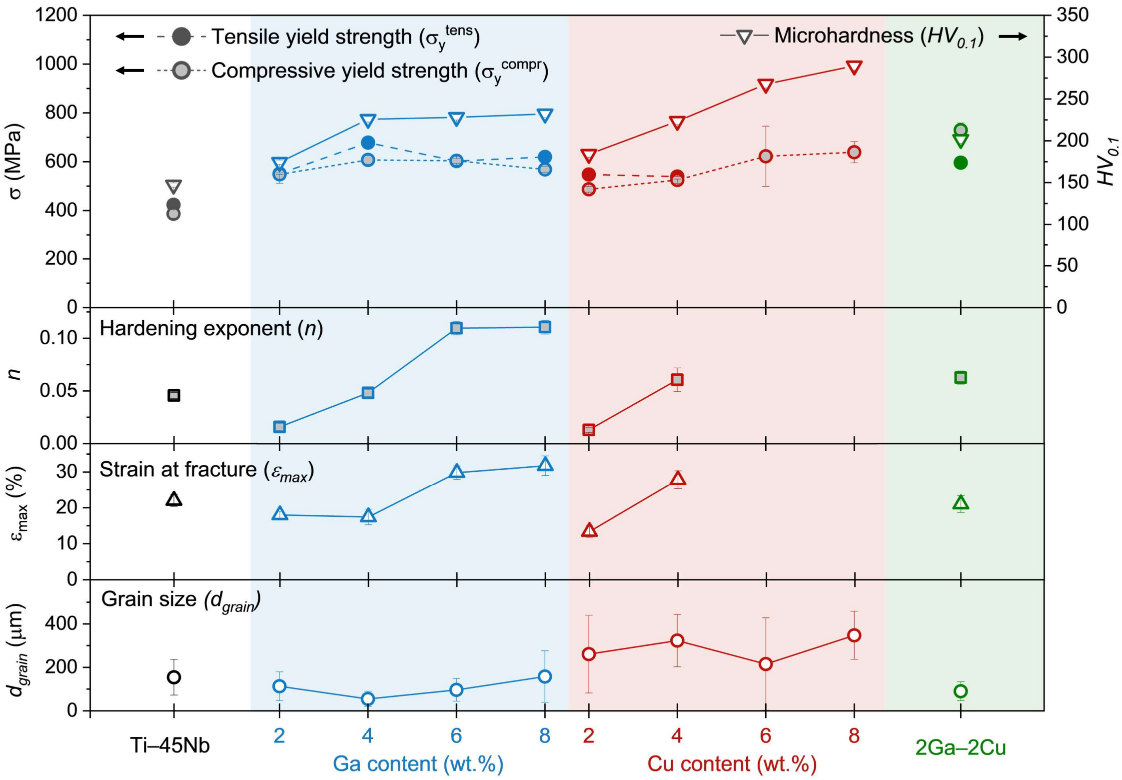

Figure 4.11: Plot correlating Ga/Cu content with various mechanical properties ($HV_{0.1}$, $\sigma_y{}^{tens}$, $\sigma_y{}^{compr}$, ε_{max}), hardening exponent (n), and grain size (d_{grain}).

size, which is at a minimum for this composition (Ga 4 wt.%). The same applies to the 2Ga–2Cu alloy, which exhibits high strength and microhardness and small grain size, if compared to the alloy with Cu 4 wt.%. On the other hand, microhardness and strength increase monotonically with Cu content. The strength-ductility trade-off, which represents a serious engineering dilemma, can also be partially overcome by careful tuning of the alloying content. For instance, the Ga 4 wt.% alloy exhibits higher strength ($\sigma_y{}^{tens} = 681$ MPa) and comparable tensile maximum strain ($\varepsilon_{max} =$ 17%) than Ti–45Nb ($\sigma_y{}^{tens} = 423$ MPa, $\varepsilon_{max} = 22\%$), similarly the alloys Cu 4 wt.% ($\sigma_y{}^{tens} = 539$ MPa, $\varepsilon_{max} = 28\%$) and 2Ga–2Cu ($\sigma_y{}^{tens} = 596$ MPa, $\varepsilon_{max} = 22\%$). Since all alloys display a single-phase microstructure, the ascertained strengthening mechanisms are grain boundary strengthening and substitutional solid solution strengthening, which induce an obstruction to the dislocation motion during plastic deformation, thereby contributing towards the improved mechanical properties. Moreover, the difference ($\approx 3-10\%$) in atomic size of the alloying elements Ga and Cu, compared to Ti and Nb, might be a conceivable factor affecting microhardness, strength and also the Young's modulus. This is because the replacement of Ti and Nb with the smaller atoms brings the alloying atoms closer in the BCC crystal lattice, corroborating the smaller lattice parameters (Fig. 4.5c), calculated via Rietveld method, and thus contributing towards the increased mechanical properties. In conclusion, the Ga 8 wt.% alloy displays the best combination of high strength ($\sigma_y{}^{tens} = 620$ MPa, $\sigma_y{}^{compr} = 568$ MPa), high hardness (232 $HV_{0.1}$), modest strain hardening, and high ductility ($\varepsilon_{max} = 32\%$).

4.6 Assessment of β-Phase Stability

The compression stress-strain curves previously discussed (Fig. 4.9) show a conspicuous strain hardening, but no double yielding effect originating from the formation of stress-induced martensite (α") [264]. To acquire a better understanding of the effect of compressive strains on the β phase stability, heavily deformed ($\varepsilon^{\mathrm{comp}} \approx 50\%$) compression specimens were cross-sectioned along the loading direction for further microstructural studies. Fig. 4.12a shows the XRD patterns collected before ($\varepsilon^{\mathrm{comp}} \approx 0\%$) and after ($\varepsilon^{\mathrm{comp}} \approx 50\%$) the compression tests, and refined lattice parameters are listed in Table 4.3. The nine diffractograms of the strained specimens (red line) display only reflections indexed with cubic BCC ($Im\bar{3}m$), indicating that the parent β phase is fully retained and no secondary phase was formed during deformation. Peak broadening (Fig. 4.12b) is due to residual compressive stresses built up in the deformed β matrix and increased dislocation density; shift to higher angles (2θ) is reflected by the shrinkage in the lattice parameters (Fig. 4.12c and Table 4.3), while changes in peak intensities suggest development of the crystallographic texture.

Table 4.3: Cubic lattice parameters a_β determined with Rietveld method from the XRD patterns of Fig. 4.12 before and after compression tests.

Alloy	${a_\beta}^{\mathrm{before}}$ (Å)	${a_\beta}^{\mathrm{after}}$ (Å)	Difference (%)
Ti–45Nb	3.298	3.286	-0.36%
98(Ti–45Nb)–2Ga	3.303	3.290	-0.38%
96(Ti–45Nb)–4Ga	3.294	3.284	-0.28%
94(Ti–45Nb)–6Ga	3.286	3.279	-0.22%
92(Ti–45Nb)–8Ga	3.277	3.276	-0.04%
98(Ti–45Nb)–2Cu	3.291	3.286	-0.16%
96(Ti–45Nb)–4Cu	3.284	3.277	-0.21%
94(Ti–45Nb)–6Cu	3.273	3.264	-0.29%
92(Ti–45Nb)–8Cu	3.268	3.263	-0.18%
96(Ti–45Nb)–2Ga–2Cu	3.290	3.280	-0.30%

EBSD analyses further confirm these results. Fig. 4.13a,b,c shows the EBSD maps of the specimens before any type of strain, where the coarse equiaxed grains have random orientations. Fig. 4.13d,e,f depicts heavily strained and elongated β-grains, due to the uniaxial compressive loading. Crystal orientation is indicated by an RGB mixture. Most of the regions correspond to the preferred orientation $[110]_\beta$, slip direction in BCC systems is always in <111>. Deformation twinning can be observed at RT in β-type Ti–Nb alloys for Nb content below 42 wt.%, above these values, the dominant deformation mode changes to dislocation slip [47], which is indeed the case in the developed alloys.

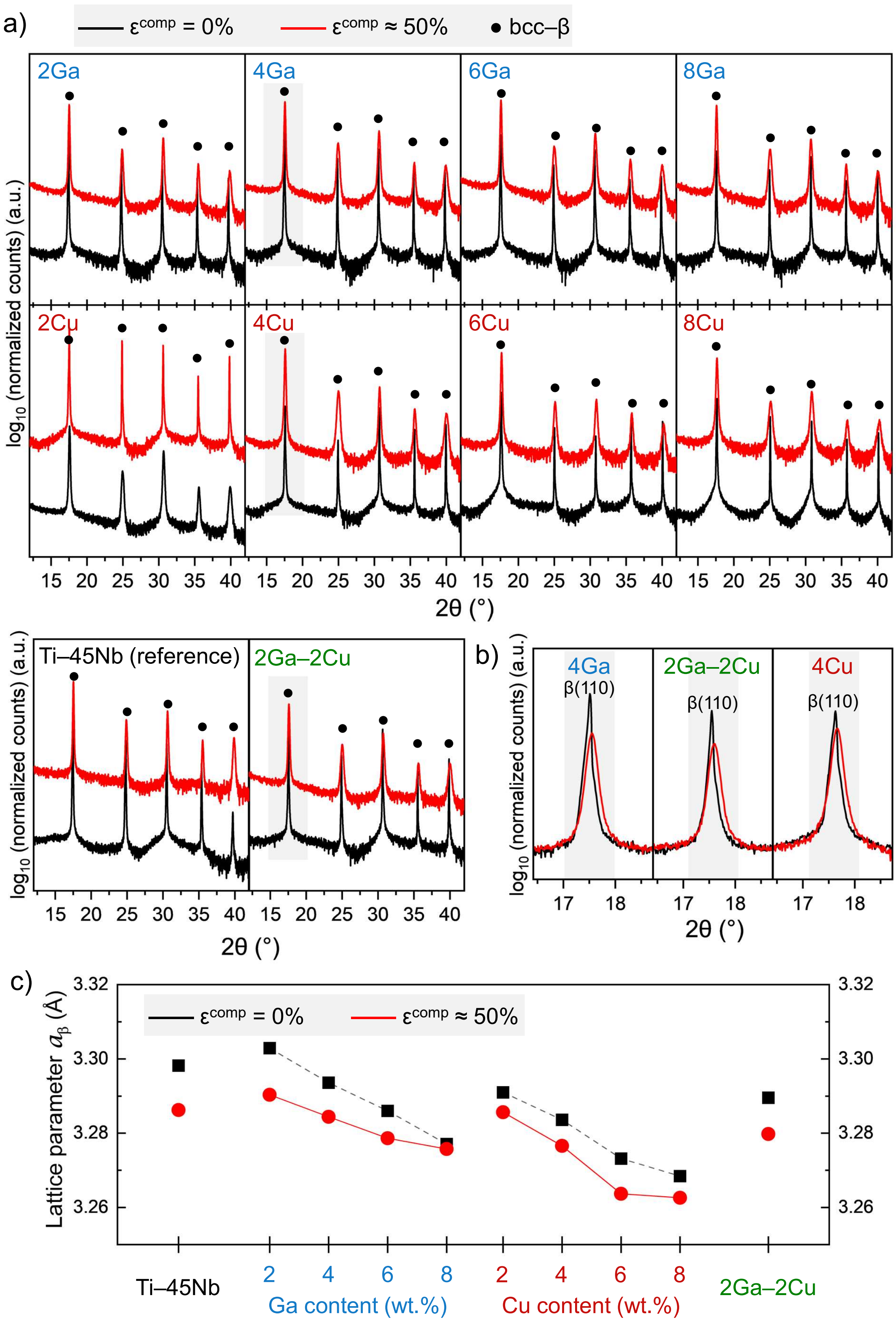

Figure 4.12: (a) X-ray diffractograms before (black line) and after (red line) the compression tests, and (b) magnification of $(110)_\beta$ diffraction peak of three alloys (shaded area). Logarithmic scale (on vertical axis) is used to amplify low intensity reflections. (c) Cubic lattice parameters a_β before (black) and after (red) compression tests determined from XRD patterns.

Another aspect to consider is strain rate: mechanical twinning occurs in BCC metals at high strain rates ($> 10^{-1}$ s^{-1}) [265], while tests in the present work were conducted in quasi-static conditions (strain rate 10^{-3} s^{-1}). Nonetheless, twinning cannot be totally excluded, and deformation bands in Fig. 4.13d,e,f, formed upon $\varepsilon^{\mathrm{comp}} \approx 50\%$, might hinder twins. Further investigations at strains right after yielding are recommended for future work. The results are in good agreement with previous studies on a β-type (Ti–40Nb)–3.5Nb alloy: after several thermomechanical treatments (hot and cold rolling with various degrees of thickness reduction), no sign of deformation-induced phase transformation was observed [133]. Similarly, the only deformation mechanism in the heavily stabilized β-type Ti–3Al–8Mo–7V–3Cr alloy was attributed to slip [266].

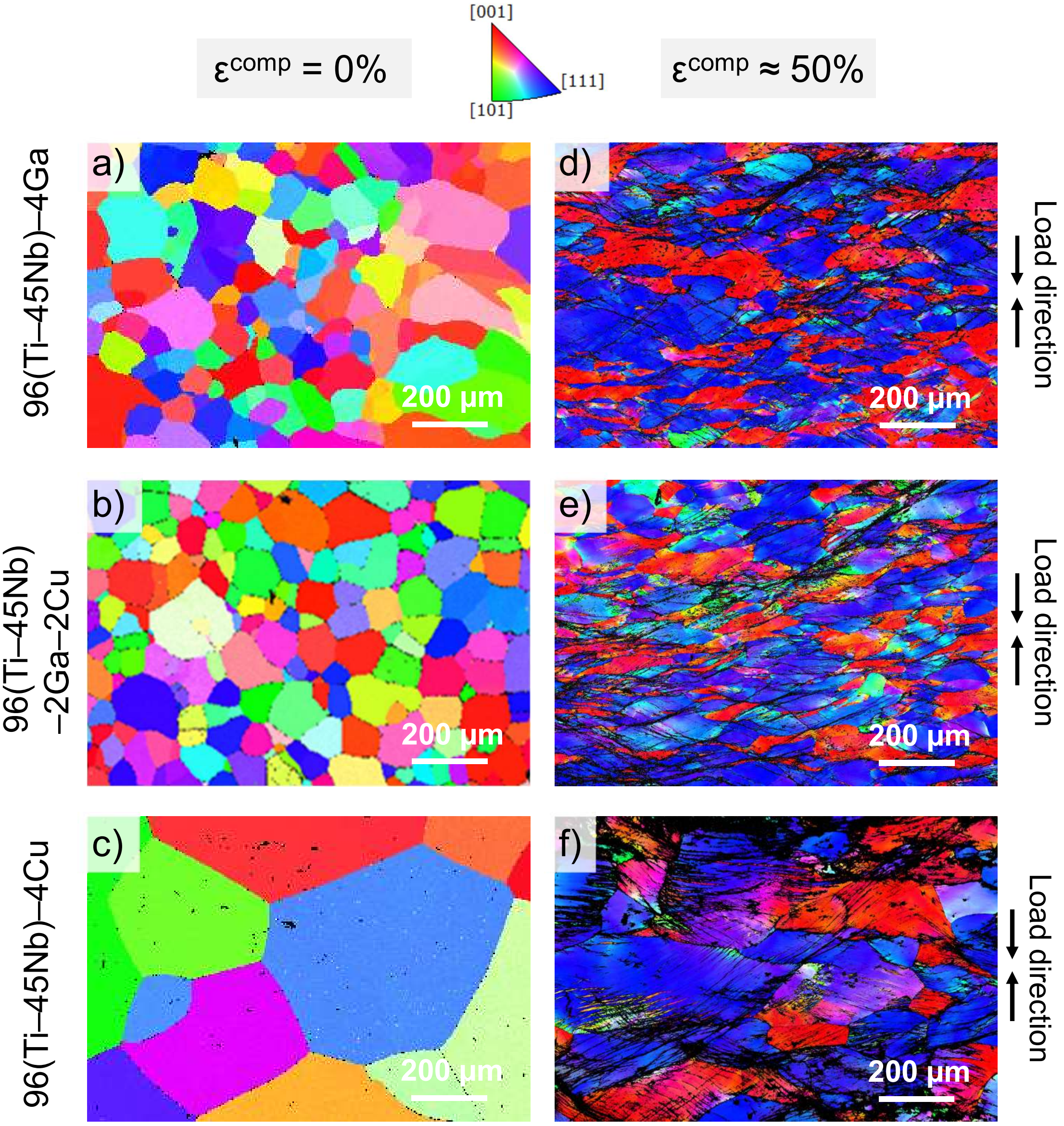

Figure 4.13: EBSD inverse pole figures (IPF) maps before (a,b,c) and after (d,e,f) compression tests of three alloys: 4Ga (a,d), 2Ga–2Cu (b,e), and 4Cu (c,f). Color coding is given with respect to the loading direction (adapted from Ref. [261]).

4.7 Discussion & Chapter Summary

Discussion

In the present chapter, the effects of minor additions of Ga and/or Cu on structural characteristics and mechanical behavior of Ti–45Nb were studied. Preliminary microstructural investigations were carried out on the as-cast alloys, while in-depth studies on phase composition, mechanical properties and phase stability were conducted on the homogenized (solution-treated and quenched, STQ) alloys.

The studied alloys were designed using electron-to-atom (e/a) and molybdenum equivalence ($[\mathrm{Mo}]_{\mathrm{eq}}$) (discussed in Ch. 2, Sec. 2.3) as empirical predictive tools for β phase stability. The β phase can be retained upon quenching when e/a is greater than 4.2 [120], which is indeed the case for all alloys, except three Ti–Nb–Cu alloys (Ch. 3, Sec. 3.2, Table 3.1). The $[\mathrm{Mo}]_{\mathrm{eq}}$ values of the alloys were determined according to Eq. 2.1 (Ch. 2, Sec. 2.3) and are reported in Fig. 4.14. The minor concentration of interstitial elements N and O, capable of drastically affecting the β phase stability, has also been considered by maintaining it in the compositional range of 0.1 wt.%. According to the classification reported by Kolli and Devaraj [107] (Fig. 4.14), the nine alloys can be classified as metastable-β and near-β alloys.

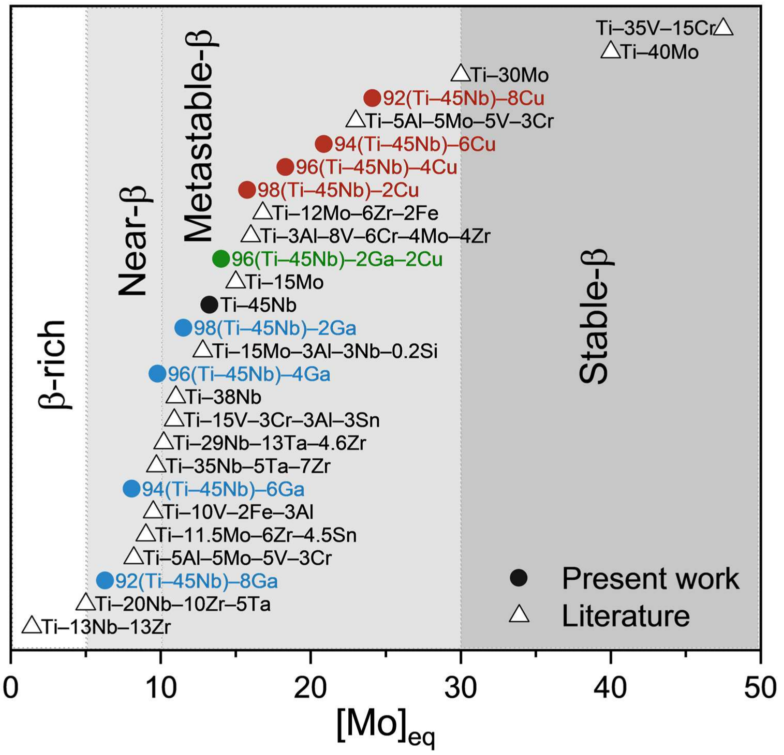

Figure 4.14: $[\mathrm{Mo}]_{\mathrm{eq}}$ of the developed alloys and other β-type Ti alloys in the literature (adapted from Ref. [261]).

Empirical predictions were experimentally confirmed by XRD studies: all alloys in STQ state display a single-phase β (BCC) Ti-based solid solution, despite the presence of the α-stabilizer Ga and β-eutectoid stabilizer Cu. This was made possible due to the combination of the enhanced β-stabilizing effect of Nb together with the high cooling rates achieved during quenching. The microstructure of the alloys is composed of coarse equiaxed β-grains of consistently different grain size (Fig. 4.6). Interestingly, Ga acts as an efficient grain refiner, which might be due to a reduced atomic mobility that slows grain growth during processing. A similar effect of Ga as grain refiner has been observed in other alloy systems [165, 167].

The electron-to-atom ratio can also be used to predict the trend of the elastic properties, for instance Kent et al. [267] suggest that the Young's modulus E of β-type Ti–Nb alloys decreases with increasing e/a, this trend finds experimental confirmation in the present work. Young's modulus E is a direct consequence of interatomic interactions and electronic properties, hence alloying elements have an influence on it [268]. Ga and Cu have a smaller atomic radius than Ti and Nb (Ch. 2, Sec. 2.5, Table 2.9), this is also evident from the cubic lattice constants, that decrease upon Ga and/or Cu addition. Substitution of Ti and Nb with the smaller Ga and Cu brings the alloying atoms closer in the β crystal lattice, and thus E increases. In the case of Ga, recent theoretical investigations, conducted in collaboration with our BIOREMIA colleagues from the University of Ioannina (Greece), concluded that Ga p-electrons create covalent-like directional bonds with Ti s-electrons, which explain both the increase in E and lattice contraction [255]. Similar theoretical studies on the effect of Cu addition on the electronic properties of Ti–45Nb are currently progressing. To a great extent, a regular pattern emerges when plotting a physical property (e.g., lattice parameter) against e/a, and anomalies indicate electronic structural changes within the alloy matrix [269]. Fig. 4.15 compares the refined cubic lattice parameters (a_β), plotted with e/a, of the alloys in the present work with those of similar β-type Ti–Nb alloys in the literature. The developed alloys fall within the range of e/a for which analogous Ti–Nb alloys exhibit low Young's modulus.

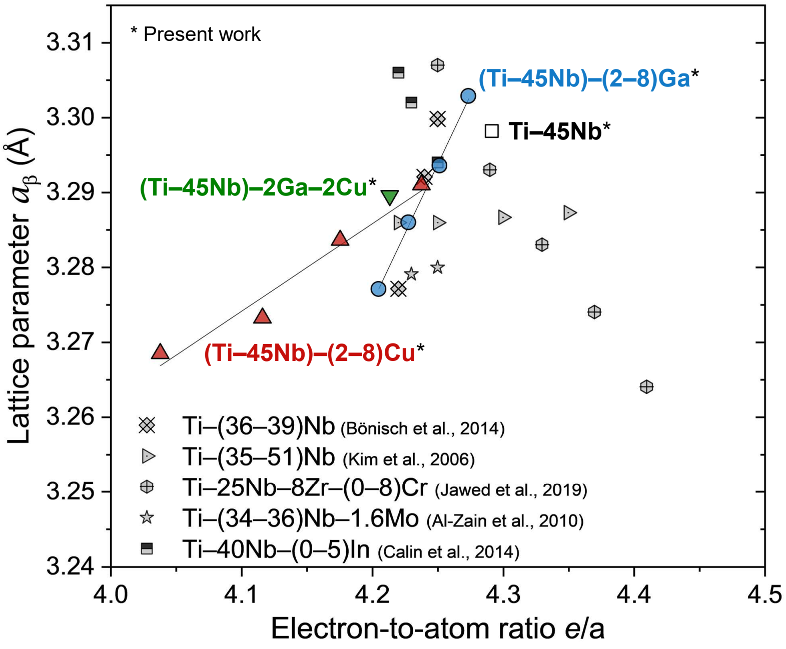

Figure 4.15: BCC lattice parameter a_β against e/a of the developed alloys compared to similar β-Ti–Nb alloys (adapted from Ref. [261]).

In the investigated alloys, grain boundary strengthening together with solid solution strengthening induce an obstruction to dislocation motion during plastic deformation, thereby contributing towards the increment in microhardness and strength upon alloying. The substitutional solid solution strengthening effect occurs due to the addition of solute elements (Ga, Cu) with smaller atomic radius, as already discussed. The underlying strengthening mechanism, arising from the increased dislocation density, is also evident from the broadening of the diffraction peaks after compressive strains. Clearly, the presence of Ga and/or Cu renders a significant strengthening effect. Moreover, the alloys display significant ductility and plasticity in both tension and compression. The dominant deformation mechanism is attributed to dislocation slip, which finds further confirmation in the low hardening exponent n values $(0.01 - 0.11)$ of the present work. Sadeghpour et al. [266] observed, in a single-phase β Ti–3Al–8Mo–7V–3Cr alloy, a sharp increase in n from 0.01 to 0.13 when the deformation mechanism changed from dislocation slip to mechanical twinning. Similarly, the β-type Ti–25Nb–3Zr–3Mo–2Sn alloy shows multiple deformation mechanisms (mechanical twinning, SIM, and ω transformation), and thus the n value is reported to be $\cong 0.23$, which is distinctly higher than n values determined for the present alloys.

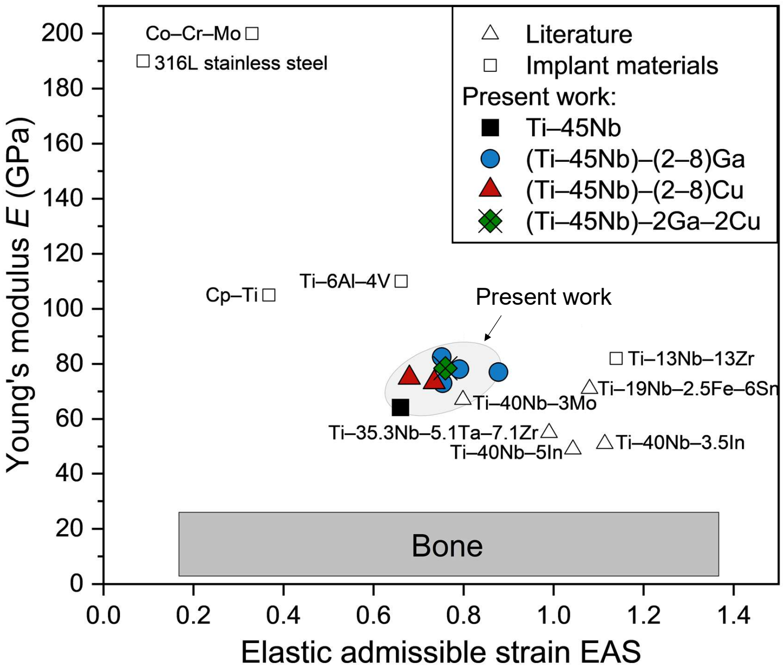

Figure 4.16: Variation of elastic admissible strain with Young's modulus of the developed alloys compared to other implant materials and bone.

As a final observation, mechanical biocompatibility and performance of an orthopedic implant material can be evaluated by the elastic admissible strain (EAS), defined as the yield stress-to-Young's modulus ratio. The higher the elastic admissible strain, the more mechanically suitable the material is [2]. The EAS values of the developed alloys are presented in Fig. 4.16. They are in the range 0.68 – 0.88, and are 3 – 33% higher than Ti–45Nb (EAS = 0.66), with Ga 4 wt.% alloy exhibiting the highest value (EAS = 0.88). It can be concluded that the nine alloys would offer a promising mechanical performance in practical load-bearing implant applications.

Chapter Summary

The main outcomes of this chapter can be summarized as follows.

- Nine different alloy compositions, (100-x)(Ti–45Nb)–xGa, (100-x)(Ti–45Nb)–xCu (where x = 2, 4, 6, 8 wt.%), and 96(Ti–45Nb)–2Ga–2Cu, were successfully fabricated by arc melting and cold crucible casting and then homogenized (solution treatment at 1000°C for 24 h and water quenched, STQ).
- All alloys in STQ state exhibit a single-phase β microstructure with a homogeneous distribution of the alloying elements within the matrix.
- Compared to the reference Ti–45Nb alloy, the developed alloys exhibit a significant increase in microhardness $HV_{0.1}$ (19 – 97%), yield strength in tension ${\sigma_\mathrm{y}}^\mathrm{tens}$ (27 – 60%) and compression ${\sigma_\mathrm{y}}^\mathrm{compr}$ (26 – 89%), strain at fracture ε_max (up to 44%) and good plasticity and workability.
- Addition of Ga and/or Cu renders a significant strengthening effect, mainly attributed to grain boundary and solid solution strengthening.
- Young's modulus E of the alloys (64 – 79 GPa for Ti–Nb–Ga, 76 – 104 GPa for Ti–Nb–Cu and 75 GPa for Ti–Nb–Ga–Cu), despite the increase in strength, remains in the acceptable ranges for implant applications when compared to the clinical alloys Ti–6Al–4V and c.p. Ti.
- The β phase is mechanically stable upon high compressive strains, with no sign of deformation-induced phase transformations. Dislocation slip is considered the dominant deformation mechanism in these β-type Ti alloys.

In conclusion, an ideal biomedical load-bearing implant material is required to exhibit the combined properties of low stiffness and high strength to sustain long-term service period. This chapter demonstrates that it is possible, by alloying and without further thermomechanical processing, to increase strength without adversely affecting the Young's modulus.

This chapter incorporates findings and insights from the following first-author original publications:

- **L.A. Alberta**, J. Vishnu., A. Hariharan., S. Pilz, A. Gebert, and M. Calin. *Novel low modulus beta-type Ti–Nb alloys by gallium and copper minor additions for antibacterial implant applications.* In: Journal of Materials Research and Technology, 20:3306–22 (2022). DOI: 10.1016/j.jmrt.2022.08.111
- **L.A. Alberta**, Y. Fortouna, J. Vishnu, A. Gebert, C. Lekka, K. Nielsch, M. Calin. *Effects of Ga on the structural, mechanical and electronic properties of β-Ti–45Nb alloy by experiments and ab initio calculations.* In: Journal of the Mechanical Behavior of Biomedical Materials, 140:105728 (2023). DOI: 10.1016/j.jmbbm.2023.105728

Chapter 5

Influence of Antibacterial Alloying Elements (Ga, Cu) on Corrosion Properties

5.1 Chapter Overview & Aims

Corrosion is among the most important mediators of the host tissue response to the implant material; therefore an accurate evaluation is absolutely necessary. This chapter aims at assessing the corrosion response and metal ion release in physiological conditions of the developed alloys.

Fundamental knowledge of the corrosion behavior of the investigated alloys in simulated body fluids at body temperature is acquired by conventional techniques: open circuit potential monitoring and potentiodynamic polarization. In addition, Ga and Cu metal ion release studies, with seven days of exposure to the same environmental conditions as for corrosion tests, are also conducted. Methods able to identify origin and amount of corrosion products and metal ions released in physiological conditions are of great interest in order to predict and preliminarily discuss safety, biocompatibility, and potential antibacterial capacity of the implant materials.

5.2 Corrosion Resistance in Simulated Physiological Environment

Electrochemical corrosion investigations are carried out at body temperature (37.5°C) in phosphate-buffered saline solution (PBS, pH $\approx$ 7.4), which closely mimics the mineral composition of the blood. The explored potential region (-0.5 to +1 V vs. SCE) is of interest when developing materials for implant applications [210]. Results are shown in Fig. 5.1 and electrochemical parameters are summarized in Table 5.1.

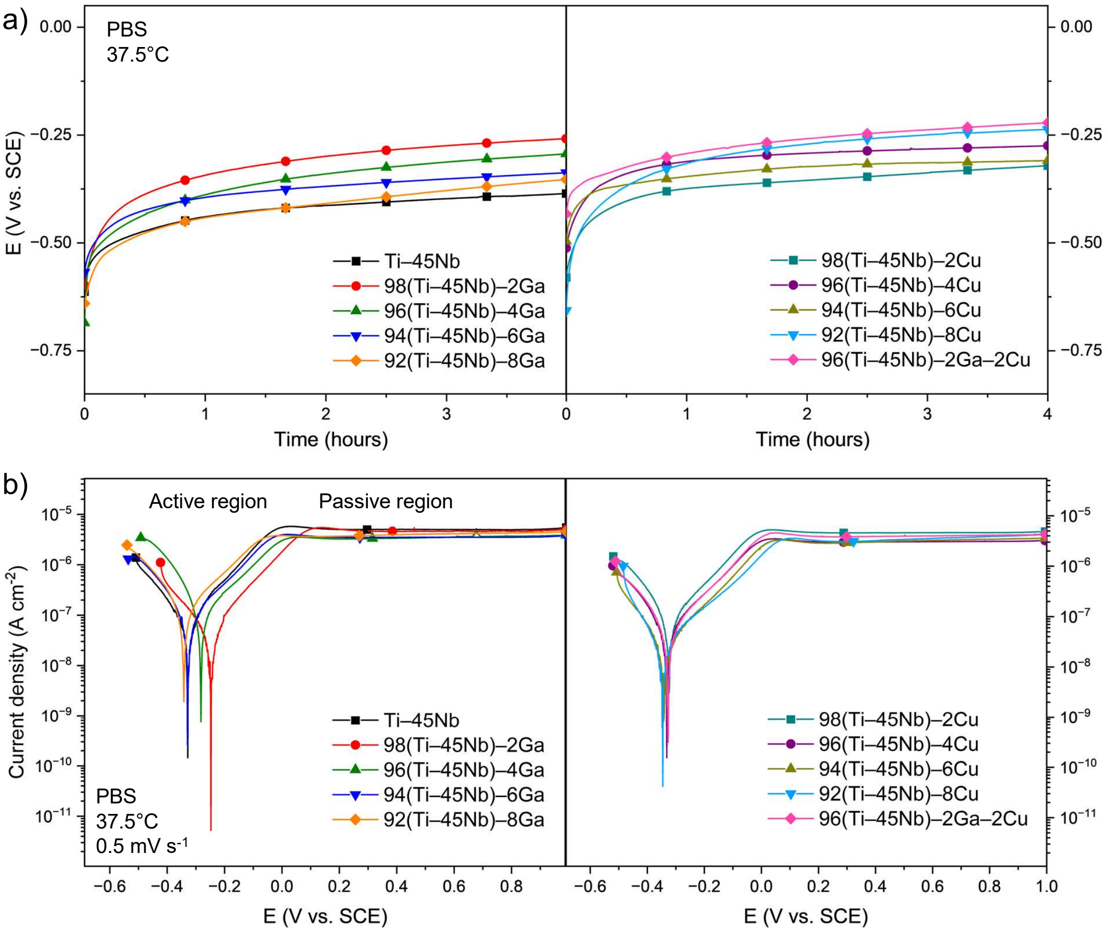

Figure 5.1: Corrosion tests in PBS solution at 37.5°C: (a) OCP during 4 h of immersion, and (b) potentiodynamic polarization curves recorded at a scan rate of 0.5 mV s^{-1} (adapted from Ref. [261]).

Fig. 5.1a shows the open circuit potential (OCP) curves over 4 hours of immersion time for the nine developed alloys, compared to Ti–45Nb. Initially, after mechanical grinding and upon immersion (t $\approx$ 0 s), potentials are in the range of approximately -750 – -400 mV vs. SCE, reflecting electrochemically active surfaces. All curves exhibit a potential increase with time, indicating the spontaneous formation of a protective oxide layer on the samples' surface. After approximately 45 minutes, the curves enter a stable regime, where potential variations are less than 1 mV/min, ending, after 4 hours, in the range of $E_{OCP} \approx$ -400 – -200 mV vs. SCE. It is very important to allow sufficient time for system's stabilization before starting any other electrochemical experiments. A stable E_{OCP} indicates that the system has reached a steady state, where involved electrochemical reactions have assumed a constant rate and net flowing current is zero. This method gives qualitative information regarding the state of the alloys, which are found to spontaneously passivate when immersed in the corrosive environment.

Table 5.1: Electrochemical parameters extrapolated from the corrosion tests: open circuit potential (E_{OCP}), corrosion potential (E_{corr}), corrosion current density (j_{corr}), and passive current density (j_{pass}) at +1 V vs. SCE.

Alloy	E_{OCP} (mV vs. SCE)	E_{corr} (mV vs. SCE)	j_{corr} (nA cm^{-2})	j_{pass} (μA cm^{-2})
Ti–45Nb	-346 ± 68	-348 ± 76	80 ± 20	5.9 ± 0.6
98(Ti–45Nb)–2Ga	-249 ± 54	-263 ± 48	73 ± 40	5.2 ± 0.6
96(Ti–45Nb)–4Ga	-342 ± 37	-360 ± 59	88 ± 24	4.4 ± 0.5
94(Ti–45Nb)–6Ga	-333 ± 71	-329 ± 76	90 ± 17	4.0 ± 0.6
92(Ti–45Nb)–8Ga	-338 ± 17	-335 ± 18	105 ± 15	4.2 ± 0.3
98(Ti–45Nb)–2Cu	-260 ± 60	-256 ± 65	106 ± 16	4.8 ± 0.2
96(Ti–45Nb)–4Cu	-307 ± 28	-312 ± 41	69 ± 16	4.5 ± 1.7
94(Ti–45Nb)–6Cu	-306 ± 9	-347 ± 11	29 ± 8	3.9 ± 0.5
92(Ti–45Nb)–8Cu	-244 ± 60	-305 ± 60	34 ± 10	4.3 ± 0.2
96(Ti–45Nb)–2Ga–2Cu	-286 ± 56	-305 ± 65	64 ± 13	4.8 ± 0.5

Potentiodynamic polarization tests (Fig. 5.1b) instantaneously follow the OCP measurements. Values of E_{corr} do not significantly differ from E_{OCP} (< 5%), indicating that the steady state was reached before starting the actual polarization tests. Electrochemical response of the nine alloys is remarkably comparable to that of the reference Ti–45Nb, when the limitations of the methods are taken into consideration. The alloys show very low corrosion current densities (j_{corr}), in the range 29 – 106 nA cm^{-2}. Albeit the increase of j_{corr} upon Ga addition, and decrease upon Cu addition, they are not significantly different. All curves transfer to a stable plateau at $\approx$ 0 V vs. SCE, referring to the passive regime, with no sign of pitting (i.e., localized corrosion). Passive current densities (j_{pass}) are also rather low, in the range 3.9 – 5.2 μA cm^{-2}. Upon Ga and/or Cu addition, j_{pass} decreases, suggesting a slight, but not significant, more reactive surface for the Ti–45Nb alloy. In conclusion, it is possible to state that the alloys exhibit great corrosion resistance in the explored experimental conditions.

These studies are fundamental to acquire knowledge on the general corrosion behavior of the alloys. Because of the slow corrosion processes taking place (i.e., high corrosion resistance and low dissolution), ion release studies, reported in the next section, were conducted on the two alloys containing the highest amount of Ga and/or Cu (8 wt.%).

5.3 Study of Ga/Cu Ion Release

Ion release studies by means of ICP-OES are performed in PBS solution at body temperature (37.5°C) with exposure time of 7 days on the following alloys: Ti–45Nb (reference), 92(Ti–45Nb)–8Ga and 92(Ti–45Nb)–8Cu. For investigating the bactericidal ion concentration released in solution, the alloys with the highest amount (8 wt.%) of Ga and Cu were selected. Results are reported in Fig. 5.2 and summarized in Table 5.2.

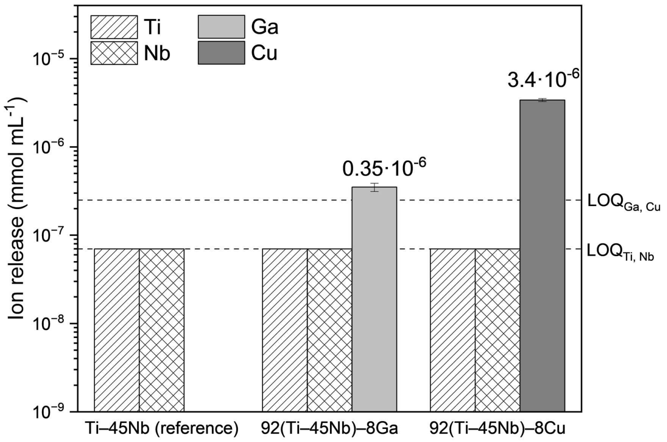

Figure 5.2: Metal ion release studies on alloys Cu 8 wt.% and Ga 8 wt.%, compared to Ti–45Nb, in PBS solution at 37.5°C after 7 days of immersion.

For all three alloys, the concentration of Ti and Nb ions remained below or near the experimental limit of quantification (LOQ), which is $7 \cdot 10^{-8}$ mmol mL^{-1} for both species. As a result, the LOQ value may be considered as a reasonable upper threshold level for the concentration of these ionic species. For 92(Ti–45Nb)–8Ga, a Ga concentration of $0.35 \cdot 10^{-6}$ mmol mL^{-1} (corresponding to 24 μg L^{-1}) was detected in solution, moderately above LOQ ($2.5 \cdot 10^{-7}$ mmol mL^{-1}). On the other hand, Cu amounts of $3.4 \cdot 10^{-6}$ mmol mL^{-1}(corresponding to 217 μg L^{-1}) were detected in solution released from 92(Ti–45Nb)–8Cu alloy, well above its LOQ ($2.5 \cdot 10^{-7}$ mmol mL^{-1}). The Cu amounts released are ten times higher than Ga, which is indicative of the high reactivity of Cu. The ICP-OES results suggest that the antibacterial mechanism via Ga ion release might not be effective in these β Ti–Nb, whereas, the higher released Cu amounts might suggest a more powerful antibacterial effect for the Cu-bearing Ti alloys.

Table 5.2: Amounts of Ga/Cu ions released from the alloys exposed to PBS solution at 37.5°C for 7 days, converted into various units for comparison purposes.

	Ga/Cu ion release		
Alloy	[mmol cm^{-2}] = [mmol mL^{-1}]	[μM]	[μg L^{-1}]
92(Ti–45Nb)–8Ga	$0.35 \pm 0.04 \cdot 10^{-6}$	0.35 ± 0.04	24 ± 3
92(Ti–45Nb)–8Cu	$3.41 \pm 0.13 \cdot 10^{-6}$	3.41 ± 0.13	217 ± 8

5.4 Discussion & Chapter Summary

Discussion

In the present chapter, the corrosion behavior of the novel Ti-based alloys by Ga and Cu minor additions is studied by conventional electrochemical methods and metal ion release in physiological conditions (PBS solution, 37.5°C).

Corrosion studies reveal that the corrosion resistance of the alloys is as high as for the reference Ti–45Nb alloy. In the explored experimental conditions, corrosion potentials E_{corr} of all nine alloys are around -300 (± 56) mV vs. SCE, and corrosion current densities j_{corr} are relatively low ($\cong$ 74 ± 20 nA cm^{-2}). Low j_{corr} indicates low charge transfer rates through the metal/fluid interface, which corroborates the observed minimal metal ions released under free exposure conditions. On the whole, the polarization behavior is similar to that of (Ti–40Nb)–4In alloy reported by Gebert et al. [63], where they observed j_{corr} of 0.1 – 0.2 μA cm^{-2}, and j_{pass} of 3 – 4 μA cm^{-2}. They concluded that the incorporation of minor amounts of indium (In), homogeneously dissolved in the β-matrix of Ti–40Nb alloy, does not yield any negative effect in terms of corrosion stability. This behavior can mainly be attributed to the strong passivating nature of valve metals Ti and Nb, which dominate and drive the whole electrochemical behavior, and to the fact that both Ga and Cu, the latter generally known to deteriorate corrosion properties, are in complete solid solution with Ti and Nb, thus preventing localized corrosion, as for example reported in multi-phase alloys [270]. In the passive regime up to +1 V vs. SCE, mainly a thermodynamically stable mixed Ti(IV)- and Nb(V)-oxide forms onto the anodically polarized alloys [271], which agrees with the traditional electrochemical equilibrium diagrams [27] of the pure alloying elements in water at RT, that spontaneously form a passive oxide layer at pH 7.4. Since the occurrence of Ga and Cu oxides cannot be completely ruled out, there are certain unanswered queries that necessitate additional research. Despite the high concentration of aggressive chloride ions in solution, coming from both NaCl and KCl for a total of 143 mM, the passive oxide films are stable and act as surface barriers, through which only a limited amount of metal ions can penetrate. In other words, no significant difference among the alloy systems could be ascertained, even though high amounts of Cu might have a deleterious effect on the corrosion resistance of Ti alloys [272]. Passive film studies (e.g. electrochemical impedance spectroscopy) could detect minor differences that are not visible in general corrosion assessment by the conventional techniques used in this work. According to the theory of passivity, metallic materials in aqueous electrolytes exhibit simultaneously active and passive surfaces, therefore a continuous process of partial dissolution and re-precipitation on the passive film occurs: if the dissolution rate is larger than the re-precipitation rate, then metal ions are gradually released [273], as observed in the present work.

The present studies, considered alongside previous literature, could offer guidance for future research aimed at accurately predicting the biological response and the antibacterial activity of the Ga-/Cu-bearing Ti alloys. Verron et al. [172] studied the effects of Ga ions on osteoblast-like cells and observed no cytotoxicity up to 100 μM, similar studies on human leukemic cells reported a threshold value (IC$_{50}$: minimal concentration required for 50% inhibition) of 80 μM [159]. These amounts are two orders of magnitude larger than those observed in the present work (< 0.5 μM), thus suggesting that the newly developed Ga-containing Ti alloys should be safe from a cytocompatibility point of view. Indeed, these results guided preliminary biological studies presented in Chapter 8. Regarding the antibacterial activity, Cochis et al. [200] showed that the presence of Ga, even in small amounts (1 – 2%), embedded in the metal matrix of Ti alloys might ensure a long-lasting antibacterial effect without any visible cytotoxic effect. For instance, the Ti alloys with Ga 1 – 2 wt.% decreased *S. aureus* biofilm activity by 50%, which is considered the minimal effective ratio to define a material as 'antibacterial' [200].

In the present work, the ion release studies were performed for the two Ti–Nb alloys with the highest amount of Ga/Cu (8 wt.%). The ICP-OES results (Table 5.2) showed low Ga release ($0.35 \cdot 10^{-6}$ mmol mL^{-1}) and Cu release ($3.41 \cdot 10^{-6}$ mmol mL^{-1}) after 7 days of immersion time in PBS solution at 37.5°C. This might suggest that Ga released is probably insufficient to exert antibacterial activity by ion release bacteria-killing mechanism. However, Cochis et al. [200] demonstrated that Ga-bearing Ti alloys can efficiently ensure long-lasting antibacterial effect by contact-killing mode (without being released), due to its ability to replace Fe(III) ion in the bacterial metabolism (so called 'Trojan horse' strategy, Ch. 2, Sec. 2.4). Additional research, including detailed microbiology tests, are necessary to elucidate the antibacterial capacity and mode of action of these Ga-bearing Ti alloys. According to relevant literature [154], both Ga and Cu are bacteria-killing elements, however the mechanism of action could be different: either by contact-killing or by ion release. The present results indicate that amounts of Cu ions released are ten times higher than Ga (Table 5.2), which might indicate a higher potential antibacterial activity by ion release bacteria-killing mechanism for the Cu-bearing alloy. It is widely believed that the antibacterial activity of Cu in Cu-modified alloys or surfaces is closely related to its amount: released Cu ions can inhibit and kill bacteria, but might also adversely affect cell growth and proliferation [274]. The balance between copper necessity and toxicity (for both bacteria and host cells) represents a serious challenge, since it is involved in many fundamental metabolic pathways, but it can also induce cellular toxicity via oxidative stress, DNA cleavage and more [178], therefore it is imperative to attentively evaluate Cu released from a biomaterial. Recent studies [96] aimed at evaluating the dose-response relationship of Cu ions and their biological effects *in vitro*. The authors reported an IC_{50} value as low as 0.7 μM for bone marrow mesenchymal stem cells, and an upper safe limit of 10 μM for osteoblasts, thus suggesting that Cu released (3.4 μM) from alloy Cu 8 wt.% in the present work might not pose a significant risk for cellular toxicity. Some preliminary biological and microbiological (bacterial) tests for the present alloys are planned in collaboration with our BIOREMIA EU project's colleagues from the University of Gothenburg (Sweden).

Chapter Summary

The corrosion behavior of the Ti–Nb–Ga/Cu alloys and their ion release were investigated by conventional electrochemical methods in simulated physiological conditions (PBS solution, 37.5°C). The following conclusions can be drawn:

- The nine studied alloys exhibit, in the explored conditions, high corrosion resistance, with no significance difference among alloys, low corrosion current densities ($<$ 106 nA cm^{-2}), and passive current densities in the range 3.9 – 5.2 μA cm^{-2}. Ga and/or Cu minor additions pose no deleterious effect to the corrosion resistance of Ti–45Nb alloy.
- The two alloys Ga 8 wt.% and Cu 8 wt.%, exposed to a simulated physiological environment for seven days, release 24 μg L^{-1} of Ga ions and 217 μg L^{-1} of Cu ions, respectively, thus indicating that Cu dissolves faster than Ga.

Altogether, the present results suggest that the studied alloys ensure high corrosion resistance with no risk for localized corrosion to occur in the body environment, due to the low alloying content of Ga and Cu. Comparing the Ga and Cu ion release capacity, one can suggest a potential antibacterial activity by Cu ion release bacteria-killing mechanism for the Cu-bearing alloy (with 8 wt.% Cu).

This chapter incorporates findings and insights from the following first-author original publications:

- **L.A. Alberta**, J. Vishnu., A. Hariharan., S. Pilz, A. Gebert, and M. Calin. *Novel low modulus beta-type Ti–Nb alloys by gallium and copper minor additions for antibacterial implant applications.* In: Journal of Materials Research and Technology, 20:3306–22 (2022). DOI: 10.1016/j.jmrt.2022.08.111
- **L.A. Alberta**, J. Vishnu., Y. Douest, K. Perrin, A.-M. Trunfio-Sfarghiu, N. Courtois, A. Gebert, B. Ter-Ovanessian, M. Calin. *Tribocorrosion behavior of β-type Ti–Nb–Ga alloys in a physiological solution.* In: Tribology International, 181:108325 (2023). DOI: 10.1016/j.triboint.2023.108325

Chapter 6

Assessment of Mechanically-Assisted Corrosion (Tribocorrosion) Behavior in Simulated Body Fluids

6.1 Chapter Overview & Aims

Implant materials are constantly exposed to severe tribological events in presence of highly corrosive electrolytes (e.g., body fluids), which lead to irreversible degradation of the implant with consequent failure. Predicting the synergistic mechanisms of corrosion and wear caused by specific combinations of materials, loads, and environments in tribocorrosion processes is challenging due to their complexity. Therefore, experimental studies are necessary.

In the present chapter, tribocorrosion mechanisms of the novel Ga-bearing Ti–Nb alloys, compared to Ti–45Nb and medical grade Ti–6Al–4V ELI, are investigated in simulated body fluids using a pin-on-disk tribometer integrated with an electrochemical setup. The following electrochemical techniques, in presence of sliding wear, were used: open circuit potential monitoring and potentiostatic polarization. The former simulates a real system, where corrosion processes are driven only by physiochemical properties of the environment and the tribological contact, while the latter allows real time measurement of depassivation and repassivation kinetics in presence of an applied potential. Afterwards, *ex situ* surface characterization techniques (e.g., electron microscopy, 3D profilometry), coupled with existing models, allowed determination of degradation mechanisms and quantification of wear. Moreover, the Ga ion content released during the tribocorrosion tests is also investigated. Assessment of tribological properties represents a further step towards potential application of the developed implant materials. Experimental studies hereby reported were mainly conducted during a secondment at INSA Lyon and Anthogyr S.A.S. (France).

6.2 Wear-Accelerated Corrosion at Open Circuit Potential

Tribocorrosion is the combined study of corrosion and wear phenomena occurring in sliding contacts. It is defined as the irreversible material degradation induced by simultaneous chemical, mechanical (wear), and electrochemical (corrosion) interactions occurring on surfaces in relative contact motion. Hence, a corrosive environment can amplify material's degradation by wear mechanisms as well as, inversely, wear can enhance the corrosion rate [275].

Valuable insights into the wear-corrosion behavior of the novel materials can be first acquired by monitoring the open circuit potential (OCP) under sliding conditions. The evolution of OCP of the four Ti–Nb–Ga alloys, together with Ti–45Nb and Ti–6Al–4V ELI alloys, sliding against an alumina pin under a normal load of 5 N in PBS solution, is monitored before, during and after sliding (Fig. 6.1a); electrochemical parameters are listed in Table 6.1.

Three distinct regions can be identified in Fig. 6.1a. In region I, up to 3600 seconds, the OCP potential has stabilized for all the alloys. Prior to the occurrence of sliding, measured OCPs for all alloys are stable, with nobler behavior for the four Ti–Nb–Ga alloys ($\cong$ -290 mV vs. Ag|AgCl). At 3600 s (region II), sliding starts under a nominal normal load of 5 N. All alloys exhibit an abrupt and substantial potential decrease, which is the typical tribocorrosion behavior of passive metals and alloys. This is caused by the mechanically-accelerated local breakdown of the passive film (depassivation process). This negative shift indicates the occurrence of local electrochemical activity, in which the fresh bare metallic surface is exposed to the corrosive chloride environment and begins to react. In general, tribological forces during sliding cause the breakdown of the passive layer on the real contact areas between the pin and the metallic sample. As a result, highly reactive regions in the wear track form, as compared to the surrounding region outside the wear area [276]. The sliding potential (E_{wear}) results from the galvanic coupling between the worn depassivated area (wear track), which acts as a local anode, and the surrounding large passive unworn area, which acts as a local cathode [277]. The lowest potential drop ($|\Delta E|$) at the onset of sliding is exhibited by Ti–6Al–4V ELI (420 ± 16 mV), on the other hand $|\Delta E|$ for the Ti–Nb alloys was comparatively higher; moreover, the curves of the former appear less noisy, especially in the first seconds after sliding started. The OCP curve of Ti–6Al–4V ELI changes from smooth to noisy after approximately 600 s, which may indicate that the surface is subjected to cyclic depassivation and repassivation. A very similar observation was made by Hacisalihoglu et al. [75] in α+β-Ti–6Al–4V alloy tested in SBF solution, where the OCP curve became very noisy after 600 s of sliding.

The curves of Ti–45Nb, 98(Ti–45Nb)–2Ga and 96(Ti–45Nb)–4Ga alloys exhibit a steady-state trend throughout the whole sliding, with potential oscillations in the range of $\cong$ 100 mV, indicating the establishment of a dynamic equilibrium between depassivation and repassivation mechanisms. The alloys with Ga content 6 and 8 wt.% show an increasing drift trend from the moment sliding started, which suggests tendency to spontaneously repassivate with Ga addition, even during mechanical

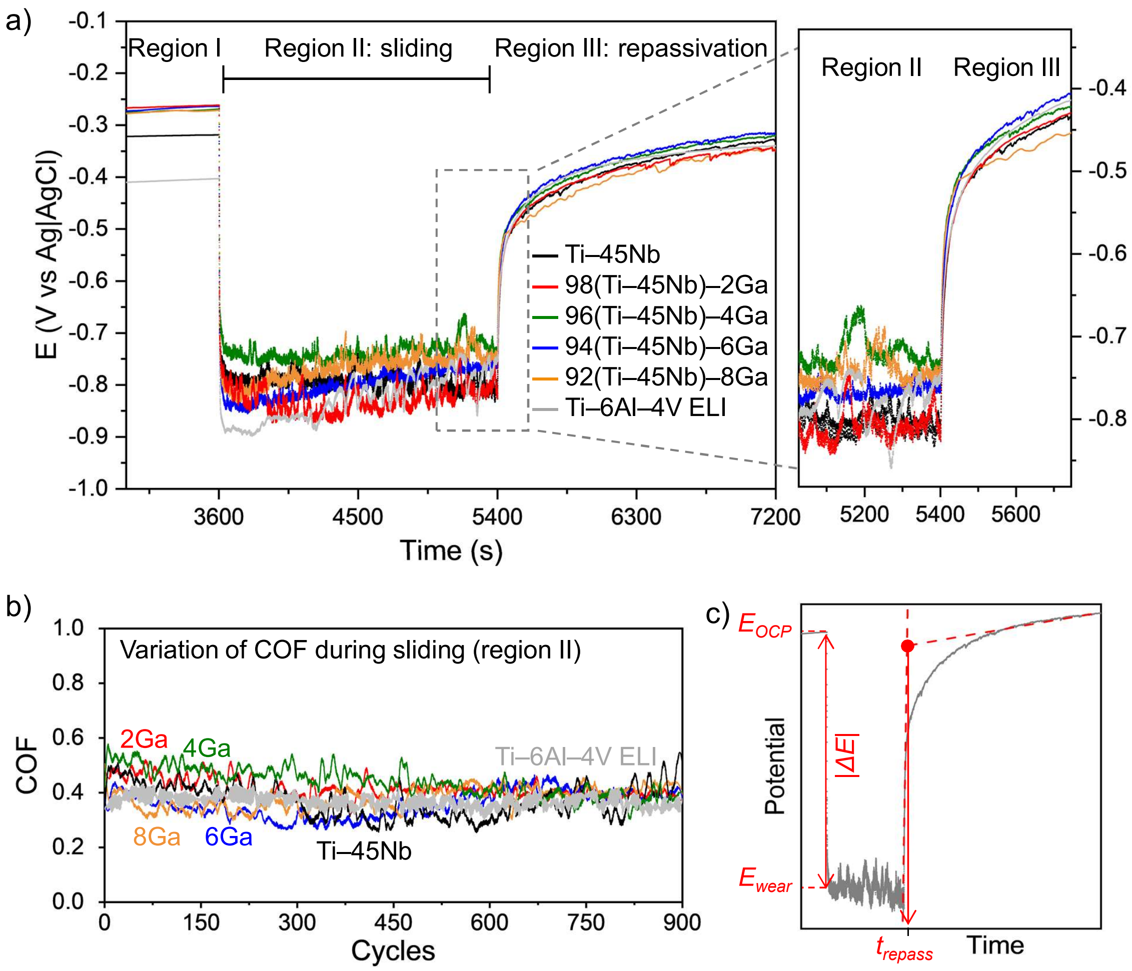

Figure 6.1: (a) OCP evolution over time before, during and after sliding of an alumina pin against the Ti alloys under a normal load of 5 N. (b) Evolution of friction coefficient (COF) during sliding (region II, 900 cycles correspond to 1800 seconds). (c) Schematic representation for the determination of the electrochemical parameters in Table 6.1: OCP before sliding (E_{OCP}), during sliding (E_{wear}), potential drop ($|\Delta E|$), and repassivation time constant (t_{repass}) (adapted from Ref. [278]).

degradation and with less extent of depassivation. At 5400 s (region III), sliding is stopped and the potential of all alloys steadily increases and stabilizes around ≅ -325 mV vs. Ag|AgCl after 1800 s, as a consequence of the reformation of the passive layer in the worn area. The post-sliding potentials could be attributed to wear debris covering the wear track and thickening of the passive film outside the wear track as a result of rapid mass transportation during sliding [279]. The potential restoration process provides important information on the alloy's ability to recover after wear. Repassivation time constants (t_{repass}), determined by graphical extrapolation (Fig. 6.1c), are listed in Table 6.1. From these results, it seems that Ga addition is beneficial to the repassivation kinetics, with t_{repass} values decreasing from 24.7 to 17.3 s with increasing Ga, while the commercial Ti–6Al–4V ELI alloy shows the slowest repassivation (t_{repass} = 27.9 s).

Table 6.1: Electrochemical parameters determined from the OCP curves shown in Fig. 6.1.

Alloy	Potential before sliding E_{OCP} (mV vs. Ag|AgCl)	Potential during sliding E_{wear} (mV vs. Ag|AgCl)	Potential drop $\|\Delta E\|$ (mV vs. Ag|AgCl)	Repassivation time constant t_{repass} (s)
Ti–45Nb	-298 ± 29	-764 ± 35	466 ± 64	24.1 ± 0.5
98(Ti–45Nb)–2Ga	-295 ± 32	-848 ± 28	554 ± 59	24.7 ± 0.9
96(Ti–45Nb)–4Ga	-267 ± 3	-736 ± 28	469 ± 31	20.3 ± 1.4
94(Ti–45Nb)–6Ga	-322 ± 81	-778 ± 28	456 ± 110	20.6 ± 0.8
92(Ti–45Nb)–8Ga	-286 ± 21	-791 ± 34	505 ± 55	17.3 ± 1.5
Ti–6Al–4V ELI	-406 ± 5	-826 ± 11	420 ± 16	27.9 ± 0.8

6.3 Electrochemically-Induced Corrosion During Sliding Wear

Potentiostatic polarization simulates the oxidizing action of a corrosive environment, in this particular case, an anodic potential of 0 V vs. final OCP was applied (Ch. 3, Sec. 3.5 for further details), after one hour of OCP stabilization. This methodology has been employed in order to achieve the same surface conditions surrounding the worn area for each independent test. Applied potentials for all tests are in the range -300 – -315 mV vs. Ag|AgCl. Results are shown in Fig. 6.2 and relevant electrochemical parameters are reported in Table 6.2. At the applied potential, the whole Ti-based surfaces are initially passive and the measured currents, before sliding, are below 10 nA. Once sliding started, the mechanical removal of the passive film causes a sharp increase in current. During the sliding period, the local worn area is forced to an anodic regime, while the surrounding unworn areas are forced to retain their OCP condition. A steady state average current is observed for the alloys throughout the sliding action (Fig. 6.2). However, significant differences are evident between the studied β-type Ti alloys and Ti–6Al–4V ELI. While the anodic current for the latter is in the range ≅ 2 – 50 μA, large oscillations up to 200 μA occur for the Ti–Nb-based alloys. At 2100 seconds sliding stops and current drops by almost two orders of magnitude, suggesting nearly instantaneous repassivation in the deteriorated area. The lowest average current after sliding (i_{final}), mainly flowing through the wear track, is recorded for Ti–6Al–4V ELI (0.06 ± 0.05 μA), the highest for Ti–45Nb (0.85 ± 0.63 μA), while the four Ti–Nb–Ga alloys exhibit intermediate values. With a maximum deviation from the average of 9%, the reproducibility of the current results was found to be satisfactory.

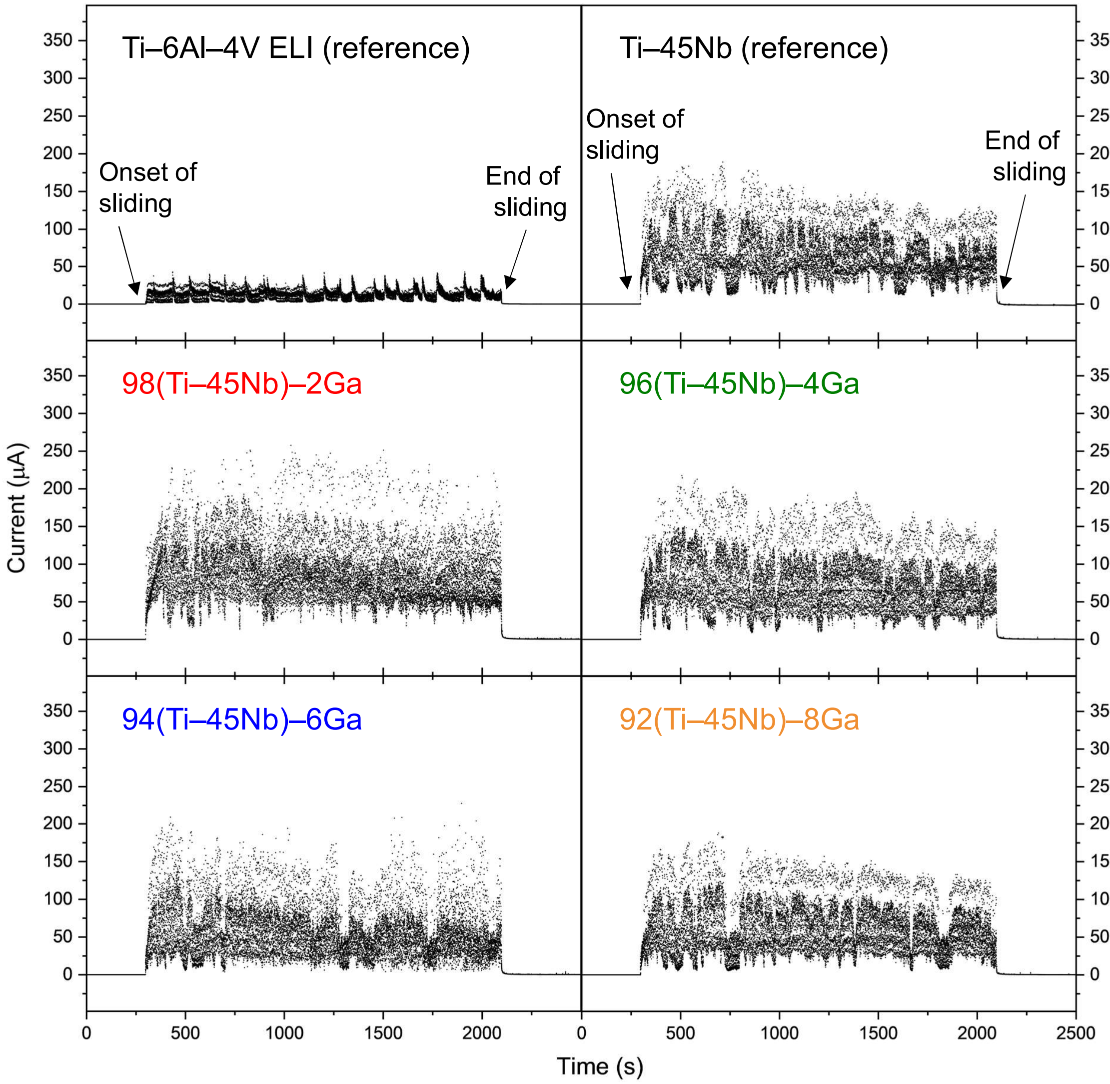

Figure 6.2: Current evolution at applied potential (0 V vs final OCP) over time before, during and after sliding (load 5 N) with an alumina pin against the investigated alloys and Ti–6Al–4V ELI.

Table 6.2: Electrochemical parameters determined from the potentiostatic curves of Fig. 6.2.

Alloy	Current during wear i_{wear} (μA)	Current after wear i_{final} (μA)
Ti–45Nb	65 ± 30	0.85 ± 0.63
98(Ti–45Nb)–2Ga	65 ± 32	0.42 ± 0.37
96(Ti–45Nb)–4Ga	75 ± 35	0.35 ± 0.16
94(Ti–45Nb)–6Ga	53 ± 32	0.23 ± 0.29
92(Ti–45Nb)–8Ga	61 ± 32	0.30 ± 0.19
Ti–6Al–4V ELI	13 ± 7	0.06 ± 0.05

6.4 *Ex Situ* Surface Analysis of Wear Tracks

Morphology and geometry (depth D, volume V_{tot}) of the wear tracks, investigated by 3D confocal profilometry (Fig. 6.3a-d) and SEM (Fig. 6.3e-p), provide insights into the underlying degradation mechanisms of wear and friction during sliding. Microstructural analyses were performed on the wear tracks of samples evaluated under OCP conditions, which were strategically selected to assess the effects of the corrosive environment in the presence of a tribological contact without the influence of any external potential. However, the computed geometric dimensions derived from samples submitted to the two types of electrochemical tests showed no significant difference.

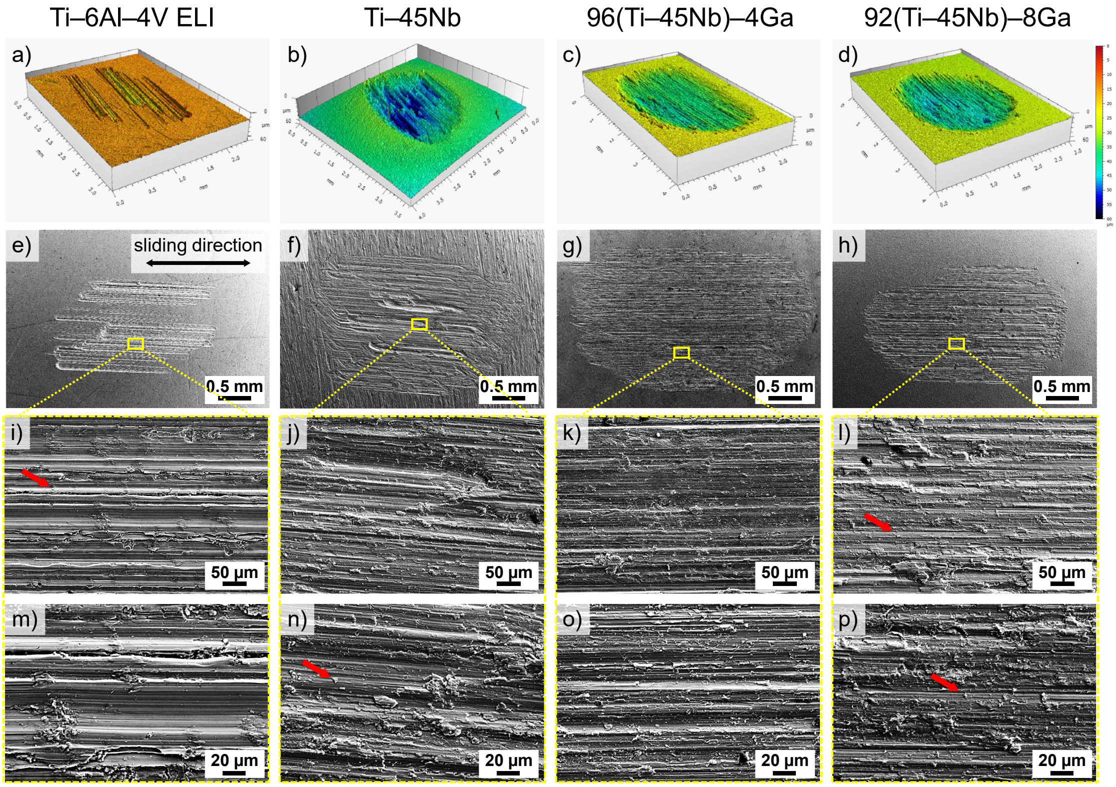

Figure 6.3: Morphological characteristics of the wear tracks caused on the Ti samples by sliding against the alumina pin at OCP conditions investigated by (a-d) 3D confocal profilometry and (e-p) SEM. Sliding direction, valid for images (e-p), is indicated by a double arrow in image (e) (adapted from Ref. [278]).

The results extracted from the sliding tests are presented in Table 6.3. Total wear volume (V_{tot}) and wear depth (D) were computed from the 3D optical profilometry measurements (Fig. 6.3a-d). It is evident how the Ti–Nb alloys have substantially different worn surfaces when compared to Ti–6Al–4V ELI. The latter shows very shallow scratches ($D = 4.05$ μm), while Ti–45Nb alloy exhibits the deepest wear track ($D = 10.16$ μm). D of the four Ti–Nb–Ga decreases with Ga content. Total wear volumes (V_{tot}) follow the same decreasing trend upon Ga addition. V_{tot} and D of 92(Ti–45Nb)–8Ga show a drastic decrease of 49% and 44%, respectively, compared to Ti–45Nb alloy. Computed geometric dimensions are observed to be similar to those reported by Feyzi et al. [72] for a Ti–6Al–4V alloy tested in PBS solution against a zirconia ball under 3.5 N and 6 N: they measured an average wear depth of $\cong 10$ μm by contact profilometry.

SEM micrographs of worn areas (Fig. 6.3e-p) confirm the features observed in the 3D profiles: visible grooves are evident along the sliding direction. Micrographs exhibit plowing grooves of varying width, depth and length running parallel to the sliding direction. Rubbing scratches deepen from the worn tracks' edge to their center. The reference Ti–45Nb and the Ti–Nb–Ga alloys show more pronounced abrasive wear, whereas the commercial Ti–6Al–4V ELI alloy (with good wear resistance) shows more superficial scratches. In all alloys, wear particles and debris are present around the edge of grooves as a consequence of severe deformation and tearing out (delamination). The extent of cutting abrasion is greater for the Ti–Nb-based alloys than for Ti–6Al–4V ELI. The former displays important amounts of wear debris (indicated by red arrows), indicating delamination wear mechanism, ranging between a few hundred nanometers to around five micrometers, the large particles appear to be agglomerations of finer debris (Fig. 6.3m-p). Wear debris may accumulate and act as third bodies that can exacerbate wear in simulated body fluid. No evidence of aggressive corrosion could be detected in any of the samples. After testing, no damage to the counter body alumina pin could be seen using optical microscopy (Appendix E, Fig. E1), but wear debris detached from the Ti samples and transferred to the pin could be observed, demonstrating adhesive wear. These findings suggest that the four (100-x)(Ti–45Nb)–xGa alloys possess wear resistance that lies between Ti–6Al–4V ELI and Ti–45Nb alloys, indicating that Ga addition is actually beneficial to improve wear resistance of the binary Ti–45Nb alloy.

6.5 Effect of Ga on Wear Resistance of Ti–45Nb

Evaluation of the friction coefficients (COF) allows for better understanding the wear behavior over time and under different load conditions of the implant materials, which are often subjected to repeated loading and unloading cycles, causing material loss and degradation.

The relationship between Ga addition and wear resistance of the alloys can be further understood by analyzing the variation of the friction coefficients during sliding. Representative COFs curves are shown in Fig. 6.1b and measured COF values are reported in Table 6.3. Values remained constant around the average with larger fluctuations for the four β-type Ti alloys compared to Ti–6Al–4V ELI. No significant difference was observed in the values of COF determined at OCP or under applied anodic potential. Similar conclusions were drawn by Feyzi et al. [72], who stated that COF is independent of the imposed potential. In contrast to Ti–6Al–4V ELI, COFs of the Ti–Nb-based alloys fluctuated more around the average. The oscillations in COF curves were greater for the β-Ti alloys compared to Ti–6Al–4V ELI, which is consistent with the changes in OCP previously shown.

Table 6.3: Summary of the results extracted from the sliding tests at OCP conditions. Total volume loss (V_{tot}) and wear depth (D), measured from 3D optical profilometry, are determined from wear tracks produced in independent sliding tests. Volume losses due to wear-accelerated corrosion (V_{wac}) and to mechanical wear (V_{mech}) are determined as previously described. Average V_{tot} is used for the determination of V_{mech}.

Alloy	Friction coefficient COF (dimensionless)	Depth D (μm)	Total volume loss V_{tot} (V_{wac}+ V_{mech}) (10^{-3} mm^3)	Volume loss due to wear-accelerated corrosion V_{wac} (10^{-3} mm^3)	Volume loss due to mechanical wear V_{mech} (10^{-3} mm^3)
Ti–45Nb	0.40 ± 0.02	10.16 ± 1.05	54.41 ± 3.72	2.81 ± 0.34	51.60 ± 3.38
98(Ti–45Nb)–2Ga	0.39 ± 0.02	8.93 ± 0.98	49.12 ± 2.09	3.56 ± 0.69	45.56 ± 1.41
96(Ti–45Nb)–4Ga	0.42 ± 0.03	8.60 ± 0.01	52.74 ± 2.44	3.22 ± 0.40	49.52 ± 2.84
94(Ti–45Nb)–6Ga	0.38 ± 0.01	7.77 ± 0.66	45.93 ± 2.15	2.96 ± 0.47	42.97 ± 2.62
92(Ti–45Nb)–8Ga	0.38 ± 0.02	5.71 ± 0.11	27.90 ± 3.98	2.33 ± 0.82	25.57 ± 3.17
Ti–6Al–4V ELI	0.40 ± 0.03	4.05 ± 0.84	10.41 ± 4.42	0.70 ± 0.09	9.71 ± 4.33

Table 6.3 contains relevant results necessary to evaluate and quantify wear: chemical (V_{wac}) and mechanical (V_{mech}) contribution to total wear volume (V_{tot}) are determined according to Eq. 3.6 – 3.8 (Ch. 3, Sec. 3.5), whereas V_{tot} and wear depth (D) are computed from 3D confocal profilometry. From the characteristic curves under applied anodic potential, it is possible to quantify wear-accelerated corrosion, and associated volume loss (V_{wac}). As it possible to infer from Table 6.3, V_{wac} accounts for approximately 6% of total wear volume (V_{tot}), while at OCP conditions, determined by the galvanic cell model (Ch. 3, Sec. 3.5, Eq. 3.8), V_{wac} is less than 3%. Guiñón Pina et al. [76] successfully applied these models to a series of β-type Ti–30Nb–(2–4)Sn alloys and concluded that wear-accelerated corrosion at applied anodic potential represents around 5% of total wear, while the contribution at OCP is less than 0.5%. In this work, Ti–6Al–4V ELI alloy has the lowest total volume loss (V_{tot}), whereas Ti–45Nb alloy shows the greatest, followed by the four Ti–Nb–Ga alloys. When Ga content is 8 wt.%, there is a significant decrease in V_{tot}. These results indicate that wear-accelerated corrosion (V_{wac}) only contributes in small amount to total wear, which is instead mostly controlled by the mechanical sliding action (V_{mech}). In conclusion, the Ga-containing alloys exhibit improved wear resistance due to Ga addition compared to the binary Ti–45Nb alloy, but slightly lower than that of the commercial Ti–6Al–4V ELI alloy.

6.6 Metal Ion Release During Tribocorrosion

A serious concern for implant applications is the release of metal ions, which can induce adverse biocompatibility issues (e.g., wear-induced aseptic loosening and osteolysis) [85]. For this purpose, the metal ion content released in the solutions after sliding tribocorrosion tests was measured by ICP-MS (secondment at INSA Lyon, France). Solutions derived from testing under OCP conditions (Sec. 6.2) were selected, as the tribocorrosion conditions are significantly affected by the application of a potential; in case of an anodic potential, metal ion release substantially increases [280]. Concentrations of all scanned elements, i.e., Ti, Nb, Ga, were within the cytotoxicity limits reported by many authors in fibroblasts and preosteoblasts progenitor cells [31, 200, 281]. Interestingly, an increasing amount of Ga^{3+} release with Ga content in the alloys tested in the same conditions was detected in the solutions. The released Ga amounts for the four Ti–Nb–Ga alloys are 1.33 (± 0.17), 1.69 (± 0.38), 3.41 (± 0.02) and 2.88 (± 0.04) ppb (or µg/L), for Ga 2, 4, 6 and 8 wt.%, respectively. The findings are consistent with the ion release studies in static conditions (Ch. 5, Sec. 5.3), where dissolution of the alloys immersed in a corrosive environment takes place very slow. Amounts of Ga ions released during sliding are significantly lower, up to approximately twenty times, than in static exposure to PBS solution.

6.7 Discussion & Chapter Summary

Discussion

Although Ti and its alloys have superior corrosion resistance, decreased Young's modulus and high specific strength, beneficial for load-bearing implant applications, their success rates are impeded by insufficient wear resistance [85]. Mechanically-assisted corrosion phenomena (i.e., tribocorrosion) severely impact the passive oxide film integrity, thereby increasing material degradation. Metal ions released during tribocorrosion can adversely affect the mechanical integrity as well as the biocompatibility of the implant [282]. Poor wear resistance causes the appearance of wear debris, the accumulation of which in periprosthetic tissues may result in osteolysis and aseptic loosening [85]. Wear particles released from Ti–6Al–4V alloy can induce the release of inflammatory mediators affecting the tissues surrounding the prosthesis, thereby causing osteolysis [283]. Corrosion behavior of β-Ti alloys is mainly controlled by the role of β-stabilizing elements, such as Nb, for which a beneficial effect on the passive oxide film has been reported [271]. However, in spite of the high corrosion resistance, β-type Ti alloys still have poor wear resistance compared to α+β Ti–6Al–4V alloy [284], which still represents a major limiting factor for their real use as biomedical implant materials. Thus, the present chapter evaluates the influence of Ga addition to the β-Ti–45Nb alloy on the tribocorrosion response and eventual Ga ion release associated with wear-accelerated corrosion.

The present results indicate that the tribocorrosion response of Ti–45Nb alloy is positively impacted by the addition of Ga. Repassivation time constants (t_{repass}) are lower when Ga content increases, indicating a faster transient to reach pre-sliding conditions (passive). The two alloys with Ga 6 and 8 wt.% show an increasing drift trend towards nobler potential during tribocorrosion (Fig. 6.1a), which suggests a pronounced repassivation state with less extent of depassivation, even during mechanical wear. Evidently, experiments with applied anodic potential reveal significant differences between the three Ti–Nb (β) alloys and Ti–6Al–4V ELI (α+β), with important current fluctuations for the former. Since pre-sliding current for all the alloys at the applied anodic potential is below 10 nA, it is presumed that during sliding, the 3-to-5 orders of magnitude greater wear current (i_{wear}) is mostly flowing through the worn areas. There is no significant difference in i_{wear} among the Ti–Nb alloys, and the influence of the chemical composition on the measured current is also not significant. The significantly lower i_{wear} of Ti–6Al–4V ELI alloy indicates slow anodic dissolution during sliding. The periodic film removal (depassivation) and formation (repassivation) keeps the current relatively high. The alloys display a behavior similar to that one of other passive systems: $\alpha+\beta$-Ti and β-Ti [75, 76], Co–Cr–Mo alloys [277], stainless steels [247, 285], Zr-based alloys [286].

The large fluctuations observed in the friction coefficients (COF) during sliding (Fig. 6.1b) for the β-Ti–Nb alloys are mainly attributed to the poorer wear resistance and lower microhardness than $\alpha+\beta$ Ti–6Al–4V ELI. The phenomena can also be ascribed to the significant quantity of wear debris generated during the sliding tests, especially for the Ti–Nb-based alloys, which serve as third bodies and promote wear and wear-accelerated corrosion. COFs in this work are comparable to those of similar alloys tested in similar conditions reported in the literature: Hacisalihoglu et al. [75] tested different Ti alloys, among which Ti–6Al–4V and Ti–45Nb, and observed COF values in the range 0.11 – 0.22, obtained using a ball-on-flat tribometer under an initial normal load of 2 N against an alumina ball (curvature radius 6 mm), which is less than half than the load applied in this work (5 N). They also observed considerable fluctuations of COF, which were mainly attributed to wear debris caused by rubbing. During tribocorrosion contribution analysis (Table 6.3), mechanical material loss (V_{mech}) is dominant for all tested alloys. In comparison, V_{mech} (and so amount of wear debris) of the β Ti–Nb alloys is higher than Ti–6Al–4V ELI. No significant difference among the Ti–Nb-based alloys could be observed in the computed volumes due to wear-accelerated corrosion (V_{wac}), suggesting a minimal effect of Ga on the overall electrochemical response, as concluded in Chapter 5. The total volumetric wear data (V_{tot}) and, therefore, mechanical wear contribution (V_{mech}) of the wear tracks, clearly show that the addition of Ga to Ti–45Nb alloy does increase its wear resistance. Archard's law [287] states that material loss is inversely proportional to the hardness of the material, which implies that materials with high hardness exhibit low volume loss. Because of the large differences in microhardness of the investigated alloys, experimental sliding data exhibit a strong correlation with Archard's law, as shown in Fig. 6.4.

The Ti–45Nb alloy has the highest volume loss, this is because it has the lowest microhardness (147 $HV_{0.1}$). On the other hand, Ti–6Al–4V ELI has the highest microhardness (354 $HV_{0.1}$) and the lowest volume loss. The four Ga-bearing alloys fall in between these two alloys. As the microhardness and Ga content of these alloys increase, their volume loss decreases. It is therefore possible to state that the wear resistance is mainly controlled by alloy composition and hardness, i.e., microstructural effects. The tribocorrosion studies of Cvijović-Alagić et al. [288] on Ti–6Al–4V ELI alloy, subjected to different thermal routes, confirm this aspect: total wear loss of a two-phase microstructure ($\alpha+\beta$) is almost twofold higher than, for example, a martensitic microstructure, because Ti martensites are relatively soft. Besides, in the present work, the microstructural analyses of the wear tracks (Fig. 6.3) provide strong support for the volumetric wear data. Oxidative wear consists of surface oxide islands which are periodically formed and mechanically removed,

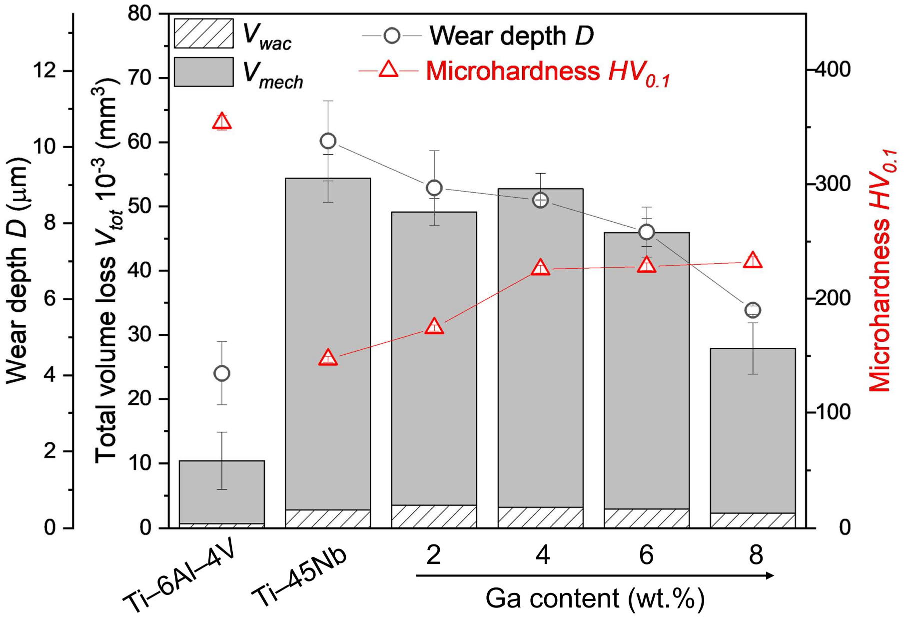

Figure 6.4: Variation of total volume loss (V_{tot}) with contributions of mechanical wear (V_{mech}) and wear-accelerated corrosion (V_{wac}), and wear depth (D) plotted versus microhardness ($HV_{0.1}$), for the four Ti–Nb–Ga alloys, together with Ti–45Nb and Ti–6Al–4V ELI reference alloys.

consequently, they are not protective, causing severe wear. In the current study, the alloys' surfaces are continuously in contact against the pin during the tribocorrosion tests. As a result, their wear resistance is impaired because they are unable to form a thicker protective oxide layer, this leads to overall wear loss being mostly controlled by hardness. Sub-surface strain deformation may also occur during sliding in the near-surface zone, which opens opportunities for further investigation. Wear-related processes are well described by Long and Rack [289] for a metastable β-type Ti–Nb alloy: the plastic deformation of the superficial layers underneath the wear track is related to the mechanisms of debris detachment. Altogether, these findings suggest that plastic deformation, abrasive wear, delamination wear, and adhesive wear are the primary causes of wear for the present alloys.

ICP-MS studies reveal the presence of Ga ions in the electrolyte solutions, suggesting minimal dissolution during tribocorrosion tests. Detected amounts are well below ($\approx$ 4 orders of magnitude) the limits reported by Chandler et al. [290], who proved no cytotoxicity on L929 mouse fibroblasts at Ga contents up to 1 mmol/L (70 mg/L). The very low amounts of Ga ions released ($<$ 4 ppb or μg L^{-1}) from the alloys can be attributed to their single-phase microstructure, i.e., solid solution. In this condition, elements are evenly distributed throughout the alloy matrix, which favors uniform corrosion over localized corrosion. The three elements Ti, Nb, and Ga all form stable and passive oxide coatings in the examined potential-pH range [27], which contribute to the low corrosion rates. Additionally, the presence of Ga can result in the creation of Ga–O–Ga bonds in the oxide layer, enhancing wear resistance and durability [281]. Further inquiries are needed for eventual real clinical applications for these alloys, among which *in vitro* tribo- and fretting corrosion in a more complex medium containing salts, organic molecules (e.g., proteins) and cells.

Chapter Summary

The present chapter aimed at enlightening the tribocorrosion behavior, in relation with microstructural features and mechanical properties, of the novel single-phase β Ga-bearing Ti–Nb alloys. Main conclusions are:

- The following wear mechanisms contribute to degradation of the alloys: plastic deformation, abrasive wear, delamination wear, and adhesive wear.
- Addition of Ga increases wear resistance of Ti–45Nb alloy. Such phenomenon was correlated to the increased microhardness observed upon Ga addition in the alloys. The lowest total volume loss V_{tot} was observed for Ti–6Al–4V ELI alloy, while Ti–45Nb alloy showed the highest. Ga addition up to 8 wt.% leads to a significant decrease in V_{tot}, thereby contributing to the improved wear resistance.
- Increasing, yet minimal, amounts of Ga ions with Ga content in the alloys are released during tribocorrosion.
- Among the investigated Ti–Nb–Ga alloys, the 92(Ti–45Nb)–8Ga alloy exhibits the greatest wear resistance, with spontaneous tendency towards repassivation even during mechanical degradation.

This chapter is based on the following first-author original publication:

- **L.A. Alberta**, J. Vishnu., Y. Douest, K. Perrin, A.-M. Trunfio-Sfarghiu, N. Courtois, A. Gebert, B. Ter-Ovanessian, M. Calin. *Tribocorrosion behavior of β-type Ti–Nb–Ga alloys in a physiological solution.* In: Tribology International, 181:108325 (2023). DOI: 10.1016/j.triboint.2023.108325

Chapter 7

Tailoring Antibacterial Microstructures by Aging Treatments

7.1 Chapter Overview & Aims

Strategic microstructural design allows for the optimization of mechanical and chemical biocompatibility, and the implementation of bio-activity against pathogens responsible for implant infections. Microstructural characteristics, in terms of type, distribution and size of different phases, significantly influence the antibacterial ability of Cu-containing Ti alloys. In this chapter, the Cu 4 wt.% alloy was subjected to controlled aging treatments to facilitate the formation of Ti_2Cu compound, which may improve the antibacterial properties of the alloys.

The present chapter focuses its attention on the feasibility of tailoring enhanced mechanical, chemical and potentially antibacterial properties by thermally induced precipitation. In Cu-containing Ti alloys, the form of Cu, i.e., incorporated in solid solution or in intermetallic compounds [197], defines the resulting antibacterial properties. Cu finds wide applications as antibacterial alloying element to Ti alloys, and its antibacterial activity is often correlated with the release of Cu ions [203]. However, achieving the minimum inhibitory concentration (MIC) of Cu required to inhibit bacteria growth through the release of Cu ions alone is not often possible [234, 291]. It was reported that MICs of Cu ions against *E. coli* and *S. aureus* are 256 and 448 μg mL^{-1}, respectively [292]; the concentration of ions released from a Ti–3Cu alloy after 24 h immersion in *S. aureus* suspension is 0.16 μg mL^{-1} [234], much lower than the MICs, therefore insufficient to provide antibacterial activity. Therefore, the precipitation of contact-killing Cu-containing phases (e.g., Ti_2Cu) has received significant attention as a potential antibacterial solution [194, 203, 204]. Heat treatments have a considerable impact on microstructure evolution, and so precipitation behavior, and they may be an efficient and feasible method for achieving enhanced mechanical properties (high strength and low modulus, in the case of implant alloys) and targeted antibacterial properties. Excessive Cu content (> 10 wt.%) in a Ti alloy can lead to material embrittlement and cytotoxicity, which are both undesirable effects [204]. Therefore, the amount of Cu must be carefully considered for microstructure optimization. For this study, the Ti–Nb-based alloy containing Cu 4 wt.% was selected for the studies reported in this chapter. The designated 96(Ti–45Nb)–4Cu was subjected to two different thermal routes (aging) and the impact of evolved microstructures on the mechanical performance and chemical behavior is presented and compared to as-cast (AC) and solution-treated (STQ) conditions.

7.2 Processing Routes and Thermal Stability of a β-Type Ti–Nb–Cu Alloy

Recent studies [218, 236] have demonstrated that the antibacterial characteristics of Cu-bearing Ti alloys may be tuned by altering the Cu content and thermal (aging) treatments, making optimization towards an antibacterial material attractive. In the previous chapters (Ch. 4, 5), the effect of Cu content on the microstructural characteristics, mechanical and chemical properties was investigated. In the present chapter, the effect of aging treatments on the resulting microstructure and properties of a selected Cu-containing alloy composition (96(Ti–45Nb)–4Cu) was studied. This alloy in homogenized (STQ) state shows a single BCC metastable β phase microstructure (Ch. 4, Sec. 4.2, Fig. 4.5), which can decompose upon heating.

Profound knowledge of an alloy thermal stability plays a central role in microstructure development for targeted properties. The β-type Ti alloys are characterized by high metastability and occurrence of several competing precipitation and decomposition reactions during heating. Thermal decomposition of the parent β phase implies various phase transformations in function of chemical composition (presence of α- or β-stabilizers), temperature (below or above β transus), holding time and cooling rates. These aspects regulate the very early phases of parent β phase decomposition and the subsequent nucleation of precipitated phases. In the specific case of Ti–Nb alloys, the aging process has been described as a competition between α phase and isothermal ω_{iso} phase precipitation [123]. The presence of the β-eutectoid stabilizer Cu in the system introduces further decomposition reactions, whose kinetics can be suppressed or induced by adjusting the cooling rate. Cu has a tendency to form intermetallic compounds with Ti, and Ti alloys with low Cu content generally exhibit α+Ti_2Cu microstructures [228, 254].

The thermal decomposition during heating into β-field of the Cu 4 wt.% alloy was investigated by differential scanning calorimetry (DSC). The selected thermal processing routes with two different aging temperatures (425°C and 640°C) are illustrated in Fig. 7.1a. Aging temperatures were chosen based on the isochronal DSC scan (Fig. 7.1b). Furnace cooling after aging was selected to induce precipitation and grain growth.

The alloy was studied in four conditions, that will be referred, from now on, as follows:

- 'AC' (as-cast);
- 'STQ' (solution-treated at 1000°C for 24 h and quenched, or homogenized);
- 'STQ & AG 425°C' (homogenized, and aged at 425°C for 8 h);
- 'STQ & AG 640°C' (homogenized, and aged at 640°C for 8 h).

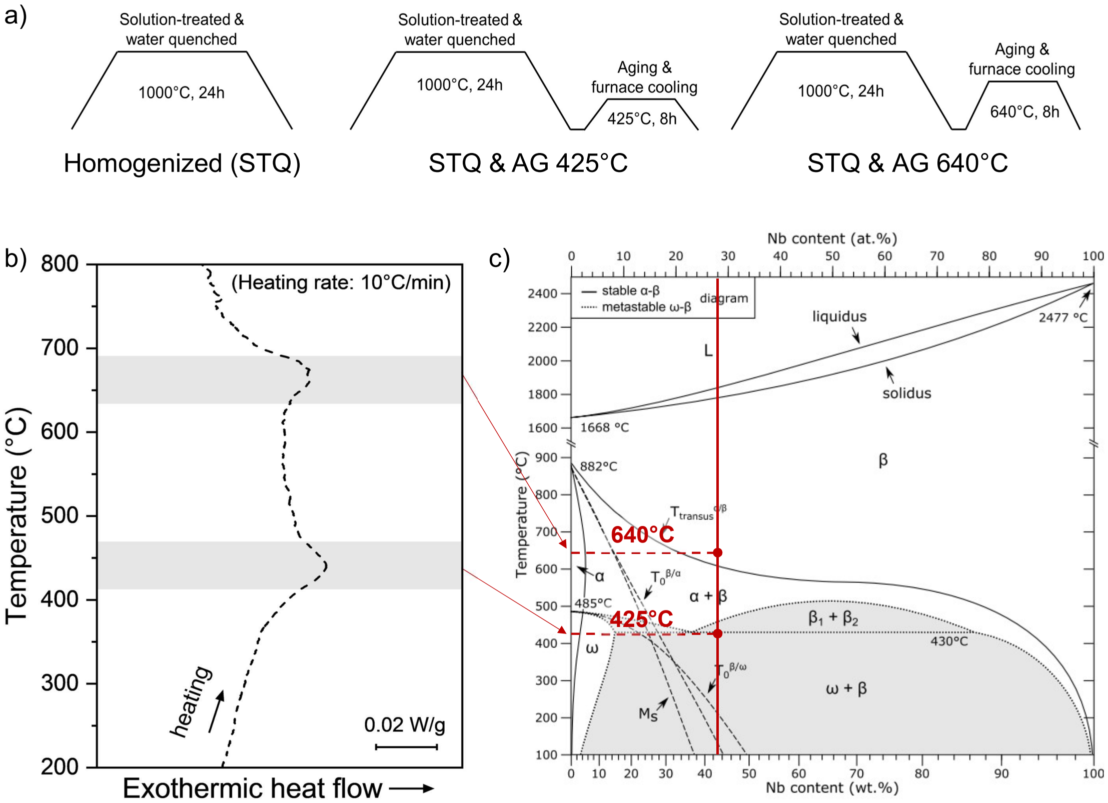

Figure 7.1: (a) Thermal processing routes and (b) heating DSC scan, collected with a heating rate of 10°C/min, of alloy 96(Ti–45Nb)–4Cu. Shaded areas show occurrence of exothermic reactions. (c) Ti–Nb phase diagram with selected aging temperatures.

The presence of two exothermal events in the DSC curve (shaded areas in Fig. 7.1b) indicates the occurrence of phase transformations. The first reaction is attributed to ω-phase precipitation, which occurs at 485°C, according to the metastable ω–β phase diagram of the Ti–Nb system (Fig. 7.1c) [119]. The second exothermic peak may be due to the eutectoid decomposition reaction β-Ti $\rightarrow$ α-Ti + Ti_2Cu, which occurs at around 656°C according to the computational thermodynamic modelling and experimental studies conducted on a series of Cu-bearing Ti–Nb–Ta–Zr alloys [212].

7.3 Decomposition of β-Phase During Aging

Microstructure and phase composition of the four alloys (AC, STQ, STQ & AG 425°C, STQ & AG 640°C) are investigated by SEM and X-ray diffraction (XRD). XRD diffractograms are reported in Fig. 7.2. For the AC and STQ samples, only sharp reflexes corresponding to the β phase (space group: $Im\bar{3}m$) were identified (Fig. 7.2a,b). After aging at 425°C, besides the high-intensity β-peaks, additional broad low-intensity reflexes appear, which are assigned to the diffraction of the ω phase (space group: $P6/mmm$), present in small amounts ($\approx$ 1.0 vol%) (Fig. 7.2c). This is in accordance with the observations of Pilz et al. [47], who studied the influence of isothermal ω_{iso} precipitation aging on the mechanical properties and deformation mechanisms of a β-type Ti–40Nb alloy. A further increase in aging temperature leads to dissolution of the ω phase, which takes place at around 485°C [119], and eutectoid decomposition of parent β phase into α phase (phase fraction: $\approx$ 3.4 vol.%, space group: $P6_3/mmc$) and tetragonal Ti_2Cu phase (phase fraction: $\approx$ 16.4 vol.%, space group: $I4/mmm$), indeed distinct peaks associated with these three phases could be indexed in its XRD pattern (Fig. 7.2d). Lattice parameters of the Ti_2Cu phase, calculated by Rietveld method, are $a = 2.944$ Å and $c = 10.783$ Å, in accordance with literature [228]. The presence of the precipitates in the β matrix leads to an increase of the BCC lattice parameters of the two aged conditions ($a_\beta{}^{\mathrm{STQ\ \&\ AG\ 425°C}} = 3.290$ Å, $a_\beta{}^{\mathrm{STQ\ \&\ AG\ 640°C}} = 3.298$ Å) compared to the STQ sample ($a_\beta{}^{\mathrm{STQ}} = 3.284$ Å).

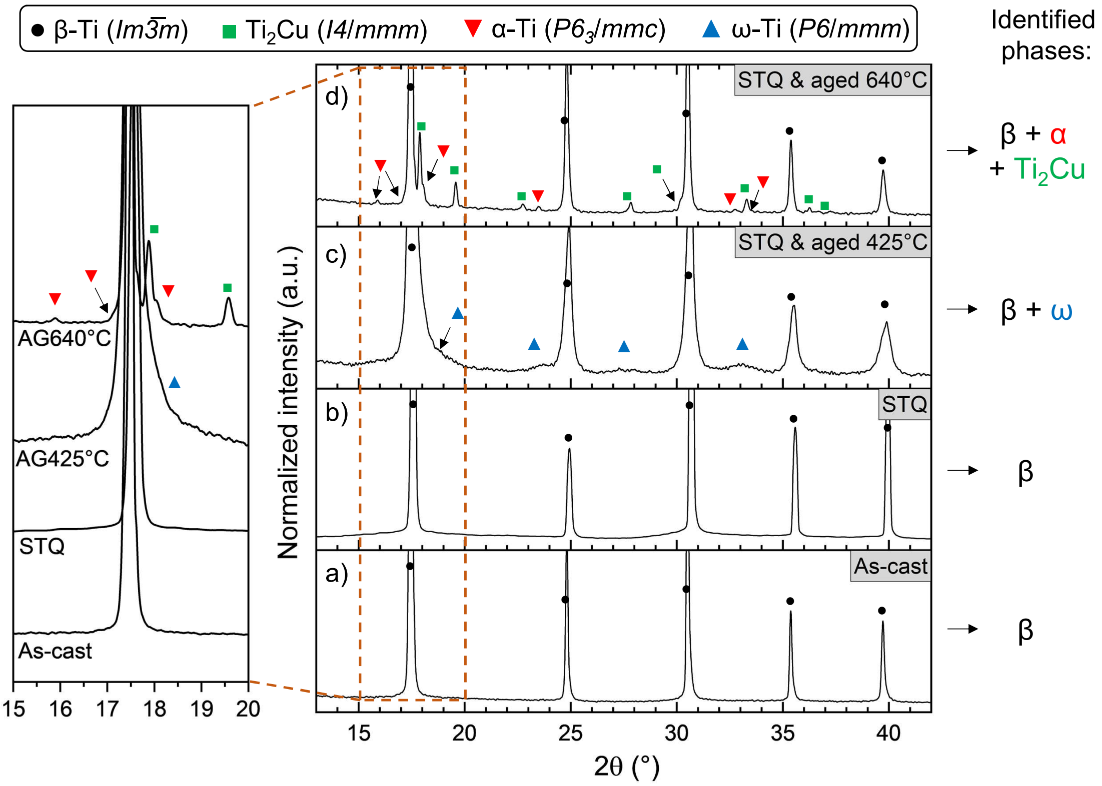

Figure 7.2: X-ray diffractograms (with identified phases), and magnification of 2θ region 15 – 20°, of 96(Ti–45Nb)–4Cu alloy in different conditions: (a) AC, (b) STQ, (c) STQ & AG 425°C, and (d) STQ & AG 640°C.

Microstructures investigated by SEM-EDX are shown in Fig. 7.3. The microstructure of the as-cast alloy consists of typical cast dendrites with Cu enriched in the Nb-lean interdendritic region, as it can be seen in the EDX mapping (Fig. 7.3b). Homogenization treatment (STQ) eliminates these chemical fluctuations, as previously demonstrated in Fig. 4.4 (Ch. 4, Sec. 4.2). EDX mappings at high magnification of the two aged alloys (Appendix F, Fig. F1) show homogeneous distribution of Ti, Nb, Cu, without any significant information with respect to the precipitates, due to their small size, below experimental detection limit. The microstructures of the homogenized (STQ) sample and the two aged alloys consist of coarse β grains, with average grain sizes d_{grain} decreasing from 323 μm to 207 μm and 127 μm for STQ, STQ & AG 425°C and STQ & AG 640°C, respectively. Investigation at high magnification (Fig. 7.3c) of the STQ & AG 640°C sample reveals the presence of finely dispersed elongated and acicular dark precipitates (Ti_2Cu), embedded in the β matrix (gray). The α phase precipitates could be in the nanoscale range, and therefore not visible by SEM, as reported for a similar β-type Ti alloy [293]. For the observation of both α and ω phases, TEM technique is required.

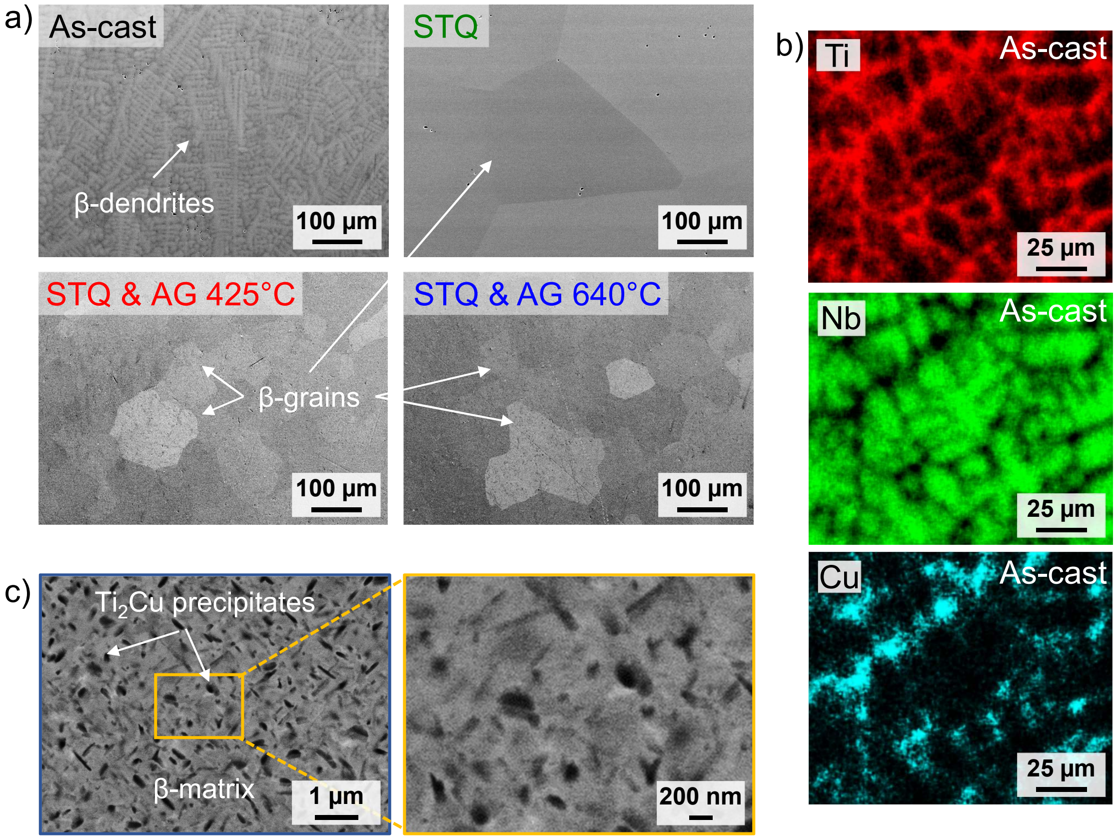

Figure 7.3: (a) SEM micrographs of 96(Ti–45Nb)–4Cu alloy in different conditions (AC, STQ, STQ & AG 425°C, and STQ & AG 640°C). (b) EDX mapping of the as-cast alloy showing elemental distribution of Ti, Nb and Cu. (c) High magnification SEM micrograph of the STQ & AG 640°C condition.

7.4 Evolution of Mechanical Properties During Aging Treatments

The mechanical properties of the aged samples were evaluated by microhardness, tensile tests and fracture analysis.

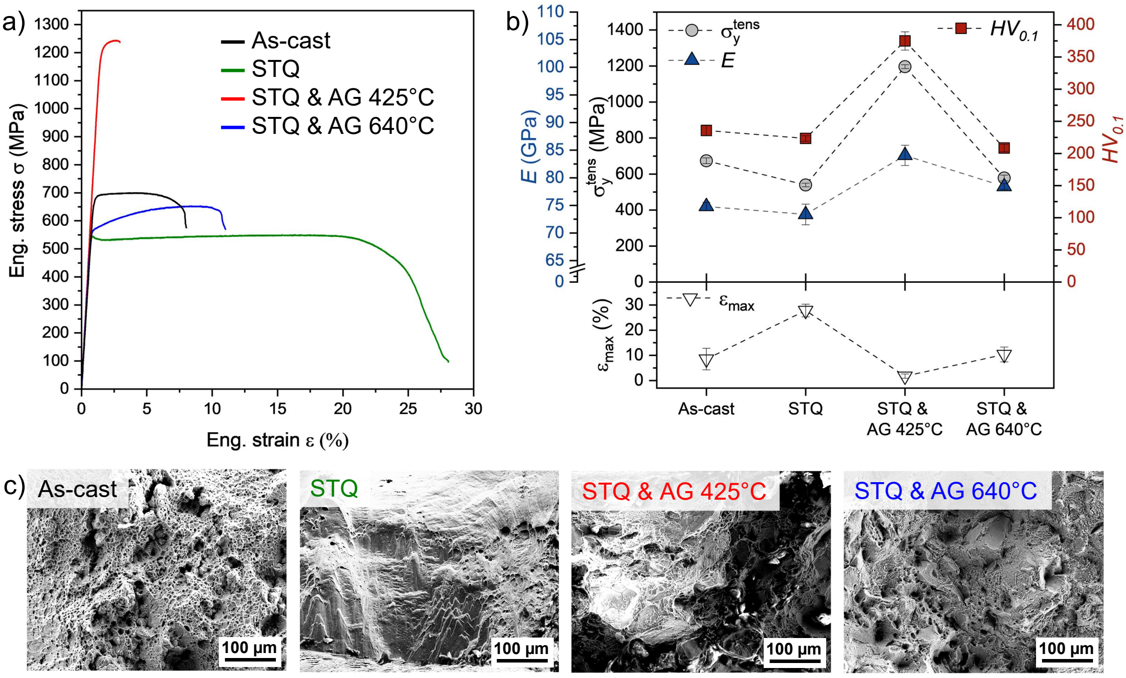

Figure 7.4: (a) Engineering tensile stress-strain curves of the four alloys. (b) Variation of Young's modulus E, yield strength $\sigma_y{}^{tens}$, fracture strain ε_{max}, determined from the tensile curves, and Vickers microhardness $HV_{0.1}$. (c) SEM micrographs of tensile fracture morphologies.

Engineering stress-strain curves in tension are presented in Fig. 7.4a, and resulting mechanical properties are showed in Fig. 7.4b and listed in Table 7.1, together with microhardness $HV_{0.1}$. The four alloy conditions exhibit significantly different behavior under tensile loading. The AC sample shows considerable yield strength ($\sigma_y{}^{tens} = 674$ MPa) and uniform elongation with limited strain hardening ($n = 0.04$), whereas the STQ sample shows the highest ductility ($\varepsilon_{max} = 28\%$) and lowest yield strength ($\sigma_y{}^{tens} = 539$ MPa). Isothermal aging at 425°C followed by furnace cooling leads to a very high $\sigma_y{}^{tens}$ value of 1196 MPa. The achievement of this high strength goes along with a drastic deterioration of ductility ($\varepsilon_{max} = 2\%$), the alloy fractures immediately after yielding, thus showing almost no plasticity. On the contrary, the sample aged at 640°C exhibits moderate yield strength ($\sigma_y{}^{tens} = 578$ MPa) and strain at fracture ($\varepsilon_{max} = 10\%$), and conspicuous strain hardening ($n = 0.11$). The four alloys display significantly different microhardness $HV_{0.1}$ (Fig. 7.4b). The highest value, exceeding 350 $HV_{0.1}$, is measured for STQ & AG 425°C, whereas the other three samples have microhardness in the range 208 – 236 $HV_{0.1}$, with an average increase of ≈ 34% compared to Ti–45Nb alloy. The Young's modulus E also varies, and it increases from 73 GPa (STQ) and 75 GPa (AC), to 78 GPa (STQ & AG 640°C), up to a maximum of 84 GPa (STQ & AG 425°C).

The plastic behavior of the alloys can impact its fracture surface characteristics, which can be evaluated through fractography to gain insight into the underlying failure mechanisms. Fig. 7.4c displays the fracture surfaces after tensile tests. Numerous micrometer-sized ($\varnothing \cong 5.3\ \mu$m) dimples are finely distributed in the surface of the AC alloy, whereas dual dimple size ($\varnothing \cong 0.65\ \mu$m, and $\varnothing \cong 9.7\ \mu$m) is present on the STQ & AG 640°C alloy. The STQ alloy exhibits largely elongated parabolic dimples along shear planes. Morphology of STQ & AG 425°C alloy shows relatively smooth areas. Dimple formation often implies ductile fracture, whereas smooth areas showing cleavage facets indicate brittle fracture [294]. Fractography results indicate that deformation of STQ sample is greater than that of the other samples, which is consistent with the large plastic strain of 28%.

Table 7.1: Mechanical properties determined from microhardness measurements and tensile tests.

Sample	$HV_{0.1}$	Tensile tests E (GPa)	$\sigma_y{}^{\text{tens}}$ (MPa)	σ_{UTS} (MPa)	σ_f (MPa)	$\varepsilon_{\max}$ (%)	δ_e (MJ m^{-3})
AC	236 ± 8	75 ± 1	674 ± 16	689 ± 23	560 ± 14	9 ± 4	3.70 ± 0.19
STQ	223 ± 4	73 ± 2	539 ± 10	544 ± 10	83 ± 19	28 ± 3	2.51 ± 0.05
STQ & AG 425°C	375 ± 14	84 ± 2	1196 ± 10	1223 ± 30	1207 ± 29	2 ± 1	9.74 ± 0.23
STQ & AG 640°C	208 ± 6	78 ± 1	578 ± 16	662 ± 23	575 ± 7	10 ± 3	2.71 ± 0.13

Investigation of elasticity is essential to ensure safe performance during service of an implant material, for which high strength and low elastic modulus are required, and that operates within the elastic limit. Elastic energy δ_e, calculated according to Eq. 3.4 (Ch. 3, Sec. 3.4), of the four alloys is presented in Table 7.1. Clearly, microstructural properties have a significant effect on the elastic energy variation. It is noted that the STQ & AG 425°C sample has the highest elastic energy (9.74 MJ m^{-3}), similar to 9.89 MJ m^{-3} reported for a β-type Ti–35Nb–7Zr–4Cu alloy [209]. However, this samples also shows the highest E (84 GPa), brittleness and almost no plasticity. On the other hand, the STQ & AG 640°C sample exhibits a good combination of mechanical characteristics: acceptable elastic energy (2.71 MJ m^{-3}), which is ≈ 7% higher than STQ alloy, and ≈ 30% higher than Ti–45Nb alloy (1.90 MJ m^{-3}), a low Young's modulus (78 GPa), and high strength (578 MPa), which is ≈ 7% higher than STQ sample and ≈ 27% higher than Ti–45Nb alloy (423 MPa), making it a promising candidate for load-bearing implant applications.

7.5 Influence of Microstructure on Corrosion & Cu Ion Release

The microstructure of the alloy, specifically the chemical nature and distribution of Cu, plays a significant role in determining the corrosion response. General corrosion assessment and ion release studies for the Cu 4 wt.% alloy in various conditions are conducted in PBS solution at 37.5°C.

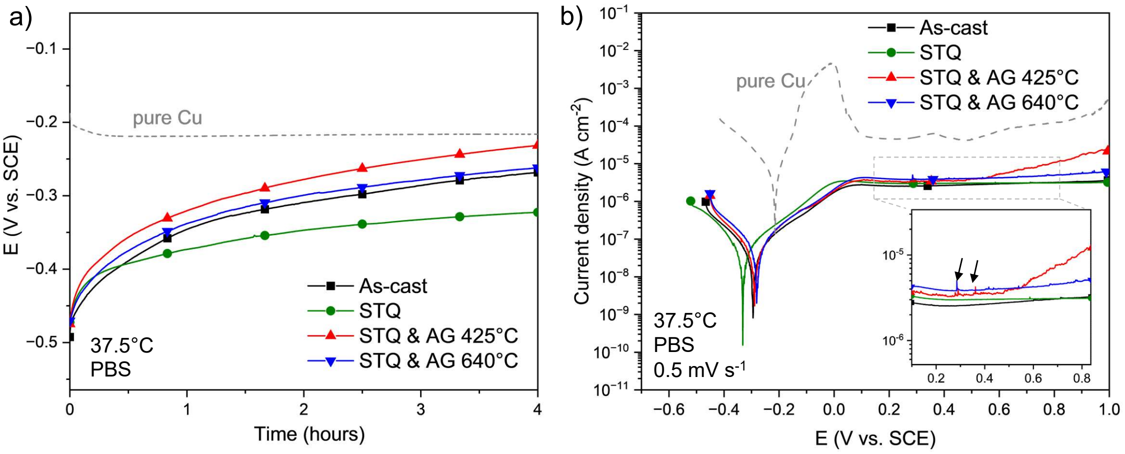

Figure 7.5: (a) Variation of open circuit potential (OCP) with time, and (b) potentiodynamic polarization curves recorded at a scan rate of 0.5 mV s^{-1} of the alloy Cu 4 wt.% in different conditions and a pure Cu electrode (for comparison purposes). All tests are conducted in PBS at 37.5°C.

Table 7.2: Electrochemical parameters extracted from the corrosion tests: open circuit potential (E_{OCP}), corrosion potential (E_{corr}), corrosion current density (j_{corr}), and passive current density determined at +0.4 ($j_{pass(+0.4\mathrm{V})}$) and +1 ($j_{pass(+1\mathrm{V})}$) V vs. SCE.

Alloy	E_{OCP} (mV vs. SCE)	E_{corr} (mV vs. SCE)	j_{corr} (nA cm^{-2})	$j_{pass(+0.4\mathrm{V})}$ (μA cm^{-2})	$j_{pass(+1\mathrm{V})}$ (μA cm^{-2})
AC	-249 ± 16	-275 ± 16	51 ± 3	3.23 ± 0.57	4.88 ± 1.30
STQ	-307 ± 28	-312 ± 41	69 ± 16	3.68 ± 0.75	4.55 ± 1.74
STQ & AG 425°C	-241 ± 12	-276 ± 20	59 ± 14	4.32 ± 0.82	38.07 ± 7.31
STQ & AG 640°C	-243 ± 24	-274 ± 23	95 ± 12	3.96 ± 0.05	5.74 ± 0.35

Corrosion tests are presented in Fig. 7.5 and the extracted electrochemical parameters are summarized in Table 7.2. Fig. 7.5a shows the variation of the open circuit potential (E_{OCP}) over a period of 4 h of the four alloy conditions, compared to a pure copper electrode. The curve of pure Cu exhibits a drop before stabilizing at -217 mV vs. SCE. The initial decrease is often attributed to the dissolution of the native oxide, formed upon exposure to the atmosphere; moreover, the shift to negative potentials signifies a very active surface [295]. On the other hand, E_{OCP} of the four samples increase to noble values, stabilizing at ≈ -260 mV vs. SCE, close to the pure Cu curve, with no significant differences within them.

Fig. 7.5b shows representative potentiodynamic polarization curves, after OCP stabilization, for the four samples and pure Cu (for comparison). Values of E_{corr} are similar to those of E_{OCP} with a difference of less than 9%, which shows that the steady state was reached prior to the initiation of the polarization tests. The polarization response of the four samples is similar among them, with j_{corr} below 100 nA cm^{-2}, which is approximately two orders of magnitude lower than j_{corr} (4290 nA cm^{-2}) for pure Cu, indicative of its high reactivity; the behavior of pure Cu in this work is comparable to that one investigated in chlorine media at pH 6.5, with similar Tafel-type active region and j_{corr} in the same order of magnitude [296]. In the case of the four Ti alloys, upon anodic polarization, a transition to a passive plateau, with j_{pass} of $\approx 4\ \mu$A cm^{-2}, takes place and remains stable up to +1 V vs. SCE, except for the STQ & AG 425°C sample, where j_{pass} starts to significantly increase up to 38 μA cm^{-2}. Spikes in the passive current, as indicated by arrows in inset of Fig. 7.5b, are visible in the two aged alloys, and can be attributed to the formation of metastable pits, or local oxidation of segregated phases. Overall, the displayed corrosion behavior is typical for valve metals, which spontaneously form barrier-type low conductive passive films, and it is indicative of their very high corrosion resistance when in contact with water-based solutions.

The Cu ion release study of the four Cu-bearing Ti alloys were performed over two weeks of immersion time in PBS solution at 37.5°C. Results are shown in Fig. 7.6 and summarized in Table 7.3. Testing procedure implies replacing the electrolyte solution with fresh one at each time point. This means that the exposure times to fresh PBS solution are 1, 24, 48, 96 and 168 hours (methodology in Ch. 3, Sec. 3.5).

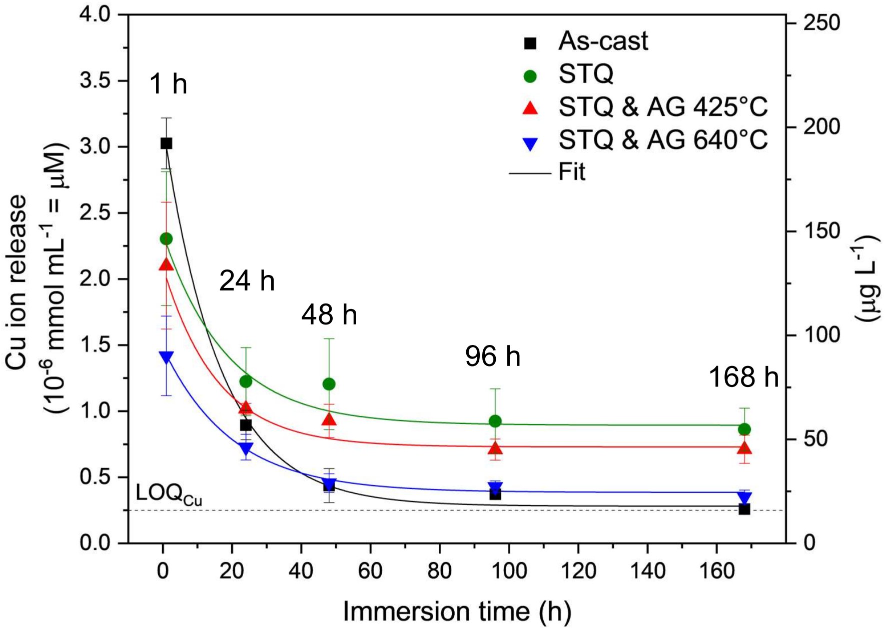

Figure 7.6: Concentration of Cu ions released (in 10^{-6} mmol mL^{-1}, μM or μg L^{-1}) from the alloys immersed for two weeks in PBS solution at 37.5°C.

Table 7.3: Results of Cu ion release studies of Fig. 7.6.

	Cu amounts [μg L^{-1}]				
Sample	1 h	24 h	48 h	96 h	168 h
AC	192 ± 12	57 ± 7	28 ± 8	24 ± 2	16 ± 1
STQ	146 ± 32	78 ± 16	77 ± 22	59 ± 16	55 ± 10
STQ & AG 425°C	133 ± 30	65 ± 3	59 ± 8	45 ± 5	45 ± 7
STQ & AG 640°C	90 ± 19	46 ± 6	29 ± 5	27 ± 3	22 ± 3

All four samples exhibit a burst release of Cu after 1 hour of immersion, which is indicative of the very high reactivity of the surfaces. The greatest amount of Cu release (192 μg L^{-1}) was recorded for the AC sample, while the STQ & AG 640°C sample showed the least release (90 μg L^{-1}), with a value almost half of the largest. Release of Cu exponentially decreases over time, and it starts to stabilize after 24 h of immersion up until 168 h with no significant difference among the four samples, which suggests a quasi-constant release with time, and therefore potentially long-lasting antibacterial activity.

7.6 Discussion & Chapter Summary

Discussion

The focus of the present chapter is on the impact of evolved microstructures on the mechanical performance and corrosion behavior of the designated alloy (96(Ti–45Nb)–4Cu), subjected to different thermal (aging) routes (homogenization followed by aging at 425°C or 640°C, for 8 h, and furnace cooled).

Investigations by X-ray diffraction (XRD) and electron microscopy (SEM) clearly show the evolution of the microstructures. The AC and STQ alloys consist both of a single-phase β (Fig. 7.2). Microstructures of similar as-cast and solution-treated Ti–Nb–Cu alloys, with Nb and Cu contents above 30 and around 4 wt.%, respectively, are also composed of a single-phase β, and exhibit equiaxed grains [210, 226]. This is attributed to the β-stabilizing effect of both Cu and Nb, that leads to a decrease of the α-β transformation temperature [261]. Isothermal holdings at 425°C and at 640°C followed by furnace cooling (i.e., aging treatments), lead first to ω phase precipitation, and then to the solid-state decomposition reaction of the parent β phase into secondary phases α and Ti_2Cu. In the recent work of Pilz et al. [47], the effect of aging heat treatments on resulting microstructures of a Ti–40Nb alloy was investigated by synchrotron XRD (SXRD). The phase composition of the Ti–40Nb alloy after recrystallization annealing consists of a single-phase β, as the diffractogram shows only reflexes corresponding to the β phase, however, after aging at 573 K for 1 h, an additional peak, associated with ω_{iso} phase, appears. With increasing aging time (up to 30 h), additional ω_{iso} reflexes become apparent, and no other peaks belonging to additional phases. Indeed, the single-phase β-type microstructure of the recrystallized state was also confirmed by TEM studies, whereas, after aging, TEM reveals the presence of fine ω_{iso} precipitates densely and homogeneously distributed in the β matrix. After an aging time of 30 h, the precipitates have dimensions below 15 nm, emphasizing the sluggish ω precipitation process due to low solute diffusion of Nb in Ti at high Nb content [119].

Microstructure significantly affects the mechanical response of the investigated alloys. The high microhardness ($HV_{0.1} = 375$) and tensile yield strength ($\sigma_{\mathrm{y}}{}^{\mathrm{tens}} = 1196$) of the β+ω sample could be due to precipitation hardening resulting from the resistance to movement of dislocations, due to the presence of a finely dispersed ω precipitate, as similarly shown by Pilz et al. [47] in an aged β-type Ti–40Nb alloy. However, TEM studies are needed to support this hypothesis. The remarkable yield strength, almost 1.2 GPa, is achieved at the expense of a limited ductility ($\varepsilon_{\max} = 2\%$), resulting in a more brittle material than the initial state (STQ). The three-phase aged alloy contains a relatively high volume fraction (16.4 vol.%) of Ti_2Cu phase. However, if compared to the STQ sample, it only leads to a mild increase in yield strength (${\sigma_y}^{\text{tens STQ \& AG 640°C}} = 578$ MPa, ${\sigma_y}^{\text{tens STQ}} = 539$ MPa) and strain hardening, with a slight decrease in microhardness (${HV_{0.1}}^{\text{STQ \& AG 640°C}} = 208$, ${HV_{0.1}}^{\text{STQ}} = 223$) and a significant reduction, nearly threefold, in ductility (${\varepsilon_{\max}}^{\text{STQ \& AG 640°C}} = 10\%$, ${\varepsilon_{\max}}^{\text{STQ}} = 28\%$). This modest precipitation hardening, together with reduced ductility and mild increase in strength, has also been observed in similar Ti–Nb–Cu alloys consisting of a β+Ti_2Cu+α microstructure, and it has been attributed to extensive precipitation of crystallized Ti_2Cu phase [226]. The STQ sample exhibits the highest ductility, because of the single-phase β microstructure. The AC condition, also consisting of a single-phase β microstructure, was expected to exhibit a similar degree of ductility. However, its lack of ductility prompted the hypothesis that some Ti_2Cu phase may be present in the alloy, perhaps in quantities below the XRD detection limit. This hypothesis is supported by the studies previously reported (Ch. 4, Sec. 4.2, Fig. 4.1), which reveal the presence of Ti_2Cu when Cu is 6 wt.% in AC state. Nevertheless, three of these alloys satisfy the requirements of elongation at fracture ($\geq 8\%$) for the manufacture of surgical implants according to international standards (ISO 5832–3:2021 [297]). Dimples, which are characteristic of ductile fracture, were observed on their fracture surfaces (Fig. 7.4c). Dimple size depends on the properties of the phases, relative strength between matrix and secondary particles, and bonding strength of the interface [226]. In the present work, dimple size well correlates with the increase in elongation ($\varepsilon_{\max}$, Table 7.1), in the order: 'STQ & AG 425°C' > 'AC' > 'STQ & AG 640°C' > 'STQ'. Regarding the Young's modulus (Table 7.1), determined from the linear elastic region of the tensile stress-strain curves (Fig. 7.4a), one can observe that E significantly increases for the STQ & AG 425°C alloy, whereas the STQ & AG 640°C sample exhibits a value of 78 GPa, comparable with the AC and STQ samples, and which is much lower than that of commercial medical Ti alloys.

Corrosion investigations were conducted in simulated physiological conditions and reveal high corrosion resistance for the four alloys. Their polarization curves (Fig. 7.5b) exhibit significant active-passive characteristics. In the cathodic zone, the current density decreases with applied potential, up to a minimum, which corresponds to the corrosion potential E_{corr}. As the potential increases further, current density increases, indicating the occurrence of oxidation reactions on the surface of the working electrode (i.e., studied alloy). Corrosion current densities (j_{corr}), determined by Tafel extrapolation, are low, in the same order of magnitude (< 100 nA cm^{-2}), and are similar to those determined for the other alloys developed in the present work (Ch. 5, Sec. 5.2, Table 5.1). The curves transfer to a stable plateau at ≈ 0 V vs. SCE, however, at $\approx +0.5$ V vs. SCE, the current density starts to significantly increase for one alloy (STQ & AG 425°C), the phenomenon is attributed to local dissolution of ω phase [298]. Passive current densities (j_{pass}) are low, and indicate the formation of a stable passive oxide film [63]. The corrosion resistance of Cu-bearing Ti alloys is reported to be largely influenced by the resulting microstructures, as the different phases have different corrosion potentials [299]. The presence of Ti_2Cu in the aged sample was expected to have a significant impact on the corrosion response of the alloys, but it did not. The corrosion mechanism of as cast binary Ti–(4,10)Cu (wt.%) alloys exhibiting α+Ti_2Cu microstructures was recently reported [300]. The authors acquired surface volt potential maps by Kelvin probe force microscopy (KPFM), and demonstrated that the Ti_2Cu has a more active potential than the α-Ti matrix. This suggests the formation of a significant number of micro-galvanic cells, where the α-Ti phase acts as local micro-anode and preferentially corrodes. However, this deleterious effect can be avoided or minimized in hypoeutectoid heat treated Ti–Cu alloys with Cu content below 5 wt.% [299]. In a similar manner, improved corrosion resistance was observed for a heat treated Ti-5Cu alloy consisting of α-Ti, Ti_2Cu and transformed β phases [221]. Many authors suggest that a uniform distribution of Ti_2Cu phase within the matrix provides a 'protective barrier', which minimizes local galvanic effects, therefore enhancing corrosion protection [65, 202, 299, 300]. On the other hand, galvanic couples cannot be minimized in non-homogeneous microstructures, resulting in deterioration of corrosion resistance [221].

These aspects also support the present ion release studies. Indeed, the lowest release is measured for the Ti_2Cu-containing microstructure, whereas the highest release occurred for the AC sample, due to the compositionally inhomogeneous microstructure with Cu segregation in the interdendritic regions (Fig. 7.3b). The amounts of Cu released are comparable with the 7-day exposure studies reported for 92(Ti–45Nb)–8Cu in STQ state (Ch. 5, Sec. 5.3). A direct relationship between Cu content in the alloy and Cu released could be established: the greater the amount of Cu in the alloy, the greater the amount of Cu that is released. The alloy Cu 4 wt.% (STQ) released 146 μg L^{-1} of Cu, whereas the alloy Cu 8 wt.% (STQ) released 217 μg L^{-1}. Interestingly, in view of the studies presented in this chapter, it is possible to confirm that the greatest burst release occurs in the first hour of exposure. The present results well correlate with the recent report of Ren et al. [301], aimed at evaluating the biosafety of Ti–6Al–4V–Cu and Ti–Cu alloys, both *in vitro* and *in vivo*. The results of their studies, among which ion release, indicate that the alloys meet the requirements of ISO standards. Amounts of Cu ion released range between $\approx$ 100 μg L^{-1} after 1 day and $\approx$ 400 μg L^{-1} after 30 days. The authors concluded that the alloys have satisfactory biocompatibility. Cumulative analysis of the present results indicate a maximum Cu release ranging between 215 – 414 μg L^{-1}, reinforcing the consistency of the present studies with those reported in previous literature. However, it should be noted that the biological response can be difficult to predict, and as such, experimental confirmation is necessary to fully establish their biocompatibility. In addition, the antibacterial properties of Ti_2Cu against relevant pathogens also requires additional experimental evaluation. It was demonstrated that heat treated Ti–(2.5–14)Cu alloys containing different morphologies (lamellar, granular) of Ti_2Cu precipitate exert powerful antibacterial activity against *S. aureus* [65]. The authors proposed a micro-galvanic corrosion model able to explain the different antibacterial behavior observed in the different Ti_2Cu morphologies, and concluded that the lamellar structure exhibits better performance, with antibacterial rates of 99.5% due to rapid release of Cu ions.

Chapter Summary

Different thermal treatments (aging) routes were implemented to evaluate the effects of evolved microstructures on mechanical biofunctionality and corrosion response of a β-type 96(Ti–45Nb)–4Cu alloy. The special focus was to facilitate, by controlled heating, the formation of a potentially bacteria-killing Ti_2Cu compound, and study the impact of the resulted Ti_2Cu-containing microstructure on the mechanical and corrosion properties. The main outcomes of the present chapter can be summarized as follows:

- Aging treatments, on the homogenized alloy, at 425°C or 640°C for 8 h and subsequent furnace cooling, lead to decomposition of the parent β phase into $\beta+\omega$ and $\beta+Ti_2Cu+\alpha$ microstructures, respectively.
- The $\beta+\omega$ alloy exhibits the highest yield strength ($\sigma_y{}^{tens} = 1196$ MPa) and microhardness ($HV_{0.1} = 375$), and reduced ductility ($\varepsilon_{max} = 2\%$). The Ti_2Cu-containing alloy exhibits a slight increase in strength ($\sigma_y{}^{tens} = 578$ MPa) compared to the STQ ($\sigma_y{}^{tens} = 539$ MPa) sample, and a significant reduction in ductility ($\varepsilon_{max} = 10\%$), which still meets ISO requirements for the manufacture of surgical implants. Strengthening effects are mainly attributed to precipitation hardening.
- The Young's modulus of the two aged alloys is 78 and 84 GPa, which is low if compared to medical alloys currently in use.
- General corrosion response in simulated physiological conditions is not significantly affected by the presence of the precipitates, with $E_{corr} \cong -240$ mV vs. SCE and $j_{corr} < 100$ nA cm^{-2}. The aged samples exhibit high corrosion resistance in the explored simulated physiological environment.
- Cu ions release studies over two weeks reveal a burst release in the first hour and then a constant release of ≈ 46 μg L^{-1} over time. The AC sample released the greatest amount of Cu because of Cu-segregated dendrites, whereas the lowest release was observed for the Ti_2Cu-containing microstructure, which might ensure a long-lasting antibacterial activity by contact-killing mechanism.

In conclusion, the promising combination of microstructure, mechanical and corrosion characteristics found in the Ti_2Cu-bearing alloy highlights the potential of strategic microstructural design. Nevertheless, evaluation of the biological safety and antibacterial properties of this alloy are necessary in determining its potential for practical medical applications.

Chapter 8

Conclusions & Future Perspectives

The rising incidence of bacterial infections and the inadequate mechanical biocompatibility of today's load-bearing implant materials constitute real challenges for the scientific community. Public health is seriously endangered if these challenges are not properly addressed and resolved. Therefore, in recent years, there has been increasing research attention towards developing materials that render the surface of implants resistant to bacterial biofilm contamination to reduce the infection risk, and thus to ultimately improve the overall quality of life of patients with implanted medical devices.

The main objective of the present work was to develop and characterize novel Ti-based alloys with low modulus and potential antibacterial properties for bone-related implant applications. The alloy design research strategy has taken into consideration the following aspects:

(i) the elastic (Young's) modulus of Ti alloys can be significantly reduced by formation of a single-phase β (BCC) microstructure, by carefully adjusting the content of biocompatible β-stabilizing alloying additions;

(ii) the antibacterial properties can be induced by incorporating bactericidal alloying elements in the alloy composition.

The starting composition was Ti–45Nb (wt.%) alloy with a single-phase β microstructure and low Young's modulus. Minor amounts of the antibacterial elements Ga and/or Cu were systematically added to it to produce, by controlled casting, nine alloys with the following chemical compositions (wt.%): (100-x)(Ti–45Nb)–xGa, (100-x)(Ti–45Nb)–xCu (where x = 2, 4, 6, 8 wt.%), and 96(Ti–45Nb)–2Ga–2Cu. The main goal of the thesis was to investigate the effect of antibacterial additions and processing conditions on the structural, mechanical and chemical properties of the Ti–Nb alloys. This fundamental study aims to contribute to the understanding of these materials, and to facilitate their future use as antibacterial biomaterials. The main conclusions are presented below and possible directions for future lines of research are suggested.

Conclusions

Nine Ti–45Nb-based alloys containing Ga and/or Cu (up to 8 wt.%) were produced by arc-melting and cold-crucible casting. Subsequently, the alloys were homogenized by a solid solution treatment for 24 h at 1000°C (β phase field) and rapidly cooled to RT by quenching into water (STQ treatment).

The conclusions of the present thesis are grouped as follows:

(A) impact of antibacterial alloying additions Ga and Cu on microstructural, mechanical, corrosion, tribocorrosion, and ion release properties (Chapters 4–6),

(B) effect of aging thermal treatments on microstructural, mechanical, corrosion, and ion release properties of one selected Cu-bearing alloy (Chapter 7).

(A) The main outcomes of the studies aimed at exploring the **effect of Ga and Cu additions** on various alloys' properties are summarized below.

- **Alloy design** tools (e/a, $[\mathrm{Mo}]_{\mathrm{eq}}$) were used to select alloys' compositions to retain a β phase upon quenching. The nine developed alloys can be classified as metastable-β and near-β alloys.
- **Microstructural investigations**, based on X-ray diffraction (XRD) analyses, reveal that the β-isomorphous stabilizing effect of Nb prevails over the α-stabilizing effect of Ga and β-eutectoid effect of Cu, therefore leading to single-phase β (BCC) microstructures for all homogenized alloys. Rietveld refinements of diffraction patterns indicate that the cubic lattice parameters a_β are sensitive to the content of both Ga and Cu. This aspect results in an almost linear contraction of the BCC lattice upon their addition, which was correlated with the improvement of the mechanical properties. Electron microscopy (SEM) studies reveal homogeneous microstructures consisting of coarse equiaxed β-grains. The addition of Ga introduces a significant grain refinement effect.
- **Mechanical characteristics**, investigated by microhardness, ultrasonic, tensile and compression tests, reveal a general strengthening effect, mainly attributed to substitutional solid solution strengthening, and to grain boundary strengthening in the case of the Ga-bearing alloys. The manufacture of surgical implants strictly adheres to international standards. In view of this, all the nine homogenized alloys meet strength ($\sigma_{\mathrm{y}} \geq 520$ MPa) and elongation requirements ($\varepsilon_{\max} \geq 8\%$) according to ISO 5832–2:2018 [302], thus making them suitable for the intended application. The studied alloys display significant plasticity and ductility in both tension and compression. The main advantage of the present alloys is represented by their low Young's modulus E, which is up to 40% lower than that of the commercial medical alloy Ti–6Al–4V ELI (E = 111 GPa), thus contributing to reduce the stress-shielding phenomenon. More specifically, Young's modulus values are 64 – 79 GPa for the four Ga-bearing Ti alloys, 76 – 104 GPa for the four Cu-bearing Ti alloys, and 75 GPa for the 2Ga–2Cu alloy.

- **Phase stability and deformation behavior** were investigated using complementary methods: compression testing, EBSD analysis and X-ray diffraction. The β phase of all nine homogenized alloys is relatively stable towards high compressive strains, with no sign of stress-induced phases, therefore suggesting dislocation slip as dominant deformation mechanism.
- **Corrosion behavior** in a simulated physiological environment (PBS solution at 37.5°C) is studied by OCP monitoring and potentiodynamic polarization tests. The results indicate that the homogenized alloys ensure high corrosion resistance in the body environment, mitigating the risk of localized corrosion, which might lead to the release of ions, and thus minimizing any adverse effects on the surrounding biological environment. This is attributed to their low alloying content of Ga and Cu, as evidenced by the low corrosion current densities ($j_{corr} < 106$ nA cm^{-2}) and passive current densities ($j_{pass} < 5.2$ μA cm^{-2}), comparable to the reference Ti–45Nb alloy.
- **Tribocorrosion properties** of the four Ti–Nb–Ga alloys in PBS solution were studied by a combination of electrochemical methods (OCP monitoring, potentiostatic tests) while sliding against an alumina pin, and *ex situ* surface investigations by 3D confocal microscopy and electron microscopy (SEM). The results indicate that the addition of Ga to Ti–45Nb alloys improves its wear resistance in the corrosive environment, as indicated by the significant decrease of total volume loss (V_{tot}), which was correlated to the increased microhardness, in accordance with Archard's law. The presence of Ga also increases repassivation kinetics compared to Ti–6Al–4V ELI, indicating that the Ga-bearing alloys possess a spontaneous tendency to repassivate even during mechanical degradation. Microstructural *ex situ* investigations revealed the prevalent tribocorrosion mechanisms: plastic deformation, abrasive wear, delamination wear, and adhesive wear. Amounts of Ga ions (< 4 ppb) released during the tribocorrosion tests, investigated by ICP-MS, suggest minimal dissolution during sliding tests and are well below (≈ 4 orders of magnitude) cytotoxicity limits reported in the literature.
- **Metal ions release** studies were conducted by exposing the two homogenized alloys with the highest amount of Ga/Cu (8 wt.%) to a corrosive environment (PBS solution at 37.5°C) for 7 days. The two alloys release 24 μg L^{-1} of Ga ions and 217 μg L^{-1} of Cu ions, respectively, indicating an ion release for Cu greater than Ga. Overall, the amounts released are considered to be within the cytotoxicity limits. The low release, and so low dissolution rate, is mainly attributed to the alloys' single-phase microstructure, i.e., solid solution. Cu ions are released from the alloys in higher amounts than Ga ions, thereby suggesting a more powerful potential antibacterial activity by Cu ion release bacteria-killing mechanism for the Cu-bearing alloy.

(B) **Aging thermal treatments** on a selected Ti–Nb–Cu alloy composition (Cu 4 wt.%) were conducted to study the impact of evolved microstructures on various properties, with the final aim of tailoring potentially antibacterial microstructures. The two aged alloys are compared to the initial states (as-cast, STQ). Main findings are:

- Homogenization followed by two isothermal holdings (aging) below β-transus (425°C or 640°C for 8 h followed by furnace cooling) lead to the decomposition of the β phase into two **microstructures** consisting of β+ω (STQ & AG 425°C) and β+Ti_2Cu+α (STQ & AG 640°C) phases.
- **Mechanical properties** are significantly affected by the aging treatments, when compared to as-cast and STQ conditions. The two aged alloys exhibit, when compared to the initial state (STQ), a substantial increase in yield strength (σ_{y} = 1196, 578 MPa) and microhardness ($HV_{0.1}$ = 375, 208) for STQ & AG 425°C and STQ & AG 640°C alloys, respectively. The increase in strength comes at the expenses of ductility, with fracture strains $\varepsilon_{\mathrm{max}}$ of 2% and 10%, for STQ & AG 425°C and STQ & AG 640°C, respectively. Strengthening effects are mainly attributed to precipitation hardening. The Young's modulus ($E^{\mathrm{STQ\ \&\ AG\ 640°C}} = 84$ GPa, $E^{\mathrm{STQ\ \&\ AG\ 640°C}} = 78$ GPa) of the two aged alloys, despite the increase ($E^{\mathrm{STQ}} = 73$ GPa), remains low if compared to clinical alloys, and therefore mechanically biocompatible.
- **Corrosion response** of the two aged alloys in simulated physiological conditions is not significantly altered by the presence of the precipitates, thus suggesting high corrosion resistance in the explored conditions. During anodic polarization, in the passive regime, the curves of the two aged alloys exhibit current spikes, which can be attributed to the formation of metastable pits, or local dissolution of segregated phases. Corrosion current densities (j_{corr}) and passive current densities (j_{pass}) are in the same order of magnitude as those determined for the homogenized alloys previously discussed. The two aged alloys exhibit corrosion behavior similar to the as-cast and STQ alloys, which is the typical behavior for valve metals (e.g., Ti, Nb), that dominate the overall corrosion response.
- Significant differences in the amounts of **Cu ions released** over two weeks, with a burst release in the first hour, were attributed to the local distribution of Cu. In the examined alloys, Cu is in different forms: either embedded in a homogeneous solid solution (STQ alloy), or enriched in the interdendritic region (as-cast alloy), or in the precipitated Ti_2Cu intermetallic compound (after aging treatment). The Ti_2Cu-containing microstructure exhibits the lowest ion release, which might ensure a long-lasting antibacterial activity by contact-killing mechanism. However, an in-depth study of the Ti_2Cu nano-scaled precipitates by TEM is required, and is currently ongoing.

The research gathered in the present work marks a substantial advancement in the field of low-modulus β-type Ti alloys for antibacterial implant applications. As a whole, the following alloys could be promising candidates for future studies:

- The ternary Ga-containing alloys (100-x)(Ti–45Nb)–xGa (x = 2, 4, 6, 8 wt.%) exhibit a great combination of mechanical properties, consisting in: low Young's modulus (E = 64 – 82 GPa), high tensile yield strength (${\sigma_y}^{\text{tens}}$ = 551 – 681 MPa) and compressive yield strength (${\sigma_y}^{\text{compr}}$ = 548 – 607 MPa), good hardness ($HV_{0.1}$ = 174 – 232), high plasticity and elongation ($\varepsilon_{\max}$ = 17 – 32 %), and therefore high load-bearing capacity. Moreover, the alloys display exceptional corrosion resistance in simulated physiological conditions. In particular, the Ga 8 wt.% alloy displays the best tribocorrosion and wear resistance with fast repassivation behavior and low ion release.
- Regarding the Cu-containing alloys, the one with Cu 4 wt.% is the best performing alloy in the homogenized state: acceptable Young's modulus (E = 98 GPa), relatively high yield strength (${\sigma_y}^{\text{tens}}$ = 539 MPa, ${\sigma_y}^{\text{compr}}$ = 525 MPa), modest elongation ($\varepsilon_{\max}$ = 28%), and high corrosion resistance.
- The quaternary (2Ga–2Cu) alloy has mechanical and corrosion properties comparable to the two alloys containing 4 wt.% of Ga or Cu.

Future Perspectives

The process of translating scientific advances from the lab bench to an industrial product, and then to a successful clinical application, which would be the end goal of the present work, is a long endeavor. The fundamental systematic studies performed in the present work, even though significant in the field of low-modulus β-type Ti–Nb alloys, do not claim to be exhaustive and there are several research aspects that deserve closer attention. The following suggestions are hereby presented for consideration.

- The β phase can be stabilized at RT upon quenching from the high-temperature β-field, despite minor additions of α- and/or β- stabilizers up to 8 wt.%. Further studies with incremental amounts of the alloying elements Ga and Cu would allow determination of the critical limit of β phase stabilization. This would permit to develop alloys with the maximum potential antibacterial activity and lowest achievable Young's modulus.
- The aging treatments carried out on the Ti–Nb–Cu alloy could be optimized by adjusting holding time to achieve optimal hardness and plasticity, while retaining low stiffness and bacteria-killing Cu-containing phases.
- Further insights into the β phase stability and deformation mechanisms could be gained by exploring different stress and strain types and levels, including static and cyclic loads in tension and compression; in the present work, these aspects were only studied by applying a quasi-static high compressive load. A deep understanding of the deformation mechanisms permits optimized alloy design to improve implant lifetime. Furthermore, by fine-tuning the amount of Nb present, these β-Ti alloys have the ability to undergo a thermoelastic martensitic transformation, shifting from parent β (BCC) phase to α" martensite (orthorhombic). This aspect results in shape recovery effects above RT,

making these alloys promising candidates that aim to replace Ti–Ni alloys for biomedical applications.

- Corrosion and tribocorrosion properties represent a possible area of development: *in vitro* tribo-electrochemical testing, including fretting conditions, at different pH, in a more complex medium and in presence of organic molecules, proteins, salts and cells. Understanding the impact of the diverse species present in body fluids is crucial for developing more precise and standardized testing procedures that can anticipate and comprehend the *in vivo* behavior of the alloys.
- Comprehensive biological compatibility and antibacterial studies are necessary to evaluate the suitability of these alloys for biomedical implant applications. Preliminary biological studies (reported below) have demonstrated good *in vitro* cytocompatibility of the developed Ga-containing alloys.
- Recognizing the critical need to bridge the gap between research and industry, collaborative academia-industry research emerges as an indispensable step. To this end, demonstrator studies (reported below) will contribute to translate the scientific findings into practical solutions.

As final considerations, additive manufacturing techniques (e.g., selective laser melting), have several advantages over conventional casting, among which higher efficiency and less material waste due to machining, production of near-net-shape components, and superior properties such as strength, wear and corrosion resistance. This is due to the ability to control the size, shape and distribution of the powder particles, which allows for tuning the resulting microstructures. Post-processing surface modifications are required for a real clinical use: surface treatment is an important aspect of the manufacturing process. Clinically-used metallic materials undergo surface treatments (e.g., anodization, sandblasting, etching), which significantly alter surface properties (chemistry and morphology), and therefore their response to the external environment. All these aspects must be attentively considered for the design of future implant technologies with enhanced safety and efficacy.

Additional Collaborative Work

Preliminary Biological Studies
(collaboration with University of Gothenburg, Sweden)

Cytocompatibility evaluation is a key step in the design and development of new biomedical materials. In order to ensure that a biomaterial is suitable for medical use, it is necessary to assess its ability to support cell adhesion, growth and function. Host cell attachment to a biomaterial could be favorable in terms of infection prevention, since it would limit bacterial colonization, and thus the risk of implant failure due to infection.

To this end, preliminary biological studies were conducted on the four Ti–Nb–Ga alloys with the help of our colleagues from the Department of Biomaterials, University of Gothenburg (Sweden). Direct adhesion assay was performed by seeding THP-1

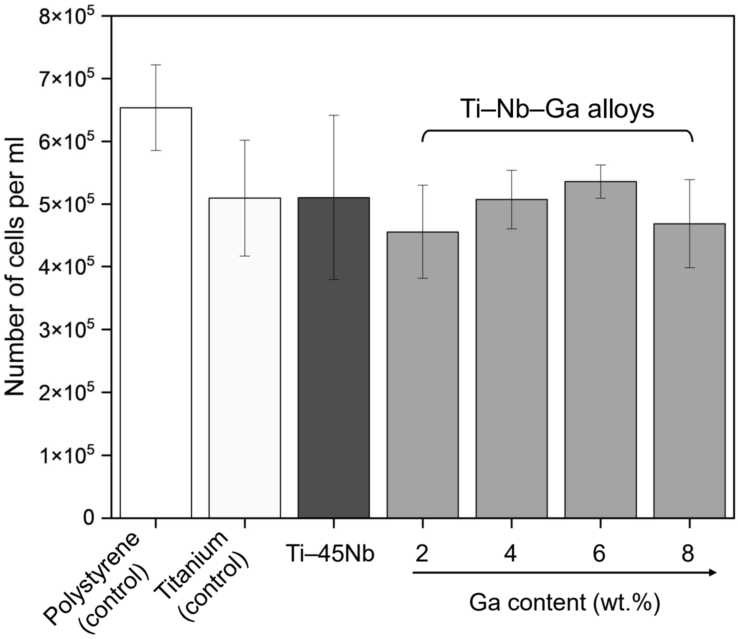

Figure 8.1: THP-1 macrophages cell adhesion on the four Ti–Nb–Ga alloys, Ti–45Nb, pure Ti and polystyrene controls after 48 h incubation.

cells, a common model cell to study macrophage activity, onto the alloys' surfaces, results of which are shown in Fig. 8.1 (detailed methodology in Appendix G). No significance was obtained when comparing the number of cells adhered to the four Ga-containing Ti–Nb alloys and the binary Ti–45Nb reference alloy. The number of cells attached to the surfaces was also comparable to the surfaces of the control materials titanium and polystyrene. These results well correlate with the high corrosion resistance and low ion release of the alloys (Ch. 5 Sec. 5.3, Ch. 6 Sec. 6.6), due to the biocompatible inert surface [271]. These findings provide preliminary evidence of the biocompatibility and safety of the developed Ga-bearing Ti–Nb alloys, which are proved to be suitable for further testing.

Fabrication of a Dental Implant Demonstrator

(collaboration with Anthogyr S.A.S., France)

A dental implant was fabricated with one of the Ga-containing alloys developed in this work as demonstrator. The project was carried out in collaboration with Anthogyr S.A.S. (France), with the aim of testing fatigue properties of the manufactured implants in artificial saliva. The choice of 92(Ti–45Nb)–8Ga alloy, in homogenized state (STQ), was based on its unique combination of suitable mechanical characteristics, excellent corrosion and wear resistance, and good biocompatibility.

Eight demonstrators were machined (Fig. 8.2a), and their structural integrity was investigated by computed tomography (CT). Initially, 2D radiographic imaging of all samples was performed (Fig. 8.2b), and then some samples were arbitrarily chosen for 3D imaging (Fig. 8.2c). 3D CT technique enables inspection of internal structures from multiple planes and provides precise location of any discontinuities along all three axes. All samples exhibit porosity, as indicated by the arrows in

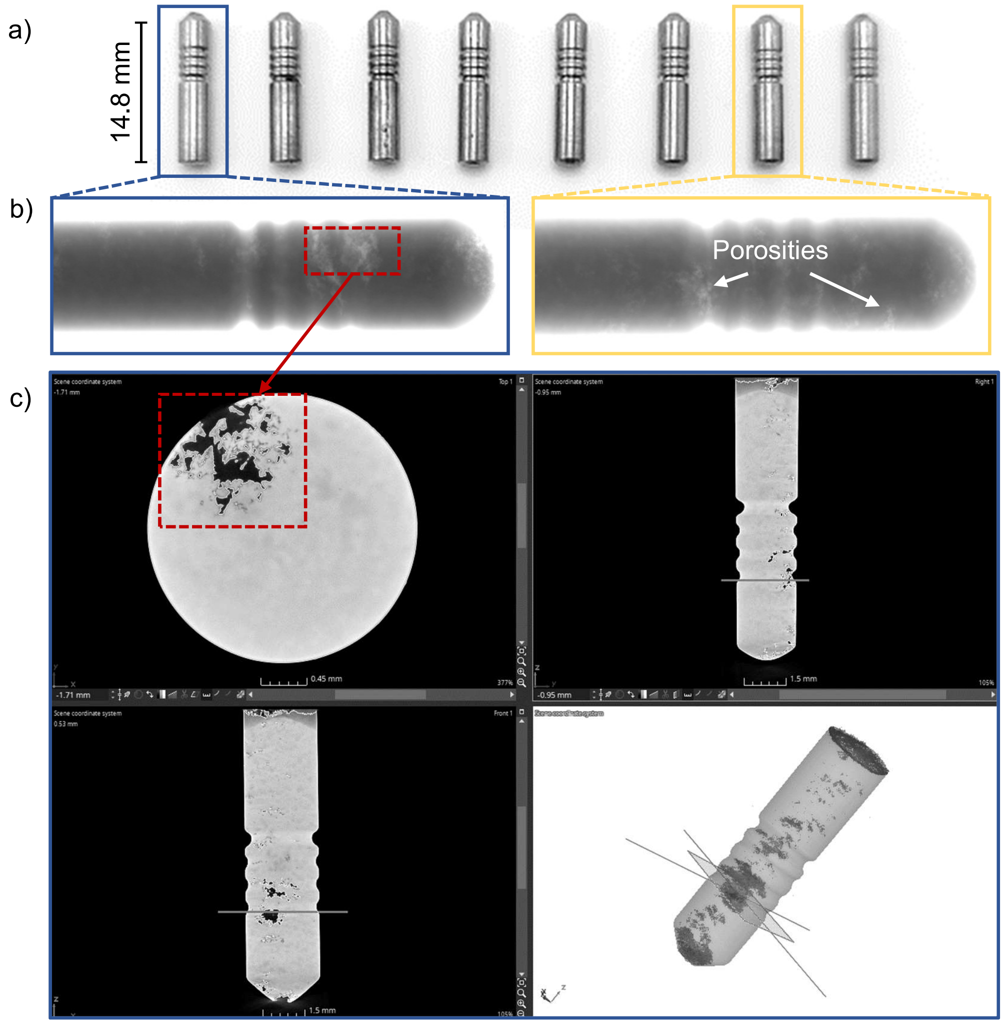

Figure 8.2: (a) Dental implant demonstrators made of 92(Ti–45Nb)–8Ga alloy (wt.%) in STQ state, (b) 2D radiographies and (c) 3D CT images showing the internal structure.

Fig. 8.2, and structural defects and were therefore considered unsuitable for fatigue testing. Nevertheless, the following positive outcomes can be highlighted:

- Demonstrator: the fabrication of the implant is itself a significant outcome. It demonstrates that the alloy can be machined and processed as a material for implant applications.
- Learning opportunity: through this process, important insights were gained into the complexities of working with these alloys, including the potential pitfalls that need to be solved in order to produce commercially viable products.

List of Publications & Conference Contributions

First-author original publications, parts of which included in the present Ph.D. work:

- **L.A. Alberta**, Y. Fortouna, J. Vishnu, A. Gebert, C. Lekka, K. Nielsch, M. Calin. *Effects of Ga on the structural, mechanical and electronic properties of β-Ti–45Nb alloy by experiments and ab initio calculations.* In: Journal of the Mechanical Behavior of Biomedical Materials, 140:105728 (2023). DOI: 10.1016/j.jmbbm.2023.105728
- **L.A. Alberta**, J. Vishnu., Y. Douest, K. Perrin, A.-M. Trunfio-Sfarghiu, N. Courtois, A. Gebert, B. Ter-Ovanessian, M. Calin. *Tribocorrosion behavior of β-type Ti–Nb–Ga alloys in a physiological solution.* In: Tribology International, 181:108325 (2023). DOI: 10.1016/j.triboint.2023.108325
- **L.A. Alberta**, J. Vishnu., A. Hariharan., S. Pilz, A. Gebert, M. Calin. *Novel low modulus beta-type Ti–Nb alloys by gallium and copper minor additions for antibacterial implant applications.* In: Journal of Materials Research and Technology, 20:3306–22 (2022). DOI: 10.1016/j.jmrt.2022.08.111

List of publications as co-author:

- J. Vishnu, A. Voss, V. Hoffmann, **L.A. Alberta**, A. Akman, B. Shankar, A. Gebert, M. Calin. *Designing Gallium-Containing Hydroxyapatite Coatings on Low Modulus Beta Ti-45Nb Alloy.* In: Coatings, 13, 1817 (2023). DOI: 10.3390/coatings13101817
- A. Bartkowska, C. Lekka, **L.A. Alberta**, I. Spasojevic, E. Pellicer, J. Sorti. *Silver-induced $\gamma \to \varepsilon$ martensitic transformation in FeMn alloys: an experimental and computational study.* In: Journal of Alloys and Compounds, 966, 171640 (2023). DOI: 10.1016/j.jallcom.2023.171640.
- A. Akman, **L.A. Alberta**, P.M. Giraldo-Osorno, A.B. Turner, M. Hantusch, A. Palmquist, M. Trobos, M.Calin, A. Gebert. *Effect of Minor Gallium Addition on Corrosion, Passivity, and Antibacterial Behaviour of Novel β-Type Ti-Nb Alloys.* In: Journal of Materials Research and Technology, 25, 4110-4124 (2023). DOI: 10.1016/j.jmrt.2023.06.219.
- M. Escobar, O. Careta, N. Fernandez Navas, A. Bartkowska, **L.A. Alberta**, J. Fornell, P. Solsona, T. Gemming, A. Gebert, E. Ibañez, A. Blanquer, C. Nogues, J. Sort, E. Pellicer. *Surface modified β-Ti–18Mo–6Nb–5Ta (wt%)*

alloy for bone implant applications: composite characterization and cytocompatibility assessment. In. Journal of Functional Biomaterials, 14:94 (2023). DOI: 10.3390/jfb14020094

- J. Vishnu, A. Ansheed, P. Hameed, K. Praveenkumar, S. Pilz, **L.A. Alberta**, S. Swaroop, M. Calin, A. Gebert, G. Manivasagam. *Insights into the surface and biocompatibility aspects of laser shock peened Ti–22Nb alloy for orthopedic implant applications.* In: Applied Surface Science, 586:152816 (2022). DOI: 10.1016/j.apsusc.2022.152816

Contributions to international conferences and workshops:

- **L.A. Alberta**, J. Vishnu, A. Hariharan, S. Pilz, A. Gebert, K. Nielsch, M. Calin. *Microstructure and mechanical properties of Ti–Nb–Ga/Cu alloys for biomedical implant applications.* THERMEC'2023 - TU Graz (Austria), 2–7 July, 2023 (oral presentation)
- **L.A. Alberta**, J. Vishnu, A. Hariharan, S. Pilz, A. Gebert, K. Nielsch, M. Calin. *Developing novel titanium-based alloys to tackle biofilm-associated infections.* Break Biofilms Workshop 2023 - TU Wien (Austria), 16–18 January, 2023 (oral presentation)
- **L.A. Alberta**, J. Vishnu, A. Hariharan, S. Pilz, A. Gebert, M. Calin. *Effect of bactericidal agents Ga and Cu on structural and mechanical properties of β-TiNb alloys.* Junior EUROMAT 2022 - University of Coimbra (Portugal), 19–22 July, 2022 (oral presentation)
- **L.A. Alberta**, Y. Fortouna, S. Pilz, A. Gebert, C. Lekka, M. Calin. *Structural and mechanical properties of novel β-type Gallium-bearing TiNb alloys for biomedical use - ab initio and experimental approach.* EUROMAT 2021 - TU Graz (Austria), 13–17 September, 2021 (virtual, poster)

Bibliography

[1] M. Long and H. Rack. “Titanium alloys in total joint replacement—a materials science perspective”. In: *Biomaterials* 19.18 (1998), pp. 1621–1639. DOI: 10.1016/S0142-9612(97)00146-4.

[2] M. Abdel-Hady Gepreel and M. Niinomi. “Biocompatibility of Ti-alloys for long-term implantation”. In: *J. Mech. Behav. Biomed. Mater.* 20 (2013), pp. 407–415. DOI: 10.1016/j.jmbbm.2012.11.014.

[3] M. I. Ridzwan, S. Shuib, A. Y. Hassan, A. A. Shokri, and M. N. Mohammad Ibrahim. “Problem of stress shielding and improvement to the hip implant designs: A review”. In: *J. Med. Sci.* 7.3 (2007), pp. 460–467. DOI: 10.3923/jms.2007.460.467.

[4] C. C. Gomes, L. M. Moreira, V. J. Santos, A. S. Ramos, J. P. Lyon, C. P. Soares, and F. V. Santos. “Assessment of the genetic risks of a metallic alloy used in medical implants”. In: *Genet. Mol. Biol.* 34.1 (2011), pp. 116–121. DOI: 10.1590/S1415-47572010005000118.

[5] E. Inan-Eroglu and A. Ayaz. “Is aluminum exposure a risk factor for neurological disorders?” In: *J. Res. Med. Sci.* 23.1 (2018), p. 51. DOI: 10.4103/jrms.JRMS_921_17.

[6] T. Ozaki, H. Matsumoto, S. Watanabe, and S. Hanada. “Beta Ti alloys with low young’s modulus”. In: *Mater. Trans.* 45.8 (2004), pp. 2776–2779. DOI: 10.2320/matertrans.45.2776.

[7] H. J. Busscher, H. C. Van Der Mei, G. Subbiahdoss, P. C. Jutte, J. J. Van Den Dungen, S. A. Zaat, M. J. Schultz, and D. W. Grainger. “Biomaterial-associated infection: Locating the finish line in the race for the surface”. In: *Sci. Transl. Med.* 4.153 (2012). DOI: 10.1126/scitranslmed.3004528.

[8] C. R. Arciola, D. Campoccia, and L. Montanaro. “Implant infections: adhesion, biofilm formation and immune evasion”. In: *Nat. Rev. Microbiol.* 16.7 (2018), pp. 397–409. DOI: 10.1038/s41579-018-0019-y.

[9] E. Seebach and K. F. Kubatzky. “Chronic Implant-Related Bone Infections—Can Immune Modulation be a Therapeutic Strategy?” In: *Front. Immunol.* 10.July (2019), p. 1724. DOI: 10.3389/fimmu.2019.01724.

[10] BIOMATERIALS FOR HEALTH A Strategic Roadmap for Research and Innovation HORIZON 2020 Biomaterials for Health. Tech. rep. 2020, pp. 1–65.

[11] L. Bolzoni, M. Alqattan, F. Yang, and L. Peters. “Design of β-eutectoid bearing Ti alloys with antibacterial functionality”. In: *Mater. Lett.* 278 (2020), p. 128445. DOI: 10.1016/j.matlet.2020.128445.

[12] D. F. Williams. Definitions in biomaterials : proceedings of a consensus conference of the European Society for Biomaterials. Amsterdam: Elsevier, 1987. ISBN: 9780444428585.

[13] D. F. Williams. “On the mechanisms of biocompatibility”. In: *Biomaterials* 29.20 (2008), pp. 2941–2953. DOI: 10.1016/j.biomaterials.2008.04.023.

[14] A. J. Teo, A. Mishra, I. Park, Y. J. Kim, W. T. Park, and Y. J. Yoon. “Polymeric Biomaterials for Medical Implants and Devices”. In: *ACS Biomater. Sci. Eng.* 2.4 (2016), pp. 454–472. DOI: 10.1021/acsbiomaterials.5b00429.

[15] W. Höland, M. Schweiger, R. Watzke, A. Peschke, and H. Kappert. “Ceramics as biomaterials for dental restoration”. In: *Expert Rev. Med. Devices* 5.6 (2008), pp. 729–745. DOI: `10.1586/17434440.5.6.729`.

[16] O. O. Ige, L. E. Umoru, and S. Aribo. “Natural Products: A Minefield of Biomaterials”. In: *ISRN Mater. Sci.* 2012 (2012), pp. 1–20. DOI: `10.5402/2012/983062`.

[17] Q. Chen and G. A. Thouas. “Metallic implant biomaterials”. In: *Mater. Sci. Eng. R Reports* 87 (2015), pp. 1–57. DOI: `10.1016/j.mser.2014.10.001`.

[18] D. Williams, R. Cahn, and M. Bever. Concise encyclopedia of medical & dental materials. Advances in materials science and engineering. Elsevier Science, 1990. ISBN: 9780080361949.

[19] S. Ozan, J. Lin, Y. Li, R. Ipek, and C. Wen. “Development of Ti-Nb-Zr alloys with high elastic admissible strain for temporary orthopedic devices”. In: *Acta Biomater.* 20 (2015), pp. 176–187. DOI: `10.1016/j.actbio.2015.03.023`.

[20] M. Niinomi. Metals for biomedical devices. 2010. ISBN: 9781845694340. DOI: `10.1533/9781845699246`.

[21] M. Niinomi, T. Narushima, M. Nakai, and B. Reactions. Advances in Metallic Biomaterials. 2015, pp. 305–321. ISBN: 9783662468357. DOI: `10.1007/978-3-662-46836-4_13`.

[22] H. K. Raut, R. Das, Z. Liu, X. Liu, and S. Ramakrishna. “Biocompatibility of Biomaterials for Tissue Regeneration or Replacement”. In: *Biotechnol. J.* 15.12 (2020), pp. 1–14. DOI: `10.1002/biot.202000160`.

[23] S. S. Tavares, F. B. Mainier, F. Zimmerman, R. Freitas, and C. M. Ajus. “Characterization of prematurely failed stainless steel orthopedic implants”. In: *Eng. Fail. Anal.* 17.5 (2010), pp. 1246–1253. DOI: `10.1016/j.engfailanal.2010.02.003`.

[24] M. Sumita, T. Hanawa, I. Ohnishi, and T. Yoneyama. “Failure Processes in Biometallic Materials”. In: *Compr. Struct. Integr.* Elsevier, 2003, pp. 131–167. ISBN: 978-0-08-043749-1. DOI: `10.1016/B0-08-043749-4/09143-6`.

[25] M. Niinomi and M. Nakai. “Titanium-based biomaterials for preventing stress shielding between implant devices and bone”. In: *Int. J. Biomater.* 2011 (2011). DOI: `10.1155/2011/836587`.

[26] N. Eliaz. “Corrosion of metallic biomaterials: A review”. In: *Materials (Basel).* 12.3 (2019). DOI: `10.3390/ma12030407`.

[27] M. Pourbaix, H. Zhang, and A. Pourbaix. Atlas of chemical and electrochemical equilibria in the presence of a gaseous phase. Vol. 251-254. 1997, pp. 143–148. DOI: `10.4028/www.scientific.net/msf.251-254.143`.

[28] S. Hiromoto. “Corrosion of metallic biomaterials”. In: *Met. Biomed. Devices* (2019), pp. 131–152. DOI: `10.1016/B978-0-08-102666-3.00004-3`.

[29] S. Mischler. “Triboelectrochemical techniques and interpretation methods in tribocorrosion: A comparative evaluation”. In: *Tribol. Int.* 41.7 (2008), pp. 573–583. DOI: `10.1016/j.triboint.2007.11.003`.

[30] W. Chen, W.-q. Zhu, and J. Qiu. “Impact of exogenous metal ions on peri-implant bone metabolism: a review”. In: *RSC Adv.* 11.22 (2021), pp. 13152–13163. DOI: `10.1039/D0RA09395E`.

[31] Y. Li, C. Wong, J. Xiong, P. Hodgson, and C. Wen. “Cytotoxicity of Titanium and Titanium Alloying Elements”. In: *J. Dent. Res.* 89.5 (2010), pp. 493–497. DOI: `10.1177/0022034510363675`.

[32] D. J. Berry, M. P. Abdel, and J. J. Callaghan. “What Are the Current Clinical Issues in Wear and Tribocorrosion?” In: *Clin. Orthop. Relat. Res.* 472.12 (2014), pp. 3659–3664. DOI: `10.1007/s11999-014-3610-1`.

[33] M. Geetha, A. K. Singh, R. Asokamani, and A. K. Gogia. Ti based biomaterials, the ultimate choice for orthopaedic implants - A review. 2009. DOI: `10.1016/j.pmatsci.2008.06.004`.

[34] S. Ali, A. M. Abdul Rani, Z. Baig, S. W. Ahmed, G. Hussain, K. Subramaniam, S. Hastuty, and T. V. Rao. “Biocompatibility and corrosion resistance of metallic biomaterials”. In: *Corros. Rev.* 38.5 (2020), pp. 381–402. DOI: `10.1515/corrrev-2020-0001`.

[35] N. Burger, P. de Vaal, and J. Meyer. “Failure analysis on retrieved ultra high molecular weight polyethylene (UHMWPE) acetabular cups”. In: *Eng. Fail. Anal.* 14.7 (2007), pp. 1329–1345. DOI: `10.1016/j.engfailanal.2006.11.005`.

[36] S. Affatato, P. Taddei, A. Leardini, S. Giannini, M. Spinelli, and M. Viceconti. “Wear behaviour in total ankle replacement: A comparison between an in vitro simulation and retrieved prostheses”. In: *Clin. Biomech.* 24.8 (2009), pp. 661–669. DOI: `10.1016/j.clinbiomech.2009.06.006`.

[37] A. Cigada, G. Cotogno, and R. Chiesa. “The ceramic-on-metal coupling in total hip replacements for young patients: a review study”. In: *J. Appl. Biomater. Biomech.* 9.1 (2011), pp. 2–10. DOI: `10.5301/JABB.2011.7730`.

[38] P. Massin, E. Viguier, B. Flautre, P. Hardouin, E. Astoin, and B. Duponchel. “Migration of Polyethylene Debris along Well-Fixed Cemented Implants”. In: *J. Biomed. Mater. Res. - Part B Appl. Biomater.* 68.2 (2004), pp. 140–148. DOI: `10.1002/jbm.b.10072`.

[39] P. Sahoo, S. K. Das, and J. Paulo Davim. “Tribology of materials for biomedical applications”. In: *Mech. Behav. Biomater.* Elsevier, 2019, pp. 1–45. ISBN: 9780081021743. DOI: `10.1016/B978-0-08-102174-3.00001-2`.

[40] C. Döbberthin, M. Herbster, and B. Karpuschewski. “A novel approach for a modular taper junction in hip stems using turn-milling”. In: *CIRP J. Manuf. Sci. Technol.* 33 (2021), pp. 256–263. DOI: `10.1016/j.cirpj.2021.03.001`.

[41] R. Radulescu, A. Badila, R. Manolescu, I. Japie, E. Badila, A. Bolocan, and D. N. Paduraru. “Degree of the polyethylene component wear - A predictive factor for the outcome of total hip arthroplasty”. In: *Mater. Plast.* 50.3 (2013), pp. 212–214.

[42] J. Hembus, L. Rößler, M. Jackszis, A. Klinder, R. Bader, and C. Zietz. “Influence of Metallic Deposition on Ceramic Femoral Heads on the Wear Behavior of Artificial Hip Joints: A Simulator Study”. In: *Materials (Basel).* 13.16 (2020), p. 3569. DOI: `10.3390/ma13163569`.

[43] B. Carlson. Implant-Based Dental Reconstruction: World Dental Implant and Bone Graft Market, 3rd Edition. Tech. rep. 2009, pp. 1–172.

[44] H. Warlimont. Titanium and Titanium Alloys. Ed. by C. Leyens and M. Peters. Wiley, 2018, pp. 195–206. DOI: `10.1002/3527602119`.

[45] E. Eisenbarth, D. Velten, M. Müller, R. Thull, and J. Breme. “Biocompatibility of β-stabilizing elements of titanium alloys”. In: *Biomaterials* 25.26 (2004), pp. 5705–5713. DOI: `10.1016/j.biomaterials.2004.01.021`.

[46] A. Helth, S. Pilz, T. Kirsten, L. Giebeler, J. Freudenberger, M. Calin, J. Eckert, and A. Gebert. “Effect of thermomechanical processing on the mechanical biofunctionality of a low modulus Ti-40Nb alloy”. In: *J. Mech. Behav. Biomed. Mater.* 65 (2017), pp. 137–150. DOI: `10.1016/j.jmbbm.2016.08.017`.

[47] S. Pilz, A. Hariharan, F. Günther, M. Zimmermann, and A. Gebert. “Influence of isothermal omega precipitation aging on deformation mechanisms and mechanical properties of a β-type Ti-Nb alloy”. In: *J. Alloys Compd.* 930 (2023), p. 167309. DOI: `10.1016/j.jallcom.2022.167309`.

[48] I.-H. Oh, N. Nomura, N. Masahashi, and S. Hanada. “Mechanical properties of porous titanium compacts prepared by powder sintering”. In: *Scr. Mater.* 49.12 (2003), pp. 1197–1202. DOI: `10.1016/j.scriptamat.2003.08.018`.

[49] K. Zhuravleva, M. Bönisch, K. Prashanth, U. Hempel, A. Helth, T. Gemming, M. Calin, S. Scudino, L. Schultz, J. Eckert, and A. Gebert. “Production of Porous β-Type Ti–40Nb Alloy for Biomedical Applications: Comparison of Selective Laser Melting and Hot Pressing”. In: *Materials (Basel).* 6.12 (2013), pp. 5700–5712. DOI: `10.3390/ma6125700`.

[50] A. Mortensen and J. Llorca. "Metal Matrix Composites". In: *Annu. Rev. Mater. Res.* 40.1 (2010), pp. 243–270. DOI: `10.1146/annurev-matsci-070909-104511`.

[51] S. F. Jawed, C. D. Rabadia, M. A. Khan, and S. J. Khan. Effect of Alloying Elements on the Compressive Mechanical Properties of Biomedical Titanium Alloys: A Systematic Review. 2022. DOI: `10.1021/acsomega.2c02096`. URL: `https://pubs.acs.org/doi/10.1021/acsomega.2c02096`.

[52] T. Hanawa. "Research and development of metals for medical devices based on clinical needs". In: *Sci. Technol. Adv. Mater.* 13.6 (2012). DOI: `10.1088/1468-6996/13/6/064102`.

[53] L.-C. Zhang and L.-Y. Chen. "A Review on Biomedical Titanium Alloys: Recent Progress and Prospect". In: *Adv. Eng. Mater.* 21.4 (2019), p. 1801215. DOI: `10.1002/adem.201801215`.

[54] K. T. Kim, M. Y. Eo, T. T. H. Nguyen, and S. M. Kim. "General review of titanium toxicity". In: *Int. J. Implant Dent.* 5.1 (2019). DOI: `10.1186/s40729-019-0162-x`.

[55] J. C. Souza, K. Apaza-Bedoya, C. A. Benfatti, F. S. Silva, and B. Henriques. "A comprehensive review on the corrosion pathways of titanium dental implants and their biological adverse effects". In: *Metals (Basel).* 10.9 (2020), pp. 1–14. DOI: `10.3390/met10091272`.

[56] S. J. MacDonald. "Can a safe level for metal ions in patients with metal-on-metal total hip arthroplasties be determined?" In: *J. Arthroplasty* 19.8 SUPPL. (2004), pp. 71–77. DOI: `10.1016/j.arth.2004.09.008`.

[57] "Implant materials". In: 28.6 (1974), pp. 613–620.

[58] J. M. Smolders, P. Bisseling, A. Hol, C. Van Der Straeten, B. W. Schreurs, and J. L. van Susante. "Metal ion interpretation in resurfacing versus conventional hip arthroplasty and in whole blood versus serum. How should we interpret metal ion data?" In: *HIP Int.* 21.5 (2011), pp. 587–595. DOI: `10.5301/HIP.2011.8643`.

[59] M. Metikoš-Huković, A. Kwokal, and J. Piljac. "The influence of niobium and vanadium on passivity of titanium-based implants in physiological solution". In: *Biomaterials* 24.21 (2003), pp. 3765–3775. DOI: `10.1016/S0142-9612(03)00252-7`.

[60] P. F. Ji, B. Li, B. H. Chen, F. Wang, W. Ma, X. Y. Zhang, M. Z. Ma, and R. P. Liu. "Effect of Nb addition on the stability and biological corrosion resistance of Ti-Zr alloy passivation films". In: *Corros. Sci.* 170.April (2020). DOI: `10.1016/j.corsci.2020.108696`.

[61] N. Hu, L. Xie, Q. Liao, A. Gao, Y. Zheng, H. Pan, L. Tong, D. Yang, N. Gao, M. J. Starink, P. K. Chu, and H. Wang. "A more defective substrate leads to a less defective passive layer: Enhancing the mechanical strength, corrosion resistance and anti-inflammatory response of the low-modulus Ti-45Nb alloy by grain refinement". In: *Acta Biomater.* 126 (2021), pp. 524–536. DOI: `10.1016/j.actbio.2021.02.045`.

[62] R. Godley, D. Starosvetsky, and I. Gotman. "Corrosion behavior of a low modulus β-Ti-45%Nb alloy for use in medical implants". In: *J. Mater. Sci. Mater. Med.* 17.1 (2006), pp. 63–67. DOI: `10.1007/s10856-006-6330-6`.

[63] A. Gebert, S. Oswald, A. Helth, A. Voss, P. F. Gostin, M. Rohnke, J. Janek, M. Calin, and J. Eckert. "Effect of indium (In) on corrosion and passivity of a beta-type Ti-Nb alloy in Ringer's solution". In: *Appl. Surf. Sci.* 335 (2015), pp. 213–222. DOI: `10.1016/j.apsusc.2015.02.058`.

[64] S. Pilz, A. Gebert, A. Voss, S. Oswald, M. Göttlicher, U. Hempel, J. Eckert, M. Rohnke, J. Janek, and M. Calin. "Metal release and cell biological compatibility of beta-type Ti-40Nb containing indium". In: *J. Biomed. Mater. Res. - Part B Appl. Biomater.* 106.5 (2018), pp. 1686–1697. DOI: `10.1002/jbm.b.33976`.

[65] C. Xin, N. Wang, Y. Chen, B. He, Q. Zhao, L. Chen, Y. Tang, B. Luo, Y. Zhao, and X. Yang. "Biological corrosion behaviour and antibacterial properties of Ti-Cu alloy with different Ti2Cu morphologies for dental applications". In: *Mater. Des.* 215 (2022), p. 110540. DOI: `10.1016/j.matdes.2022.110540`.

[66] S. Y. Yu and J. R. Scully. "Corrosion and Passivity of Ti-13% Nb-13% Zr in Comparison to Other Biomedical Implant Alloys". In: *CORROSION* 53.12 (1997), pp. 965–976. DOI: `10.5006/1.3290281`.

[67] M. Q. Neto, S. Radice, D. J. Hall, N. B. Frisch, M. T. Mathew, A. Fischer, J. J. Jacobs, and R. Pourzal. "Microstructure and Electrochemical Behavior of Contemporary Ti6Al4V Implant Alloys". In: *J. Bio- Tribo-Corrosion* 8.1 (2022), p. 26. DOI: `10.1007/s40735-021-00623-3`.

[68] M. Hussein, A. Mohammed, and N. Al-Aqeeli. "Wear Characteristics of Metallic Biomaterials: A Review". In: *Materials (Basel).* 8.5 (2015), pp. 2749–2768. DOI: `10.3390/ma8052749`.

[69] A. Choubey, B. Basu, and R. Balasubramaniam. "Tribological behaviour of Ti-based alloys in simulated body fluid solution at fretting contacts". In: *Mater. Sci. Eng. A* 379.1-2 (2004), pp. 234–239. DOI: `10.1016/j.msea.2004.02.027`.

[70] M. O. Alam and A. S. Haseeb. "Response of Ti-6Al-4V and Ti-24Al-11Nb alloys to dry sliding wear against hardened steel". In: *Tribol. Int.* 35.6 (2002), pp. 357–362. DOI: `10.1016/S0301-679X(02)00015-4`.

[71] É. Martin, M. Azzi, G. A. Salishchev, and J. Szpunar. "Influence of microstructure and texture on the corrosion and tribocorrosion behavior of Ti-6Al-4V". In: *Tribol. Int.* 43.5-6 (2010), pp. 918–924. DOI: `10.1016/j.triboint.2009.12.055`.

[72] M. Feyzi, K. Fallahnezhad, M. Taylor, and R. Hashemi. "The Tribocorrosion Behaviour of Ti-6Al-4 V Alloy: The Role of Both Normal Force and Electrochemical Potential". In: *Tribol. Lett.* 70.3 (2022), pp. 1–16. DOI: `10.1007/s11249-022-01624-0`.

[73] M. Feyzi, K. Fallahnezhad, M. Taylor, and R. Hashemi. "What role do normal force and frequency play in the tribocorrosion behaviour of Ti-6Al-4 V alloy?" In: *Tribol. Int.* 172.March (2022), p. 107634. DOI: `10.1016/j.triboint.2022.107634`.

[74] I. Çaha, A. Alves, C. Chirico, A. Pinto, S. Tsipas, E. Gordo, and F. Toptan. "Corrosion and Tribocorrosion Behavior of Ti-40Nb and Ti-25Nb-5Fe Alloys Processed by Powder Metallurgy". In: *Metall. Mater. Trans. A Phys. Metall. Mater. Sci.* 51.6 (2020), pp. 3256–3267. DOI: `10.1007/s11661-020-05757-6`.

[75] I. Hacisalihoglu, A. Samancioglu, F. Yildiz, G. Purcek, and A. Alsaran. "Tribocorrosion properties of different type titanium alloys in simulated body fluid". In: *Wear* 332-333 (2015), pp. 679–686. DOI: `10.1016/j.wear.2014.12.017`.

[76] V. G. Pina, A. Dalmau, F. Devesa, V. Amigó, and A. I. Muñoz. "Tribocorrosion behavior of beta titanium biomedical alloys in phosphate buffer saline solution". In: *J. Mech. Behav. Biomed. Mater.* 46 (2015), pp. 59–68. DOI: `10.1016/j.jmbbm.2015.02.016`.

[77] A. K. Pandey, R. Gautam, and C. Behera. "Corrosion and wear behavior of Ti–5Cu-xNb biomedical alloy in simulated body fluid for dental implant applications". In: *J. Mech. Behav. Biomed. Mater.* 137.110 (2023), p. 105533. DOI: `10.1016/j.jmbbm.2022.105533`.

[78] N. S. More, N. Diomidis, S. N. Paul, M. Roy, and S. Mischler. "Tribocorrosion behavior of β titanium alloys in physiological solutions containing synovial components". In: *Mater. Sci. Eng. C* 31.2 (2011), pp. 400–408. DOI: `10.1016/j.msec.2010.10.021`.

[79] M. Q. Neto and W. M. Rainforth. "Effect of Potential and Microstructure on the Tribocorrosion Behaviour of Beta and Near Beta Ti Alloys II". In: *J. Bio- Tribo-Corrosion* 7.4 (2021), pp. 1–12. DOI: `10.1007/s40735-021-00578-5`.

[80] M. Q. Neto and W. M. Rainforth. "Effect of Potential and Microstructure on the Tribocorrosion Behaviour of Beta and Near Beta Ti Alloys I". In: *Biotribology* 24.July (2020), p. 100141. DOI: `10.1016/j.biotri.2020.100141`.

[81] P. Chapala, S. G. Acharyya, S. M. Shariff, and A. Bhattacharjee. "Studying the effect of composition on the in vitro wear behavior and elastic modulus of titanium-niobium-based alloys for biomedical implants". In: *Biomed. Phys. Eng. Express* 4.2 (2018), p. 027003. DOI: `10.1088/2057-1976/aa9f78`.

[82] S. J. Li, R. Yang, S. Li, Y. L. Hao, Y. Y. Cui, M. Niinomi, and Z. X. Guo. "Wear characteristics of Ti-Nb-Ta-Zr and Ti-6Al-4V alloys for biomedical applications". In: *Wear* 257.9-10 (2004), pp. 869–876. DOI: `10.1016/j.wear.2004.04.001`.

[83] R. Dong, W. Zhu, C. Zhao, Y. Zhang, and F. Ren. "Microstructure, Mechanical Properties, and Sliding Wear Behavior of Spark Plasma Sintered Ti-Cu Alloys". In: *Metall. Mater. Trans. A* 49.12 (2018), pp. 6147–6160. DOI: `10.1007/s11661-018-4953-0`.

[84] J. Liu, F. Li, C. Liu, H. Wang, B. Ren, K. Yang, and E. Zhang. "Effect of Cu content on the antibacterial activity of titanium-copper sintered alloys". In: *Mater. Sci. Eng. C* 35.1 (2014), pp. 392–400. DOI: `10.1016/j.msec.2013.11.028`.

[85] J. Vishnu and G. Manivasagam. "Surface Modification and Biological Approaches for Tackling Titanium Wear-Induced Aseptic Loosening". In: *J. Bio- Tribo-Corrosion* 7.1 (2021), pp. 1–19. DOI: `10.1007/s40735-021-00474-y`.

[86] S. S. Sidhu, H. Singh, and M. A. H. Gepreel. "A review on alloy design, biological response, and strengthening of β-titanium alloys as biomaterials". In: *Mater. Sci. Eng. C* 121.August 2020 (2021). DOI: `10.1016/j.msec.2020.111661`.

[87] Y. Okazaki and E. Gotoh. "Comparison of metal release from various metallic biomaterials in vitro". In: *Biomaterials* 26.1 (2005), pp. 11–21. DOI: `10.1016/j.biomaterials.2004.02.005`.

[88] Y. Okazaki. "A New Ti–15Zr–4Nb–4Ta alloy for medical applications". In: *Curr. Opin. Solid State Mater. Sci.* 5.1 (2001), pp. 45–53. DOI: `10.1016/S1359-0286(00)00025-5`.

[89] M. Niinomi. "Recent Research and Development in Metallic Materials for Biomedical, Dental and Healthcare Products Applications". In: *Mater. Sci. Forum.* Vol. 539-543. PART 1. 2007, pp. 193–200. ISBN: 0878494286. DOI: `10.4028/0-87849-428-6.193`.

[90] M. Niinomi. "Mechanical biocompatibilities of titanium alloys for biomedical applications". In: *J. Mech. Behav. Biomed. Mater.* 1.1 (2008), pp. 30–42. DOI: `10.1016/j.jmbbm.2007.07.001`.

[91] G. Lütjering and J. C. Williams. Titanium. Engineering Materials and Processes. Berlin, Heidelberg: Springer Berlin Heidelberg, 2003. ISBN: 978-3-662-13222-7. DOI: `10.1007/978-3-540-71398-2`.

[92] S. F. Jawed, C. D. Rabadia, Y. J. Liu, L. Q. Wang, Y. H. Li, X. H. Zhang, and L. C. Zhang. "Beta-type Ti-Nb-Zr-Cr alloys with large plasticity and significant strain hardening". In: *Mater. Des.* 181 (2019), pp. 1–10. DOI: `10.1016/j.matdes.2019.108064`.

[93] A. Gupta, R. Khatirkar, and J. Singh. "A review of microstructure and texture evolution during plastic deformation and heat treatment of β-Ti alloys". In: *J. Alloys Compd.* 899 (2022), p. 163242. DOI: `10.1016/j.jallcom.2021.163242`.

[94] X. Zhao, M. Niinomi, M. Nakai, G. Miyamoto, and T. Furuhara. "Microstructures and mechanical properties of metastable Ti–30Zr–(Cr, Mo) alloys with changeable Young's modulus for spinal fixation applications". In: *Acta Biomater.* 7.8 (2011), pp. 3230–3236. DOI: `10.1016/j.actbio.2011.04.019`.

[95] M. R. Dal Bó, C. A. Salvador, M. G. Mello, D. D. Lima, G. A. Faria, A. J. Ramirez, and R. Caram. "The effect of Zr and Sn additions on the microstructure of Ti-Nb-Fe gum metals with high elastic admissible strain". In: *Mater. Des.* 160 (2018), pp. 1186–1195. DOI: `10.1016/j.matdes.2018.10.040`.

[96] P. Li, X. Ma, D. Wang, and H. Zhang. "Microstructural and Mechanical Properties of β-Type Ti–Nb–Sn Biomedical Alloys with Low Elastic Modulus". In: *Metals (Basel).* 9.6 (2019), p. 712. DOI: `10.3390/met9060712`.

[97] J. Chen, F. Ma, P. Liu, C. Wang, X. Liu, W. Li, and Q. Han. "Effects of Nb on Superelasticity and Low Modulus Properties of Metastable β-Type Ti-Nb-Ta-Zr Biomedical Alloys". In: *J. Mater. Eng. Perform.* 28.3 (2019), pp. 1410–1418. DOI: `10.1007/s11665-019-03897-4`.

[98] I. Mutlu. “Single-step sinter-aging heat treatment of metastable-beta type Ti–Nb–Cu alloy”. In: *Powder Metall.* 64.1 (2021), pp. 43–53. DOI: `10.1080/00325899.2020.1843258`.

[99] H. Matsumoto, S. Watanabe, and S. Hanada. “Beta TiNbSn alloys with low Young’s modulus and high strength”. In: *Mater. Trans.* 46.5 (2005), pp. 1070–1078. DOI: `10.2320/matertrans.46.1070`.

[100] J. Vishnu, M. Sankar, H. Rack, N. Rao, A. Singh, and G. Manivasagam. “Effect of phase transformations during aging on tensile strength and ductility of metastable beta titanium alloy Ti–35Nb–7Zr–5Ta-0.35O for orthopedic applications”. In: *Mater. Sci. Eng. A* 779.February (2020), p. 139127. DOI: `10.1016/j.msea.2020.139127`.

[101] M. Calin, A. Helth, J. J. Gutierrez Moreno, M. Bönisch, V. Brackmann, L. Giebeler, T. Gemming, C. E. Lekka, A. Gebert, R. Schnettler, and J. Eckert. “Elastic softening of β-type Ti-Nb alloys by indium (In) additions”. In: *J. Mech. Behav. Biomed. Mater.* 39 (2014), pp. 162–174. DOI: `10.1016/j.jmbbm.2014.07.010`.

[102] P. Li, X. Ma, T. Tong, and Y. Wang. “Microstructural and mechanical properties of β-type Ti–Mo–Nb biomedical alloys with low elastic modulus”. In: *J. Alloys Compd.* 815 (2020), p. 152412. DOI: `10.1016/j.jallcom.2019.152412`.

[103] Y. Bai, Y. Deng, Y. Zheng, Y. Li, R. Zhang, Y. Lv, Q. Zhao, and S. Wei. “Characterization, corrosion behavior, cellular response and in vivo bone tissue compatibility of titanium-niobium alloy with low Young’s modulus”. In: *Mater. Sci. Eng. C* 59 (2016), pp. 565–576. DOI: `10.1016/j.msec.2015.10.062`.

[104] A. Mehjabeen, W. Xu, D. Qiu, and M. Qian. “Redefining the β-Phase Stability in Ti-Nb-Zr Alloys for Alloy Design and Microstructural Prediction”. In: *JOM* 70.10 (2018), pp. 2254–2259. DOI: `10.1007/s11837-018-3010-1`.

[105] J. D. Cotton, R. D. Briggs, R. R. Boyer, S. Tamirisakandala, P. Russo, N. Shchetnikov, and J. C. Fanning. “State of the Art in Beta Titanium Alloys for Airframe Applications”. In: *JOM* 67.6 (2015), pp. 1281–1303. DOI: `10.1007/s11837-015-1442-4`.

[106] C. E. Shamblen and T. K. Redden. “Creep Resistance and High-Temperature Metallurgical Stability of Titanium Alloys Containing Gallium.” In: *Met. Trans* 3.5 (1972), pp. 1299–1305. DOI: `10.1007/BF02642464`.

[107] R. P. Kolli and A. Devaraj. “A review of metastable beta titanium alloys”. In: *Metals (Basel).* 8.7 (2018), pp. 1–41. DOI: `10.3390/met8070506`.

[108] M. Morinaga, M. Kato, T. Kamimura, M. Fukumoto, I. Harada, and K. Kubo. “Theoretical design of beta-type titanium alloys”. In: *Titanium’92 Sci. Technol.* (1993), pp. 217–224.

[109] D. Kuroda, M. Niinomi, M. Morinaga, Y. Kato, and T. Yashiro. “Design and mechanical properties of new β type titanium alloys for implant materials”. In: *Mater. Sci. Eng. A* 243.1-2 (1998), pp. 244–249. DOI: `10.1016/s0921-5093(97)00808-3`.

[110] M. Abdel-Hady, K. Hinoshita, and M. Morinaga. “General approach to phase stability and elastic properties of β-type Ti-alloys using electronic parameters”. In: *Scr. Mater.* 55.5 (2006), pp. 477–480. DOI: `10.1016/j.scriptamat.2006.04.022`.

[111] C. Wang, A. Russell, and G. Cao. “A semi-empirical approach to the prediction of deformation behaviors of β-Ti alloys”. In: *Scr. Mater.* 158 (2019), pp. 62–65. DOI: `10.1016/j.scriptamat.2018.08.035`.

[112] C. D. Rabadia, S. F. Jawed, J. Wang, M. Siddhpura, and A. Siddhpura. “Revised Semiempirical Approach to Predict the Occurrence of Twinning in Titanium Alloys”. In: *ACS Omega* 6.49 (2021), pp. 34056–34064. DOI: `10.1021/acsomega.1c05474`.

[113] P. Laheurte, F. Prima, A. Eberhardt, T. Gloriant, M. Wary, and E. Patoor. “Mechanical properties of low modulus β titanium alloys designed from the electronic approach”. In: *J. Mech. Behav. Biomed. Mater.* 3.8 (2010), pp. 565–573. DOI: `10.1016/j.jmbbm.2010.07.001`.

[114] T. Inamura, Y. Fukui, H. Hosoda, K. Wakashima, and S. Miyazaki. “Mechanical properties of Ti-Nb biomedical shape memory alloys containing Ge or Ga”. In: *Mater. Sci. Eng. C* 25.3 (2005), pp. 426–432. DOI: `10.1016/j.msec.2005.01.025`.

[115] Y. Al-Zain, H. Y. Kim, H. Hosoda, T. H. Nam, and S. Miyazaki. “Shape memory properties of Ti-Nb-Mo biomedical alloys”. In: *Acta Mater.* 58.12 (2010), pp. 4212–4223. DOI: `10.1016/j.actamat.2010.04.013`.

[116] H. Y. Kim and S. Miyazaki. “Several Issues in the Development of Ti–Nb-Based Shape Memory Alloys”. In: *Shape Mem. Superelasticity* 2.4 (2016), pp. 380–390. DOI: `10.1007/s40830-016-0087-7`.

[117] M. Bönisch. “Structural properties, deformation behavior and thermal stability of martensitic Ti-Nb alloys”. PhD thesis. 2016.

[118] Y. Zhang, H. Liu, and Z. Jin. “Thermodynamic assessment of the Nb-Ti system”. In: *Calphad* 25.2 (2001), pp. 305–317. DOI: `10.1016/S0364-5916(01)00051-7`.

[119] M. Bönisch, A. Panigrahi, M. Calin, T. Waitz, M. Zehetbauer, W. Skrotzki, and J. Eckert. “Thermal stability and latent heat of Nb–rich martensitic Ti-Nb alloys”. In: *J. Alloys Compd.* 697 (2017), pp. 300–309. DOI: `10.1016/j.jallcom.2016.12.108`.

[120] M. Bönisch, M. Calin, L. Giebeler, A. Helth, A. Gebert, W. Skrotzki, and J. Eckert. “Composition-dependent magnitude of atomic shuffles in Ti–Nb martensites”. In: *J. Appl. Crystallogr.* 47.4 (2014), pp. 1374–1379. DOI: `10.1107/S1600576714012576`.

[121] D. L. Moffat and U. R. Kattner. “Stable and metastable Ti-Nb phase diagrams”. In: *Metall. Trans. A, Phys. Metall. Mater. Sci.* 19 A.10 (1988), pp. 2389–2397. DOI: `10.1007/BF02645466`.

[122] S. A. Mantri, D. Choudhuri, T. Alam, V. Ageh, F. Sun, F. Prima, and R. Banerjee. “Change in the deformation mode resulting from beta-omega compositional partitioning in a Ti-Mo alloy: Room versus elevated temperature”. In: *Scr. Mater.* 130 (2017), pp. 69–73. DOI: `10.1016/j.scriptamat.2016.11.013`.

[123] M. Bönisch, M. Calin, T. Waitz, A. Panigrahi, M. Zehetbauer, A. Gebert, W. Skrotzki, and J. Eckert. “Thermal stability and phase transformations of martensitic Ti–Nb alloys”. In: *Sci. Technol. Adv. Mater.* 14.5 (2013), p. 055004. DOI: `10.1088/1468-6996/14/5/055004`.

[124] M. Bönisch, M. Calin, J. Van Humbeeck, W. Skrotzki, and J. Eckert. “Factors influencing the elastic moduli, reversible strains and hysteresis loops in martensitic Ti-Nb alloys”. In: *Mater. Sci. Eng. C* 48 (2015), pp. 511–520. DOI: `10.1016/j.msec.2014.12.048`.

[125] M. Bönisch, A. Panigrahi, M. Stoica, M. Calin, E. Ahrens, M. Zehetbauer, W. Skrotzki, and J. Eckert. “Giant thermal expansion and α-precipitation pathways in Ti-alloys”. In: *Nat. Commun.* 8.1 (2017), p. 1429. DOI: `10.1038/s41467-017-01578-1`.

[126] M. Bönisch, T. Waitz, M. Calin, W. Skrotzki, and J. Eckert. “Tailoring the Bain strain of martensitic transformations in Ti-Nb alloys by controlling the Nb content”. In: *Int. J. Plast.* 85 (2016), pp. 190–202. DOI: `10.1016/j.ijplas.2016.07.010`.

[127] M. Bönisch, M. Stoica, and M. Calin. “Routes to control diffusive pathways and thermal expansion in Ti-alloys”. In: *Sci. Rep.* 10.1 (2020), pp. 1–9. DOI: `10.1038/s41598-020-60038-x`.

[128] S. Hanada, T. Ozaki, E. Takahashi, S. Watanabe, K. Yoshimi, and T. Abumiya. “Composition Dependence of Young’s Modulus in Beta Titanium Binary Alloys”. In: *Mater. Sci. Forum* 426-432.4 (2003), pp. 3103–3108. DOI: `10.4028/www.scientific.net/MSF.426-432.3103`.

[129] M. H. Tan, A. D. Baghi, R. Ghomashchi, W. Xiao, and R. H. Oskouei. “Effect of niobium content on the microstructure and Young’s modulus of Ti-xNb-7Zr alloys for medical implants”. In: *J. Mech. Behav. Biomed. Mater.* 99.May (2019), pp. 78–85. DOI: `10.1016/j.jmbbm.2019.07.014`.

[130] J. Strásky, D. Preisler, H. Seiner, L. Bodnárová, M. Janovská, T. Košutová, P. Harcuba, K. Šalata, K. Halmešová, J. Džugan, and M. Janeček. “Achieving high strength and low elas-

tic modulus in interstitial biomedical Ti–Nb–Zr–O alloys through compositional optimization". In: *Mater. Sci. Eng. A* 839 (2022), p. 142833. DOI: `10.1016/j.msea.2022.142833`.

[131] P. E. Moraes, R. J. Contieri, E. S. Lopes, A. Robin, and R. Caram. "Effects of Sn addition on the microstructure, mechanical properties and corrosion behavior of Ti–Nb–Sn alloys". In: *Mater. Charact.* 96 (2014), pp. 273–281. DOI: `10.1016/j.matchar.2014.08.014`.

[132] B. Zhu, Y. Zhang, Y. Chen, P. Yuan, W. Wang, H. Duan, and Z. Wang. "Synthesis, Characterization and Antimicrobial Studies of Ti-40Nb-10Ag Implant Biomaterials". In: *Metals (Basel).* 12.8 (2022), p. 1391. DOI: `10.3390/met12081391`.

[133] S. Pilz, D. Geissler, M. Calin, J. Eckert, M. Zimmermann, J. Freudenberger, and A. Gebert. "Thermomechanical processing of In-containing β-type Ti-Nb alloys". In: *J. Mech. Behav. Biomed. Mater.* 79.August 2017 (2018), pp. 283–291. DOI: `10.1016/j.jmbbm.2017.12.028`.

[134] Y. H. Hon, J. Y. Wang, and Y. N. Pan. "Influence of hafnium content on mechanical behaviors of Ti-40Nb-xHf alloys". In: *Mater. Lett.* 58.25 (2004), pp. 3182–3186. DOI: `10.1016/j.matlet.2004.06.009`.

[135] H. Y. Kim, J. Fu, H. Tobe, J. I. Kim, and S. Miyazaki. "Crystal Structure, Transformation Strain, and Superelastic Property of Ti–Nb–Zr and Ti–Nb–Ta Alloys". In: *Shape Mem. Superelasticity* 1.2 (2015), pp. 107–116. DOI: `10.1007/s40830-015-0022-3`.

[136] Y. L. Hao, S. J. Li, S. Y. Sun, C. Y. Zheng, and R. Yang. "Elastic deformation behaviour of Ti-24Nb-4Zr-7.9Sn for biomedical applications". In: *Acta Biomater.* 3.2 (2007), pp. 277–286. DOI: `10.1016/j.actbio.2006.11.002`.

[137] N. Mavros, T. Larimian, J. Esqivel, R. K. Gupta, R. Contieri, and T. Borkar. "Spark plasma sintering of low modulus titanium-niobium-tantalum-zirconium (TNTZ) alloy for biomedical applications". In: *Mater. Des.* 183 (2019). DOI: `10.1016/j.matdes.2019.108163`.

[138] S. X. Liang, X. J. Feng, L. X. Yin, X. Y. Liu, M. Z. Ma, and R. P. Liu. "Development of a new β Ti alloy with low modulus and favorable plasticity for implant material". In: *Mater. Sci. Eng. C* 61 (2016), pp. 338–343. DOI: `10.1016/j.msec.2015.12.076`.

[139] A. R. Vieira Nunes, S. Borborema, L. S. Araújo, L. Malet, J. Dille, and L. Henrique de Almeida. "Influence of thermo-mechanical processing on structure and mechanical properties of a new metastable β Ti–29Nb–2Mo–6Zr alloy with low Young's modulus". In: *J. Alloys Compd.* 820.xxxx (2020), p. 153078. DOI: `10.1016/j.jallcom.2019.153078`.

[140] F. Ghilini, D. E. Pissinis, A. Miñán, P. L. Schilardi, and C. Diaz. "How Functionalized Surfaces Can Inhibit Bacterial Adhesion and Viability". In: *ACS Biomater. Sci. Eng.* 5.10 (2019), pp. 4920–4936. DOI: `10.1021/acsbiomaterials.9b00849`.

[141] H. Koo, R. N. Allan, R. P. Howlin, P. Stoodley, and L. Hall-Stoodley. "Targeting microbial biofilms: Current and prospective therapeutic strategies". In: *Nat. Rev. Microbiol.* 15.12 (2017), pp. 740–755. DOI: `10.1038/nrmicro.2017.99`.

[142] M. Riool, A. de Breij, J. W. Drijfhout, P. H. Nibbering, and S. A. Zaat. "Antimicrobial peptides in biomedical device manufacturing". In: *Front. Chem.* AUG.2017 (2017), pp. 1–13. DOI: `10.3389/fchem.2017.00063`.

[143] E. M. Hetrick and M. H. Schoenfisch. "Reducing implant-related infections: active release strategies". In: *Chem. Soc. Rev.* 35.9 (2006), p. 780. DOI: `10.1039/b515219b`.

[144] S. V. V. S. Narayana P. and S. V. V. Srihari P. "A Review on Surface Modifications and Coatings on Implants to Prevent Biofilm". In: *Regen. Eng. Transl. Med.* 6 (2020), pp. 330–346. DOI: `10.1007/s40883-019-00116-3`.

[145] J. G. S. Souza, M. M. Bertolini, R. C. Costa, B. E. Nagay, A. Dongari-Bagtzoglou, and V. A. R. Barão. "Targeting implant-associated infections: titanium surface loaded with antimicrobial". In: *iScience* 24.1 (2021). DOI: `10.1016/j.isci.2020.102008`.

[146] A. Juhlin, S. Svensson, P. Thomsen, and M. Trobos. “Staphylococcal biofilm gene expression on biomaterials - A methodological study”. In: *J. Biomed. Mater. Res. Part A* 105.12 (2017), pp. 3400–3412. DOI: `10.1002/jbm.a.36171`.

[147] F. Song, H. Koo, and D. Ren. “Effects of material properties on bacterial adhesion and biofilm formation”. In: *J. Dent. Res.* 94.8 (2015), pp. 1027–1034. DOI: `10.1177/0022034515587690`.

[148] A. G. Gristina. “Biomaterial-Centered Infection: Microbial Adhesion Versus Tissue Integration”. In: *Science (80-.).* 237.4822 (1987), pp. 1588–1595. DOI: `10.1126/science.3629258`.

[149] S. Spriano, V. Sarath Chandra, A. Cochis, F. Uberti, L. Rimondini, E. Bertone, A. Vitale, C. Scolaro, M. Ferrari, F. Cirisano, G. Gautier di Confiengo, and S. Ferraris. “How do wettability, zeta potential and hydroxylation degree affect the biological response of biomaterials?” In: *Mater. Sci. Eng. C* 74 (2017), pp. 542–555. DOI: `10.1016/j.msec.2016.12.107`.

[150] S. Veerachamy, T. Yarlagadda, G. Manivasagam, and P. K. Yarlagadda. “Bacterial adherence and biofilm formation on medical implants: A review”. In: *Proc. Inst. Mech. Eng. Part H J. Eng. Med.* 228.10 (2014), pp. 1083–1099. DOI: `10.1177/0954411914556137`.

[151] E. Zhang, X. Zhao, J. Hu, R. Wang, S. Fu, and G. Qin. “Antibacterial metals and alloys for potential biomedical implants”. In: *Bioact. Mater.* 6.8 (2021), pp. 2569–2612. DOI: `10.1016/j.bioactmat.2021.01.030`.

[152] S. Duan, R. Wu, Y. H. Xiong, H. M. Ren, C. Lei, Y. Q. Zhao, X. Y. Zhang, and F. J. Xu. “Multifunctional antimicrobial materials: From rational design to biomedical applications”. In: *Prog. Mater. Sci.* 125.October 2021 (2022), p. 100887. DOI: `10.1016/j.pmatsci.2021.100887`.

[153] J. J. Harrison, H. Ceri, C. A. Stremick, and R. J. Turner. “Biofilm susceptibility to metal toxicity”. In: *Environ. Microbiol.* 6.12 (2004), pp. 1220–1227. DOI: `10.1111/j.1462-2920.2004.00656.x`.

[154] J. A. Lemire, J. J. Harrison, and R. J. Turner. “Antimicrobial activity of metals: Mechanisms, molecular targets and applications”. In: *Nat. Rev. Microbiol.* 11.6 (2013), pp. 371–384. DOI: `10.1038/nrmicro3028`.

[155] J. W. Betts, M. Hornsey, and R. M. La Ragione. Novel Antibacterials: Alternatives to Traditional Antibiotics. 1st ed. Vol. 73. Elsevier Ltd., 2018, pp. 123–169. ISBN: 9780128151907. DOI: `10.1016/bs.ampbs.2018.06.001`.

[156] F. Minandri, C. Bonchi, E. Frangipani, F. Imperi, and P. Visca. “Promises and failures of gallium as an antibacterial agent”. In: *Future Microbiol.* 9.3 (2014), pp. 379–397. DOI: `10.2217/fmb.14.3`.

[157] C. Bonchi, F. Imperi, F. Minandri, P. Visca, and E. Frangipani. “Repurposing of gallium-based drugs for antibacterial therapy”. In: *BioFactors* 40.3 (2014), pp. 303–312. DOI: `10.1002/biof.1159`.

[158] C. R. Chitambar. “Gallium-containing anticancer compounds”. In: *Future Med. Chem.* 4.10 (2012), pp. 1257–1272. DOI: `10.4155/fmc.12.69`.

[159] C. R. Chitambar. “Gallium and its competing roles with iron in biological systems”. In: *Biochim. Biophys. Acta - Mol. Cell Res.* 1863.8 (2016), pp. 2044–2053. DOI: `10.1016/j.bbamcr.2016.04.027`.

[160] E. Verron, J. M. Bouler, and J. C. Scimeca. “Gallium as a potential candidate for treatment of osteoporosis”. In: *Drug Discov. Today* 17.19-20 (2012), pp. 1127–1132. DOI: `10.1016/j.drudis.2012.06.007`.

[161] C. R. Chitambar. “The therapeutic potential of iron-targeting gallium compounds in human disease: From basic research to clinical application”. In: *Pharmacol. Res.* 115 (2017), pp. 56–64. DOI: `10.1016/j.phrs.2016.11.009`.

[162] F. Kurtuldu, N. Mutlu, A. R. Boccaccini, and D. Galusek. “Gallium containing bioactive materials: A review of anticancer, antibacterial, and osteogenic properties”. In: *Bioact. Mater.* 17.December 2021 (2022), pp. 125–146. DOI: `10.1016/j.bioactmat.2021.12.034`.

[163] D. M. Pickup, S. P. Valappil, R. M. Moss, H. L. Twyman, P. Guerry, M. E. Smith, M. Wilson, J. C. Knowles, and R. J. Newport. “Preparation, structural characterisation and antibacterial properties of Ga-doped sol–gel phosphate-based glass”. In: *J. Mater. Sci.* 44.7 (2009), pp. 1858–1867. DOI: `10.1007/s10853-008-3237-2`.

[164] K. Girija, S. Thirumalairajan, and D. Mangalaraj. “Morphology controllable synthesis of parallely arranged single-crystalline β-Ga2O3 nanorods for photocatalytic and antimicrobial activities”. In: *Chem. Eng. J.* 236 (2014), pp. 181–190. DOI: `10.1016/j.cej.2013.09.088`.

[165] S. Nazri and M. A. A. M. Salleh. “The Effects of Gallium Additions on the Microstructure of Lead-Free Solder Materials: A Short Review”. In: *Solid State Phenom.* 280 (2018), pp. 187–193. DOI: `10.4028/www.scientific.net/SSP.280.187`.

[166] D. G. Kolman and L. P. Colletti. “Aqueous Corrosion Behavior of Plutonium Metal and Plutonium–Gallium Alloys Exposed to Aqueous Nitrate and Chloride Solutions”. In: *J. Electrochem. Soc.* 155.12 (2008), p. C565. DOI: `10.1149/1.2976352`.

[167] A. A. Hernández-Cortés, J. C. Escobedo-Bocardo, D. A. Cortés-Hernández, and J. M. Almanza-Robles. “Effect of Gallium Content and Heat Treatment on the Microstructure and Corrosion Rate of Magnesium Binary Alloys”. In: *Metals (Basel).* 9.9 (2019), p. 990. DOI: `10.3390/met9090990`.

[168] K. J. Qiu, W. J. Lin, F. Y. Zhou, H. Q. Nan, B. L. Wang, L. Li, J. P. Lin, Y. F. Zheng, and Y. H. Liu. “Ti-Ga binary alloys developed as potential dental materials”. In: *Mater. Sci. Eng. C* 34.1 (2014), pp. 474–483. DOI: `10.1016/j.msec.2013.10.004`.

[169] X. Liu, S. Chen, J. K. Tsoi, and J. P. Matinlinna. “Binary titanium alloys as dental implant materials-a review”. In: *Regen. Biomater.* 4.5 (2017), pp. 315–323. DOI: `10.1093/rb/rbx027`.

[170] J. Kubásek, D. Vojtěch, J. Lipov, and T. Ruml. “Structure, mechanical properties, corrosion behavior and cytotoxicity of biodegradable Mg–X (X=Sn, Ga, In) alloys”. In: *Mater. Sci. Eng. C* 33.4 (2013), pp. 2421–2432. DOI: `10.1016/j.msec.2013.02.005`.

[171] J. A. Lessa, G. L. Parrilha, and H. Beraldo. “Gallium complexes as new promising metallodrug candidates”. In: *Inorganica Chim. Acta* 393 (2012), pp. 53–63. DOI: `10.1016/j.ica.2012.06.003`.

[172] E. Verron, M. Masson, S. Khoshniat, L. Duplomb, Y. Wittrant, M. Baud’Huin, Z. Badran, B. Bujoli, P. Janvier, J. C. Scimeca, J. M. Bouler, and J. Guicheux. “Gallium modulates osteoclastic bone resorption in vitro without affecting osteoblasts”. In: *Br. J. Pharmacol.* 159.8 (2010), pp. 1681–1692. DOI: `10.1111/j.1476-5381.2010.00665.x`.

[173] A. Cochis, B. Azzimonti, C. Della Valle, E. De Giglio, N. Bloise, L. Visai, S. Cometa, L. Rimondini, and R. Chiesa. “The effect of silver or gallium doped titanium against the multidrug resistant Acinetobacter baumannii”. In: *Biomaterials* 80 (2016), pp. 80–95. DOI: `10.1016/j.biomaterials.2015.11.042`.

[174] C. H. Goss, Y. Kaneko, L. Khuu, G. D. Anderson, S. Ravishankar, M. L. Aitken, N. Lechtzin, G. Zhou, D. M. Czyz, K. McLean, O. Olakanmi, H. A. Shuman, M. Teresi, E. Wilhelm, E. Caldwell, S. J. Salipante, D. B. Hornick, R. J. Siehnel, L. Becker, B. E. Britigan, and P. K. Singh. “Gallium disrupts bacterial iron metabolism and has therapeutic effects in mice and humans with lung infections”. In: *Sci. Transl. Med.* 10.460 (2018), pp. 1–12. DOI: `10.1126/scitranslmed.aat7520`.

[175] L. C. Antunes, F. Imperi, F. Minandri, and P. Visca. “In Vitro and In Vivo antimicrobial activities of gallium nitrate against multidrug-resistant acinetobacter baumannii”. In: *Antimicrob. Agents Chemother.* 56.11 (2012), pp. 5961–5970. DOI: `10.1128/AAC.01519-12`.

[176] P. Wang, Y. Yuan, K. Xu, H. Zhong, Y. Yang, S. Jin, K. Yang, and X. Qi. “Biological applications of copper-containing materials”. In: *Bioact. Mater.* 6.4 (2021), pp. 916–927. DOI: `10.1016/j.bioactmat.2020.09.017`.

[177] L. M. Gaetke and C. K. Chow. "Copper toxicity, oxidative stress, and antioxidant nutrients". In: *Toxicology* 189.1-2 (2003), pp. 147–163. DOI: `10.1016/S0300-483X(03)00159-8`.

[178] M. Valko, H. Morris, and M. Cronin. "Metals, Toxicity and Oxidative Stress". In: *Curr. Med. Chem.* Vol. 12. 10. 2005, pp. 1161–1208. DOI: `10.2174/0929867053764635`.

[179] M. Vincent, P. Hartemann, and M. Engels-Deutsch. "Antimicrobial applications of copper". In: *Int. J. Hyg. Environ. Health* 219.7 (2016), pp. 585–591. DOI: `10.1016/j.ijheh.2016.06.003`.

[180] V. Govind, S. Bharadwaj, M. R. Sai Ganesh, J. Vishnu, K. V. Shankar, B. Shankar, and R. Rajesh. "Antiviral properties of copper and its alloys to inactivate covid-19 virus: a review". In: *BioMetals* 4 (2021). DOI: `10.1007/s10534-021-00339-4`.

[181] G. Grass, C. Rensing, and M. Solioz. "Metallic copper as an antimicrobial surface". In: *Appl. Environ. Microbiol.* 77.5 (2011), pp. 1541–1547. DOI: `10.1128/AEM.02766-10`.

[182] J. Inkinen, R. Mäkinen, M. Keinänen-Toivola, K. Nordström, and M. Ahonen. "Copper as an antibacterial material in different facilities". In: *Lett. Appl. Microbiol.* 64.1 (2017), pp. 19–26. DOI: `10.1111/lam.12680`.

[183] I. B. Gomes, M. Simões, and L. C. Simões. "Copper Surfaces in Biofilm Control". In: *Nanomaterials* 10.12 (2020), p. 2491. DOI: `10.3390/nano10122491`.

[184] J. S. Fernandes, P. Gentile, R. A. Pires, R. L. Reis, and P. V. Hatton. "Multifunctional bioactive glass and glass-ceramic biomaterials with antibacterial properties for repair and regeneration of bone tissue". In: *Acta Biomater.* 59 (2017), pp. 2–11. DOI: `10.1016/j.actbio.2017.06.046`.

[185] S. Kargozar, M. Montazerian, S. Hamzehlou, H.-W. Kim, and F. Baino. "Mesoporous bioactive glasses: Promising platforms for antibacterial strategies". In: *Acta Biomater.* 81 (2018), pp. 1–19. DOI: `10.1016/j.actbio.2018.09.052`.

[186] L. Tamayo, M. Azócar, M. Kogan, A. Riveros, and M. Páez. "Copper-polymer nanocomposites: An excellent and cost-effective biocide for use on antibacterial surfaces". In: *Mater. Sci. Eng. C* 69 (2016), pp. 1391–1409. DOI: `10.1016/j.msec.2016.08.041`.

[187] E. L. Zhang, S. Fu, R. X. Wang, H. X. Li, Y. Liu, Z. Q. Ma, G. K. Liu, C. S. Zhu, G. W. Qin, and D. F. Chen. "Role of Cu element in biomedical metal alloy design". In: *Rare Met.* 38.6 (2019), pp. 476–494. DOI: `10.1007/s12598-019-01245-y`.

[188] L. Zhang, M.-L. Ward, A. R. Phillips, S. Zhang, J. Kennedy, B. Barry, M. B. Cannell, and G. J. Cooper. "Protection of the heart by treatment with a divalent-copper-selective chelator reveals a novel mechanism underlying cardiomyopathy in diabetic rats". In: *Cardiovasc. Diabetol.* 12.1 (2013), p. 123. DOI: `10.1186/1475-2840-12-123`.

[189] T. Fukai, M. Ushio-Fukai, and J. H. Kaplan. "Copper transporters and copper chaperones: roles in cardiovascular physiology and disease". In: *Am. J. Physiol. Physiol.* 315.2 (2018), pp. C186–C201. DOI: `10.1152/ajpcell.00132.2018`.

[190] L. Ren, H. M. Wong, C. H. Yan, K. W. Yeung, and K. Yang. "Osteogenic ability of Cu-bearing stainless steel". In: *J. Biomed. Mater. Res. - Part B Appl. Biomater.* 103.7 (2015), pp. 1433–1444. DOI: `10.1002/jbm.b.33318`.

[191] J. Konieczny, Z. Rdzawski, B. Li, J. Drelich, J. Konieczny, and Z. Rdzawski. "Antibacterial properties of copper and its alloys". In: *Arch. Mater. Sci. Eng.* 56.2 (2012), pp. 53–60.

[192] M. Li, Z. Ma, Y. Zhu, H. Xia, M. Yao, X. Chu, X. Wang, K. Yang, M. Yang, Y. Zhang, and C. Mao. "Toward a Molecular Understanding of the Antibacterial Mechanism of Copper-Bearing Titanium Alloys against Staphylococcus aureus". In: *Adv. Healthc. Mater.* 5.5 (2016), pp. 557–566. DOI: `10.1002/adhm.201500712`.

[193] R. Liu, K. Memarzadeh, B. Chang, Y. Zhang, Z. Ma, R. P. Allaker, L. Ren, and K. Yang. "Antibacterial effect of copper-bearing titanium alloy (Ti-Cu) against Streptococcus mutans and Porphyromonas gingivalis". In: *Sci. Rep.* 6.1 (2016), p. 29985. DOI: `10.1038/srep29985`.

[194] D. Xu, T. Wang, S. Wang, Y. Jiang, Y. Wang, Y. Chen, Z. Bi, and S. Geng. "Antibacterial Effect of the Controlled Nanoscale Precipitates Obtained by Different Heat Treatment Schemes with a Ti-Based Nanomaterial, Ti–7.5Mo–5Cu Alloy". In: *ACS Appl. Bio Mater.* 3.9 (2020), pp. 6145–6154. DOI: `10.1021/acsabm.0c00716`.

[195] A. Jacobs, G. Renaudin, C. Forestier, J. M. Nedelec, and S. Descamps. "Biological properties of copper-doped biomaterials for orthopedic applications: A review of antibacterial, angiogenic and osteogenic aspects". In: *Acta Biomater.* 117 (2020), pp. 21–39. DOI: `10.1016/j.actbio.2020.09.044`.

[196] V. Brezova, M. Valko, M. Breza, H. Morris, J. Telser, D. Dvoranova, K. Kaiserova, L. Varecka, M. Mazur, and D. Leibfritz. "Role of Radicals and Singlet Oxygen in Photoactivated DNA Cleavage by the Anticancer Drug Camptothecin: An Electron Paramagnetic Resonance Study". In: *J. Phys. Chem. B* 107.10 (2003), pp. 2415–2425. DOI: `10.1021/jp027743m`.

[197] P. Mahmoudi, M. R. Akbarpour, H. B. Lakeh, F. Jing, M. R. Hadidi, and B. Akhavan. "Antibacterial Ti–Cu implants: A critical review on mechanisms of action". In: *Mater. Today Bio* 17.September (2022), p. 100447. DOI: `10.1016/j.mtbio.2022.100447`.

[198] O. N. Senkov and D. B. Miracle. "Effect of the atomic size distribution on glass forming ability of amorphous metallic alloys". In: *Mater. Res. Bull.* 36.12 (2001), pp. 2183–2198. DOI: `10.1016/S0025-5408(01)00715-2`.

[199] F. Cardarelli. Materials Handbook: A Concise Desktop Reference. Cham: Springer Cham, 2018. ISBN: 978-3-319-38923-3. DOI: `10.1007/978-3-319-38925-7`.

[200] A. Cochis, B. Azzimonti, R. Chiesa, L. Rimondini, and M. Gasik. "Metallurgical Gallium Additions to Titanium Alloys Demonstrate a Strong Time-Increasing Antibacterial Activity without any Cellular Toxicity". In: *ACS Biomater. Sci. Eng.* 5.6 (2019), pp. 2815–2820. DOI: `10.1021/acsbiomaterials.9b00147`.

[201] H. Y. Kim, Y. Ohmatsu, J. Kim, H. Hosoda, and S. Miyazaki. "Mechanical properties and shape memory behavior of Ti-Mo-Ga alloys". In: *Mater. Trans.* 45.4 (2004), pp. 1090–1095. DOI: `10.2320/matertrans.45.1090`.

[202] E. Zhang, J. Ren, S. Li, L. Yang, and G. Qin. "Optimization of mechanical properties, biocorrosion properties and antibacterial properties of as-cast Ti–Cu alloys". In: *Biomed. Mater.* 11.6 (2016), p. 065001. DOI: `10.1088/1748-6041/11/6/065001`.

[203] J. H. Wu, K. K. Chen, C. Y. Chao, Y. H. Chang, and J. K. Du. "Effect of Ti2Cu precipitation on antibacterial property of Ti-5Cu alloy". In: *Mater. Sci. Eng. C* 108.November 2019 (2020). DOI: `10.1016/j.msec.2019.110433`.

[204] L. Fowler, N. Masia, L. A. Cornish, L. H. Chown, H. Engqvist, S. Norgren, and C. Öhman-Mägi. "Development of Antibacterial Ti-Cux Alloys for Dental Applications: Effects of Ageing for Alloys with Up to 10 wt% Cu". In: *Materials (Basel).* 12.23 (2019), p. 4017. DOI: `10.3390/ma12234017`.

[205] E. Zhang, X. Wang, M. Chen, and B. Hou. "Effect of the existing form of Cu element on the mechanical properties, bio-corrosion and antibacterial properties of Ti-Cu alloys for biomedical application". In: *Mater. Sci. Eng. C* 69 (2016), pp. 1210–1221. DOI: `10.1016/j.msec.2016.08.033`.

[206] E. Zhang, F. Li, H. Wang, J. Liu, C. Wang, M. Li, and K. Yang. "A new antibacterial titanium-copper sintered alloy: Preparation and antibacterial property". In: *Mater. Sci. Eng. C* 33.7 (2013), pp. 4280–4287. DOI: `10.1016/j.msec.2013.06.016`.

[207] S. Moniri Javadhesari, S. Alipour, and M. R. Akbarpour. "Biocompatibility, osseointegration, antibacterial and mechanical properties of nanocrystalline Ti-Cu alloy as a new orthopedic material". In: *Colloids Surfaces B Biointerfaces* 189.August 2019 (2020), p. 110889. DOI: `10.1016/j.colsurfb.2020.110889`.

[208] A. K. Pandey, R. K. Gautam, and C. K. Behera. “Microstructure, mechanical strength, chemical resistance, and antibacterial behavior of Ti–5Cu–x%Nb biomedical alloy”. In: *Biomed. Mater.* 17.4 (2022), p. 045022. DOI: `10.1088/1748-605X/ac7763`.

[209] C. Yi, Y. Yuan, L. Zhang, Y. Jiang, and Z. He. “Antibacterial Ti-35Nb-7Zr-xCu alloy with excellent mechanical properties generated with a spark plasma sintering method for biological applications”. In: *J. Alloys Compd.* 879 (2021), p. 160473. DOI: `10.1016/j.jallcom.2021.160473`.

[210] Y. Horiuchi, K. Nakayama, T. Inamura, H. Y. Kim, K. Wakashima, S. Miyazaki, and H. Hosoda. “Effect of Cu addition on shape memory behavior of Ti-18 mol%Nb alloys”. In: *Mater. Trans.* 48.3 (2007), pp. 414–421. DOI: `10.2320/matertrans.48.414`.

[211] M. Takahashi, M. Kikuchi, and Y. Takada. “Grindability of Ti−Nb−Cu Alloys for Dental Machining Applications”. In: *Metals (Basel).* 12.5 (2022), pp. 1–11. DOI: `10.3390/met12050861`.

[212] L. Fowler, A. J. van Vuuren, W. Goosen, H. Engqvist, C. Öhman-Mägi, and S. Norgren. “Investigation of copper alloying in a TNTZ-Cux alloy”. In: *Materials (Basel).* 12.22 (2019), pp. 1–13. DOI: `10.3390/ma12223691`.

[213] Z. Ma, L. Ren, R. Liu, K. Yang, Y. Zhang, Z. Liao, W. Liu, M. Qi, and R. D. Misra. “Effect of Heat Treatment on Cu Distribution, Antibacterial Performance and Cytotoxicity of Ti-6Al-4V-5Cu Alloy”. In: *J. Mater. Sci. Technol.* 31.7 (2015), pp. 723–732. DOI: `10.1016/j.jmst.2015.04.002`.

[214] S. Guo, Y. Lu, S. Wu, L. Liu, M. He, C. Zhao, Y. Gan, J. Lin, J. Luo, X. Xu, and J. Lin. “Preliminary study on the corrosion resistance, antibacterial activity and cytotoxicity of selective-laser-melted Ti6Al4V- x Cu alloys”. In: *Mater. Sci. Eng. C* 72 (2017), pp. 631–640. DOI: `10.1016/j.msec.2016.11.126`.

[215] N. V. Antonova and L. A. Tretyachenko. “Phase diagram of the Ti-Ga system”. In: *J. Alloys Compd.* 317-318 (2001), pp. 398–405. DOI: `10.1016/S0925-8388(00)01416-X`.

[216] H. Okamoto, M. Schlesinger, and E. Mueller, eds. ASM Handbook: Alloy Phase Diagrams (Volume 3). ASM International, 2016. ISBN: 978-1-62708-163-4. DOI: `10.31399/asm.hb.v03.9781627081634`.

[217] H. Hosoda, Y. Fukui, T. Inamura, K. Wakashima, and S. Miyazaki. “Mechanical Properties of Ti-Nb Biomedical Shape Memory Alloys Containing 13- and 14-Group Elements”. In: *Mater. Sci. Forum* 475-479 (2005), pp. 2329–2332. DOI: `10.4028/www.scientific.net/msf.475-479.2329`.

[218] J. W. Sim, J. H. Kim, C. H. Park, J.-K. Hong, J.-T. Yeom, and S. W. Lee. “Effect of phase conditions on tensile and antibacterial properties of Ti-Cu alloys with Ti2Cu intermetallic compound”. In: *J. Alloys Compd.* 926 (2022), p. 166823. DOI: `10.1016/j.jallcom.2022.166823`.

[219] M. Kikuchi, Y. Takada, S. Kiyosue, M. Yoda, M. Woldu, Z. Cai, O. Okuno, and T. Okabe. “Mechanical properties and microstructures of cast Ti-Cu alloys”. In: *Dent. Mater.* 19.3 (2003), pp. 174–181. DOI: `10.1016/S0109-5641(02)00027-1`.

[220] T. Shirai, H. Tsuchiya, T. Shimizu, K. Ohtani, Y. Zen, and K. Tomita. “Prevention of pin tract infection with titanium-copper alloys”. In: *J. Biomed. Mater. Res. - Part B Appl. Biomater.* 91.1 (2009), pp. 373–380. DOI: `10.1002/jbm.b.31412`.

[221] J. Wang, S. Zhang, Z. Sun, H. Wang, L. Ren, and K. Yang. “Optimization of mechanical property, antibacterial property and corrosion resistance of Ti-Cu alloy for dental implant”. In: *J. Mater. Sci. Technol.* 35.10 (2019), pp. 2336–2344. DOI: `10.1016/j.jmst.2019.03.044`.

[222] C. Liu and E. Zhang. “Biocorrosion properties of antibacterial Ti–10Cu sintered alloy in several simulated biological solutions”. In: *J. Mater. Sci. Mater. Med.* 26.3 (2015). DOI: `10.1007/s10856-015-5459-6`.

[223] M. R. Akbarpour, H. M. Mirabad, A. Hemmati, and H. S. Kim. “Processing and microstructure of Ti-Cu binary alloys: A comprehensive review”. In: *Prog. Mater. Sci.* 127.March 2021 (2022), p. 100933. DOI: `10.1016/j.pmatsci.2022.100933`.

[224] M. Koike, Z. Cai, Y. Oda, M. Hattori, H. Fujii, and T. Okabe. “Corrosion behavior of cast Ti-6Al-4V alloyed with Cu”. In: *J. Biomed. Mater. Res. - Part B Appl. Biomater.* 73.2 (2005), pp. 368–374. DOI: `10.1002/jbm.b.30225`.

[225] S. Wang, Z. Ma, Z. Liao, J. Song, K. Yang, and W. Liu. “Study on improved tribological properties by alloying copper to CP-Ti and Ti-6Al-4V alloy”. In: *Mater. Sci. Eng. C* 57 (2015), pp. 123–132. DOI: `10.1016/j.msec.2015.07.046`.

[226] M. Takahashi, K. Sato, G. Togawa, and Y. Takada. “Mechanical Properties of Ti-Nb-Cu Alloys for Dental Machining Applications”. In: *J. Funct. Biomater.* 13.4 (2022), p. 263. DOI: `10.3390/jfb13040263`.

[227] H. Xu, Y. Du, B. Huang, and S. Liu. “Phase equilibria of the Cu–Nb–Ti system at 850°C”. In: *J. Alloys Compd.* 399.1-2 (2005), pp. 92–95. DOI: `10.1016/j.jallcom.2005.02.039`.

[228] H. Donthula, B. Vishwanadh, T. Alam, T. Borkar, R. Contieri, R. Caram, R. Banerjee, R. Tewari, G. Dey, and S. Banerjee. “Morphological evolution of transformation products and eutectoid transformation(s) in a hyper-eutectoid Ti-12 at% Cu alloy”. In: *Acta Mater.* 168 (2019), pp. 63–75. DOI: `10.1016/j.actamat.2019.01.044`.

[229] M. A. Turchanin, P. G. Agraval, and A. R. Abdulov. “Thermodynamic assessment of the Cu-Ti-Zr system. II. Cu-Zr and Ti-Zr systems”. In: *Powder Metall. Met. Ceram.* 47.7-8 (2008), pp. 428–446. DOI: `10.1007/s11106-008-9039-x`.

[230] D. J. Chakrabarti and D. E. Laughlin. “The Cu−Nb (Copper-Niobium) system”. In: *J. Phase Equilibria* 2.4 (1982), pp. 455–460. DOI: `10.1007/BF02876162`.

[231] M. Hämäläinen, K. Jääskeläinen, R. Luoma, M. Nuotio, P. Taskinen, and O. Teppo. “A thermodynamic analysis of the binary alloy systems Cu-Cr, Cu-Nb and Cu-V”. In: *Calphad* 14.2 (1990), pp. 125–137. DOI: `10.1016/0364-5916(90)90014-Q`.

[232] Y. Zhang, B. Hu, G. Zeng, S. Liu, Y. Du, and H. Yin. “Experimental investigation, thermodynamic modeling and solidified microstructure of the Cu–Ti–Nb ternary system”. In: *Calphad* 76.6 (2022), p. 102395. DOI: `10.1016/j.calphad.2022.102395`.

[233] M. Takahashi, M. Kikuchi, and Y. Takada. “Mechanical properties and microstructures of dental cast Ti-6Nb-4Cu, Ti-18Nb-2Cu, and Ti-24Nb-1Cu alloys”. In: *Dent. Mater. J.* 35.4 (2016), pp. 564–570. DOI: `10.4012/dmj.2015-354`.

[234] Z. Zhang, G. Zheng, H. Li, L. Yang, X. Wang, G. Qin, and E. Zhang. “Anti-bacterium influenced corrosion effect of antibacterial Ti-3Cu alloy in Staphylococcus aureus suspension for biomedical application”. In: *Mater. Sci. Eng. C* 94.August 2018 (2019), pp. 376–384. DOI: `10.1016/j.msec.2018.09.057`.

[235] V. G. Pina, V. Amigó, and A. I. Muñoz. “Microstructural, electrochemical and tribo-electrochemical characterisation of titanium-copper biomedical alloys”. In: *Corros. Sci.* 109 (2016), pp. 115–125. DOI: `10.1016/j.corsci.2016.02.014`.

[236] Y. Xu, J. Jiang, Z. Yang, Q. Zhao, Y. Chen, and Y. Zhao. “The Effect of Copper Content on the Mechanical and Tribological Properties of Hypo-, Hyper- and Eutectoid Ti-Cu Alloys”. In: *Materials (Basel).* 13.15 (2020), p. 3411. DOI: `10.3390/ma13153411`.

[237] L. Bolzoni, M. Alqattan, L. Peters, Y. Alshammari, and F. Yang. “Ternary Ti alloys functionalised with antibacterial activity”. In: *Sci. Rep.* 10.1 (2020), p. 22201. DOI: `10.1038/s41598-020-79192-3`.

[238] R. Liu, Y. Tang, L. Zeng, Y. Zhao, Z. Ma, Z. Sun, L. Xiang, L. Ren, and K. Yang. “In vitro and in vivo studies of anti-bacterial copper-bearing titanium alloy for dental application”. In: *Dent. Mater.* 34.8 (2018), pp. 1112–1126. DOI: `10.1016/j.dental.2018.04.007`.

[239] R. A. Young. The Rietveld method. 1993.

[240] S. J. Wu, P. C. Chin, and H. Liu. "Measurement of elastic properties of brittle materials by ultrasonic and indentation methods". In: *Appl. Sci.* 9.10 (2019). DOI: `10.3390/app9102067`.

[241] ISO 6892-1:2019 - Metallic materials — Tensile testing — Part 1: Method of test at room temperature. 2020. URL: `https://www.iso.org/standard/78322.html`.

[242] DIN 50106:2016-11 - Testing of metallic materials - Compression test at room temperature. 2016. URL: `https://www.beuth.de/de/norm/din-50106/257662838`.

[243] A. E. Matusevich, J. C. Massa, and R. A. Mancini. "Computation of tensile strain-hardening exponents through the power-law relationship". In: *J. Test. Eval.* 40.4 (2012). DOI: `10.1520/JTE104226`.

[244] ASTM E646-16 - Standard Test Method for Tensile Strain-Hardening Exponents (n - Values) of Metallic Sheet Materials. URL: `https://www.astm.org/e0646-16.html`.

[245] W. Rasband. ImageJ, U. S. National Institutes of Health, Bethesda, Maryland, USA. URL: `https://imagej.nih.gov/ij/`.

[246] M. Stemp, S. Mischler, and D. Landolt. "The effect of mechanical and electrochemical parameters on the tribocorrosion rate of stainless steel in sulphuric acid". In: *Wear* 255.1-6 (2003), pp. 466–475. DOI: `10.1016/S0043-1648(03)00085-1`.

[247] V. Dalbert, N. Mary, B. Normand, C. Verdu, and S. Saedlou. "In situ determinations of the wear surfaces, volumes and kinetics of repassivation: Contribution in the understanding of the tribocorrosion behaviour of a ferritic stainless steel in various pH". In: *Tribol. Int.* 150.October 2019 (2020), p. 106374. DOI: `10.1016/j.triboint.2020.106374`.

[248] J. Stojadinović, D. Bouvet, M. Declercq, and S. Mischler. "Effect of electrode potential on the tribocorrosion of tungsten". In: *Tribol. Int.* 42.4 (2009), pp. 575–583. DOI: `10.1016/j.triboint.2008.04.009`.

[249] S. Mischler, A. Spiegel, M. Stemp, and D. Landolt. "Influence of passivity on the tribocorrosion of carbon steel in aqueous solutions". In: *Wear* 250-251.PART 2 (2001), pp. 1295–1307. DOI: `10.1016/s0043-1648(01)00754-2`.

[250] S. Cao, S. Guadalupe Maldonado, and S. Mischler. "Tribocorrosion of passive metals in the mixed lubrication regime: Theoretical model and application to metal-on-metal artificial hip joints". In: *Wear* 324-325 (2015), pp. 55–63. DOI: `10.1016/j.wear.2014.12.003`.

[251] A. C. Vieira, L. A. Rocha, N. Papageorgiou, and S. Mischler. "Mechanical and electrochemical deterioration mechanisms in the tribocorrosion of Al alloys in NaCl and in NaNO3 solutions". In: *Corros. Sci.* 54.1 (2012), pp. 26–35. DOI: `10.1016/j.corsci.2011.08.041`.

[252] DIN EN ISO 10993-15:2009-10 - Biological evaluation of medical devices - Part 15: Identification and quantification of degradation products from metals and alloys. URL: `https://www.beuth.de/en/standard/din-en-iso-10993-15/119643001`.

[253] JASP Team. JASP (Version 0.16.2). 2022. URL: `https://jasp-stats.org/`.

[254] A. O. Hayama, P. N. Andrade, A. Cremasco, R. J. Contieri, C. R. Afonso, and R. Caram. "Effects of composition and heat treatment on the mechanical behavior of Ti-Cu alloys". In: *Mater. Des.* 55 (2014), pp. 1006–1013. DOI: `10.1016/j.matdes.2013.10.050`.

[255] L. A. Alberta, Y. Fortouna, J. Vishnu, S. Pilz, A. Gebert, C. Lekka, K. Nielsch, and M. Calin. "Effects of Ga on the structural, mechanical and electronic properties of β-Ti-45Nb alloy by experiments and ab initio calculations". In: *J. Mech. Behav. Biomed. Mater.* 140 (2023), p. 105728. DOI: `10.1016/j.jmbbm.2023.105728`.

[256] H. Y. Kim, S. Hashimoto, J. I. Kim, H. Hosoda, and S. Miyazaki. "Mechanical Properties and Shape Memory Behavior of Ti-Nb Alloys". In: *Mater. Trans.* 45.7 (2004), pp. 2443–2448. DOI: `10.2320/matertrans.45.2443`.

[257] H. Aboulfadl, J. Deges, P. Choi, and D. Raabe. "Dynamic strain aging studied at the atomic scale". In: *Acta Mater.* 86 (2015), pp. 34–42. DOI: `10.1016/j.actamat.2014.12.028`.

[258] G. W. R. Ardley and A. H. S. Cottrell. “Yield points in brass crystals”. In: *Proc. R. Soc. London. Ser. A. Math. Phys. Sci.* 219.1138 (1953), pp. 328–340. DOI: `10.1098/rspa.1953.0150`.

[259] G. Ananthakrishna. “Current theoretical approaches to collective behavior of dislocations”. In: *Phys. Rep.* 440.4-6 (2007), pp. 113–259. DOI: `10.1016/j.physrep.2006.10.003`.

[260] M. J. Lai, C. C. Tasan, and D. Raabe. “Deformation mechanism of ω-enriched Ti-Nb-based gum metal: Dislocation channeling and deformation induced ω-β transformation”. In: *Acta Mater.* 100 (2015), pp. 290–300. DOI: `10.1016/j.actamat.2015.08.047`.

[261] L. A. Alberta, J. Vishnu, A. Hariharan, S. Pilz, A. Gebert, and M. Calin. “Novel low modulus beta-type Ti–Nb alloys by gallium and copper minor additions for antibacterial implant applications”. In: *J. Mater. Res. Technol.* 20 (2022), pp. 3306–3322. DOI: `10.1016/j.jmrt.2022.08.111`.

[262] M. Radovic, E. Lara-Curzio, and L. Riester. “Comparison of different experimental techniques for determination of elastic properties of solids”. In: *Mater. Sci. Eng. A* 368.1-2 (2004), pp. 56–70. DOI: `10.1016/j.msea.2003.09.080`.

[263] A. Badidi Bouda. “Grain size influence on ultrasonic velocities and attenuation”. In: *NDT E Int.* 36.1 (2003), pp. 1–5. DOI: `10.1016/S0963-8695(02)00043-9`.

[264] W. Elmay, F. Prima, T. Gloriant, B. Bolle, Y. Zhong, E. Patoor, and P. Laheurte. “Effects of thermomechanical process on the microstructure and mechanical properties of a fully martensitic titanium-based biomedical alloy”. In: *J. Mech. Behav. Biomed. Mater.* 18 (2013), pp. 47–56. DOI: `10.1016/j.jmbbm.2012.10.018`.

[265] A. Reck, S. Pilz, M. Kuczyk, A. Gebert, and M. Zimmermann. “Cyclic deformation characteristics of the metastable β-type Ti–40Nb alloy”. In: *Mater. Sci. Eng. A* 761.May (2019), p. 137966. DOI: `10.1016/j.msea.2019.05.096`.

[266] S. Sadeghpour, V. Javaheri, S. Bruschi, J. Kömi, and P. Karjalainen. “Strain rate and mechanical stability in determining deformation behavior of beta Ti alloys”. In: *Mater. Sci. Eng. A* 798.July (2020). DOI: `10.1016/j.msea.2020.140274`.

[267] D. Kent, G. Wang, and M. Dargusch. “Effects of phase stability and processing on the mechanical properties of Ti–Nb based β Ti alloys”. In: *J. Mech. Behav. Biomed. Mater.* 28 (2013), pp. 15–25. DOI: `10.1016/j.jmbbm.2013.07.007`.

[268] T. Saito, T. Furuta, J.-H. Hwang, S. Kuramoto, K. Nishino, N. Suzuki, R. Chen, A. Yamada, K. Ito, Y. Seno, T. Nonaka, H. Ikehata, N. Nagasako, C. Iwamoto, Y. Ikuhara, and T. Sakuma. “Multifunctional Alloys Obtained via a Dislocation-Free Plastic Deformation Mechanism”. In: *Science (80-.).* 300.5618 (2003), pp. 464–467. DOI: `10.1126/science.1081957`.

[269] G. P. Tiwari and R. V. Ramanujan. “Relation between the electron to atom ratio and some properties of metallic systems”. In: *J. Mater. Sci.* 36.2 (2001), pp. 271–283. DOI: `10.1023/A:1004853304704`.

[270] L. Ren, Z. Ma, M. Li, Y. Zhang, W. Liu, Z. Liao, and K. Yang. “Antibacterial properties of Ti-6Al-4V-xCu alloys”. In: *J. Mater. Sci. Technol.* 30.7 (2014), pp. 699–705. DOI: `10.1016/j.jmst.2013.12.014`.

[271] J. Vishnu, A. Ansheed, P. Hameed, K. Praveenkumar, S. Pilz, L. A. Alberta, S. Swaroop, M. Calin, A. Gebert, and G. Manivasagam. “Insights into the surface and biocompatibility aspects of laser shock peened Ti-22Nb alloy for orthopedic implant applications”. In: *Appl. Surf. Sci.* 586.June (2022), p. 152816. DOI: `10.1016/j.apsusc.2022.152816`.

[272] I. Mutlu, S. Yeniyol, and E. Oktay. “Characterisation of corrosion properties of Ti–Nb–Cu alloy foam by electrochemical impedance spectroscopy method”. In: *Corros. Eng. Sci. Technol.* 51.2 (2016), pp. 110–117. DOI: `10.1179/1743278215Y.0000000037`.

[273] T. Hanawa. “Metal ion release from metal implants”. In: *Mater. Sci. Eng. C* 24.6-8 (2004), pp. 745–752. DOI: `10.1016/j.msec.2004.08.018`.

[274] E. Zhang, L. Zheng, J. Liu, B. Bai, and C. Liu. “Influence of Cu content on the cell biocompatibility of Ti–Cu sintered alloys”. In: *Mater. Sci. Eng. C* 46 (2015), pp. 148–157. DOI: `10.1016/j.msec.2014.10.021`.

[275] J. C. M. Souza, M. Henriques, W. Teughels, P. Ponthiaux, J.-P. Celis, and L. A. Rocha. “Wear and Corrosion Interactions on Titanium in Oral Environment: Literature Review”. In: *J. Bio- Tribo-Corrosion* 1.2 (2015), p. 13. DOI: `10.1007/s40735-015-0013-0`.

[276] R. Yazdi, H. Ghasemi, M. Abedini, and M. Monshi. “Interplay between mechanical wear and electrochemical corrosion during tribocorrosion of oxygen diffusion layer on Ti–6Al–4V in PBS solution”. In: *Appl. Surf. Sci.* 518.November 2019 (2020), p. 146048. DOI: `10.1016/j.apsusc.2020.146048`.

[277] S. Guadalupe Maldonado, S. Mischler, M. Cantoni, W. J. Chitty, C. Falcand, and D. Hertz. “Mechanical and chemical mechanisms in the tribocorrosion of a Stellite type alloy”. In: *Wear* 308.1-2 (2013), pp. 213–221. DOI: `10.1016/j.wear.2013.04.007`.

[278] L. A. Alberta, J. Vishnu, Y. Douest, K. Perrin, A.-M. Trunfio-Sfarghiu, N. Courtois, A. Gebert, B. Ter-Ovanessian, and M. Calin. “Tribocorrosion behavior of β-type Ti-Nb-Ga alloys in a physiological solution”. In: *Tribol. Int.* 181 (2023), p. 108325. DOI: `10.1016/j.triboint.2023.108325`.

[279] P. Ren, H. Meng, Q. Xia, Z. Zhu, and M. He. “Influence of seawater depth and electrode potential on the tribocorrosion of Ti6Al4V alloy under the simulated deep-sea environment by in-situ electrochemical technique”. In: *Corros. Sci.* 180.June 2020 (2021), p. 109185. DOI: `10.1016/j.corsci.2020.109185`.

[280] N. Espallargas, C. Torres, and A. I. Muñoz. “A metal ion release study of CoCrMo exposed to corrosion and tribocorrosion conditions in simulated body fluids”. In: *Wear* 332-333 (2015), pp. 669–678. DOI: `10.1016/j.wear.2014.12.030`.

[281] A. Łapa, M. Cresswell, I. Campbell, P. Jackson, W. H. Goldmann, R. Detsch, and A. R. Boccaccini. “Gallium- and Cerium-Doped Phosphate Glasses with Antibacterial Properties for Medical Applications”. In: *Adv. Eng. Mater.* 22.9 (2020), p. 1901577. DOI: `10.1002/adem.201901577`.

[282] A. Vieira, A. Ribeiro, L. Rocha, and J. Celis. “Influence of pH and corrosion inhibitors on the tribocorrosion of titanium in artificial saliva”. In: *Wear* 261.9 (2006), pp. 994–1001. DOI: `10.1016/j.wear.2006.03.031`.

[283] D. R. Haynes, S. D. Rogers, S. Hay, M. J. Pearcy, and D. W. Howie. “The differences in toxicity and release of bone-resorbing mediators induced by titanium and cobalt-chromium-alloy wear particles”. In: *J. Bone Jt. Surg. - Ser. A* 75.6 (1993), pp. 825–834. DOI: `10.2106/00004623-199306000-00004`.

[284] M. Kaur and K. Singh. “Review on titanium and titanium based alloys as biomaterials for orthopaedic applications”. In: *Mater. Sci. Eng. C* 102.December 2018 (2019), pp. 844–862. DOI: `10.1016/j.msec.2019.04.064`.

[285] N. Mary, B. Ter-Ovanessian, and B. Normand. “Growth mechanism and repassivation kinetic determinations on stainless steel under sliding: Role of the solution pH and dissolved oxygen concentration”. In: *Wear* 460-461.March (2020), p. 203478. DOI: `10.1016/j.wear.2020.203478`.

[286] R. Priya, C. Mallika, and U. K. Mudali. “Wear and tribocorrosion behaviour of 304L SS, Zr-702, Zircaloy-4 and Ti-grade2”. In: *Wear* 310.1-2 (2014), pp. 90–100. DOI: `10.1016/j.wear.2013.11.051`.

[287] J. F. Archard. “Contact and rubbing of flat surfaces”. In: *J. Appl. Phys.* 24.8 (1953), pp. 981–988. DOI: `10.1063/1.1721448`.

[288] I. Cvijović-Alagić, Z. Cvijović, S. Mitrović, V. Panić, and M. Rakin. “Wear and corrosion behaviour of Ti-13Nb-13Zr and Ti-6Al-4V alloys in simulated physiological solution”. In: *Corros. Sci.* 53.2 (2011), pp. 796–808. DOI: `10.1016/j.corsci.2010.11.014`.

[289] M. Long and H. J. Rack. "Subsurface deformation and microcrack formation in Ti-35Nb-8Zr-5Ta-O(x) during reciprocating sliding wear". In: *Mater. Sci. Eng. C* 25.3 (2005), pp. 382–388. DOI: `10.1016/j.msec.2005.01.027`.

[290] J. E. Chandler, H. H. Messer, and G. Ellender. "Cytotoxicity of Gallium and Indium Ions Compared with Mercuric Ion". In: *J. Dent. Res.* 73.9 (1994), pp. 1554–1559. DOI: `10.1177/00220345940730091101`.

[291] S. Mathews, M. Hans, F. Mücklich, and M. Solioz. "Contact Killing of Bacteria on Copper Is Suppressed if Bacterial-Metal Contact Is Prevented and Is Induced on Iron by Copper Ions". In: *Appl. Environ. Microbiol.* 79.8 (2013), pp. 2605–2611. DOI: `10.1128/AEM.03608-12`.

[292] W. L. Du, S. S. Niu, Y. L. Xu, Z. R. Xu, and C. L. Fan. "Antibacterial activity of chitosan tripolyphosphate nanoparticles loaded with various metal ions". In: *Carbohydr. Polym.* 75.3 (2009), pp. 385–389. DOI: `10.1016/j.carbpol.2008.07.039`.

[293] H. Jin, S. Shi, J. Li, X. Wang, and C. Yang. "A new β-Ti alloy with good tensile properties by the mixed microstructure characteristics of α phase". In: *J. Alloys Compd.* 925 (2022), p. 166755. DOI: `10.1016/j.jallcom.2022.166755`.

[294] S. Ehtemam-Haghighi, Y. Liu, G. Cao, and L. C. Zhang. "Phase transition, microstructural evolution and mechanical properties of Ti-Nb-Fe alloys induced by Fe addition". In: *Mater. Des.* 97 (2016), pp. 279–286. DOI: `10.1016/j.matdes.2016.02.094`.

[295] S. L. Chi-Ucán, A. Castillo-Atoche, P. Castro Borges, J. A. Manzanilla-Cano, G. González-García, R. Patiño, and L. Díaz-Ballote. "Inhibition Effect of Glycerol on the Corrosion of Copper in NaCl Solutions at Different pH Values". In: *J. Chem.* 2014.Figure 1 (2014), pp. 1–10. DOI: `10.1155/2014/396405`.

[296] A. M. Alfantazi, T. M. Ahmed, and D. Tromans. "Corrosion behavior of copper alloys in chloride media". In: *Mater. Des.* 30.7 (2009), pp. 2425–2430. DOI: `10.1016/j.matdes.2008.10.015`.

[297] ISO 5832-3:2021 - Implants for surgery — Metallic materials — Part 3: Wrought titanium 6-aluminium 4-vanadium alloy. 2021. URL: `https://www.iso.org/standard/79626.html`.

[298] Q. Li, J. Li, G. Ma, X. Liu, and D. Pan. "Influence of ω phase precipitation on mechanical performance and corrosion resistance of Ti–Nb–Zr alloy". In: *Mater. Des.* 111 (2016), pp. 421–428. DOI: `10.1016/j.matdes.2016.09.026`.

[299] W. R. Osório, A. Cremasco, P. N. Andrade, A. Garcia, and R. Caram. "Electrochemical behavior of centrifuged cast and heat treated Ti-Cu alloys for medical applications". In: *Electrochim. Acta* 55.3 (2010), pp. 759–770. DOI: `10.1016/j.electacta.2009.09.016`.

[300] Z. Wang, B. Fu, Y. Wang, T. Dong, J. Li, G. Li, X. Zhao, J. Liu, and G. Zhang. "Effect of Cu Content on the Precipitation Behaviors, Mechanical and Corrosion Properties of As-Cast Ti-Cu Alloys". In: *Materials (Basel).* 15.5 (2022), p. 1696. DOI: `10.3390/ma15051696`.

[301] L. Ren, X. Xu, H. Liu, K. Yang, and X. Qi. "Biocompatibility and Cu ions release kinetics of copper-bearing titanium alloys". In: *J. Mater. Sci. Technol.* 95 (2021), pp. 237–248. DOI: `10.1016/j.jmst.2021.03.074`.

[302] ISO 5832-2:2018 - Implants for surgery — Metallic materials — Part 2: Unalloyed titanium. 2018. URL: `https://www.iso.org/standard/69907.html`.

Acknowledgements

This endeavor would not have been possible without my supervisor at IFW Dresden, Prof. Dr. M. Calin. You offered me the opportunity of starting my Ph.D. journey, providing invaluable trust, freedom, constant support, and encouragement. You created a highly stimulating environment, which greatly contributed to my development as a researcher and as a person. I particularly thank Prof. Dr. K. Nielsch from IFW Dresden and TU Dresden for agreeing to supervise this work.

I want to thank all the colleagues from my research group for the stimulating discussions and for the invaluable time spent together at work and outside work: group leader Dr. A. Gebert, Dr. S. Pilz, Dr. A. Hariharan, Dr. J. Vishnu, Dr. P. Goldberg, Dr. V. Shtefan, Dr. C. Querebillo, N. Fernández Navas, F. Sgarbi Stabellini, A. Akman, A. Jose. I would like to extend my sincere gratitude to Dr. S. Pilz, for his invaluable support throughout my Ph.D., and to Dr. J. Vishnu, whose expertise and knowledge provided me with valuable lessons and insights. I would also like to express my gratitude to Dr. P. Goldberg for his diligent proofreading of the German version of the abstract. I am indebted to several people in IFW Dresden: Prof. Dr. J. Freudenberger, Dr. K. Neufeld, Dr. L. Giebeler, M. Otto, K. Hennig, A. Voß, H. Bußkamp, N. Geißler, B. Bartusch, K. Baumgart, D. Sven, D. Seifert. For assistance with various organizational issues, I thank B. Präßler-Wüstling. Special thanks to Prof. B. Normand, Prof. B. Ter-Ovanessian, Prof. J. Chevalier, and Dr. A.-M. Trunfio-Sfarghiu for welcoming me in their research facilities at INSA Lyon (France). I also want to thank their whole research group, especially Dr. K. Perrin and J. Quibel. I would like to extend my sincere thanks to Dr. N. Courtois and Dr. A. L. Chopard-Lallier for giving me the opportunity of exploring the universe of Anthogyr S.A.S. during my secondment in France.

And now comes the great BIOREMIA family. The whole Ph.D. journey would not have been the same without you all. First, many thanks go to all supervisors, from both academia and industry, because you created an incredible multidisciplinary team of enthusiast close-knit young researchers, and friends. Special thanks go to the project coordinator and my supervisor, Prof. Dr. M. Calin, and to the project manager A. Hönemann. For fruitful research collaborations, I want to thank Prof. C. Lekka and Y. Fortouna from the University of Ioannina (Greece), Prof. M. Trobos, Prof. A. Palmquist, P. Giraldo Osorno, and A. Turner from the University of Gothenburg (Sweden), Dr. A. Gebert and A. Akman from IFW Dresden (Germany), Prof. J. Sort, Dr. E. Pellicer, M. Escobar, and A. Bartkowska from the University of Barcelona (Spain), and, last but not least, Y. Douest (Anthogyr S.A.S., France), Dr. N. Courtois (Anthogyr S.A.S., France) and Prof. B. Ter-Ovanessian (INSA Lyon, France).

I want to thank one by one my BIOREMIA fellows, with no particular order. We have spent an absolutely invaluable, special and memorable time together during our meetings, workshops and secondments around Europe. Aleksandra, my polish great friend. Kirti, I am glad you largely enjoyed living in my sweet country. Sebastião, I found a precious friend in you, we lived tons of adventures together. Yannick, *on s'est bien amusés ensemble, tu es un bon ami.* Miguel, I spent fantastic time with you, but Italian wine is better than Portuguese. Tim, I admire your resilience during our crazy workshops' nights. Paula, more than a colleague, a true supporter. Adnan, I appreciated discussing, collaborating and sharing the office with you. Fei-Fan, you truly are fun. Michael, I am very impressed by your wine-induced talkativeness. Adam, I just say *Poivron Bleu.* Yohan, *mon voisin et ami de France, j'espère qu'on ne se perd pas de vue.* David, I truly learned a lot from you, and there is one special video from our night in that remote bar in Ioannina which is unforgettable. Juan José, there is also a video, a precious pearl, of the two of us from the same night in Ioannina, let's not forget about it.

Lastly, I would like to express my heartfelt gratitude to my beloved ones.
Alle Nonne.

Ludovico

Appendices

This section includes supporting data and additional information relevant to the research presented in this thesis.

A Alloy Nomenclature

Relative proportions of elements in an alloy can be expressed either in atomic percent (at.%) or in weight percent (wt.%). Generally, the percentage is not shown for the first element, but is made explicit for the subsequent elements. In the present work, the following formula M_1–xM_2, where the element content x precedes the general element M, is used for fractions in weight percent (wt.%), while the formula M_1–M_{2x}, where x follows M as subscript, refers to alloys expressed in atomic percent (at.%). For example, Ti–45Nb is an alloy with 55 wt.% of Ti and 45 wt.% of Nb, whereas Ti–Nb_{30} refers to the same alloy but expressed in at.%, with 70 at.% of Ti and 30 at.% of Nb. In the present work, the alloys were prepared starting from the commercial Ti–45Nb alloy, therefore, the following nomenclature is used: (100-x)(Ti–45Nb)–xM, where M = Ga/Cu and x = content in wt.%.

B Mechanical Properties of Alloys in As-Cast State

Preliminary studies on the mechanical behavior (microhardness $HV_{0.1}$ and Young's modulus E^{US}, investigated by ultrasonic method) of the alloys in as-cast state are hereby reported. These results expand and complement the findings presented in Chapter 4.

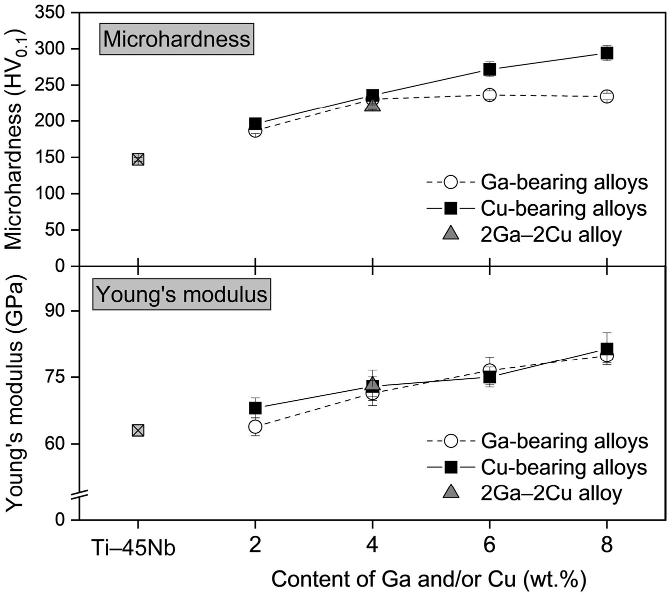

Figure B1: Microhardness and Young's modulus (determined by ultrasonic pulse-echo method) of the nine alloys in as-cast state, compared to Ti–45Nb.

C Tensile Samples Not Suitable for Testing

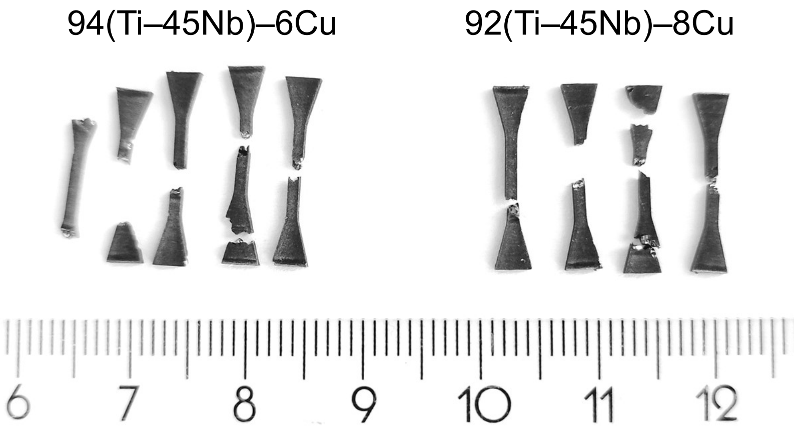

Figure C1: Samples of 94(Ti–45Nb)–6Cu and 92(Ti–45Nb)–8Cu homogenized alloys for tensile testing immediately after machining.

D Properties of Medical Grade Ti–6Al–4V ELI

Medical grade $\alpha+\beta$ Ti–6Al–4V ELI (ASTM grade 23) alloy, provided by Anthogyr S.A.S. (France) in the shape of disks (thickness = 1 mm, $\varnothing$ = 15 mm), is used as received. Microstructural, mechanical and corrosion properties are investigated according to the procedures reported in Chapter 3, and the results are hereby reported. Tribocorrosion results are discussed in Chapter 6.

Table D1: Microstructure and mechanical properties of Ti–6Al–4V ELI.

Microstructure	$\alpha+\beta$	
$HV_{0.1}$	354 ± 6	
E^{US}	111 ± 0	GPa
E (tensile)	117 ± 2	GPa
σ_y	1025 ± 20	MPa
σ_{UTS}	1074 ± 19	MPa
σ_f	768 ± 14	MPa
ε_{max}	13 ± 1	%
δ_e	5.51 ± 0.16	MJ m^{-3}

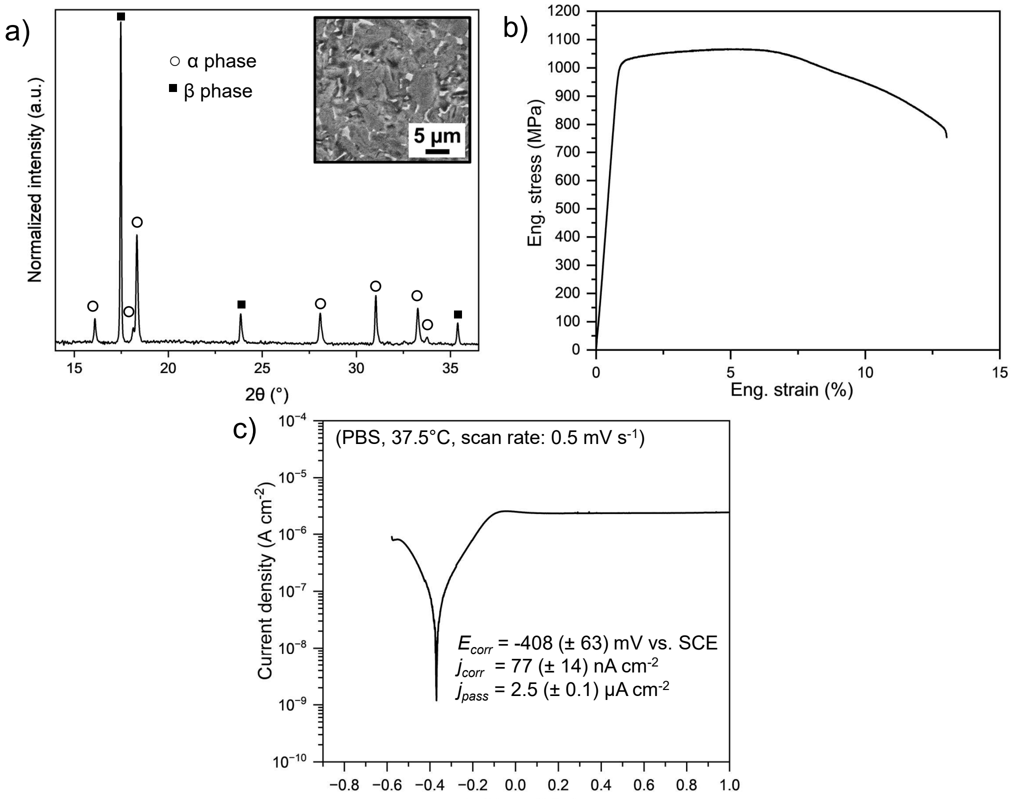

Figure D1: (a) XRD diffractogram, inset: SEM micrograph, (b) engineering stress-strain curve in tension, and (c) potentiodynamic polarization with relevant electrochemical parameters.

E Optical Microscopy of the Alumina Pin

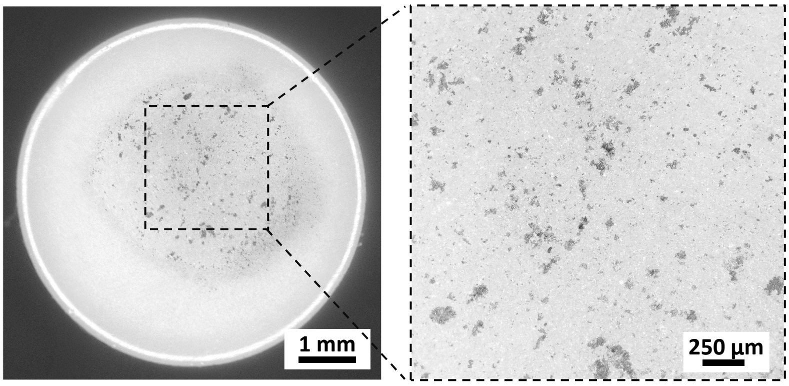

Figure E1: Optical micrograph of the alumina (Al_2O_3) pin observed after sliding against 96(Ti–45Nb)–4Ga alloy in PBS solution during a tribocorrosion test (Chapter 6).

F EDX Mapping of Aged Ti–Nb–Cu Alloys

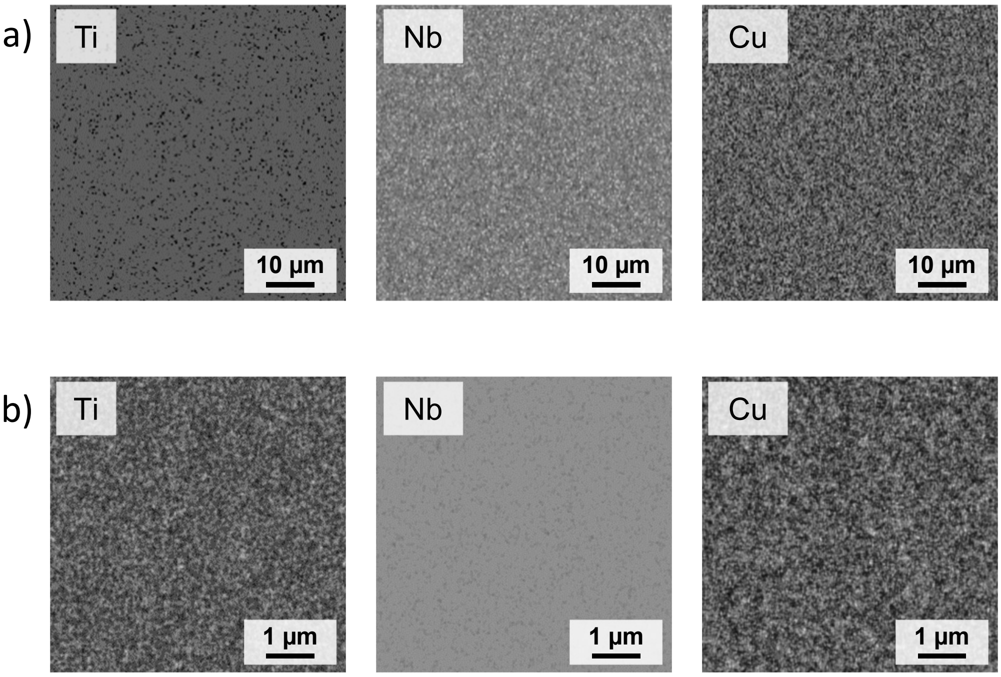

Figure F1: EDX mappings showing elemental distribution of Ti, Nb and Cu of 96(Ti–45Nb)–4Cu alloy in two aged conditions: (a) STQ & AG 425°C and (b) STQ & AG 640°C. Bright areas contain higher concentration of the element indicated. These results supplement the findings in Chapter 7.

G Experimental Method: Cell Adhesion Assay

Biological studies, reported in Chapter 8 and whose methodology is here described, were performed by P. Giraldo Osorno, colleague of BIOREMIA EU project, from the Department of Biomaterials, University of Gothenburg (Sweden).

The human monocytic cell line THP-1 (ATCC) was grown in RPMI 1640 medium supplemented with 10% FBS, 0.5% β-mercaptoethanol (Sigma Aldrich) and 1% penicillin/streptomycin (PEST) solution (Gibco Life Technologies) in a 37°C humidified incubator with 5% CO_2. Cells between passages 6 and 9 were used. THP-1 monocytes were stimulated with 10 ng/ml phorbol-12-myristate-13-acetate (PMA) for 48 h to induce macrophage differentiation, followed by 24 h of resting time in fresh media without PMA. After being differentiated, THP-1 macrophages were seeded at a density of 700 000 cells/ml on the surface of the material in Nunc 24-well plates (Thermo Fisher Scientific) in 1 ml media. The number of adhered cells was assessed after 24 h. The wells were gently washed twice with PBS to remove nonadherent nonviable cells before the addition of NucleoCounter® lysis and stabilization buffer (200 + 200 μl). Lysed samples were loaded in a Nucleocassette™ precoated with fluorescent propidium iodide, which stains cell nuclei, and the results were then quantified using a NucleoCounter® NC-200 (ChemoMetec A/S). Two independent experiments were performed, with two technical replicates. Metallic disk specimens ($\varnothing = 9$ mm, thickness = 2 mm) were mechanically ground both sides up to P2400 SiC paper, ultrasonically rinsed in water and sterilized in pure ethanol.

This page was intentionally left blank.